PROPAGATION AND ATTENUATION OF SEISMIC RAYLEIGH WAVES ALONG SINGLE PATHS IN SCOTLAND

COLIN D. MACBETH, B.A. (OXON)

DOCTOR OF PHILOSOPHY

UNIVERSITY OF EDINBURGH

1983

ACKNOWLEDGEMENTS

The research, and the composition of this thesis were executed while a member of the Global Seismology Unit, I.G.S. Edinburgh and the Geophysics department of Edinburgh University. For this, I am grateful to C.W.A. Browitt for allowing me to use the facilities of the unit, K.M. Creer for accepting me as a student in his department and the Natural Environment Research Council for providing me with a three year studentship.

I am extremely grateful to my supervisor P.W. Burton for suggesting the notion of a single-station attenuation measurement, and for his continual support, encouragement and constructive criticism.

I would like to express my gratitude to G. Neilson and D.C. Booth who were most obliging in assisting me with a variety of problems. During the research, I derived great benefit from many illuminating discussions with the research students in G.S.U., namely J. Singh, A.J.W. McDonald, G. Roberts and I.G. Main. I must also thank R.W. McGonigle for providing many useful computer programs and assisting me with problems in the earlier stages of the research. I am most appreciative of the help received from C.J. Fyfe, who answered a wide variety of computing problems and made freely available his considerable software library. A special thanks is extended to J.B. Young and A. Douglas for providing me with a copy of their synthetic seismogram program 'BIGE', and for tolerating my questions on its operation. I also wish to thank R.F. King for providing various information regarding the LISPB experiment.

ABSTRACT

A new technique is developed for measuring the depth distribution of the shear wave specific attenuation factor (Q_β^{-1}) in the earth, from the recording of a Rayleigh wave which has travelled along a single isolated path. This technique is applied to data in the frequency range 0.7 - 5.5 Hz generated by small underground explosions, underwater explosions, and an earthquake of magnitude 3.7 (M_L), recorded during the LISPB experiment and on the LOWNET local network in Scotland. In parallel with this, group velocity characteristics of the data are analysed to obtain estimates of the distribution of shear wave velocity (β) laterally and at depth in the earth.

The single-station technique utilizes an expression for the amplitude spectrum as a series of multiplicative linear functions, each characterized by a finite set of parameters. The components which describe each particular source are investigated to obtain the smallest set of parameters which can accurately represent the excitation of the waves in the medium. To reduce the number of parameters specifying the spectrum, group velocity data are inverted to yield single-station and regional β depth profiles. Fundamental mode group velocity data generated by underwater explosions in Kirkcaldy Bay recorded on LOWNET show a marked correlation with the surface geological expression, β in the top 400m of the single-station profiles ranging from 1.5 to 2.1 km/sec. First and second higher mode group velocity data generated by the earthquake yield well resolved regional profiles down to depths of 17km, β increasing from around 3.1

km/sec to 3.7 km/sec. These studies also elucidate some interesting features of high frequency Rayleigh wave propagation.

The explicit form of each function composing the amplitude spectrum is used to identify the most important effects. These are measured by the extent of the fluctuations in the spectrum resulting from an a priori perturbation (representing a realistic error) in each parameter. The results of this analysis guide the development of the single-station methodology for each source. The most influential parameters pertain to the Q_β^{-1} distribution and source strength. The inverse time constant of the time action and shot depth for underground and underwater explosions respectively are also important. The earthquake is the most complex source, having a large number of important variables. The method consists of correcting for the least important functions (such as instrument and medium response), and obtaining estimates for the remaining parameters by mapping the expected functional form onto this corrected spectrum.

A preliminary survey of the attenuation is attempted using an approximate formula relating the frequency of the spectral peak to an average Q_β^{-1} value. Applying the single-station method to the underground and underwater data recorded on the LISPB and LOWNET arrays respectively, yields well resolved single-station Q_β^{-1} values of between 0.02 - 0.09 in the top 400m of the upper crust for up to 50km from the source. The values at greater depths are weakly constrained, but the Q_β^{-1} estimates imply a decrease to < 0.01 between 400 - 800m depth, followed by an increase to 0.04 below 800m. The underground explosion spectra are modelled most accurately by the theory. The

inverse time constant and shot depth are also discerned. There is no observable correlation between the surface geological expression and the spatial distribution of single-station Q_β^{-1} measurements. The fundamental mode and higher mode data generated by the underwater explosion and earthquake respectively recorded on LISPB, could not be modelled. However an average of the earthquake source function is obtained by fitting to the decay of spectral amplitude with distance, from which a seismic moment of 9.10^{15} Nm is calculated, in good agreement with a value obtained using the surface wave magnitude.

More refined techniques to isolate the prominent Rayleigh modes on high frequency recordings are required before accurate Q_β^{-1} values and hence the exact mechanism of attenuation can be elucidated.

CONTENTS

APPENDIX D....COMPUTER PROGRAMS

D.1 Program 'WINDOW'

D.2 Program 'MLR'

D.3 Program 'SSQ'

REFERENCES

ENCLOSURE : MacBeth, C.D. & Burton, P.W., 1983. Single-station Q : attenuation of 2Hz Rayleigh waves along single isolated propagation paths in Scotland, Annales Geophysicae, 1, No.3, 223 - 228.

In human works, tho' labour'd on with pain,
A thousand movements scarce one purpose gain;
So Man, who here seems principal alone,
Perhaps acts second to some sphere unknown,
Touches some wheel, or verges to some goal;
'Tis but a part we see, and not a whole.

An Essay on Man

Alexander Pope

To Fiona -

'For they are each in each, and cannot stand
Dividually'.

CHAPTER 1

INTRODUCTION

1.1 Preview

Seismic waves of finite energy, generated by natural or man-made events, are emitted with a characteristic amplitude and shape which depend on the particular source of the disturbance. These waves are modified due to the passage through the earth, this being determined mainly by the distribution of the velocity and attenuative properties of the rocks, and the type of waves. Attenuation distorts the waveform, and in particular, reduces the amplitude of the signal with distance (below that of geometric spreading), until it eventually reaches the threshold below which it cannot be detected. Were it otherwise, every signal emitted by seismic sources would ring forever around the earth, and seismology would be an impossible science. Attenuation is important as it is more sensitive to changes in the earth's structure produced by thermal or chemical activity than is elasticity. Unfortunately, accurate amplitude information is more difficult to obtain than the travel-times of waves, due to scattering, mode conversions, focussing/defocussing, source characteristics, and many other effects. These tend to obscure the amplitude variation due to the true energy dissipation, and the measurements of this property based on recordings at many stations may be biased, and have large uncertainties. A measurement taken along a single event-station path minimizes many of these undesirable effects. Single event-station measurements can be used to monitor the

magnitude and extent of horizontal variations in the dissipative properties. These features should be reliably elucidated by Rayleigh waves, which suffer relatively less degradation due to inhomogeneities than body waves.

The main objective of the research covered in this thesis is to develop and apply a new technique for measuring the attenuation of a seismic Rayleigh wave, along single isolated paths in Scotland, using the recordings of events at single seismograph stations. These 'single-station' estimates will be achieved by utilizing a simple factorization of the amplitude of the Fourier transform spectrum of a Rayleigh wave-packet, into functions which represent the effects of the source, propagation of waves in the earth, and the recording instrument. These phenomena will be investigated to identify the most important physical parameters shaping the theoretical amplitude spectrum. The observations will then be corrected for the remaining spectral effects, and the resulting curve specified by a small number of simple variables. Estimates of the variables will be obtained by mapping the observed spectral shape onto the expected functional form. The technique shall be applied to Rayleigh wave data generated by small underground explosions, underwater explosions, and an earthquake recorded on the vertical component instruments of local networks within Scotland; the observations covering the frequency range 0.7 - 5.5 Hz. A prerequisite of the technique is knowledge of the seismic velocity structure under the corresponding region in Scotland. This will be determined by inverting group velocity dispersion measurements.

The velocity and attenuation results shall provide detailed information on the shallow anelastic crustal structure, and a measure of the lateral variations in the anelastic seismic wave properties in

the shallow crust of Scotland.

1.2 Theoretical Spectrum of a Rayleigh Wave

The development of the technique for measuring single-station attenuation is based on the expression of the theoretical amplitude of a Rayleigh wave as a series of independent multiplicative functions, each representing the effect of a particular phenomenon on the waves. In this section we describe the underlying assumptions from which this expression is derived, and interpret the general requirements of the single-station estimate in terms of this description.

Seismic Rayleigh waves emitted by a source of excitation and recorded at the free surface of the earth close to the event, are formed from the interference of compressional (P) and shear (SV) wavefields which have resonated in the source and near-source environment. As the disturbance propagates radially outwards it is distorted by the many complex phenomena involved with the structure and composition of the medium between the epicentre and seismometer. These disguise and degrade the source signature and dominate the signal at large distances. The measured displacements generally depend on angular frequency, distance, azimuth, mode number, and the variety of parameters characterizing the propagation medium and the source.

The majority of techniques based on spectral measurements for estimating specific geophysical parameters, rely on the ability to separate the effects of the various phenomena by representing each as a 'filter' with an apparent impulse response. The composite effect of these is synthesized by their commutative product in the frequency

domain. This cascade is justified if the effective filters obey the laws of linearity and stationarity.

The vertical component of complex spectral displacement $A_z^*(\omega)$ recorded and output on a surface seismometer at an epicentral distance r from a source embedded in a horizontally stratified and anelastic earth model, with homogeneous and isotropic layers, can be written

$$A_z^*(\omega) = M_z^*(\omega;\ r,\phi;\ h,s_j;\ \alpha_\ell^*,\beta_\ell^*,\rho_\ell,t_\ell)P^*(\omega)I^*(\omega) \qquad (1.1)$$

ϕ is the azimuth with respect to the event, h the depth of the source, and $s_j : j = 1,n$ corresponds to a set of n parameters characterizing the source. α_ℓ^*, β_ℓ^* : $\ell = 1,m$, are the complex intrinsic body wave-speeds in each of the m layers and are given by (Lee and Solomon, 1979)

$$\alpha^* = \alpha_R + i\alpha_I$$

$$\beta^* = \beta_R + i\beta_I$$

where α_R, α_I, β_R, β_I are real quantities. ρ_ℓ : $\ell = 1,m$ is the density in each layer (we assume that there are no losses due to imperfect inertia (Anderson et al., 1965)), and t_ℓ : $\ell = 1,m$ are the layer thicknesses. As is usual in surface wave studies, the medium represents the average anelastic structure for the source-receiver travel path.

$M_z^*(\omega)$

This represents the interaction of a general source with the medium in which it is contained, and the effect of propagation through the common source-receiver model. The function includes information about the extent

to which different frequencies in the generated wavefields combine at the free surface to form the Rayleigh waves. In this general form, the factor also contains the source terms describing the character and nature of the excitation in space and time, geometric spreading, phase shifts due to propagation, and the attenuation of the waves.

The most common method of representing the source mechanism of a small event, is by a distribution of equivalent body forces acting at a point. This is the force system which would have to be applied in the absence of the source to produce the same radiation. These force equivalents are useful physical tools for studies as they replace the complicated non-linear interactions of the source by an equivalent set of linear interactions. Although used most prevalently, this method leads to many algebraic complexities for involuted sources (such as large earthquakes) and media. In such cases, other representations are more suitable (see Hudson,1969a). $M_z^*(\omega)$ depends on the geometry and orientation of the source force system. In general it is a function of azimuth for earthquakes, whereas for an underground explosion the radiation pattern is usually circularly symmetric.

Assuming that all the body forces have the same time variation $s_T(t)$, with Fourier transform spectrum $S_T^*(\omega)$, this function can be factorized from $M_z^*(\omega)$ along with the magnitude or strength of the action S_o. In the case of an explosion, S_o is related to the yield, and for earthquakes it is related to the average slip of the fault surfaces. If the source time function is non-zero at long periods, the seismic moment of the event is defined and is given by S_o. If the source has a finite spatial extension, the overall disturbance must be related to an integral of the various contributions

from the source region. For most systems an additional multiplicative function of frequency and azimuth $S_F(\omega;\phi)$ can be used to approximate this effect. Mathematically the separation of these factors is not permitted for an arbitrary heterogeneous medium. For far-field Rayleigh waves (for which the cylindrical wavefronts are approximately plane) in a weakly anelastic medium ($\alpha_I << \alpha_R$, $\beta_I << \beta_R$), we may isolate the effects of anelasticity in the function

$$D(\omega) = \exp(\gamma(\omega)r) = \exp(-\omega r/2U(\omega)\, Q_\gamma^{-1}(\omega)). \qquad (1.2)$$

$U(\omega)$ is the group velocity, $Q_\gamma^{-1}(\omega)$ is the Rayleigh wave specific attenuation, and $\gamma(\omega)$ is the attenuation coefficient. $Q_\gamma^{-1}(\omega)$ is dimensionless and is a more fundamental parameter than $\gamma(\omega)$, although the latter is simpler to measure and most often used. To satisfy causality, the body wave velocities are required to be frequency dependent. This leads to an additional dispersive term in the phase of the complex spectrum.

The amplitude spectrum $A_z(\omega)$ and phase spectrum $\phi_z(\omega)$ are related to the complex displacement $A_z^*(\omega)$ via

$$A_z(\omega) = |\, A_z^*(\omega)|$$

$$\phi_z(\omega) = arg(\, A_z^*(\omega)) \quad .$$

In this thesis we concentrate on only the amplitude of spectral displacement, for which we can now make the approximation

$$M_z(\omega;\, r,\phi;\, h,s_j;\, \alpha_\ell^*,\beta_\ell^*,\rho_\ell,t_\ell) \simeq M_z(\omega;\, r,\phi;\, h,s_j;\, \alpha_\ell,\beta_\ell,\rho_\ell,t_\ell)D(\omega) \qquad (1.3)$$

where $M_z(\omega)$ is evaluated for an elastic earth model.

The attenuation coefficient $\gamma(\omega)$ can be expanded explicitly in terms of the body wave specific attenuation factors $Q_{\alpha\ell}^{-1}$ and $Q_{\beta\ell}^{-1}$ in each homogeneous layer (Burton, 1977)

$$\gamma(\omega) = \sum_{\ell=1}^{m} \left(\frac{\partial k}{\partial \alpha_\ell} \frac{\alpha_\ell}{2} Q_{\alpha\ell}^{-1} + \frac{\partial k}{\partial \beta_\ell} \frac{\beta_\ell}{2} Q_{\beta\ell}^{-1}\right) \qquad (1.4)$$

where k is the frequency dependent Rayleigh wavenumber for the elastic model. Q_α^{-1} and Q_β^{-1} are related to the complex wavespeeds (Lee and Solomon, 1979)

$$Q_\alpha^{-1} = 2\alpha_I/\alpha_R$$
$$Q_\beta^{-1} = 2\beta_I/\beta_R \quad .$$

The amplitude spectrum can be further factorized by extracting the geometric spreading function for Rayleigh waves in the far-field

$$M_z(\omega;\ r,\phi;\ h,s_j;\ \alpha_\ell,\ \beta_\ell,\ \rho_\ell,\ t_\ell) = r^{-\frac{1}{2}} M_z(\omega;\phi;\ h,s_j;\alpha_\ell,\beta_\ell,\rho_\ell,t_\ell).$$

$M_z(\omega)$ now represents the Rayleigh wave spectral response of the medium to a particular source mechanism, and $s_j : j = 1,n$ are the orientation parameters of the force system.

$P^*(\omega)$

This function represents the departure of the properties of the Rayleigh wave propagation path from the idealized model assumed above. It is related to changes in the elastic and anelastic parameter distributions in the earth along the path. Further, it contains any effects of diffraction or scattering from surface irregularities or inhomogeneities,

lateral refractions, focussing and defocussing, mode conversions, and transmission coefficients between different sections of the path.

Surface wave amplitudes generated in one particular medium, and recorded in a geologically different environment may be computed using a transmission coefficient which corrects the observed displacement spectrum back to the source medium (Bache et al., 1978). These coefficients depend on the nature of the boundary between the two models, and are in general frequency dependent. A specific form of $P(\omega)$ corresponding to this effect will be shown later in Section 6.2.1.

Lateral variations in velocity have a much larger effect on the spectral amplitudes than on the velocity of the Rayleigh waves (McGarr, 1972). These can result in horizontal refractions which cause focussing or defocussing (depending on the type of variation), and interference due to waves travelling along multiple paths from epicentre to station. Focussing is the convergence or concentration of waves travelling nearly the same path (McGarr, 1969b). This causes an increase in the absolute spectral amplitude, but has no effect on the waveform. However, interference between two closely separated wave packets travelling along different paths alters the spectrum, modulating it by a function dependent on the path length difference (Pilant and Knopoff, 1964).

$\underline{I^*(\omega)}$

This function represents the frequency response of the recording system which converts the ground displacement into a fluctuating voltage at the seismometer output. This is fully discussed

in Section 1.3 for specific networks of seismometers.

Equation 1.1 can now be generalized for spectral amplitude

$$A_z(\omega) = S_o S_T(\omega) S_F(\omega;\phi) M_z(\omega;\phi;\ h, s_j;\ \alpha_\ell, \beta_\ell, \rho_\ell, t_\ell) r^{-\frac{1}{2}}\ P(\omega)\ D(\omega)\ I(\omega) \tag{1.5}$$

where the conditions under which this factorization is valid are described above. Each of the functions in this equation are characterized by a finite set of parameters, connected with some physical interpretation of the effect they represent. S_o, $S_T(\omega)$, and $S_F(\omega)$ can be parametrized if the behaviour of the source is understood. $M_z(\omega)$ can be determined if the source type, position, orientation, and the distribution of elastic constants with depth are known. $D(\omega)$ depends on the distribution of elastic and anelastic constants with depth. $I(\omega)$ for a seismograph system is usually specified by several determinable parameters. The propagation path correction $P(\omega)$ can be evaluated only under certain conditions.

From the theory above, the requirements of a method for measuring single-station attenuation can be clearly visualized. Fundamentally, the function $D(\omega)$ must be separated from all other effects by estimating values for each of the variables representing the other functions. In practice, the parameters are known to different degrees of certainty, and only a partial isolation can be achieved. Accordingly, a procedure must be constructed for obtaining estimates of the attenuation and the remaining parameters. This would be considerably simplified if the number of parameters specifying the amplitude spectrum are reduced to a minimum. This can be achieved by determining accurate values for some of the variables using prior information, a priori reasoning, or

prudential modelling of each effect.

We have already reduced the number of variables describing the amplitude spectrum to a finite set by approximating the velocity, density, and attenuation gradients in the earth by a piecewise continuous model. The velocity structure can be further simplified by utilizing a relationship between compressional wave velocity α and shear wave velocity β

$$\alpha = \left[\frac{2(1-\sigma)}{1-2\sigma}\right]^{\frac{1}{2}} \beta \qquad (1.6)$$

where σ is Poisson's constant and is approximately 1/4 for most rocks in the earth. In some regions of Scotland a distribution of this constant with depth is available (Assumpção and Bamford, 1978). A connection can also be made between density and shear velocity (Stuart, 1978)

$$\rho = 0.286\beta + 1.736 \qquad (1.7)$$

Similarly, when modelling the attenuation properties we follow Burton and Kennett (1972)

$$Q_\alpha^{-1} = \frac{4}{3}\left(\frac{\beta}{\alpha}\right)^2 Q_\beta^{-1} \qquad (1.8)$$

which implies no dissipation attributable to the bulk modulus (Anderson et al., 1965). From this, Equation 1.4 can be re-written in terms of Q_β^{-1}

$$\gamma(\omega) = \sum_{\ell=1}^{m} K_\ell(\omega) Q_{\beta\ell}^{-1} \qquad (1.9)$$

where $$K_\ell(\omega) = \frac{1}{2}\left(\frac{\partial k(\omega)}{\partial \alpha_\ell} \frac{4\beta_\ell^2}{3\alpha_\ell} + \frac{\partial k(\omega)}{\partial \beta_\ell} \beta_\ell \right)$$

α_ℓ being determined from Equation 1.6.

These reductions are justified as the Rayleigh waves are in general more sensitive to changes in the shear constants than any other parameters (Bloch et al., 1969). Throughout the thesis we use the set of anelastic parameters :- β_ℓ, $Q_{\beta\ell}^{-1}$, t_ℓ : $\ell = 1,m$. A further reduction is made possible by independently inverting Rayleigh wave dispersion data to obtain the shear velocity structure. This step will be covered in Chapter 4.

1.3 The Rayleigh Wave Data

The data used in this thesis are derived from recordings of Rayleigh waves generated by a mixture of small local sources, consisting of underground explosions, underwater explosions, and an earthquake in Scotland. This separates into three distinct event-station configurations. In the first set, a number of apparently identical underwater explosions generate Rayleigh waves which are recorded at a variety of different azimuths and distances. The latter two configurations consist of underground and underwater explosions positioned co-linearly with respect to a line of stations, and an earthquake source offset from this line.

Between February 1979 and March 1980 a number of small underwater explosions were shot in the Kirkcaldy Bay region of the Firth of Forth, and recorded on the Lowland Network (LOWNET) in Scotland. Eight events of apparently similar yield and depth were selected, their epicentral

coordinates being within three kilometres. Table 1.1 lists the shot times and geographical coordinates of each explosion, while Figure 1.1 shows the common epicentral area with respect to the array. LOWNET consisted of eight stations, each being equipped with a vertically mounted Willmore Mk. II seismometer, in addition to which the Edinburgh station EDI had two horizontally mounted seismometers. The LOWNET stations were re-equipped with Willmore Mk.III seismometers in 1981.

The 1974 Lithospheric Seismic Profile in Britain (LISPB) (Bamford et al., 1976, 1977, 1978) provided surface wave recordings of small explosions. Although intended for body wave studies, Evans (1981) showed that the seismograms could be accessible to Rayleigh wave analysis. Due to a combination of noise, inability to separate phases at small distances, instrument failure, drop-outs and exclusion of the slower surface waves at large distances, the data were restricted to that generated by 4 out of 29 shots. These consisted of two underwater explosions (N1 and N2), and two underground explosions (L1 and L2). The shot times and geographical coordinates are listed in Table 1.1, and the relative position of the LISPB line and the explosions are shown in Figure 1.1. The underwater explosion events were fired in Loch Eriboll near the northern end of the array, while the land shots were at Dunkeld, between the ALPHA and BETA segments. The surface wave data of Evans (1981) proved to be of sufficient quality to enable accurate measurements of frequency dependent group velocity, inter-station phase velocity, and the specific attenuation factor. Analysing these according to the surface geological expression provided important information at high resolution of velocity and attenuation in the crustal structure down to a depth of approximately

Kirkcaldy Bay Explosions

SHOT	DATE	TIME (hr:m:sec)	LATITUDE (^{o}N)	LONGITUDE (^{o}W)
1	14/6/79	10:36:40.3	56.12	3.00
2	1/2/80	12:21:37.3	56.12	2.98
3	21/3/80	9:56:59.8	56.12	2.98
4	6/2/79	12:44:22.1	56.15	2.99
5	8/2/79	16:10:18.4	56.11	3.00
6	6/4/79	11:38:36.8	56.11	2.99
7	8/6/79	12:51:00.8	56.11	2.97
8	12/6/79	12:16:29.0	56.12	3.00

LISPB Explosions

L1	30/7/74	19:01:11.4	56.60	3.68
L2	1/8/74	19:01:14.8	56.60	3.68
N1	4/8/74	20:58:49.8	58.58	4.64
N2	5/8/74	21:12:02.6	58.58	4.64

TABLE 1.1: Shot times and geographical coordinates for underwater explosions recorded on LOWNET array, and underwater and underground explosions recorded on LISPB.

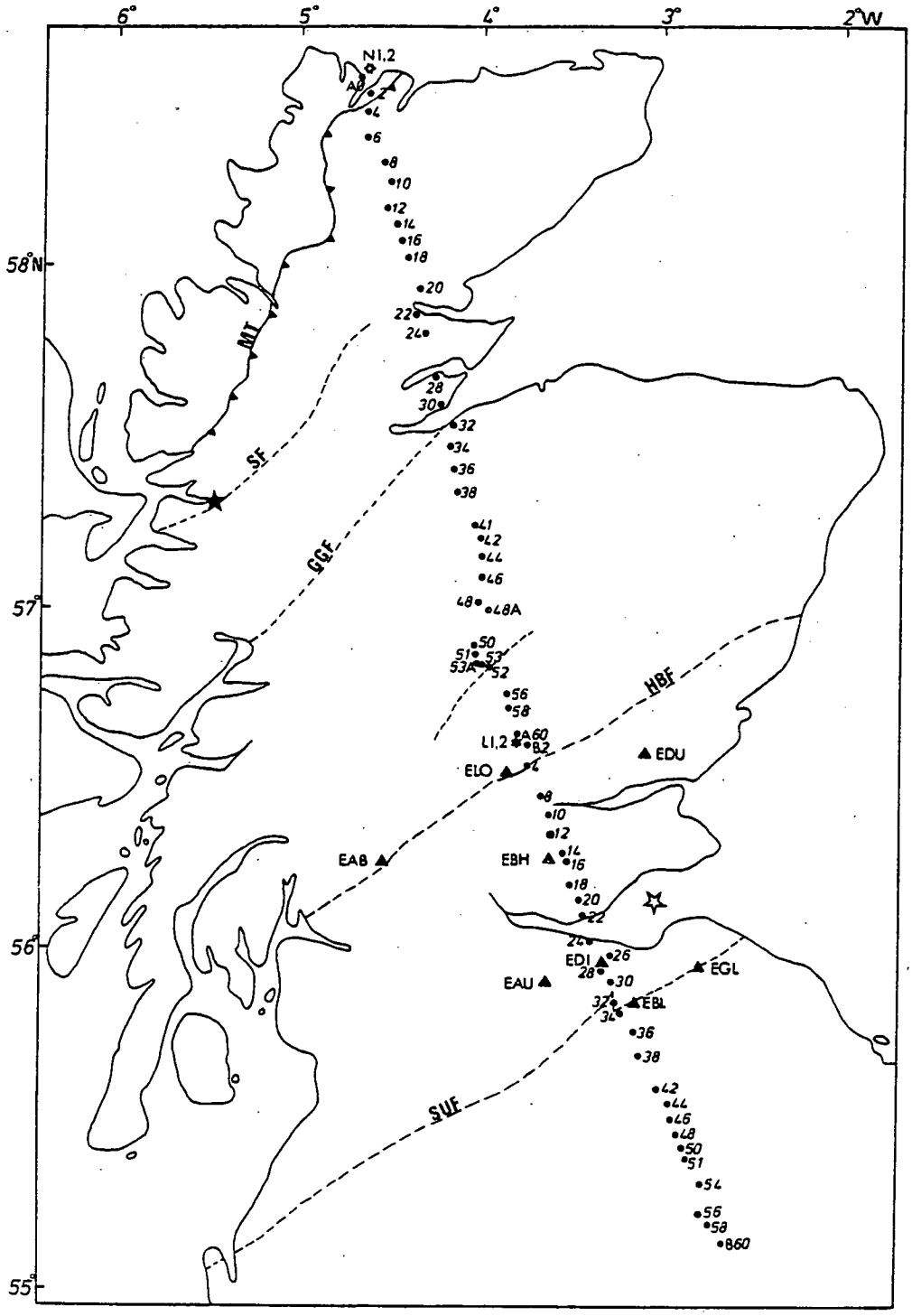

★ Kyle earthquake
☆ Kirkcaldy Bay shots
✡ Underwater explosions
✱ Underwater explosions

MT Moine Thrust

▲ LOWNET stations
. LISPB stations

SUF Southern Uplands Fault
GGF Great Glen Fault
HBF Highland Boundary Fault
SF Strathconan Fault

Figure 1.1. Relative positions of LISPB and LOWNET stations, Kyle earthquake epicentre, Kirkcaldy Bay shots, and LISPB explosions in Scotland.

2 km.

We have chosen this data set as the velocity models were readily available and attenuation models existed which could corroborate the single-station values.

The mobile LISPB array consisted of about sixty stations, each operating either an FS60, HS10, or a Willmore Mk. II seismometer. The underground and underwater explosions were 'dispersed', that is, for convenience the source package was split into smaller charges, and these positioned in a co-linear fashion with uniform spacing. In addition to this, the underwater explosions were fired at the seismically efficient 'optimum depth' in the water. These terms and their significance regarding spectral shape will be fully explained in Chapter 2.

In August 1974 a swarm of earthquakes occurred in the Kintail region of NW Scotland, with a maximum surface wave magnitude of 4.6. One earthquake of the series, hereafter referred to as KEQ (M_L = 3.7), was recorded on the LISPB ALPHA and BETA arrays, giving a range of epicentral distances 79 - 300 km, and an azimuthal range of 15 - 146°. The relative position of KEQ with respect to the lines is shown in Figure 1.1. Kaminski et al. (1976) determined the hypocentre as well as a plane layered velocity model for the region by fitting to first and second P-arrival data. Assumpção (1981) relocated the earthquake with P and S arrivals using the LISPB P-velocity model of Bamford et al. (1978), and the shear velocity model of Assumpção and Bamford (1978). The structure at the epicentre was assumed on geological grounds to be similar to that of the LISPB profile north of the Loch Tay Fault (Figure 1.1). The focal solution was given by Assumpção (1981)

6th August 1974, Origin Time 18hr 17min 36.93 ± 0.2secs

Latitude 57.227°N ± 2 km

Longitude 5.338°W ± 3 km

Depth 10.6 ± 2 km

allowing for uncertainties in the crustal structure. The depth was over 3 km shallower than the Kaminski et al. (1976) model. Well correlated signal waveforms implied that the Kintail events had the same focal mechanism. A composite focal plane solution was obtained for these events using polarities of the first P-arrivals. The predominant rupture mechanism was left lateral strike-slip with a strike of 52° of N, and a dip of 74° S, but the latter was not well constrained as it depended on essentially one data point. The Strathconan fault system appeared to be associated with the swarm.

Within the working seismic pass-band, the recording, radio transmission, and play-back systems employed for the LOWNET and LISPB arrays can be assumed to be independent of frequency. The seismic spectrum is therefore limited by the shape of the transfer function of the seismometer. The general amplitude response is described by

$$I(\omega) = \frac{K\omega^3}{\left[(\omega_o^2-\omega^2)^2 + 4\eta\omega_o\omega(\omega_o^2-\omega^2)\right]^{\frac{1}{2}}} \qquad (1.10)$$

where K is the transducer constant, ω_o the natural frequency of the instrument, and η is the damping constant. Evans (1981) gives the particular values of η and ω_o appropriate to the seismometers mentioned above.

1.4 Techniques for Estimating the Attenuation of Rayleigh Waves

The following is a discussion of the variety of techniques available to compute the Rayleigh wave attenuation coefficient, or alternatively the Rayleigh wave specific attenuation factor, which exploit the relatively simple form of Equation 1.5. The majority of methods presented have been applied to teleseismic observations as there is a sparsity of work reporting attenuation measurements of local events using the spectral factorization. The main difference between the two sets of observations is the extent and nature of the lateral variations in the earth. Equation 1.5 is a general expression which holds for both local and teleseismic observations. The main emphasis in this section is utilization of this equation for attenuation measurements, and single-station techniques in this context. The methods presented below assume there are no irregular changes in the propagation path, $P(\omega) = 1$. Further, in all cases the spectra have been corrected for geometric spreading and instrument distortion, and source finiteness is neglected unless otherwise mentioned. Spectral amplitudes are not usually measured as continuous functions, but as discrete values at particular frequency harmonics. For this reason the functions of frequency are to be recognized as being discrete.

Perhaps the simplest and most effective method for estimating a regional average of attenuation is that of Burton (1974). The decay of the logarithmic spectral amplitude A_{ik} at the kth station and ith frequency is given by Equations 1.2 and 1.5.

$$\ell n(A_{ik}) = \ell n(S_o S_{Ti} S_{Fi} M_i) + \gamma_i r_k \quad . \tag{1.11}$$

This equation has the effect of separating the source terms from the attenuation terms. Assuming that there are no circular asymmetries in the radiation pattern from the source, a least squares linear fit to the decay for a number of stations over a range of distances, and at particular frequencies, gives $\gamma(\omega)$ and an estimate of $S_o S_T(\omega) S_F(\omega) M(\omega)$. The attenuation is an average over the region enclosed by the station array. Theoretically, this technique should only be applied to those explosions or cavity collapses which are not accompanied by release of tectonic strain energy. However, Burton and McGonigle (1979) show that in some cases it can be applied to earthquakes with equal success. The larger the number of stations, the more reliable the measurements become.

This method is extremely useful for examining lateral variations in attenuation with a co-azimuthal line of stations. The earth is divided into a number of homogeneous provinces on the basis of geophysical and geological arguments, each of which is intersected by the array. The above technique is then applied to all stations within each province to obtain a measure of the attenuation in each formation. The method has the advantage in that any frequency dependent transmission effects between provinces group with the source terms, and thus do not effect the estimate of attenuation. Evans (1981) applied this method to the small explosions recorded on LISPB.

The large scatter of spectral amplitudes when applying this method to earthquakes may be reduced by accounting for the azimuthal amplitude variation which arises from the function $S_F(\omega;\phi)M(\omega;\phi)$. This requires a known focal mechanism, focal depth, fault length, and velocity-depth model. In the method of Tsai and Aki (1969) the source finiteness is neglected, and the source time action is assumed

to be a heaviside step function. Compensating the spectral amplitude at each station and frequency for the effect of the earthquake radiation pattern, Equation 1.11 becomes

$$\ell n \frac{A_{ik}}{S_{Ti}\, M_{ik}} = \ell n(S_o) + \gamma_i\, r_k \quad . \tag{1.12}$$

From this, a regional average $\gamma(\omega)$ and seismic moment S_o can be simultaneously determined by fitting a straight line to the observations. Herrmann and Mitchell (1975) extended this method using

$$\ell n \frac{A_{ik}}{M_{ik}} = \ell n(S_o\, S_{Ti}) + \gamma_i\, r_k \tag{1.13}$$

to obtain an estimate for $S_o S_T(\omega)$ and $\gamma(\omega)$. This was applied by them to Rayleigh waves generated by earthquakes and explosions. Correig et al. (1982) used this method to determine primary estimates from earthquake-generated Rayleigh waves. The source function was then combined with $M(\omega;\phi)$ and single-station attenuation values were obtained by dividing the observed amplitudes by this factor.

Mitchell (1973) corrected earthquake spectra using a nominal attenuation coefficient, and estimated the focal solution (source parameters which shape $M(\omega;\phi)$) by a trial and error method. Using these estimates and a step source time action, a least squares procedure fitted the radiation pattern to the observed pattern to obtain a regional average $\gamma(\omega)$ and S_o for fundamental and higher mode surface waves. The attenuation coefficient obtained was not sensitive to the inaccuracies in determining the earthquake source solution.

A similar technique was pursued by Mitchell (1975) and Yacoub (1981) for nuclear explosions in which there was a superimposed

tectonic strain release component, giving a departure from the ideal circular pattern. The theoretical amplitude

$$A_{ik} = A_{ei}(1 + F_i \sin(2\phi_i)) \exp(\gamma_i r_k) \qquad (1.14)$$

was fitted to the observed Rayleigh wave amplitudes, using a non-linear iterative least squares technique (detailed in Yacoub, 1981). Values for the explosion spectral function $A_e(\omega)$, average attenuation coefficient $\gamma(\omega)$, relative strength of tectonic component $F(\omega)$, and orientation of the double couple mechanism $\phi(\omega)$ were estimated. No knowledge of the source functions S_o, $S_T(\omega)$ or $M(\omega)$ was necessary as this information was contained in $A_e(\omega)$.

All the above methods result in an average dissipative characteristic over the broad region enclosed by the seismic array. A large number of stations yielding one attenuation value ensure a reliable result. However, this may have large statistical errors due to lateral variations in attenuation, effects of refraction, reflection and multi-pathing. The cause and extent of these fluctuations depend on the frequencies of the waves and the geographical region crossed by the paths. These effects also produce a bias of the estimates, and the measured attenuation values become dependent on the station configuration. Discrete measurements by a single event-station method are useful in monitoring the extent of these fluctuations. There is a particular advantage when only a few stations record an event, as the relative amplitudes may not be reliable. Therefore, methods of evaluating the attenuation along a single event-station path are a necessary extension of the solution to the problem of lateral heterogeneity. There are basically two types of single-station technique:

(1) those which yield attenuation values along single paths using many stations

(2) those which are applied to only an isolated event-station path.

In the first category is the two-station method (Tsai and Aki, 1969). For stations k and k' on the same great circle, the azimuthal effects of the source are identical and the waves share a part-common path. Thus

$$\gamma_i = \frac{\ell n(A_{ik}/A_{ik'})}{(r_k - r_{k'})} \quad . \qquad (1.15)$$

Canas and Mitchell (1978) applied this technique to Rayleigh wave data to measure lateral variations. The method was extremely effective, but demanded a special configuration for the two stations and source, which restricted the available data.

Correig and Mitchell (1980) developed a reference station method, whereby a set of event-station attenuation coefficients $\gamma_k(\omega)$ were obtained relative to the attenuation coefficient $\gamma_o(\omega)$ measured between some reference station and the event. All the amplitudes were initially corrected for the medium response $M(\omega;\phi)$, and again the focal mechanism, depth, and velocity model had to be known. The difference between the attenuation coefficients for the kth station and the reference station was

$$\gamma_{ik} - \gamma_{io} = \left\{ \ell n\left(\frac{A_{ik}}{A'_{io}} \right) - \ell n\left(\frac{S_{Fik}}{S_{Fio}} \right) \right\} / r_k \qquad (1.16)$$

where $A'_{io} = A_{io} \exp[(\gamma_{io}(r_o - r_k)]$. r_k was the distance of the kth station from the event, and r_o the distance of the reference station from the source. The source finiteness function could not be eliminated

because of the size of the events.

In the second category is the Mitchell (1981) 'frequency-ratio' method. The source time function of the event is assumed known. At each station, the spectral amplitude at the ith frequency ω_i with respect to the amplitude at some reference frequency ω_o is given by

$$\frac{A_i}{A_o} = \left[\frac{M_i\ S_{Ti}}{M_o\ S_{To}}\right] \exp\ [-(\gamma_i - \gamma_o)r] \quad . \tag{1.17}$$

The technique senses the change in the spectral shape due to the attenuation function. The problem with this method is that a well determined attenuation coefficient at the reference frequency is required to evaluate the complete attenuation function, which is therefore only as accurate as the chosen value. Also there is no scope for comparisons between stations.

In conclusion, there were basically two classes of techniques outlined above for obtaining the attenuation. The first set of methods used a large number of stations usually spread out over a broad region and only an average for this area was obtained. The techniques should be mainly confined to events with circular radiation patterns or co-azimuthal recordings. Methods of single-station measurement sub-divided into two groups. The two-station method reduced the constraint of common attenuation for all paths, but the application was limited to special geometric arrangements. With single event-station measurements utilizing a reference frequency or station, the estimated attenuation was only as accurate as the value at the reference point.

Clearly what we require is an absolute measure of attenuation along an isolated path, the technique being applied to each station

independent of its neighbours.

1.5 Measurement of Lateral Variations

This section examines the way in which single-station measurements of velocity or attenuation can be used to extract information regarding the extent of the lateral variations in the earth, and how dependent this is on the station configuration.

No practical theory has yet been developed for computing the dispersion or attenuation in a generally heterogeneous model. Regionalization techniques approximate the earth by sub-dividing into a number of homogeneous provinces. The simplest system for examining the lateral variations is a co-azimuthal line of stations. As mentioned above, a linear array intersecting a variety of provinces can be used to obtain the attenuation coefficients in each province. A linear fit of propagation time with distance for stations within a particular province also gives a measure of the average group velocity within that formation. Again, the method is attractive in that the velocity results are not influenced by delays associated with boundary transmission and the source, reflected only in the intercept of the line fit to the observations.

The most general system is an azimuthal distribution of stations around an event, each passing through different homogeneous provinces and sampling different path lengths. For this type of system one usually discounts any lateral refractions, amplitude changes, or time delays at the boundaries between provinces. The group velocity dispersion U_{ik} and attenuation coefficient γ_{ik} at the ith frequency along the kth mixed-path are linearly related to the pure provincial

values via

$$\frac{1}{U_{ik}} = \sum_q \left(\frac{L_{kq}}{U^p_{iq}} \right) \tag{1.18}$$

$$\gamma_{ik} = \sum_q L_{kq} \gamma^p_{iq} \tag{1.19}$$

where L_{kq} is the fraction of the total surface wave path through each distinct formation, U^p_{iq} and γ^p_{iq} are group velocity and attenuation coefficient for the qth province. The solution of such a linear system is quite straightforward. The resolution of each pure provincial value depends on the number and length of the paths traversing that region. This technique has been applied to group velocity and phase velocity data by Yu and Mitchell (1979), and to group velocity data by Feng and Teng (1983). The large uncertainties in attenuation coefficient measurements preclude accurate calculations of pure provincial attenuation using this formula. These formulae will be used in Chapter 4 in connection with group velocity measurements, and in Chapter 6 in connection with comparing single-station and multi-station attenuation measurements.

1.6 Outline of Research Covered

The main intention of this thesis is to develop and apply a technique for estimating attenuation from the spectrum of a Rayleigh wave travelling along a single event-station path, using Equation 1.5. The method will be applied to data generated

by small underground explosions, underwater explosions, and an earthquake, recorded on local networks in Scotland, within the frequency range 0.7 - 5.5 Hz.

To extract the dissipative properties, a thorough survey of the source functions and medium response must be covered with the aim of representing these efficiently with the minimum number of parameters. For this, the source functions will be described, and effects which shape the source spectral imprint for these particular events will be reviewed. Explosion sources shall be described in Chapter 2, and earthquakes in Chapter 3.

In Chapter 4 measurements of group velocity dispersion will be inverted to yield velocity - depth structures. These will be used to compute the medium response and attenuation function. The velocity analysis will be undertaken in the light of the discussion on inhomogeneities. Interesting aspects of the seismograms which might help to paint a picture of the source function shall be highlighted.

Having parameterized the source spectral shape, parameters describing the source, medium, and instrument will be investigated in Chapter 5, to examine which are the most 'important' in shaping the overall spectral amplitude; the definition of the word 'important' being included. This chapter uses these results and the theory of the preceding chapters to guide the development of a technique to estimate the event-station attenuation along a single isolated path. These methods will be applied to the Rayleigh wave spectral data in Chapter 6. The extent to which Equation 1.5 models the true amplitude spectra is then revealed. In the final chapter these results shall be evaluated collectively to ascertain the success with which we have estimated the spectrum and lateral variations in the earth.

CHAPTER 2

UNDERGROUND AND UNDERWATER EXPLOSION SOURCE FUNCTIONS

2.1 Introduction

The amplitude spectrum of a seismic Rayleigh wave is basically influenced by three separate contributions from the seismic source. The spectral medium response $M_z(\omega)$ represents the process of interaction between the source mechanism and the surrounding medium, and the subsequent production of Rayleigh waves. If the source is described by a distribution of body forces, this function is the impulse response of the medium to a unit force system, and depends on the source geometry, orientation, and depth, in addition to the distribution of elastic constants with depth. The function $S_T(\omega)$ is the Fourier transform of the time action of the force system and S_o is the amplitude or strength of this action. These three factors combine multiplicatively to produce the source imprint on the wave spectra. In circumstances in which the finite dimensions of the source are important, an extra factor $S_F(\omega)$ must be included to represent the effect. Each term depends on the type of source which excites the Rayleigh waves.

In this chapter and the following one, the variety of physical interactions which shape these functions for the events recorded in this thesis will be described and examined with the aim of constructing a set of parameters which accurately represent the effects of

each source. In view of the overall objective of this work, which is to devise a method to measure single-station attenuation, an emphasis will be placed on using the minimum number of variables to represent these effects. The sources consist of single underwater explosions, a dispersed array of 'optimum depth' underwater explosions, a dispersed array of underground explosions in boreholes, and a small local earthquake with surface wave magnitude of 3.7, recorded in the frequency range 0.7 - 5.5 Hz.

2.2 Underground Explosions

2.2.1 Introduction

Early work on underground explosion source functions was concerned with chemical explosions in connection with seismic prospecting. Due to the advent of new and more predictable seismic sources for investigations, the majority of these studies are of the past. In the last two decades a great deal of literature has been published on the modelling of seismic displacements from underground nuclear explosions, especially in relation to the discrimination from earthquakes. The variety of results and phenomena discussed below are drawn from literature on nuclear and chemical explosions of different yields and initial energy densities, and observed for different epicentral distances and wave phases. These, however, can be used to obtain a uniform view of the explosion source if the principle of similarity between events is invoked: seismic sources of the same type are physically similar, and therefore have identical mechanisms of seismic excitation whether they are large or small. In practice, for observations taken outside

the largest source dimension, the source effects can be related by approximate laws for which length and time scale as the cube root of yield (Carpenter, 1967). The discussion below will be entirely general, unless otherwise specified.

2.2.2 Physical Interactions of the Source with the Medium

The initiating disturbance is in the form of a sharp pressure impulse confined to the explosive-medium boundary. For a chemical explosion the impulse from the primary detonator generates a shock compression which initiates a secondary explosive. The end product is a high pressure gas within an explosive cavity and an intense shock wave propagating radially outward from the cavity wall.

The shock wave pulse propagation is non-linear, and a large fraction of its initial energy is dissipated as mechanical and chemical work in plastic deformation and cracking or fracturing. These inelastic processes eventually reduce the amplitude of the pulse to below the elastic limit. The surface which marks this transition is known as the equivalent radiator surface. The zones of importance in the above interactions are delineated in Figure 2.1.

Simultaneous with the shock wave generation, the gas pressure does mechanical work on the surrounding rock resulting in an outward displacement of the wall. This motion ceases when the gas pressure is in equilibrium with the resisting stress field of the rock in the inelastic zone and the external lithostatic pressure. The radius of the new region is called the cavity radius r_c. O'Brien (1967b) found the empirical relationship

$$r_c = 0.4\ H\ W^{1/3} \qquad (2.1)$$

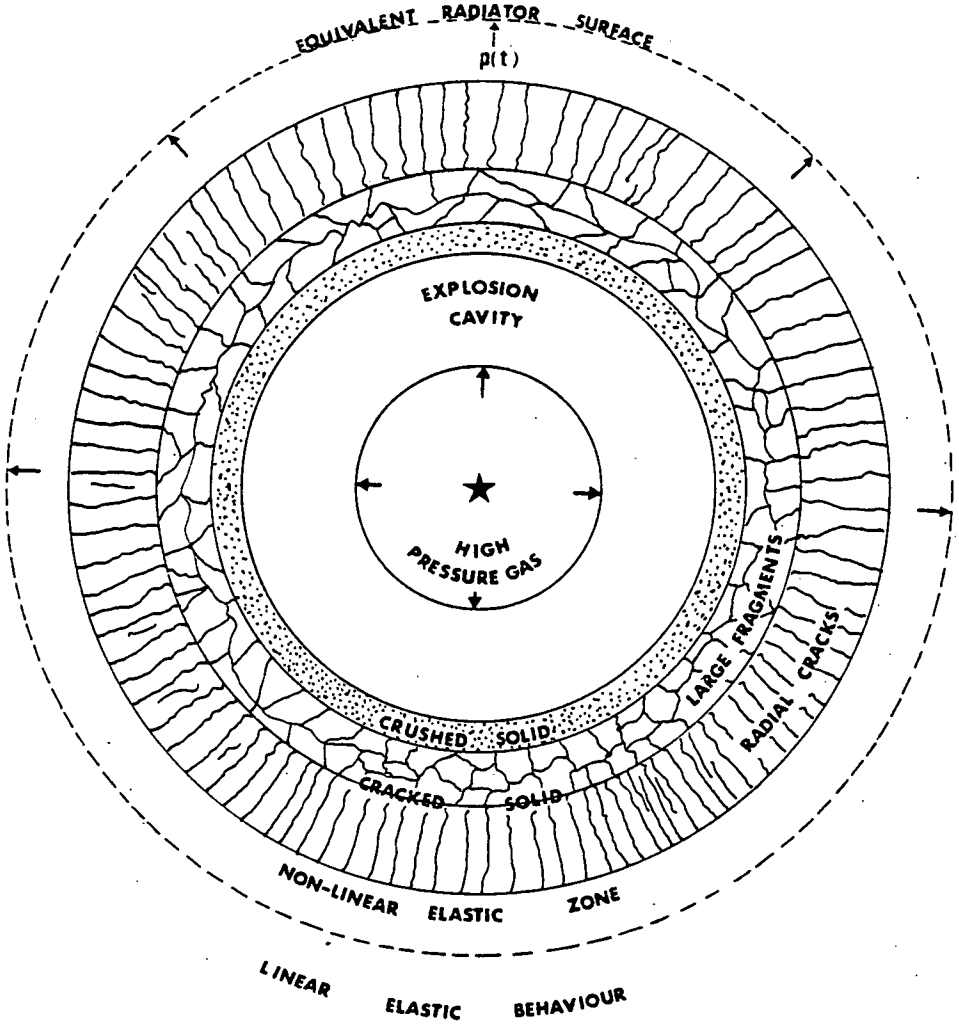

Figure 2.1. Schematic diagram of nonlinear and inelastic zones around an underground explosion (after Aki et al., 1964).

where W is in kg of TNT, and H is a medium dependent quantity in the range 0.18 - 0.52 - this covers materials from hard granite to soft sandstone. The radius of the equivalent radiator surface $r_{e\ell}$ is two or three times the cavity radius.

If the non-linear explosion process is symmetric, the source can be represented by a spherical cavity of radius $r_{e\ell}$ whose internal surface is subject to a uniform pressure pulse $p(t)$. For long wavelengths this generates a wavefield equivalent to three mutually orthogonal double couples without moment (Figure 2.2a); the time-action $s_T(t)$ of the force system being proportional to the time history of the spherical stress field at the cavity boundary.

In practice there are gross departures from this idealized geometry, for example an elongated charge placed in a drilled borehole. However, if the seismic wavelengths are much larger than all the source dimensions, then the Rayleigh wavefield generated by the underground source is approximately equivalent to that from a spherical radiator.

The model is however inadequate in explaining SH and Love waves generated by the event, and the asymmetry of observed radiation patterns. A variety of mechanisms have been proposed to model these features. Each accounts for aspects that the others do not, but none adequately explain all the observations. Massé (1981) presented a critical review of these models, and suggested that a combination of several mechanisms may provide a solution. These complications are not considered further due to the range of possible models and the increase in the number of parameters specifying the explosion which these entail.

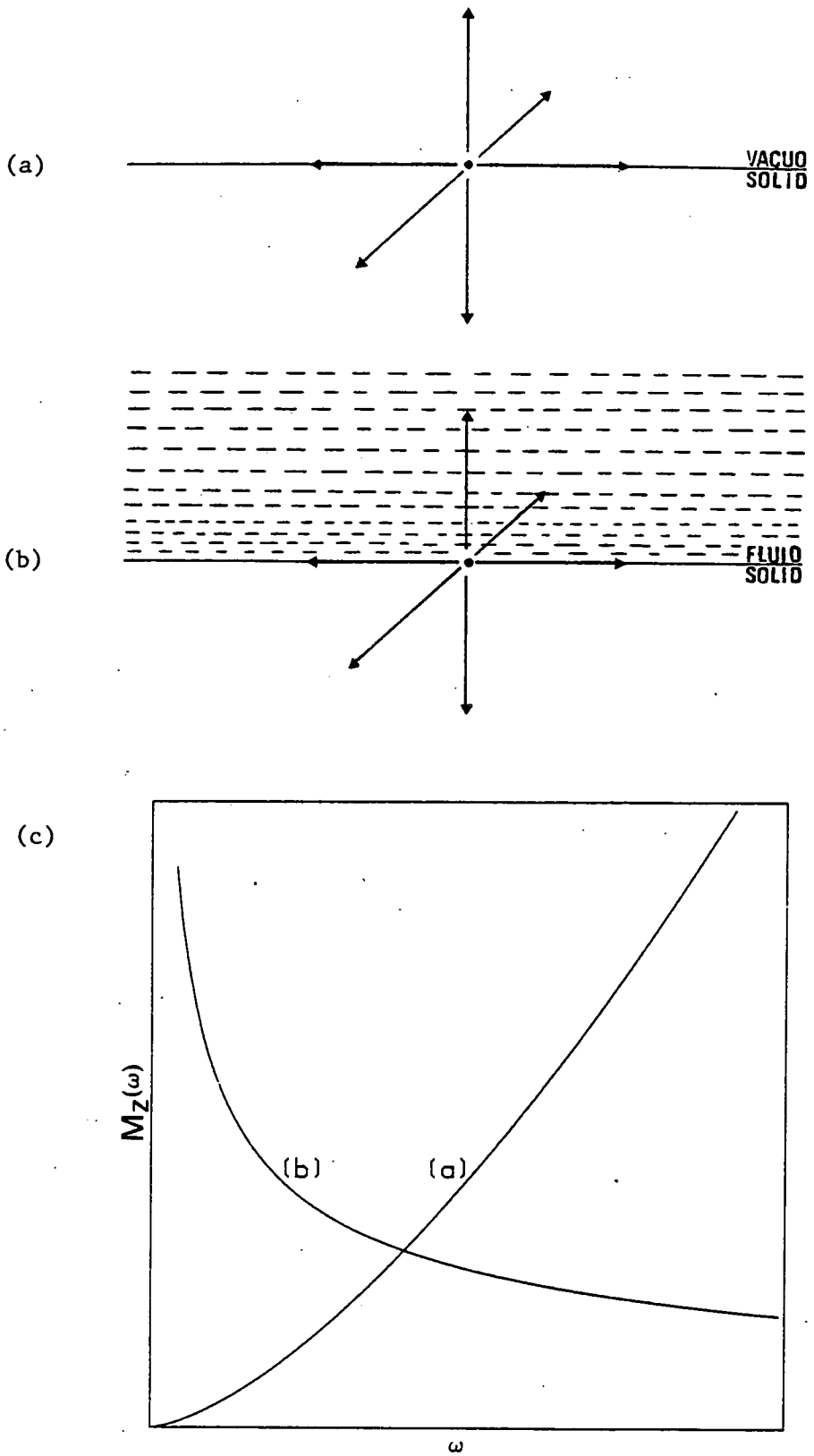

Figure 2.2. Equivalent body force distribution and simple source media for (a) an underground explosion, (b) an underwater explosion, and (c) corresponding frequency dependent medium responses to those systems.

2.2.3 Rayleigh Wave Medium Response

The underground explosion medium response function corresponding to a homogeneous, isotropic, unstressed and semi-infinite source medium is specified by a small number of descriptive parameters. The vertical component of the spectral response of this medium to excitation by a dilatational source of unit magnitude at a depth z_s is given by the analytic expression calculated in Appendix A.2, which can be written

$$M_z(\omega) = G\,\omega^{3/2}\,e^{-\omega m z_s} \tag{2.2}$$

where G and m are dependent on the elastic constants of the solid. This function is monotonically increasing for a surface source (Figure 2.2c), implying that high frequency waves interact most strongly to produce Rayleigh motion. A finite source depth reduces the high frequency spectral content. A multi-layered medium response depends on many more parameters than those described above. The function is sensitive to the contrasts between the elastic constants in different layers. A formula to compute this medium response for a general source is presented in Appendix A.4.

2.2.4 Source Finiteness Effect

If the underground explosion is effectively a point source, the strength and Fourier transform of the time action of each element in the explosive mechanism are directly related to the spectral amplitude of the spherical pressure pulse $P(\omega)$ at the elastic radius via

$$S_o S_T(\omega) = \frac{\pi \alpha^2 \rho r_{e\ell}^3}{\mu} |P(\omega)| \qquad (2.3)$$

where α is the compressional wave velocity, ρ the density, and μ the shear modulus of the rock in the source region. The radius of the equivalent radiator surface is important at high frequencies, and the effect of source finiteness is to introduce an additional frequency dependence (Rodean, p. 57, 1971; Harkrider, 1964)

$$S_o S'_T(\omega) = \frac{\pi \alpha^2 \rho r_{e\ell}^3}{\mu} \frac{|P(\omega)|}{[(1-\Omega^2)^2 + 4\Omega^2\zeta^2]^{\frac{1}{2}}}$$

where $\Omega = \omega/\omega_o$, ω_o is the natural frequency of the cavity ($\omega_o = \beta\pi/2r_{e\ell}$) and ζ is the damping ratio β/α. From this, we define the finiteness function

$$S_F(\omega) = \frac{1}{[(1-\Omega^2)^2 + 4\Omega^2\zeta^2]^{\frac{1}{2}}} \qquad (2.4)$$

$S_F(\omega)$ acts as a transfer function relating the pressure at the spherical boundary to the induced displacement field in a homogeneous medium, and depends on the shear wave velocity of the surrounding rock and the elastic radius which is in turn related to the explosive yield. The function is a unit constant at low frequencies (or small $r_{e\ell}$), and a roll-off at the natural frequency is followed by a $1/\omega^2$ decay at high frequencies (Figure 2.3).

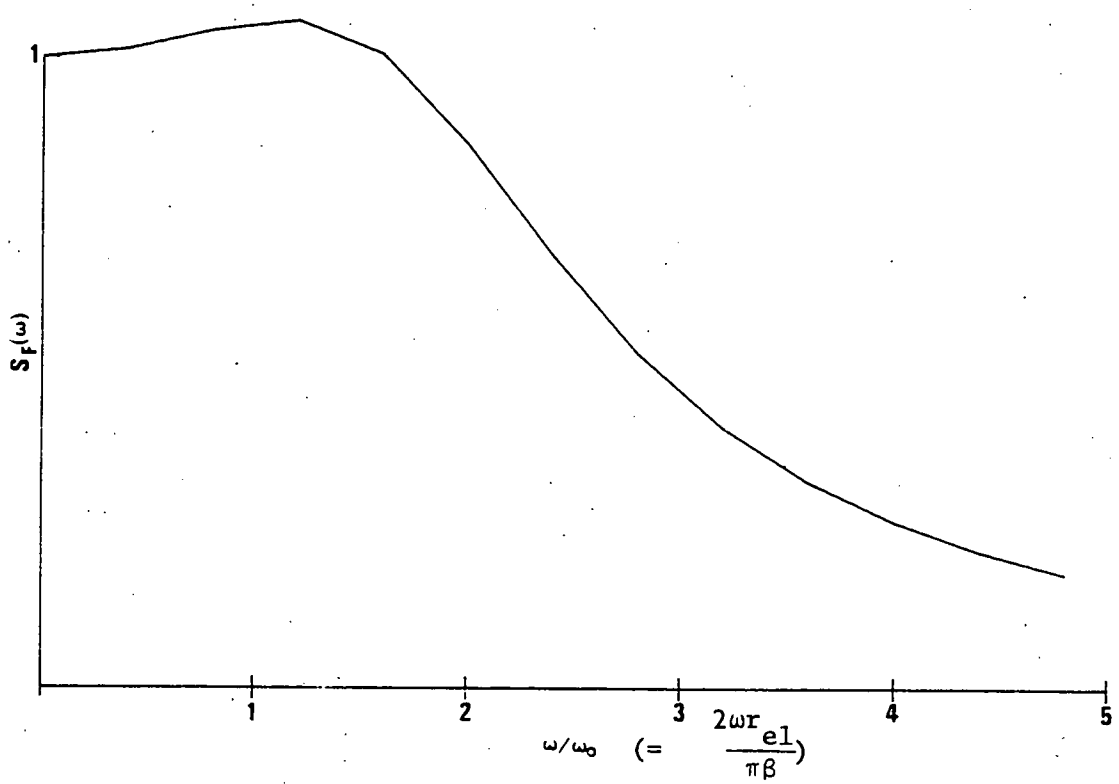

Figure 2.3. Finiteness function $S_F(\omega)$ for an underground explosion. r_{el} is the elastic radius of the source and β is the shear velocity of the surrounding rock.

2.2.5 Spectrum of the Source Time Action

There are a large number of proposed time variations for the pressure field at the equivalent radiator surface. Although some theoretical predictions of the pressure function have been made by following the shock wave step-by-step through the non-linear zone (Holzer, 1966; Cherry and Hudlow, 1966), numerical computations have not been successful in resolving a particular model. Table 2.1 lists the most notable time functions, their corresponding spectra, and the authors concerned.

The simplest model of the source pressure is a step function in time (Sharpe, 1942; Blake, 1952; King et al., 1972). However this is physically unreasonable as it implies an excessive amount of long period energy, and a function which is invariant with explosive yield. A more realistic form is the exponentially decaying step, which is characterized by an inverse time constant. Near-field measurements have confirmed this pulse shape for the small charges used in seismic prospecting (O'Brien, 1967b; Morris, 1950; Peet, 1960; Schenk, 1971).

Near-field velocity measurements from nuclear explosions by Werth and Herbst (1963), implying considerable overshoot in the source functions, stimulated the development of a number of more complex models. Haskell (1967) mapped a family of simple analytic functions described by two adjustable parameters onto these recordings. From free-field observations on a number of explosions, Mueller and Murphy (1971) considered an analytic approximation to the pressure pulse which also involved two variables. Other models worth mentioning are the von Seggern and Blandford (1972) and Helmberger and Hadley (1981) revisions of Haskell's (1967)

	Time function	Spectral function	Reference
	Step function		
1	$H(t) = \begin{cases} 0 \text{ for } t < 0 \\ 1 \text{ for } t \geq 0 \end{cases}$	$\frac{1}{\omega}$	Sharpe (1942), Blake (1952), King et al. (1972)
2	$H(t)\exp(-\omega_T t)$	$(\omega^2{}_T+\omega^2)^{-\frac{1}{2}}$	O'Brien (1967b), Morris (1950), Peet (1960), Schenk (1971).
4	$H(t)[1-\exp(-\omega_T t)f(\omega_T t)]$ where $f(\omega_T t) = 1+\omega_T t + \frac{(\omega_T t)^2}{2!} + \frac{(\omega_T t)^3}{3!} - b(\omega_T t)^4$	$\frac{[(1+24b)^2\omega^2 + \omega^2{}_T]^{\frac{1}{2}}}{\omega(\omega^2 + \omega^2{}_T)^{5/2}}$	Haskell (1967)
5	$H(t)(b\exp(-\omega_T t)+ 1)$	$\frac{[(b+1)^2\omega^2 + \omega^2{}_T]^{\frac{1}{2}}}{\omega(\omega^2+\omega^2{}_T)^{1/2}}$	Mueller & Murphy (1971)
6	$H(t)[1-\exp(-\omega_T t)f(\omega_T t)]$ where $f(\omega_T t) = 1+\omega_T t - b(\omega_T t)^2$	$\frac{[(1+24b)^2\omega^2+\omega^2{}_T]^{\frac{1}{2}}}{\omega(\omega^2+\omega^2{}_T)^{3/2}}$	von Seggern & Blandford (1972) (Revised Haskell)
	$H(t)[1-\exp(-\omega_T t)f(\omega_T t)]$ where $f(\omega_T t) = 1+\omega_T t + \frac{(\omega_T t)^2}{2!} - b(\omega_T t)^3$	$\frac{[(1+24b)^2\omega^2+\omega^2{}_T]^{\frac{1}{2}}}{\omega(\omega^2+\omega^2{}_T)^2}$	Helmberger & Hadley (1981) (Revised Haskell)
7	$H(t)t^{\zeta} e^{-\omega_T t}$	$\left\lvert \frac{\Gamma(\zeta + 1)}{(\omega_T+i\omega)^{-(\zeta+1)}} \right\rvert$ where Γ is a Gamma-function	Toksöz et al. (1964)

TABLE 2.1 Proposed time functions and their corresponding spectra which represent the pressure pulse on the equivalent radiator surface of an underground explosion. ω_T is an inverse time constant.

model. These maintain the number of parameters describing the source, but modify certain physical constraints.

Opposing the step-like behaviour at long periods, which the two-parameter models above exhibit, is the decaying pressure pulse obtained by Toksöz et al. (1964) using spectral techniques on Rayleigh waves. This has an infinite overshoot ratio, and is again described by two variables. O'Brien (1967b) supports an initial sharp impulse followed by a later decay for small chemical explosions.

It is apparent that one cannot ascribe a definite function to the general time action at the elastic radius - the models being largely data dependent. There is a particular dispute about the long period behaviour of the source. The different source time functions and their corresponding spectra are plotted in Figure 2.4. It is immediately noticeable that although the time functions display considerable variety in shape, all the spectral functions are monotonically decreasing. This is the reason why there is so much uncertainty in the time functions. In the light of this and the main objective of single-station attenuation measurement, it seems highly inefficient to use a source function with more than one parameter, yet physically restrictive to use a step or a Dirac impulse. Therefore, the simple exponential step, which can model the behaviour of both extremes, is chosen for our work on underground explosions.

2.2.6 The Amplitude of the Source Mechanism and the Explosive Seismic Moment

The dipolar amplitude S_o of the source mechanism is dependent

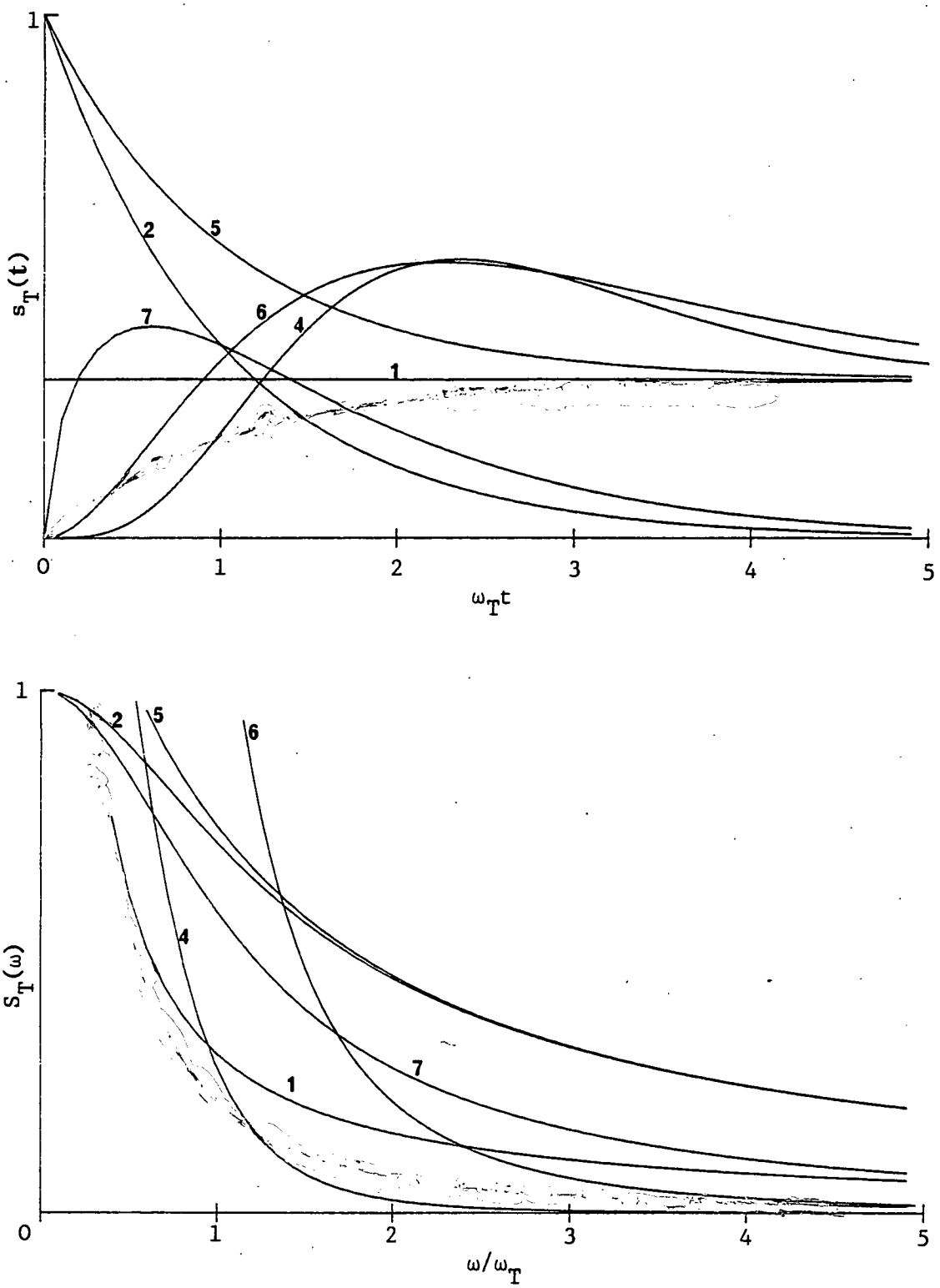

1 step function

2 step exponential

4 Haskell (1967) function (b = 0.24)

5 Mueller and Murphy (1971) function

6 von Seggern and Blandford (1972) (Revised Haskell; b = 2.0)

7 Toksöz et al. (1964) pulse (ζ = 0.6)

Figure 2.4. The variety of time functions and corresponding spectra which have been proposed to represent the action of an underground explosion force system. The temporal and spectral functions are plotted against the dimensionless independent variables $\omega_T t$ and ω/ω_T respectively, where ω_T is the inverse time constant of the time pulse.

on the strength of the surrounding rock and the yield of the explosive. It is related to the static strain energy stored in the medium by the formation of the cavity. If the source time function $s_T(t)$ possesses a final steady state value (step-like variation), then a static seismic moment can be defined for this source (Rodean, 1981), and is given by S_o. Mueller and Murphy (1971) derived an expression for the amplitude of the pressure pulse P_o at the elastic boundary

$$P_o = \frac{4\mu}{3} \left(\frac{r_c}{r_{e\ell}} \right)^3$$

from which one may obtain S_o using Equation 2.3

$$S_o = \frac{4\pi}{3} \rho \alpha^2 r_c^3 \quad . \tag{2.5}$$

This moment is not well defined for explosions because of the doubt about the long period behaviour of $s_T(t)$.

2.3 Underwater Explosions

2.3.1 Physical Interactions of the Source with the Medium

Cole (1948) gives an explicit account of the physical interactions occurring in the near vicinity of an underwater explosion. Here we outline the processes which initiate the propagation of seismic waves in the underlying solid medium.

Detonation results in a rapid discontinuity in pressure at the explosive-water boundary. This is to a large extent relieved by an intense shock wave propagating radially outwards, and to a lesser extent

by the motion of the boundary in a radially symmetric manner. The shock wave dissipates energy as it propagates outwards, and beyond a certain radius the amplitude reduces below the limit of non-linearity. At this point the wave propagates as a hydroacoustic wave and obeys linear equations of motion. In general, this zone extends to a distance much smaller than a seismic wavelength (Wielandt, 1975; Carpenter, 1967), and there is no need to introduce the finiteness function $S_F(\omega)$ for underwater explosions.

As the bubble of hot gaseous products is at a much higher pressure than the hydrostatic equilibrium value the boundary will dilate. There is a simultaneous decrease in the internal gas pressure, and the bubble stops when the internal pressure is slightly less than the external hydrostatic (due to inertia). The motion of the boundary then reverses, and the bubble contracts. The motion in this direction ceases at a limit determined by the finite compressibility of the gases and again there is an increase in size, however the maximum radius now reached is smaller due to loss of energy from viscosity, turbulent flow, and radiation of acoustical energy. The system thus undergoes damped oscillations and radiates waves throughout the cycle with most of the energy emitted at each volume minimum. These acoustic pulses force the sediments into vibration, and in turn this motion is transmitted to the firmer propagation medium. Provided the pressure at the transition from water to solid medium does not exceed the elastic limit there will be no permanent distortion and a reasonable representation of the incident pulses is transmitted.

In the absence of interfering effects such as boundaries,

the frequency of bubble oscillation f_b is related to the charge size W (kg) and the source depth h (m) via a formula given by Willis (1948):

$$f_b = 0.48\, W^{-1/3}(h + 10)^{5/6} . \qquad (2.6)$$

If the charge is fired at or near the sea-bottom the radial flow of water is disturbed and the oscillations die out rapidly. Higher order pulses become very weak and only the first pulse contributes substantially to the seismic signal (Wielandt, 1975). Bubble migration, the bubble rising under the influence of gravity due to its finite buoyancy, also reduces the relative contributions of each pulse to the signal. Migration effects become pronounced if the ratio of the maximum bubble radius a to the vertical rise in depth between time of initiation and the first bubble pulse b, exceeds 0.3. These are computed using formulae from Weston (1960):

$$a = 4.3[W/(h+10)]^{1/3} \qquad (2.7)$$

$$b \simeq 22W^{1/3}/(h + 10) \qquad (2.8)$$

2.3.2 The Amplitude and the Spectrum of the Source Time Action

As a fluid cannot support shear stresses, one may regard the source as a spherically symmetric emitter of compressional waves. The magnitude and frequency dependence of the source force system are related to the pressure $P(\omega;r)$ measured at a reference distance r_a from the source origin via Hudson (1969a)

$$S_o S_T(\omega) = 4\pi\alpha_1^2 r_a \frac{|P(\omega;r_a)|}{\omega^2}$$

where α_1 is the compressional velocity of the water. The pressure function due to the bubble oscillations can be written

$$P(\omega;r_a) = P_a S_b(\omega)$$

where P_a is the magnitude of the pressure profile and $S_b(\omega)$ is the shape of the function. Thus

$$S_o = 4\pi\alpha_1^2 r_a P_a \qquad (2.9)$$

and

$$S_T(\omega) = S_b(\omega)$$

where the factor $1/\omega^2$ has been absorbed into the medium response (Section 2.3.5) in order to maintain a uniform treatment of the underground and underwater explosions. P_a is dependent on the explosive yield.

2.3.3 Pressure Function due to the Bubble Oscillations

Pressure time functions have been recorded close to underwater explosions by Arons (1948), Christain and Blaik (1965), and Mitchell and Bedford (1976). The shock wave profile is well approximated by an initial sharp rise followed by an exponential decay with a typical time constant of a few milliseconds. The bubble pulses are approximately symmetric double exponentials with slightly longer time constants (Weston, 1960; Carpenter, 1967). In order that the total impulse under

the pressure-time profile is zero, a negative pressure (less than hydrostatic) must prevail between the shock wave and the pulses (Figure 2.5a). The time constants associated with the shock wave and bubble pulses are usually much smaller than a typical seismic period. Therefore one can replace the time function by a series of sharp pulses with separation intervals governed by the bubble periods (Figure 2.5b) (Wielandt, 1975; Weston, 1960). If two bubble pulses contribute to the signal, then the amplitude of the negative pressure P_n is given by

$$P_n = \frac{(1 + B + C)}{\omega(T_c + T_b)}$$

where B and C are the relative amplitudes of the first and second bubble pulses with respect to the shock wave respectively, and T_b and T_c the time intervals between the shock wave and the first bubble pulse, and the first and second bubble pulse. Wielandt (1975) found the best value of the constant B as 0.6, and Weston (1960) gave $C = 0.4B$ and $T_c = 0.72\ T_b$. The amplitude spectrum $S_b(\omega)$ of this idealized signal is:

$$S_b(\omega) = \left| 1 + B\exp(i\omega T_b) + C\exp(i\omega(T_c + T_b)) + iP_n[1 - \exp(i\omega(T_b + T_c))] \right| . \qquad (2.10)$$

The function has smooth oscillations which peak slightly below the bubble frequencies of f_b ($^1/T_b$) and f_c ($^1/T_c$) (due to the negative pressure effect), and at approximate multiples of these frequencies. A consequence of the negative pressure is that the low-frequency asymptote is directly proportional to frequency and passes

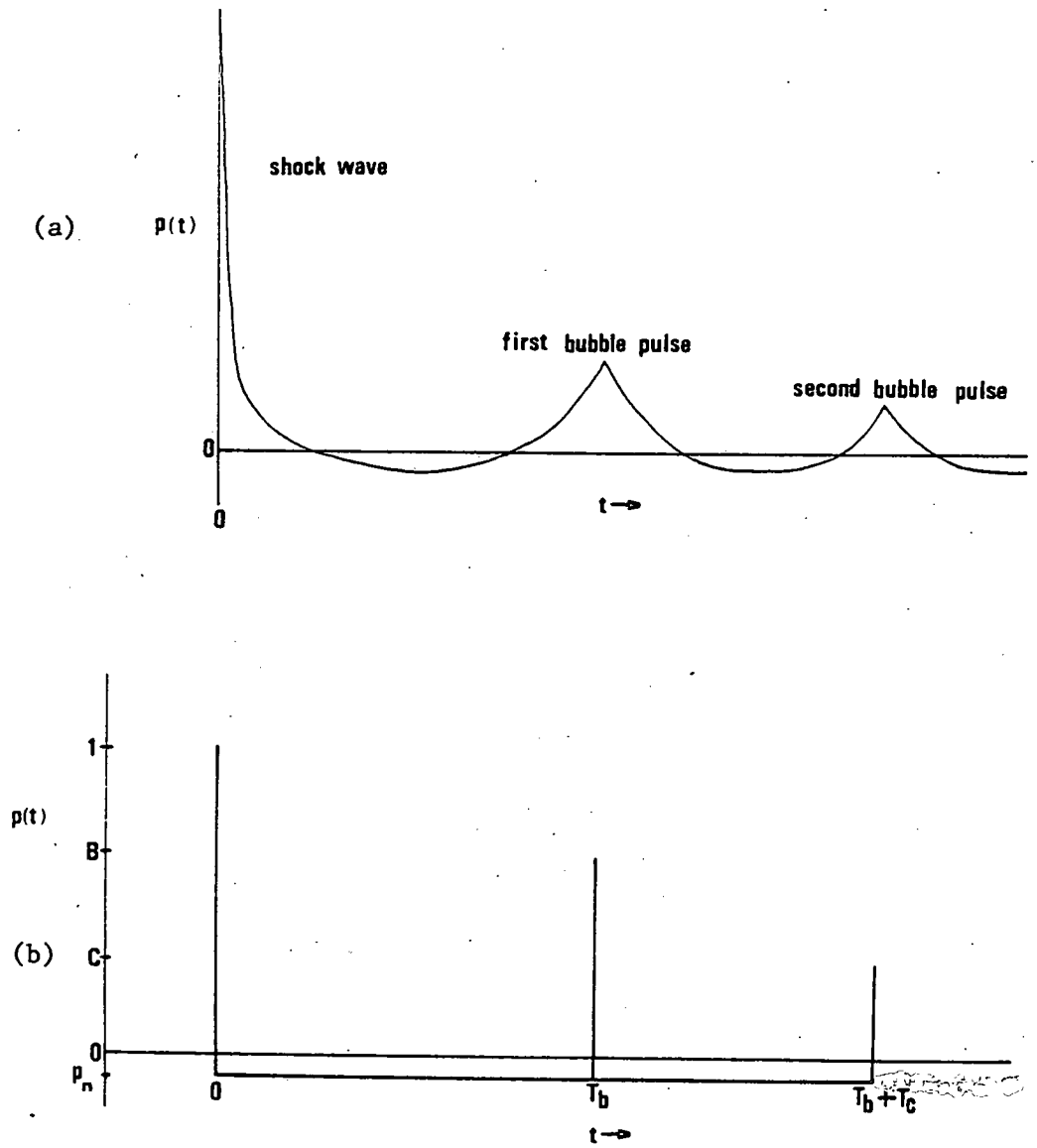

Figure 2.5. (a) Hydro-acoustic pressure-time profile from an underwater explosion.

(b) Approximation of pressure function (a) for seismic waves.

through the origin. This spectral function is specified by the explosive yield and shot depth through the variables T_c and T_b.

2.3.4 Reverberation Response of Water Layer

The effect of interference between reflected multiples of waves from the free surface of the water and the sea-bottom is to modulate the spectrum by a function which depends on the thickness of the water layer in the source region and the depth of the shot (Bancroft, 1966; Plutchock and Broome, 1969; O'Brien, 1967a; et alia). If the sea-bottom and the water surface were to act as perfect reflectors, the final signal would be composed of an infinite series of ray reflections. However, in practice, absorption occurs at the sea-bottom - which is fortunate, as otherwise we would not detect any seismic signals. Also, a small amount of energy is lost at the sea surface and by means of geometric spreading. Due to these losses, the spectral effect of the reverberations is well approximated by one bottom bounce (Plutchok and Broome, 1969; Tanimoto and Sato, 1980). Wielandt (1975) gives a formula for the impulse response of the water layer using first reflected waves from the water surface and the sea-bottom only:

$$S_r(\omega) = \frac{1 + R \exp(i\omega T_s)}{1 + S \exp(i\omega T_r)} \qquad (2.11)$$

where $T_r = \frac{2d}{v}$ and $T_s = \frac{2h}{v}$. v is the speed of sound in water, d the shot depth, and h the thickness of the water layer. The values obtained for the reflection coefficients at the free surface

(R = -0.5) and sea-bottom (S = 0.45) are best-fit estimates based on recorded spectra. This function has a number of sharp peaks at odd harmonic frequencies corresponding to the fundamental frequencies v/4h and v/4d. $S_r(\omega)$ modulates the spectrum from the source force system, and the complete source function must now be given by $S_o S_b(\omega) S_r(\omega)$.

If the pulses from the bubble oscillations are in phase with the reverberations from the water layer, then both contributions reinforce each other and the explosive energy is converted to seismic waves at optimum efficiency. The shot depth at which this occurs is related to the yield of the explosion and is independent of the water thickness, Jacob (1975)

$$W = \left[\frac{d(d + 10)^{5/6}}{803}\right]^3 . \qquad (2.12)$$

The underwater explosions recorded on the LISPB array were fired at this optimum depth.

2.3.5 Rayleigh Wave Medium Response

The medium response for underwater explosions is dependent on the source position and the depth distribution of elastic constants in the water and the solid medium. The function corresponding to an infinite elastic fluid layer overlying a solid elastic half-space (Figure 2.2b) is specified by a small number of parameters. The reverberations between the free surface of the fluid and solid bottom have been considered in Section 2.3.4. The separation of this effect from the medium response can only be achieved if the seismometer is placed on

the solid. The spectral response corresponding to the Rayleigh wave displacement in the solid generated by a unit body force distribution in the fluid at a distance z_s from the interface is given by (Appendix A.3):

$$M_z(\omega) = E\,\omega^{-\frac{1}{2}}\,e^{-\omega m z_s} \qquad (2.13)$$

where E and m are medium dependent constants. A factor of $1/\omega^2$ has been absorbed from the source function (Section 2.3.2). In this case, unlike underground explosions, high frequencies are attenuated and long period Rayleigh waves are preferred. The response is compared in Figure 2.2c with that for the underground explosion. Although this function is specified by more variables than for the underground explosion, the compressional velocity and density of the water layer may be regarded as well known quantities.

2.4 Dispersed Shots

This particular source configuration is used in the LISPB refraction experiment for both underground and underwater explosions. For this, a large single charge is replaced by a co-linear arrangement of equal smaller shots spaced apart and fired simultaneously. The formation has distinct advantages over the single shot. These benefits are related to the economy of long range firing coupled with an ability to overcome source site problems.

Consider a dispersed shot line of N shots spaced a distance d apart. Each shot acts as if it were an independent radiator if the separation between each is much larger than the non-linear source

extension. If the line length is comparable to a seismic wavelength, then the field generated depends on the azimuth of the recording station with respect to the line. This directionality arises due to interference between each different contribution. The amplitude A observed at an epicentral distance r ($r >> N\,d$), and recorded at an angle ϕ to the normal of the array axis, is given by Jacob (1975)

$$A = \frac{A_o \sin(Nx)}{\sin(x)} \tag{2.14}$$

where $x = 2\pi d \sin\phi/\lambda$, and A_o is the individual shot amplitude. This function has a number of principal maxima and small modulations. When ϕ is small or λ large, the recorded amplitude is the linear sum of the single amplitudes from each shot.

O'Brien (1976b) considered the usefulness of splitting an underground explosion into a number of smaller packages. Jacob (1975) noticed advantages in dispersing underwater shot arrays. There is a problem with these arrays in that each member will be subject to an acoustic pressure field generated by the other members. The net result is a pushing apart of the array and an alteration of the bubble pulse function. This effect is not considered in the analysis.

2.5 Summary

In this chapter we have been concerned with the influence of underground and underwater explosions on the amplitude spectrum of the Rayleigh waves which they generate, and the accurate representation of the source effects in terms of a small number of simple variables.

The character of the source time functions for underwater and underground explosions results from the different properties of the media of emplacement. A fluid cannot support shear motion and can adjust to displacement by flow whilst a solid has a finite shear strength.

We have shown that there are many proposed functions describing the spectrum of the time action $S_T(\omega)$ for an underground explosion, but none can represent the general behaviour of the source. The shape of $s_T(t)$ was intermediate between a step and a Dirac impulse. Considering this uncertainty, a simple one-parameter exponential step function which can display the characteristics of both of these extremes is thought sufficient to specify the action $S_T(\omega)$, and this simple function will be used later in the thesis. There were two different physical phenomena associated with the underwater explosion contributing to the overall spectrum of the time action $S_T(\omega)$. These were the oscillations of the gas bubble and the reverberation of the hydroacoustic waves from the source between the sea-bottom and the water surface. These effects have been incorporated into the functions $S_b(\omega)$ and $S_r(\omega)$ respectively, and were defined by the shot depth and explosive yield, and the thickness of the water layer and the shot depth, respectively.

The medium response $M_z(\omega)$ for an underground explosion in a half-space solid depended on the elastic constants of the medium and the source depth. The medium response for underwater explosions also depended on the solid medium, and the vertical distance from the solid-fluid interface. The source strength of underground explosions can be related to the explosive yield and the properties of the source medium. The source strength for underwater explosions was dependent on similar quantities.

CHAPTER 3

EARTHQUAKE SOURCE FUNCTIONS

3.1 Introduction

In this chapter, the variety of physical phenomena which shape the amplitude spectra of Rayleigh waves generated by an earthquake with a magnitude similar to KEQ will be described and examined with the aim, as was in Chapter 2, to obtain accurate expressions for the four basic factors S_o, $S_T(\omega)$, $S_F(\omega)$ and $M_z(\omega)$ using a minimum number of independent parameters. This completes the account of the seismic sources used in this thesis.

3.2 Earthquakes

3.2.1 Introduction

In Chapter 2 we constructed equivalent mathematical models for underground and underwater explosions from which one could synthesize the theoretical source spectrum. These sources were effectively localized in space, and both were modelled by a simple symmetric point force system with a frequency dependent amplitude $S_o S_T(\omega)$. The medium response was dependent on the source depth and the elastic parameters of the medium.

Earthquakes are in general relatively extended in both time and space and as a consequence of the latter, the spectrum is sensitive to the orientation of the source. In addition to this, most of these

events occur at non-negligible depths compared to a seismic wavelength. Therefore there are more parameters describing the earthquake than the explosive source. However there are also a proliferation of inter-relationships between the physical and geometric, or kinematic and dynamic variables describing this event, and the observations - see Kanamori and Anderson (1975), and Geller (1976).

3.2.2 Physical Interactions of the Source with the Medium

The most widely accepted explanation of shallow earthquakes is Reid's elastic rebound theory. This regards the focal region to be continually subject to a regional dynamic stress field generated by long term tectonic motions, upon which smaller local stresses super-impose. As a result of these, the strain energy progressively accumulates until it exceeds the fracture strength of the material. A relief of this stress occurs by a sudden mechanical rupture across which the released energy creates new crack surfaces. The movement finally stops due to cohesive and frictional forces. The residual strain energy is radiated as seismic waves and transformed into heat by friction, or stored as potential energy elsewhere in the region. The dominant failure mechanism for shallow (< 20 km) intra-plate earthquakes in the crust is a transverse fracture which usually occurs along pre-existing faults or cracks.

To relate the non-linear earthquake processes to the shape of the Rayleigh wave spectrum it is convenient to use a linear kine-matic description. This visualizes the event as an internal surface or fracture plane across which there occurs a tangential slip

displacement. Within this framework there are two possible representations of the seismic source. The Haskell (1964b) approach is to specify the relative displacement between the opposite faces of the fault plane by a definite function of the temporal and spatial coordinates. Haskell (1966, 1969) took the statistical approach and assumed that the high frequency components of the fault displacement are only coherent over segments of the fault (radiation from adjacent portions is statistically independent). Geometrically, the deterministic and statistical models are identical, although in the latter case the parameters specifying the source represent ensemble averages. Aki (1967) connected the seismic spectrum to earthquake magnitude, and derived a family of one-parameter scaling laws using a statistical dislocation model and by assuming physical similarity. However these laws only provide a satisfactory fit for earthquakes with $M_s > 5$ (Aki, 1972). For small earthquakes such as KEQ, a simple coherence over the full length of the fault gives an adequate description, and thus the deterministic model is chosen. For this, we assume a rectangular fault of width w and length L, the rupture front forming instantaneously across the width and propagating with a uniform velocity over the fault length. This implies the function $S_o S_T(\omega)$ and the source mechanism are identical for all points on the fault.

There are many modifications to the kinematic description of an earthquake which have been introduced in order to obtain a better match with the observations. For example, the rupture may be assumed to accelerate rather than maintain a constant velocity, or the fault surface may be more circular than linear (Savage, 1966). In view of the ultimate aim of the single-station attenuation procedure, these complicated models are not considered further.

3.2.3 Earthquake Source Mechanism, Seismic Moment, and Medium Response

For long seismic wavelengths an earthquake can be regarded as a point source. Burridge and Knopoff (1964) derived an explicit expression for the body force system which generates identical radiation to that from a shear dislocation. A double couple is an exact equivalent even for an inhomogeneous and anisotropic medium. The system has zero total moment and zero resultant force at all instants of time.

This dynamical equivalence defines the seismic moment of an earthquake as the strength of the individual couples constituting the double couple. The moment S_o can be further related to the fault averaged dislocation and the stress-strain drop which occurs at the earthquake focus (Aki, 1966). This parameter cannot be computed from known source constants in a similar manner to underground and underwater explosions, but must be determined from inter-relations with other physical quantities. For example, surface wave magnitude can be used to give an estimate of seismic moment (Kanamori and Anderson, 1975).

The spectral medium response of an earthquake is a function of the parameters describing the inclination of the fault plane and the direction of motion between the two sides of the fault. These can be specified by a vector $\underline{\hat{n}}$ which is normal to the plane and a slip vector $\underline{\hat{f}}$ on the causative fault respectively (Figure 3.1a). The convention usually adopted is that $\underline{\hat{f}}$ represents the displacement of the hanging wall relative to the footwall (Ben-Menahem and Singh, p. 184, 1981). From this description, an alternative set of angular parameters can be formed. The inclination of the fault with the horizontal is given by the dip angle δ $(0 \leq \delta \leq \frac{\pi}{2})$. The angle between $\underline{\hat{f}}$ and the strike direction,

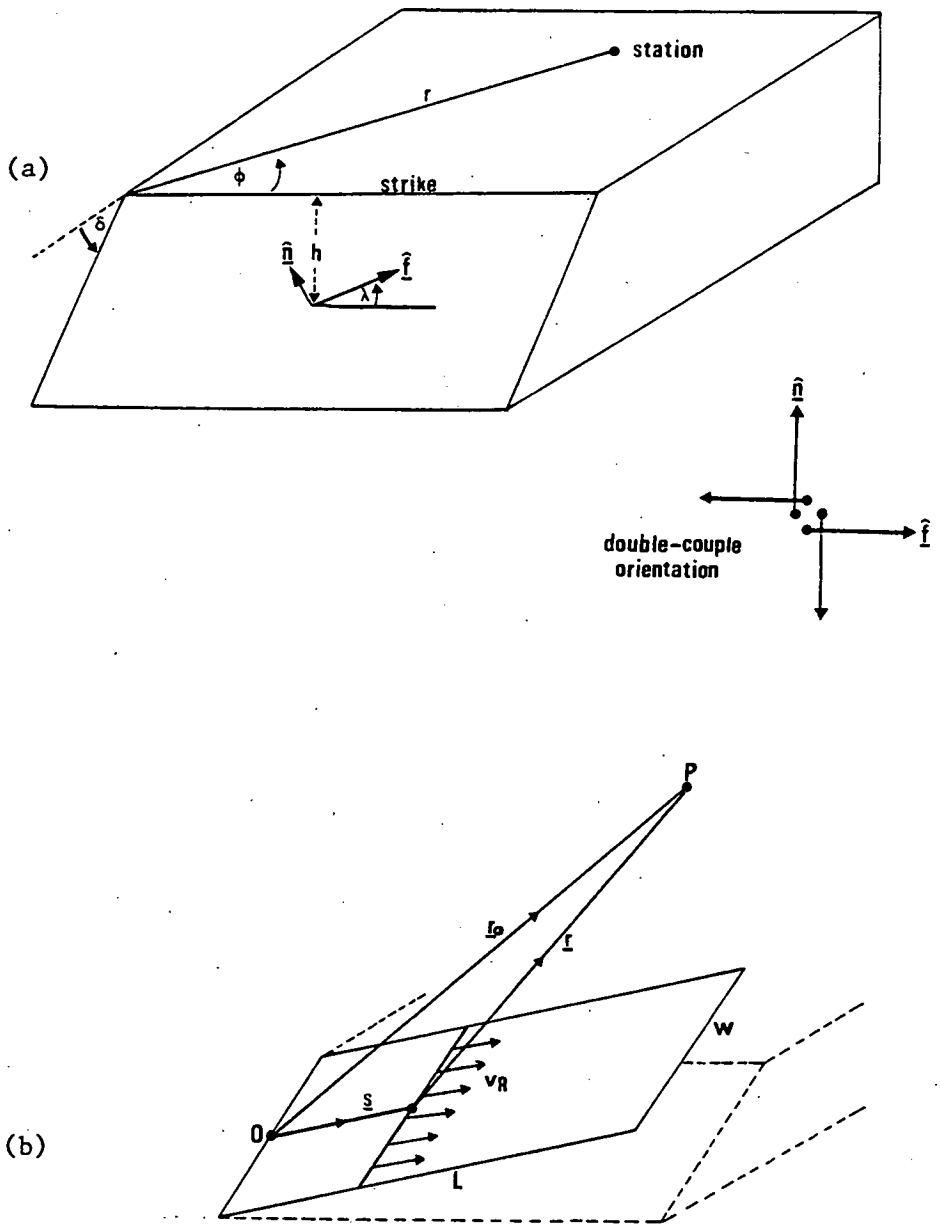

Figure 3.1. (a) Geometric description of parameters which define the orientation of the earthquake source mechanism. (b) Rupture on a rectangular fault of finite dimensions.

measured in the plane of the fault, is the rake $\lambda (0 \leq \lambda \leq 2\pi)$. δ and λ completely specify the orientation of the fault surfaces and therefore the type of faulting, these being related to the orientation of the double-couple mechanism in Figure 3.1a. To reduce the number of parameters specifying the source, the strike azimuth of the fault and the azimuth of the observer are combined. The azimuth ϕ is now defined as the angle between the strike direction and the line from the epicentre to the recording station.

Therefore, the medium response is generally a function of frequency, azimuth, source depth, dip and rake, in addition to the earth's structure. The response to a point double couple source of arbitrary orientation is thus represented formally by $M_z^p(\omega;\phi;h,\delta,\lambda)$. This dependence has been used by Aki (1960, 1962), Ben-Menahem et al. (1970), Kanamori (1970), Mendiguren (1977), and Kanamori and Given (1981) and many more, to determine the fault plane solutions. This collection of source parameters leads to some interesting effects such as the spectrum possessing a hole for certain focal depths. This occurs at a frequency corresponding to $\omega h/c \simeq 1$ for the fundamental mode Rayleigh wave (Douglas et al., 1971). A formula which can be used to compute the earthquake medium response for the frequencies and Rayleigh wave modes used in this thesis, is presented in Appendix A.4.

3.2.4 Derivation of the Source Finiteness Effect

If the fault length is comparable to a seismic wavelength, the point source equivalence does not apply. The earthquake size affects

the spectrum in two ways:- diffraction of the seismic waves around the source area and the finite propagation time of the rupture front over the fault.

The total radiation field generated by the source must now be expressed as the superposition of the individual point double couple fields corresponding to the medium response $M_z^p(\omega;\phi;h,\delta,\lambda)$, weighted by the temporal and spatial dependence of the source strength and time action (Aki and Richards, p. 50, 1981). As we have assumed the functions S_o and $S_T(\omega)$ are uniform over the fault, the total effective medium response is given by:

$$M_z(\omega;\bar{\phi};\bar{h},\delta,\lambda) = \frac{1}{\bar{r}^{-\frac{1}{2}}A} \int_{\Sigma} r^{-\frac{1}{2}} M_z^p(\omega;\phi;z,\delta,\lambda)\,dA \qquad (3.1)$$

where A is the total fault area, and $\bar{r}$, $\bar{\phi}$ and $\bar{h}$ are the mean epicentral distance, azimuth and depth of the fault with respect to the observer.

The spectral effect of a finite rupture on surface waves was introduced by Ben-Menahem (1961). A fault plane was realized by a line of point sources moving with a uniform velocity along the fracture length and radiating constant energy as they propagate. The solutions were obtained by integrating the basic surface displacements for a concentrated point source over a rectangle of finite width and length. Far-field expressions were given for specific cases of a vertical strike-slip and dip-slip fault, and for the general case of an arbitrary dip-angle. These are generally useful, but the formulae are explicit for only a point or single couple source. The one-dimensional rupture propagation model can be extended to cover the general case of an arbitrary direction of

propagation and a double couple source, by making some simple assumptions regarding the far-field medium response.

The total spectral response at an observation point P can be computed by substituting the expression for $M_z^P(\omega;\phi;z,\delta,\lambda)$ in Equation A.19 (Appendix A.4) into Equation 3.1. The integral can be approximated by assuming the rupture front travels along the length L of a thin rectangular fault with a constant slip velocity v_R, and the disturbance propagates apparently instantaneously over the fault width. As we have assumed that S_o, $S_T(\omega)$, and the source mechanism are uniform over the whole fault area, any variations in $r^{-\frac{1}{2}}M_z^P(\omega;\phi;z,\delta,\lambda)$ over the surface arise from the changes in r, ϕ, and z.

Consider the fault at some time $t > 0$ when the rupture has propagated a distance s_o along the slip direction. The position of the mid-point of the leading edge of the fracture, with respect to the origin O of rupture initiation, is specified by the vector $\underline{s}(s_o,0,0)$. $\underline{r}_o(r_o, \phi_o, h)$ is the position vector of P with respect to O, and $\underline{r}(r, \phi, z)$ is the position of P with respect to the rupture edge (Figure 3.1b). The components of these vectors are related via

$$r = r_o - s_o(f_1 \cos \phi_o + f_2 \sin \phi_o);$$

$$\phi = \phi_o + s_o/r(f_1 \sin \phi_o - f_2 \cos \phi_o)$$

and $$z = h - s_o f_3$$

where f_1, f_2 and f_3 are the components of the vector $\hat{\underline{f}}$ and are given by:

$$f_1 = \cos \lambda, \quad f_2 = -\sin \lambda \cos \delta \quad \text{and} \quad f_3 = -\sin \lambda \sin \delta.$$

The azimuth and distance changes of the medium response are contained in the terms $\cos n\phi$ and $\sin n\phi$ of Equation A.17, and the geometric spreading term $r^{-\frac{1}{2}}$. These factors can be treated as constant in the far-field, for which L, $s_o \ll r$. Consequently one need only consider the phase factor $\exp(-ikr)$, the depth term $\exp(-ph)$ ($p = \sqrt{k^2-\frac{\omega^2}{\alpha^2}}$ or $\sqrt{k^2-\frac{\omega^2}{\beta^2}}$), and the time delay s_o/v_R of a radiating element on the fault (Haskell, 1963). Thus, Equation 3.1 becomes

$$M_z(\omega;\bar{\phi};\bar{h};\delta,\lambda) = M_z^p(\omega;\phi_o;h,\delta,\lambda)\,\frac{1}{L}\int_o^L \exp\left[iks_o\,(f_1\cos\phi_o + f_2\sin\phi_o) - \frac{i\omega s_o}{v_R} + s_o f_3 p\right] ds_o \,.$$

Solving this gives

$$M_z(\omega;\bar{\phi};\bar{h},\ \delta,\ \lambda) = M_z^p(\omega;\phi_o;h,\delta,\lambda)S_F(\omega;\ \phi_o)$$

and the main effect of the finite source size is represented by the factor:

$$S_F(\omega;\phi_o) = \left|\frac{\exp(X) - 1}{X}\right| \qquad (3.2)$$

where $X = \frac{i\omega L}{c}\,(f_1\cos\ \phi_o + f_2\sin\ \phi_o - c/v_R) + f_3 Lp$, and c is the phase velocity of the emitted Rayleigh waves. For a strike-slip rupture $X = \frac{i\omega L}{c}(\cos\ \phi_o - c/v_R)$, and Equation 3.2 reduces to Ben-Menahem's (1961) expression of sinc (Y), where $Y = \frac{\omega L}{2c}(\frac{c}{v_R} - \cos\ \phi_o)$. This result is independent of the dip angle of the fault. For the case of a dip-slip fault the finiteness is dependent on δ.

The effect of source finiteness is therefore to modulate the amplitude spectrum and the radiation pattern by an azimuthal and frequency

dependent factor $S_F(\omega;\phi_o)$. This function increases the high frequency content of the spectrum in the direction of rupture propagation, and creates an asymmetry in the radiation pattern. Ben-Menahem formulated a directivity function using $S_F(\omega;\phi_o)$. This was used to measure the fault length and rupture velocity (Press et al., 1961; Udias, 1971).

The shape of the frequency dependence of the finiteness function is shown in Figure 3.2 for a strike-slip fault observed at an azimuth of 0°. The curve has minima at frequencies satisfying the condition

$$\frac{\omega L}{2c}(c/v_R - \cos\phi_o) = n\pi : \quad n = 1,2,3, \ldots \qquad (3.3)$$

The amplitude spectrum for an earthquake with a rupture length comparable to a seismic wavelength should therefore have holes at regular frequencies, which vary with azimuth. This effect superimposes the holes produced by the medium response function due to the focal depth. As $S_F(\omega;\phi_o)$ contains the phase velocity $c(\omega)$, it will be dependent on the particular Rayleigh mode.

The theory above implies that in order to account for the spectral effect of a finite fault size, the rupture length, rupture velocity and phase velocity of the emitted Rayleigh waves must be specified. This set of parameters can be reduced slightly, as the rupture velocity is approximately medium dependent and is given by $0.7\beta_s$, where β_s is the shear velocity at the source focus.

3.2.5 Spectrum of the Source Time Action

With earthquakes there is little doubt about the long period behaviour of the source time action as static measurements confirm the

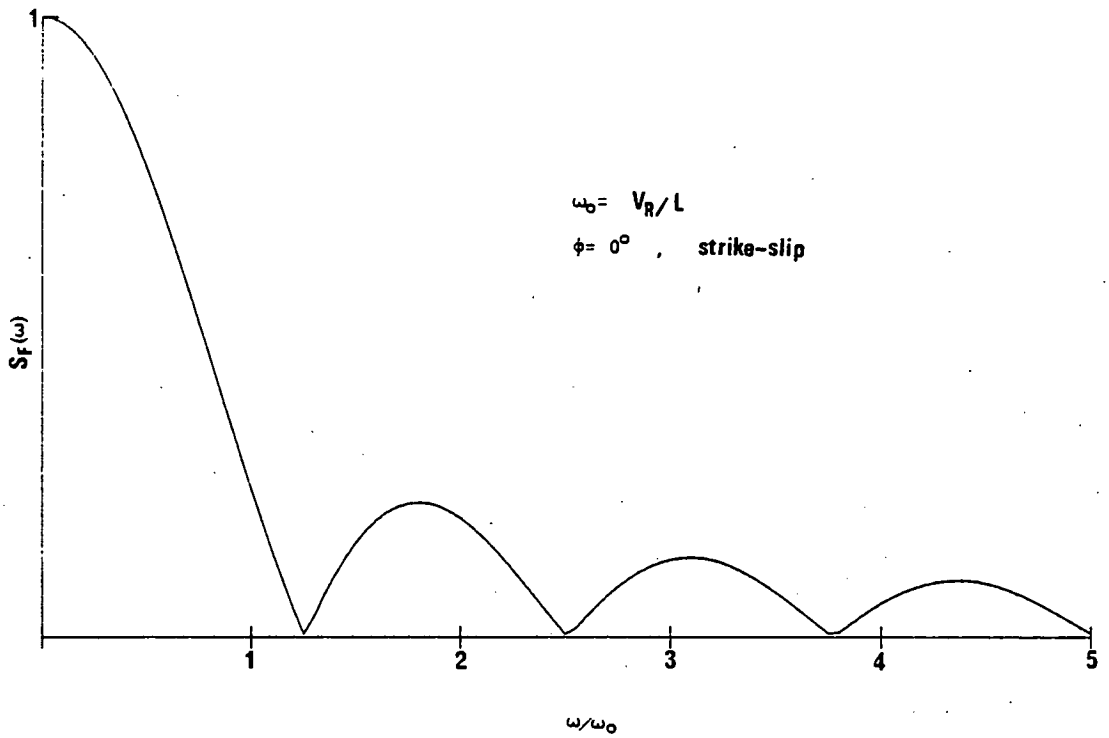

Figure 3.2. Source finiteness function for a strike-slip earthquake with rupture length L, rupture velocity v_R, at an azimuth of 0^o.

permanent dipolar change. At any fixed point on the fault the relative slip displacement increases to a final offset on the arrival of the rupture front. It is mainly the high frequency source information which is in doubt - namely, the shape of the source time function between onset and final displacement. This is determined by the initial stress field surrounding the focal region and the failure properties of the rock. The source time functions described in the following discussion are listed in Table 3.1 together with the corresponding spectral expression and relevant author. All the functions chosen to represent the source time history consist of gradually increasing steps rather than the simple discontinuous step functions of Section 2.2.5.

Haskell (1964b) and Haskell (1969) chose a simple ramp function consisting of a linear increase to the final displacement. A similar, but more physical function was the exponential ramp of Ben-Menahem and Toksöz (1962) and Marshall (1970). Both of these functions are characterized by the inverse time constant of the rise.

In many studies a significant increase in the high frequency spectrum of the source function has been observed. This has been interpreted as a rapid series of accelerations and de-accelerations of the fault. Haskell (1964b) took account of this chattering motion by modulating a linear ramp function, and Haskell (1969) used a sequence of ramp steps. The chattering phenomenon becomes important when the dimensions of the asperity are comparable with a seismic period. The increase in the number of parameters needed to specify this effect outweighs its usefulness in this thesis.

The time functions and corresponding spectra are compared in Figure 3.3. Unlike the underground explosion spectra, the models

Time Function	Spectral Function	Reference
$\begin{cases} 0 & t < 0 \\ \omega_T t & 0 \leq t \leq \omega_T^{-1} \\ 1 & t > \omega_T^{-1} \end{cases}$	$\dfrac{2\lvert\sin(\omega/2\omega_T)\rvert}{\omega^2/\omega_T}$	Haskell (1964b) Haskell (1969)
$\begin{cases} 0 & t < 0 \\ \omega_T(t - \frac{1}{2n\pi\omega_T})\sin(2n\pi\omega_T t) & 0 \leq t \leq \omega_T^{-1} \\ 1 & t > \omega_T^{-1} \end{cases}$ n integer	$\dfrac{2\lvert\sin(\omega/2\omega_T)\rvert}{\frac{\omega^2}{\omega_T}\ (1 - \frac{\omega}{2n\pi\omega_T})}$	Haskell (1964b)
$\begin{cases} 0 & t < 0 \\ \sum_{i=1}^{N} a_i u(t-t_i) & t \geq 0 \end{cases}$ where $\sum_{i=1}^{N} a_i = 1$ and $u(t)$ (some arbitrary step function) has a spectrum $U(\omega)$	Take e.g. $a_i = \frac{1}{N}$, and t_i regular: $U(\omega)\left\lvert\dfrac{\sin(\omega/2\omega_T)}{\sin(\omega/2N\omega_T)}\right\rvert$	Haskell (1969)
$\begin{cases} 0 & t < 0 \\ 1 - e^{-\omega_T t} & t \geq 0 \end{cases}$	$\dfrac{1}{\omega(1 + (\frac{\omega}{\omega_T})^2)^{\frac{1}{2}}}$	Ben-Menahem & Toksöz (1962), Marshall (1970)

Table 3.1 A selection of the proposed time functions for an earthquake process and their corresponding spectra.

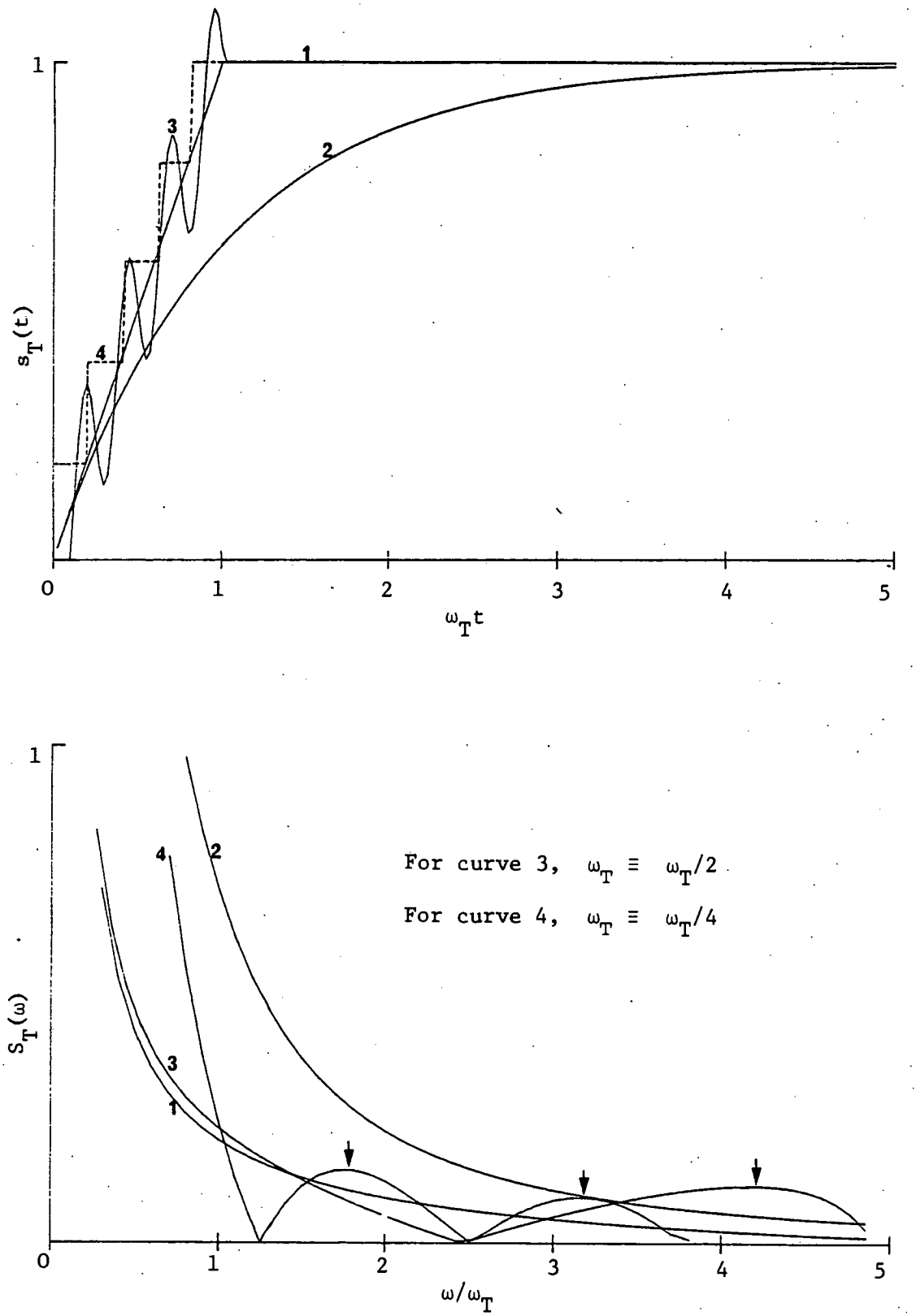

Figure 3.3. Time functions and corresponding spectra which have been proposed to represent the action of an earthquake force system. The temporal and spectral functions are plotted against the dimensionless independent variables $\omega_T t$ and ω/ω_T respectively, where ω_T is the inverse time constant of the time pulse.

in both the time and frequency domain are in close agreement. Under these circumstances, the continuous model of Ben-Menahem and Toksöz (1962) is chosen instead of the other one-parameter model, on a purely arbitrary basis.

3.3 Summary

Chapter 2 showed that the theoretical spectrum for explosions was determined by a small number of simple parameters. The corresponding theory for earthquakes was complicated by the orientation of the source mechanism, factors of rupture propagation, fault dimensions, and the depth of the source in the earth.

Using a kinematic description of the earthquake process the faulting was expressed in terms of the four linear factors defined in Chapter 1; being the medium response of a point double couple force system $M_z^P(\omega)$, strength of the time action S_o, slip displacement function $S_T(\omega)$, and the effect of source finiteness $S_F(\omega)$.

The medium response for the earthquake was a function of the dip, rake, depth of the causative fault plane, and of the azimuth of the observer with respect to the line of strike, in addition to the distribution of elastic constants with depth in the earth. The large number of variables parameterizing this function led to spectral hole effects which are uncommon in explosions. The source finiteness factor also produced spectral holes, and was specified by the fault length, azimuth of observer, and the phase velocity of the Rayleigh waves. The spectrum of the time action was a function of the inverse time constant only. The absolute amplitude S_o can

be related to the surface wave magnitude.

The most outstanding contribution to the number of parameters which express the behaviour of the equivalent elastic sources representing an underground explosion, underwater explosion, and the earthquake process arises from the elastic structure of the source medium. To include the elastic constants in the final parameterization of the source spectral functions would severely restrict the potential resolution of the variables, especially for a multi-layered medium. There is however, an alternative approach to the problem. Using group velocity dispersion information which can be obtained independent of the spectral information from the seismogram, multi-layered velocity profiles can be determined by inversion. A description of this procedure, together with other associated details, will be given in Chapter 4.

CHAPTER 4

PROPAGATION OF RAYLEIGH WAVES IN SCOTLAND

4.1 Introduction

In this chapter we intend to concentrate mainly on a velocity analysis of the Rayleigh wave data generated by the underwater explosions in the Firth of Forth and the KEQ earthquake in Scotland, recorded on the local networks LOWNET and LISPB respectively. The aim is to obtain estimates for the shear wave velocity structure of the earth and hence reduce the number of parameters specifying the amplitude spectrum (Section 1.2).

The most salient features of the seismograms will be described, with particular emphasis on the frequency content and the velocities of propagation of the Rayleigh waves. Methods will be presented and applied for confirming the identity of the prominent Rayleigh modes. To facilitate this, results from a previous surface wave velocity analysis in Scotland will be utilized. Certain unusual characteristics of the seismograms will be exemplified using the velocity models extracted from this work. A technique for deriving the Fourier transform spectrum and group velocity dispersion characteristics of each selected wavepacket will then be applied to the data. Finally, the group velocities will be inverted to yield single-station and pure-provincial models of the distribution of shear velocity with depth in the earth.

4.2 Data Processing

The data described in Section 1.3 were initially in the form of analogue tape recordings. To make the seismograms accessible to computer analysis, the records were digitized. This consisted of reading the wave amplitudes at small finite intervals in time. All aspects of the subsequent data processing for high frequency Rayleigh waves which are used in this thesis are described in Evans (1981).

The seismograms derived from the LOWNET array were digitized at a constant interval of 0.0625 sec, which implies a Nyquist frequency of 8 Hz. The LISPB recordings of the underground and underwater explosions were already digitized at an interval of 0.04 sec, corresponding to a Nyquist frequency of 12.5 Hz. The recordings of KEQ were originally sampled at 0.01 sec intervals, but were decimated to 0.04 sec. The different sampling rates for the LOWNET and LISPB recordings do not alter the conclusions of the analysis in this chapter nor the application of the single-station method in Chapter 6.

The desired Rayleigh wavepackets are selected from the digital seismograms using the program 'WINDOW' listed in Appendix D.1. To obtain the amplitude spectra, these digits are base-lined, cosine-tapered, and zeros added to increase the array number to a power of 2. The waves are then transformed into the frequency domain using the fast Fourier transform (FFT) algorithm of Cooley and Tukey (1965). The size of the time series array is chosen to accommodate different seismogram lengths, and is maintained constant for a complete data set. This ensures that the spectra at each station are evaluated at the same Fourier harmonics. The LOWNET data give spectral amplitudes

at harmonics separated by 0.0078 Hz, and the LISPB data have a larger interval of 0.024 Hz.

The observed group velocities are obtained at identical harmonics to the amplitude spectrum by the 'multiple-filter' technique of Dziewonski et al. (1969) as modified by Burton and Blamey (1972). In this procedure, the instrument-corrected spectrum is passed through a set of narrow-band truncated Gaussian filters, centred at the exact Fourier harmonics. In correcting for the instrument, which is done by dividing the recorded spectrum by the instrument response, one must be careful in interpreting lower frequencies of the corrected signal, as this process will amplify unwanted noise at these frequencies. The point at which this occurs determines the low frequency cut-off. The filtered in-phase and quadrature spectra, for each frequency point, are then transformed back into the time domain and combined to form a smooth envelope of instantaneous amplitude. The complete set of amplitudes for all signal frequencies therefore describe the signal in both the velocity and frequency domain. These amplitudes are normalized with respect to the maximum value, and the results displayed as a contour diagram in the frequency-velocity domain. The group velocity of a dispersed Rayleigh wave can be found by following the ridge representing the signal across the diagram. Evans (1981) modified this procedure for analysing high frequency Rayleigh waves by altering the filter constants and the way in which the algorithm searches the signal ridge, to account for interference by the higher modes and SV-waves. The curve is drawn by first finding a frequency and group velocity for which the amplitude can be unambiguously attributed to a particular Rayleigh mode.

The dispersion curve is then traced to higher and lower frequencies following the relative maxima of amplitude.

4.3 Kirkcaldy Bay Data

4.3.1 Description of Seismograms

Eight underwater explosions, with similar geographical coordinates and shot parameters were fired in Kirkcaldy Bay, and the Rayleigh waves were recorded on the LOWNET array in Scotland (Section 1.3). Each charge had a yield equivalent to 155 kg of TNT and was detonated at the sea-bottom in about 24 m of water (G. Neilson, personal com.). A typical set of vertical component recordings from the array are displayed as a function of distance in Figure 4.1 for event 5; the azimuth of each station relative to the source being indicated. Each seismogram is normalized with respect to its maximum amplitude.

Immediately after the SV-waves there are one or two relatively compact Rayleigh wavepackets which arrive with a velocity of 2.2 - 2.5 km/sec, with dominant frequencies of 2.5 Hz. These are followed by a generally larger amplitude, longer duration, and lower frequency wave (1.0 - 1.5 Hz) with velocities of approximately 1.3 - 2.2 km/sec. The latter is probably the fundamental mode and the faster arrivals are higher modes. A noticeable feature on the majority of seismograms is a long, apparently monochromatic (1.2 Hz) wavetrain, propagating with a velocity less than 1.0 km/sec, which suggests some sort of resonant phenomenon. The signal to noise ratio in the frequency range of interest is good enough to enable detection of the signal at the furthest station EAB. There is considerable interference and distortion

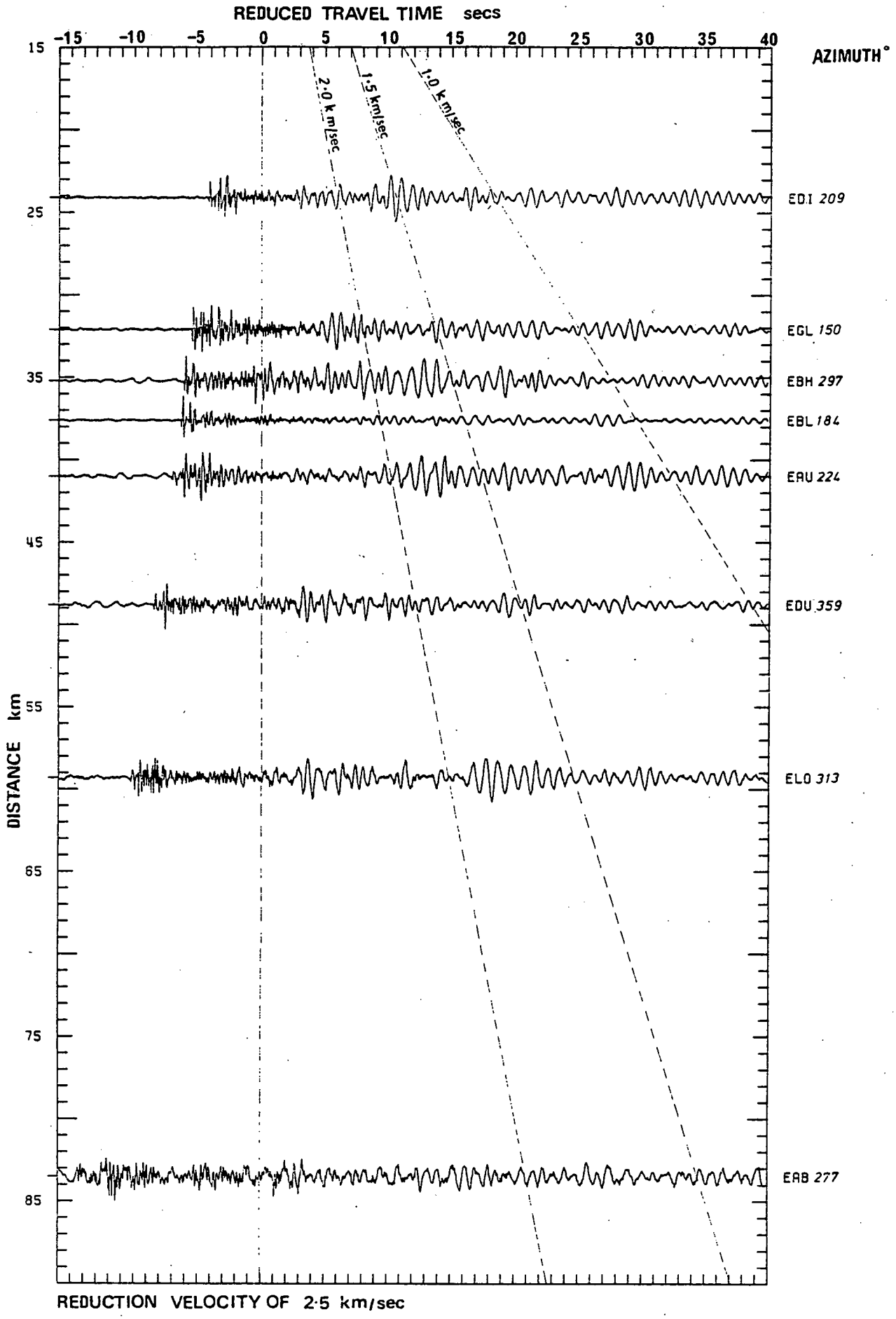

Figure 4.1. Vertical component recordings from Lownet array of Kirkcaldy Bay underwater shot 5.

of the waves, some of the waveforms differing widely between events. This implies a time variant process is dominant in shaping the seismograms, e.g. tide or currents. Despite this, 70% of the data are suitable for further analysis.

The waves have a wavelength of approximately 1 - 2 km and are therefore sensitive to the surface geological expression. Figure 4.2 shows that the propagation paths to the stations intersect a variety of geological provinces, and therefore we expect a variation in the wave velocity recorded across the network.

4.3.2 Particle Motions

Particle motion plots provide a means of distinguishing S-waves from surface waves. The elliptical motion of the Rayleigh waves can be discerned from the relatively linear shear wave motion in the sagittal plane. One cannot use such plots to distinguish the fundamental mode from higher modes if the structure between the event and the station determining the relative sense of rotation is unknown.

Early work on relative particle motions was initiated by Sezawa and Kanai (1940), however they considered unrealistic contrasts in the structural parameters. Mooney and Bolt (1966) carried out an extensive theoretical analysis using a model consisting of one layer overlying a half-space, and computed particle motions for a variety of shear velocity contrasts, Poissons ratio, and density. The ellipticity $E(\omega)$, defined as the ratio of the radial to vertical particle displacement at the free surface of the earth, was investigated. It was found that for most models the fundamental and higher modes

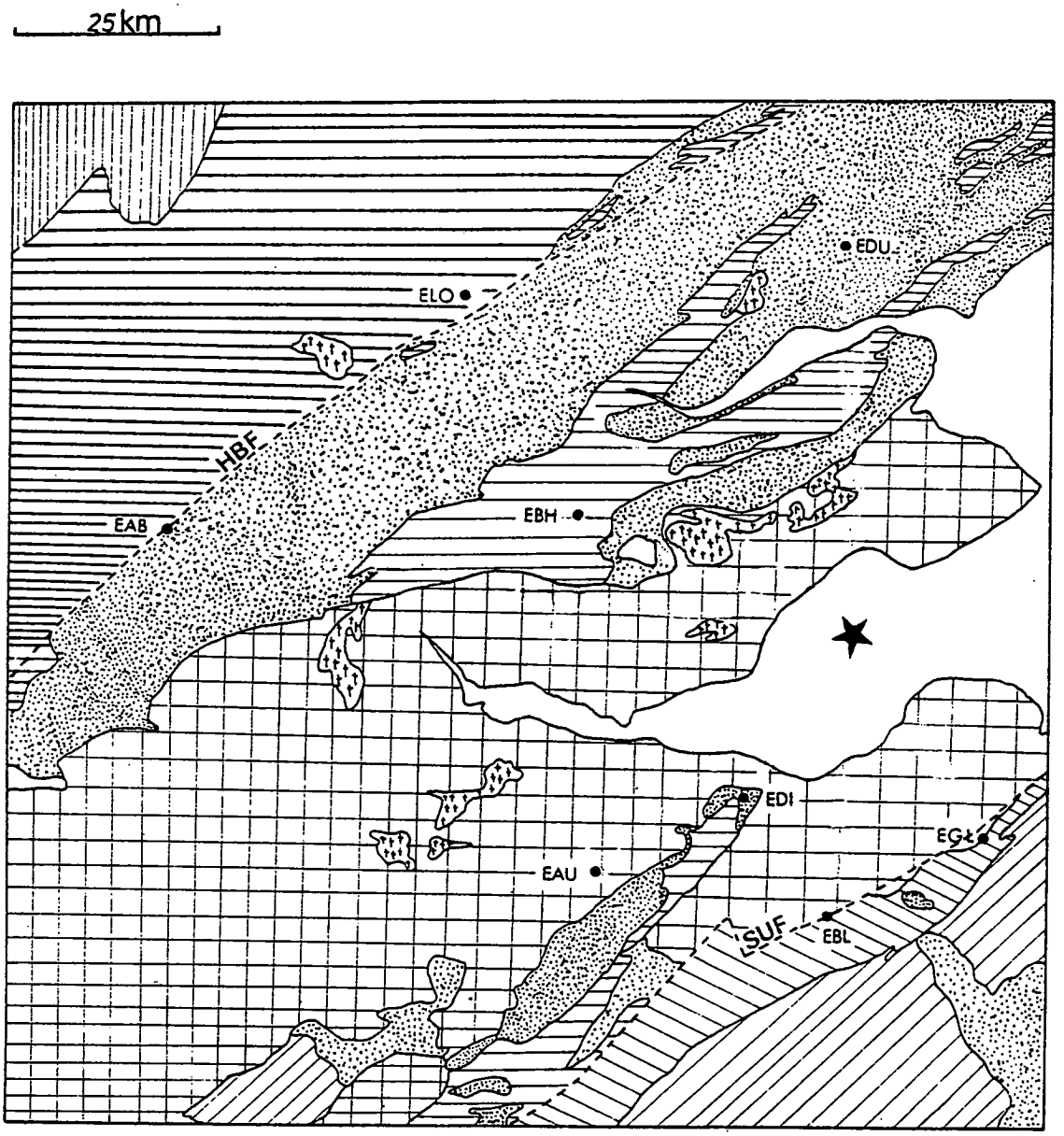

Figure 4.2. Surface geology of Midland Valley region of Scotland with relative positions of LOWNET array and Kirkcaldy Bay explosions.

have normal retrograde motion with $E(\omega)$ in the range 0.5 - 0.7, especially at higher frequencies.

The path to station EDI is almost completely enclosed in the Carboniferous province. Theoretical particle motions for EDI are computed using the Thomson-Haskell matrix theory (Appendix A.4), and Evans' (1981) Carboniferous velocity structure. The program 'MLR' (listed in Appendix D.2) contains a small section which computes the ellipticity. $E(\omega)$ is plotted in Figure 4.3 as a function of frequency, in the approximate range 0.5 - 5 Hz, for the fundamental and the first two higher modes. The first and second higher modes have distinct low frequency cut-offs at 0.8 and 1.3 Hz respectively. At these frequencies the phase velocity is equal to the shear velocity in the half-space. The fundamental mode particle motion is retrograde over the entire frequency range, and the ellipticity is constant over most of this, but increases sharply below 1 Hz. Due to the high shear velocity contrast between the surface layers and the lower layer, the ellipticity of the higher modes changes from retrograde at high frequencies to prograde at low frequencies (Oliver and Ewing, 1957). The two higher modes therefore pass through a region of transition where the particle motion is dominantly vertical.

The three component recordings of shot 7 at station EDI were rotated and bandpassed around 1 Hz using a Martin-Graham filter, applied in the frequency domain without phase distortion (Kulhanek, 1976). The seismograms and corresponding particle motions, averaged over a 1 second window, are shown in Figure 4.4. The orbitals show considerable fluctuation about the ideal elliptical shapes. A tilt

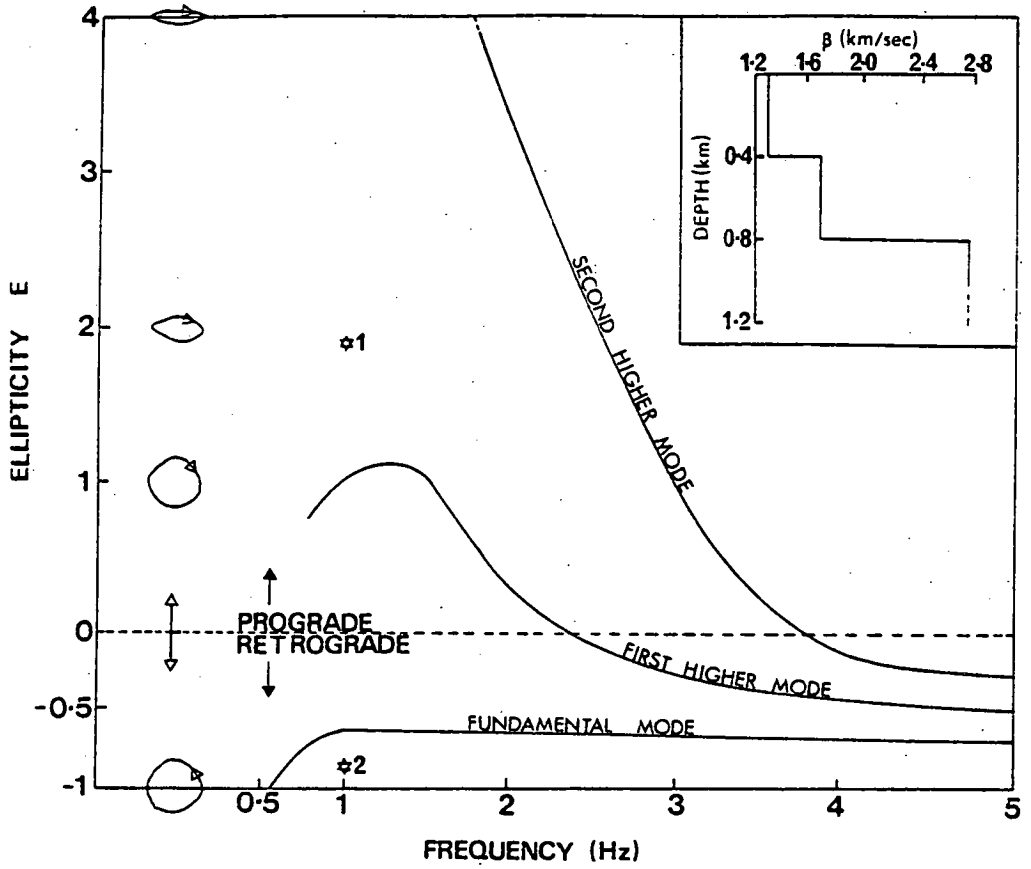

Figure 4.3. Theoretical frequency dependent ellipticity for the first three Rayleigh wave modes computed using Thomson-Haskell matrix theory and Evans' (1981) Carboniferous province model (shown inset). Points '1' and '2' correspond to values of ellipticity estimated from observed particle motion plots.

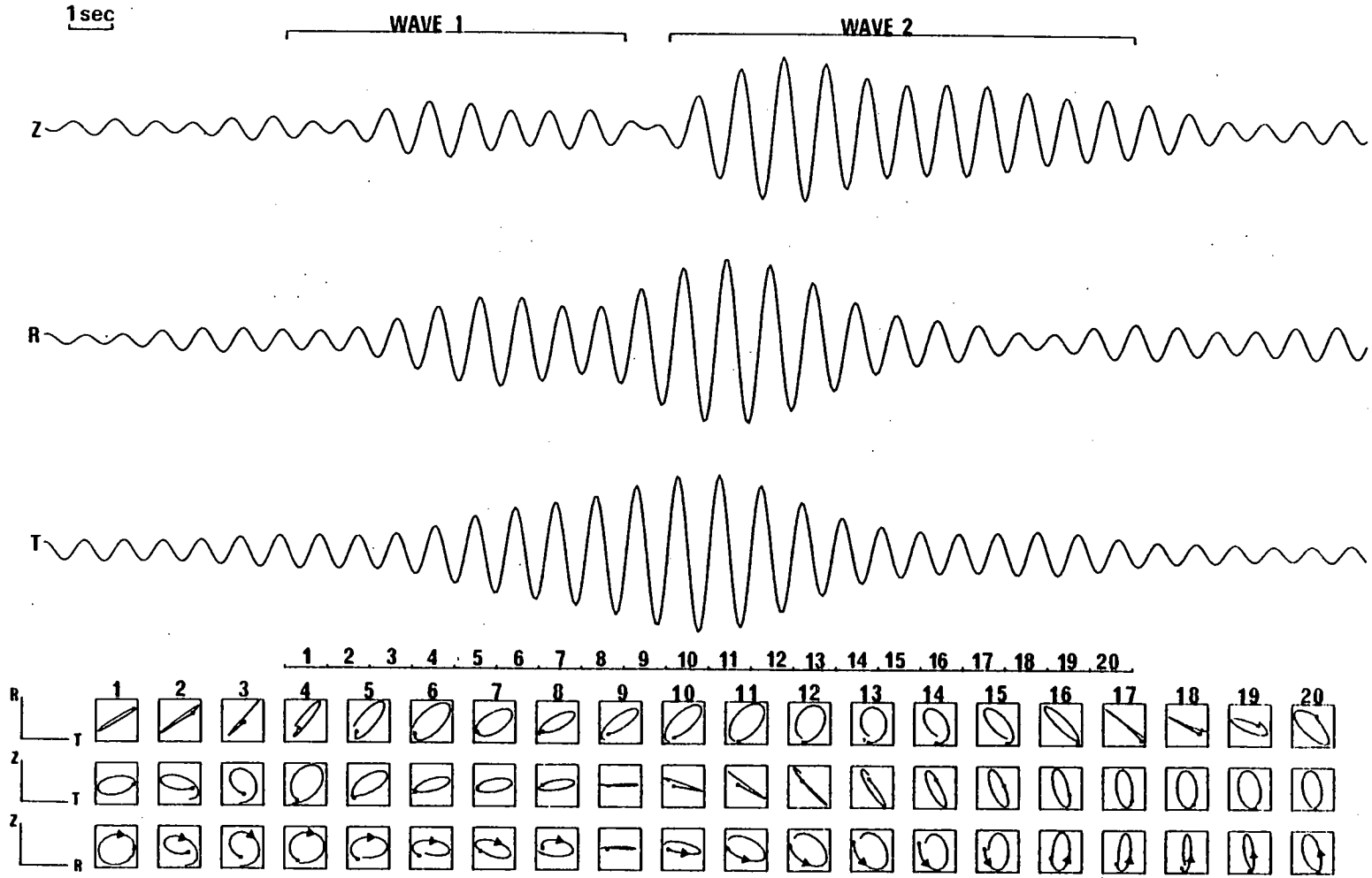

Figure 4.4. Rotated three component recording of Kirkcaldy Bay shot 7 at station EDI, band-pass filtered around 1 Hz using a Martin-Graham filter. Particle motions were averaged over a one second time window. Average ellipticity of waves 1 and 2 are evaluated and plotted in Figure 4.3.

of the motion in the sagittal plane may be caused by anelasticity (Boore and Toksöz, 1969). The particle motions are also likely to be affected by the Firth of Forth and the way in which the energy propagates to the station.

The first Rayleigh wavepacket '1' has a prograde motion with an average ellipticity of 1.9, there being a transition to a retrograde motion for the later arrival '2' with an average ellipticity of 0.9. These values are marked on Figure 4.3 at a frequency of 1 Hz. Both ellipticities are higher than expected (according to theoretical calculations), but the sense of rotation is conclusive: the higher frequency first arrival is the first higher mode, and the slower arrival is the fundamental mode.

A noticeable feature of the rotated seismograms is the considerable Love wave energy on the transverse component. SV and SH body wave energy was also present in the original seismograms. The SV field is probably due to the asymmetric position of the source - in a fluid above a solid medium (O'Brien, 1967b). The SH and Love waves cannot be explained so easily as they are not generated by simple conversions from P and SV. A possible mechanism could be scattering from the surface topography or inhomogeneities (Gupta and Blandford, 1983), or anisotropy at the source (Crampin, 1966).

In many seismograms, the first higher mode has a relatively large amplitude which cannot be explained by the instrument response. As the source is effectively at the surface of the earth then the fundamental mode should be the largest surface wave arrival. This highlights a peculiar generating mechanism for the Rayleigh waves.

4.3.3 Quantitative Explanation of Fundamental Mode Waveform

The duration of the fundamental wave from the Kirkcaldy Bay explosions ranges from 6 - 12 secs, although the body waves do not appear to be longer than one would expect from an explosion. This observation suggests that the propagation path is the major cause of the length of the Rayleigh wavepackets.

At the source the water layer increases the length of the generated wave due to bubble pulsations and wave reverberations (Sections 2.3.3 and 2.3.4). The bubble period and the time for one reverberation are 0.64 secs and 0.03 secs respectively for the Kirkcaldy Bay shots. Thus several reverberations and bubble pulses are clearly insufficient to account for this phenomenon. The waves are also characteristic of propagation paths which have a steep group dispersion, which occurs for example, when a large proportion of the path has a surficial water layer (Ewing, Jardetsky, and Press, p. 169, 1957).

To contrast these effects, four synthetic seismograms generated by underwater explosions, with identical source parameters to those shot in Kirkcaldy Bay, are derived by computing the complex spectrum using Equation 1.5, the complex source functions of Sections 2.3.3 and 2.3.4, the medium response of Section 2.3.5, and the instrument response corresponding to a Willmore Mk. II seismometer described in Section 1.3. The Rayleigh waveforms obtained by taking the inverse Fourier transform of the overall spectral shape are shown in Figure 4.5a. Each is calculated for a distance of 25 km. In the first, third and fourth ('1', '3', and '4') seismograms, the shock wave contributes to the signal, whereas the source for the second seismogram '2' undergoes one bubble pulse. The first two Rayleigh waves propagate in a multi-layered solid medium with velocity model

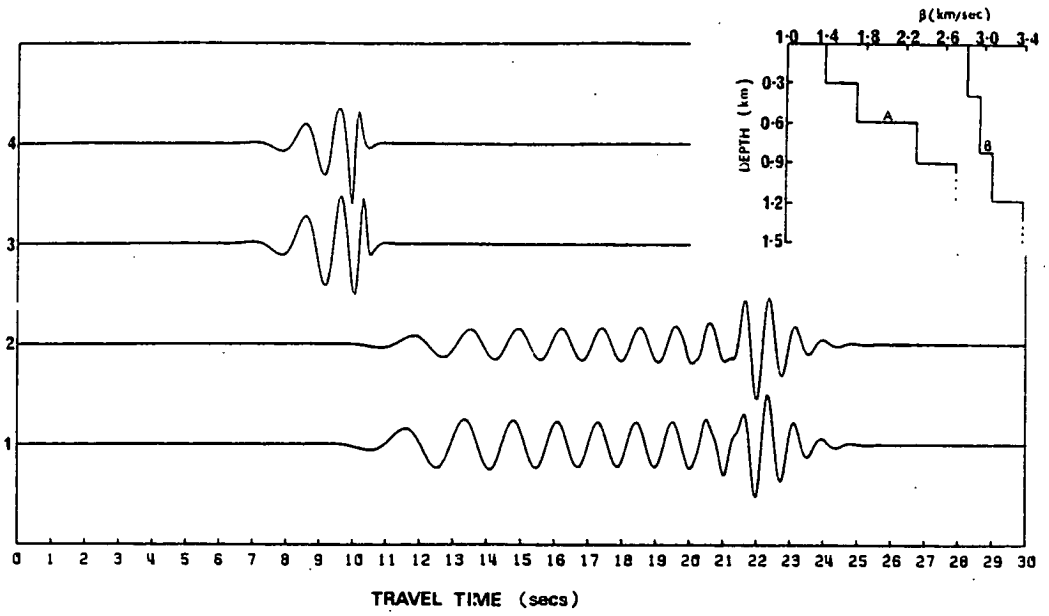

Figure 4.5a. Synthetic seismograms from underwater explosions recorded at a distance of 25 km on a Willmore Mk. II seismometer. Seismograms 1 and 2 correspond to shear wave velocity model A, and 3 and 4 to model B. For 1, 3 and 4 the shock wave alone contributes to the signal. The source undergoes one bubble pulse to generate 2.

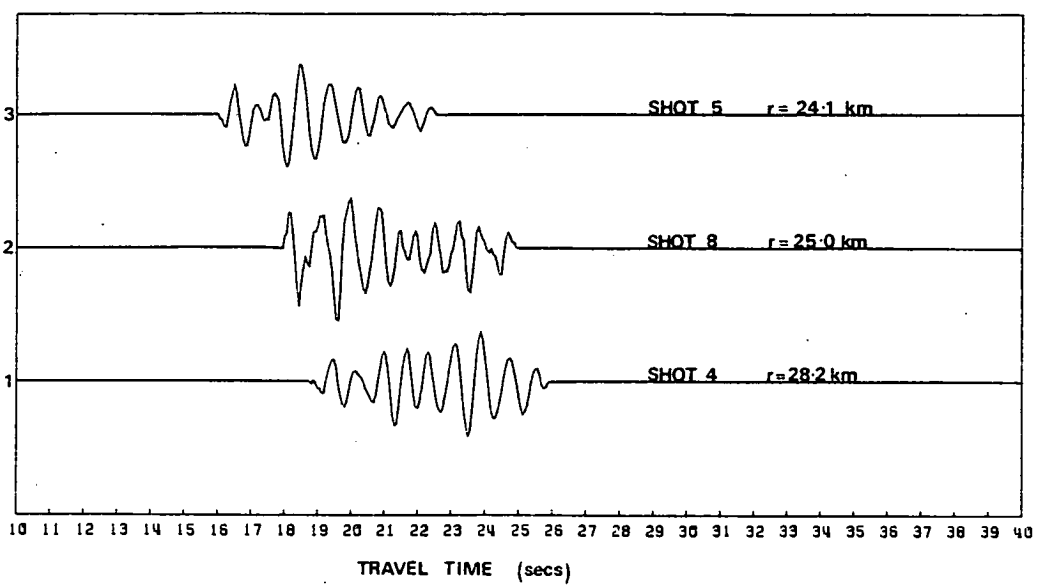

Figure 4.5b. Observed waveforms at station EDI for similar epicentral distances to the synthetic seismograms.

A (typifying the Midland Valley - derived from Evans, 1981). The third wave propagates in velocity model B (typifying the faster velocities of the Moine province - again from Evans, 1981) with smaller velocity contrasts, and the last wave corresponds to the same model but with a 30 m layer of water at the surface. An anelastic half-space with $Q_\beta^{-1} = 0.04$ is assumed throughout and the attenuation function computed using Equation 1.2.

Comparing '1' and '2', the bubble pulsations have no significant effect on the length of the wave-train, although the shape of the waves is slightly different. The pulsations affect mainly the higher frequencies and these are rapidly attenuated by the attenuation function and the medium response. A similar argument applies to seismograms '3' and '4', as the water does not influence the length of the wave-train, since only high frequencies are affected by the thin ($<<\lambda$) layer. The pairs of seismograms '1' and '2' have a length of 14 secs, and '3' and '4', a length of 4 secs. This is caused by the different contrasts in the velocity models, and in particular, the low velocity sediment layers in model A. Low velocity unconsolidated sediments in the Firth of Forth could enhance this effect for a fraction of the propagation paths.

Three observed seismograms recorded at stations EDI are shown in Figure 4.5b. Their duration is about 7 secs, and they display the characteristic shape of the synthetics '1' and '2'. The initial long period motion is not observed due to interference with the SV-wave and higher-mode arrivals. The discrepancies between observed and theoretical seismograms may be a result of the mechanism of Rayleigh wave excitation through the sediments, propagation to the coastline,

or the transmission coefficient at this boundary. However the major part of the unusual duration of the observed Rayleigh waves can be explained by the velocity structure of the Midland valley and Firth of Forth.

4.3.4 Group Velocities and Single-Station Velocity Structure

Fundamental mode group velocity dispersion curves and amplitude spectra are obtained from the seismograms using the analysis program described in Section 4.2. The distortion of the Rayleigh wavepackets inhibits automatic ridge searching of the frequency - velocity matrix, and group velocities are obtained by visual inspection of the contour diagram. The low frequency limit of the data, which depends on the type of instrument and the signal to noise ratio, is 0.6 Hz. In most cases the signal could only be traced up to a frequency of 2.5 Hz. For stations EAB and EBL, the upper frequency limit is about 1.5 Hz. Group velocities and amplitude spectra at the same station, but for different events, have similar frequency ranges. The data are averaged every eight frequency harmonics, thus increasing the separation between the spectral estimates to 0.0625 Hz.

The group velocities at each station are averaged over the different events, the scheme being shown in Table 4.1. This data is then smoothed using a five point weighted running mean. The corresponding velocities and standard deviations are plotted in Figures 4.6 - 4.7, and given numerically in Appendix C.1. The abrupt changes in magnitude of the standard deviations for stations EBH, EAB, and EBL are caused by a change in the number of stations contributing to the

	1	2	3	4	5	6	7	8
EDI	D	-	D	D	D	D	D	D
EAU	D	D	D	D	-	D	D	D
EBH	D	D	D	D	D	D	D	-
EGL	D	D	D	-	D	D	D	D
EAB	D	D	D	-	-	D	-	D
EBL	N	D	D	-	D	D	D	N
EDU	D	D	-	-	D	D	N	D
ELO	D	N	N	D	D	D	D	D

D data used
\- data excluded
N no seismogram

TABLE 4.1. Events and stations used to compute the event-averaged group velocity dispersion data.

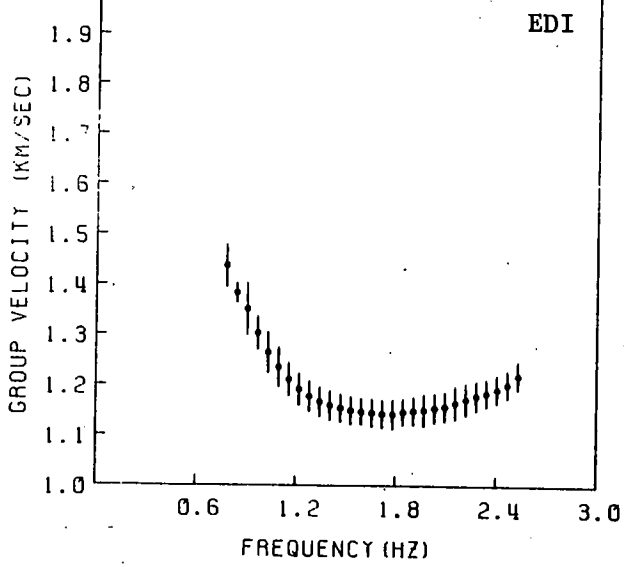

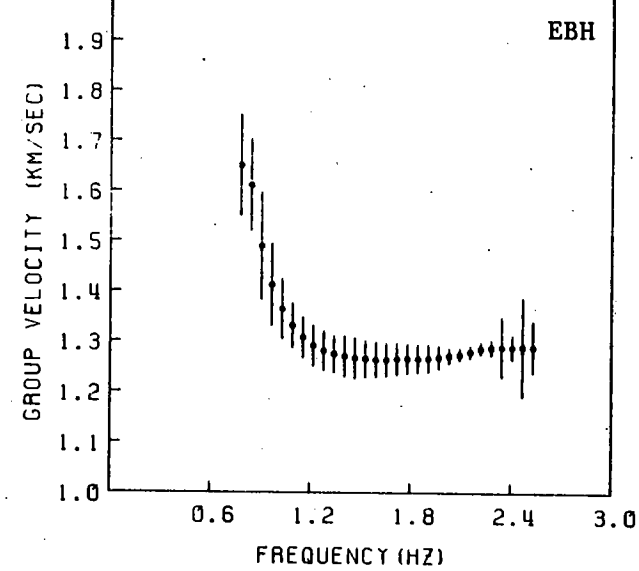

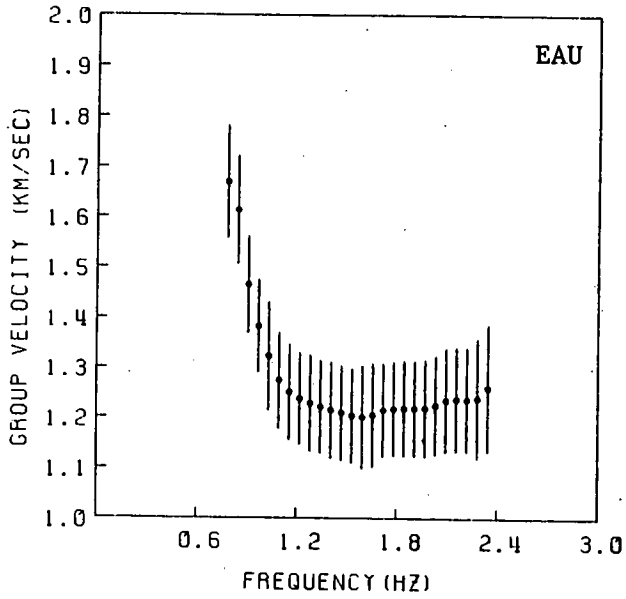

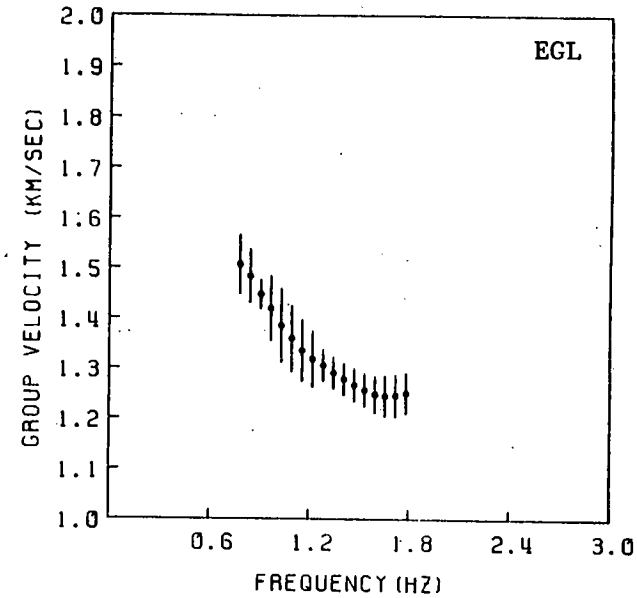

Figures 4.6. Smoothed and event-averaged group velocities, and corresponding standard deviations, for paths to LOWNET stations EDI, EAU, EBH and EGL.

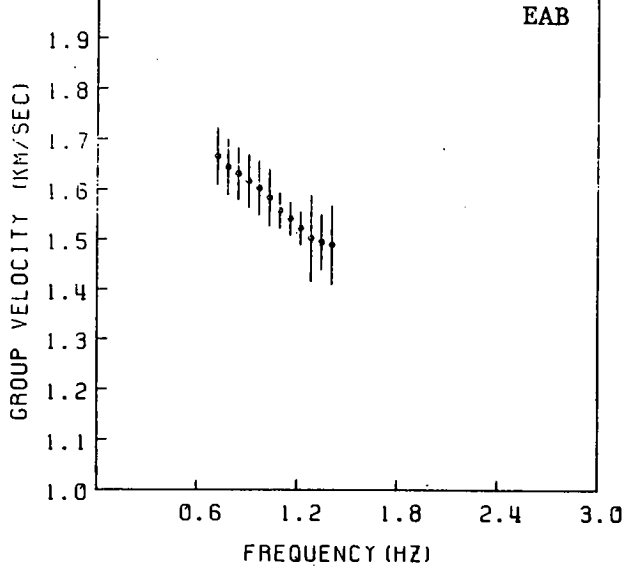

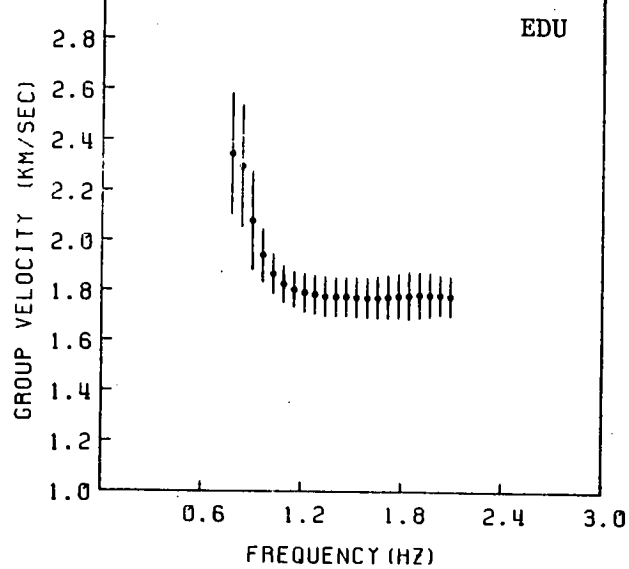

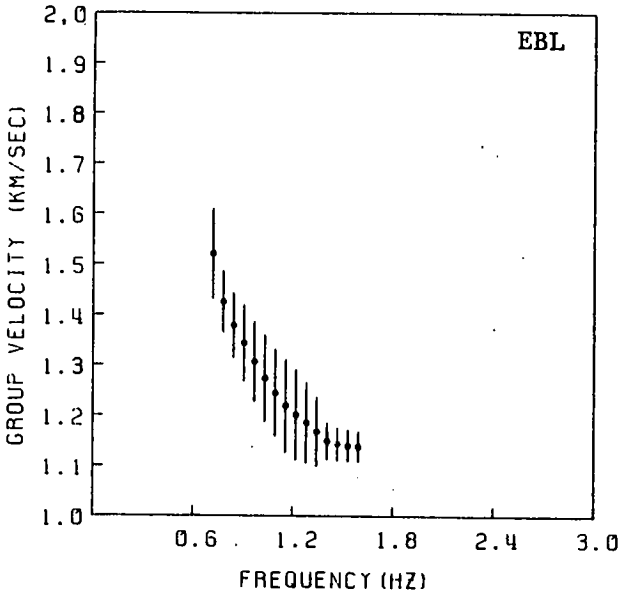

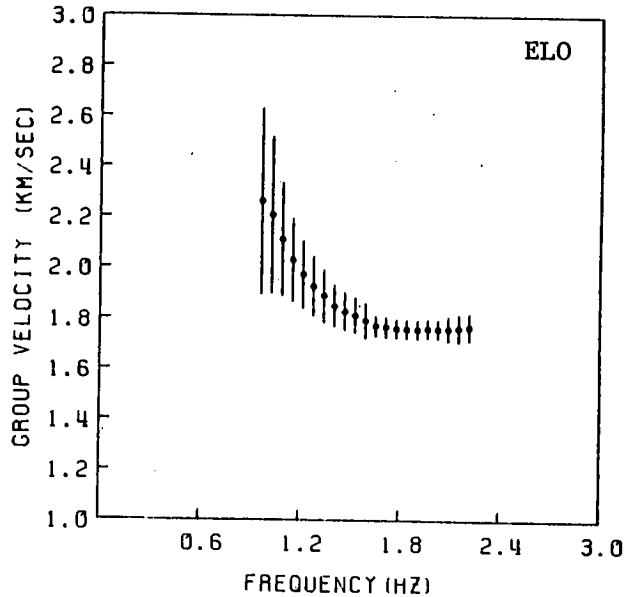

Figures 4.7. Smoothed and event-averaged group velocities, and corresponding standard deviations, for paths to LOWNET stations EAB, EBL, EDU, and ELO.

complete average.

The group velocity dispersion data at each station contains coded information on the elastic properties of the earth along each event-station path. The aim of this chapter is to interpret these discrete measurements of group velocity over a range of frequencies, in terms of estimates of the distribution of specific wave velocity with depth. An inversion procedure which accomplishes this is discussed below.

To invert the group velocity curves we approximate the distribution of shear wave velocity in the earth by a finite number of flat homogeneous layers overlying a half-space, each specified by a shear velocity β_ℓ and a constant thickness t_ℓ ($\ell = 1,m$). The corresponding group velocity for this model is readily computed using the theory of Schwab and Knopoff (1970) (see Appendix A.4), and the relationships between shear wave velocity and compressional wave velocity, and density which are given in Equations 1.6 and 1.7 respectively. Although group velocity is a non-linear function of shear wave velocity, depending mainly on the location of strong velocity contrasts (Cloetingh et al., 1980), small perturbations $\delta\beta_\ell$ about an initial earth model can be connected to the corresponding fluctuations in the group velocity at different frequencies by an approximately linear relation. This is obtained by retaining only the first order term in the Taylor's series expansion about the initial model, which gives

$$\delta U_i = U_i^t - U_i^o = \sum_{\ell=1}^{m} (\partial U_i/\partial \beta_\ell)\delta\beta_\ell$$

for the ith frequency ($i = 1, n$). U_i^o is the group velocity corresponding

to the initial shear wave velocity model and U_i^t the group velocity corresponding to the perturbed model.

Using this approximation, and representing the observed data by U_i^o, we can construct a matrix relation between the observations and the unknown model parameters

$$\underline{y} = A\underline{x} \tag{4.1}$$

$\underline{y}$ is an n×1 column vector of the differences between the group velocity corresponding to a trial model and the observed group velocity, $\underline{x}$ is an m×1 column vector of perturbations in the m layer velocities of this model, and A is an m×n matrix of the partial derivatives connecting the two vectors. The inversion problem is therefore solved by finding an inverse matrix H, which leads to an estimate of $\underline{x}$ ($\hat{\underline{x}} = H\underline{y}$), knowing the vector $\underline{y}$ and matrix A, and adjusting the parameters of the trial model by the corresponding corrections. The algebraic process of singular value decomposition (Lanczos, 1961) is used here to compute H. This inverse minimizes the norm $||\underline{y}||$. As Equation 4.1 is only a first approximation, the best fit between the theory and the observations will not be obtained upon a single application of this procedure. This step is applied many times in an iterative process, until the fit reduces to a satisfactory level.

In practice we find wild fluctuations in $\hat{\underline{x}}$ using the above inverse. To stabilize the procedure we therefore introduce the stochastic inverse (Jordan and Franklin, 1971) or damped least squares inverse

$$H = (A^TA + \theta^2 I)^{-1}A^T$$

where θ is the Levenberg-Marquardt damping parameter which is

adjusted for stability.

The estimated changes $\hat{\underline{x}}$ used to perturb the trial model are connected to the changes required to reduce $||\underline{y}||$ to zero via

$$\hat{\underline{x}} = HA\underline{x} = R\underline{x}$$

where R is called the resolution matrix. This expresses the particular solution $\hat{\underline{x}}$ as a weighted average of the true solution $\underline{x}$, with weights given by the row vectors of the matrix R. The rows of R are known as resolving kernels. The degree to which R approximates to an identity matrix is a measure of the resolution of the model.

As in any inversion procedure, there is an uncertainty attached to each parameter correction depending on the extent of non-uniqueness in the system and the errors on the observations. Estimates of the variance of a particular solution $\hat{\underline{x}}$ can be obtained in terms of the variance of the data for a particular H (Crosson, 1976). To take account of the varying uncertainty between data points, a matrix is introduced which weights each matrix or vector element according to the standard errors of the observations and the model layer thickness (Wiggins, 1972).

A property of the damped least squares inversion is that it allows one to affect a trade-off between the resolution and the variance of the model. If the damping factor θ is small, the variance on each parameter correction is large but R is delta-like. As we increase θ, the variance decreases at the expense of degrading the resolution matrix. θ is initially set large enough to give a stable solution, and is then varied at each

iteration until the minimum with the best trade-off is found. The fit between the observed and theoretical group velocity curves is monitored using the reduced χ^2 function

$$\chi^2_\nu = \frac{1}{n-m} \sum_{i=1}^{n} \left(\frac{U_i^o - U_i^t}{\delta U_i^o} \right)^2 \qquad (4.2)$$

where δU_i^o is the error on the group velocity datum at a particular frequency. This differs from $||\underline{y}||$ by only a constant factor, but is statistically more interpretable. The threshold value for a good fit can now be given at a particular confidence level corresponding to the number of degrees of freedom in the system (Bevington, p. 189, 1969).

The results of the group velocity inversions for the Kirkcaldy Bay data are given in Figures 4.8 - 4.11. Each diagram shows the theoretical group velocity superimposed upon the observed dispersion and its error envelope. The uncertainties on each layer velocity corresponding to this error are drawn on the final solution, and the corresponding resolution kernels, individually normalized with respect to their maximum value, are presented adjacent to this. The majority of χ^2_ν - fits to the observed curves are significant at a 1% level, and the theoretical curves and observations match to within 0.04 km/sec. EDU is the exception, it being necessary to reduce the level to 5%. For this station the low frequency slope cannot be modelled by a shear velocity distribution with reasonable physical contrasts between the layers. In this case a 'best-fit' model is chosen with similar velocities to station ELO.

The layers of the velocity model for each station are initially

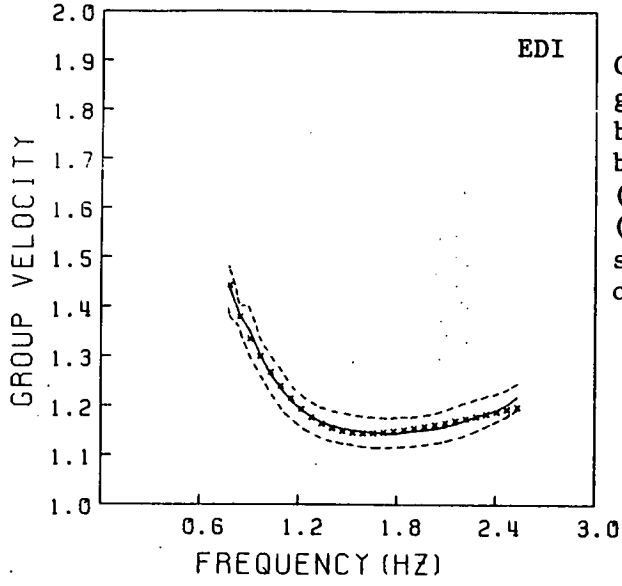

Comparison between theoretical group velocity points generated by shear velocity model found by linearized inversion (x x x), and observed curve (——). Dotted lines indicate standard deviations on the observations.

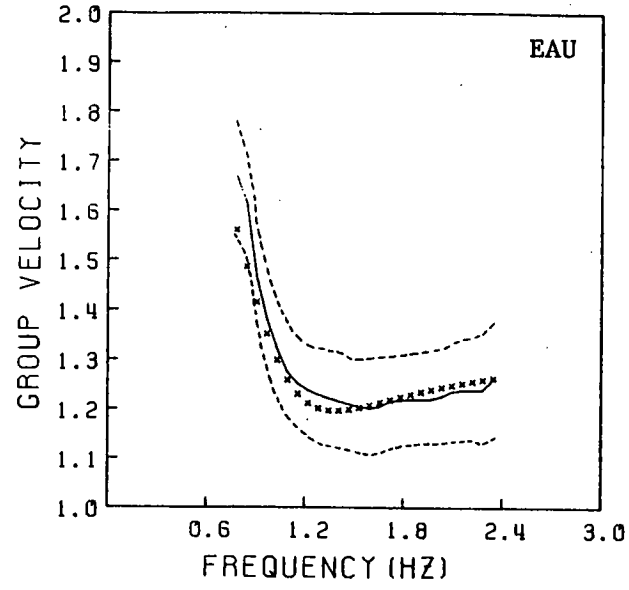

(a) (b)

(a) (b)

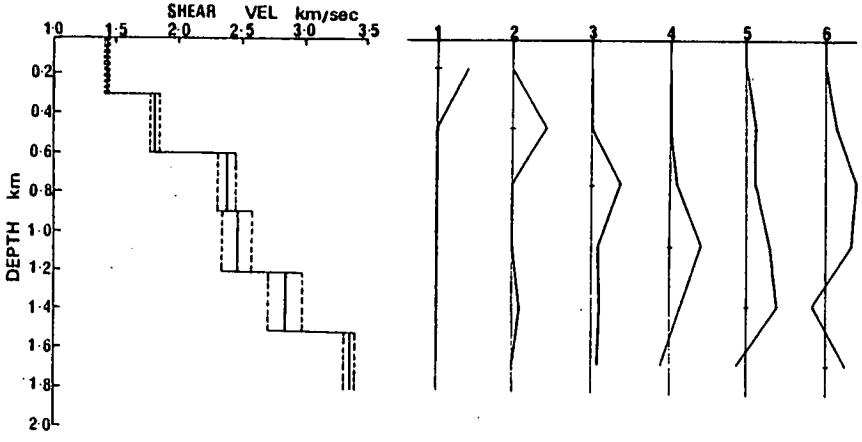

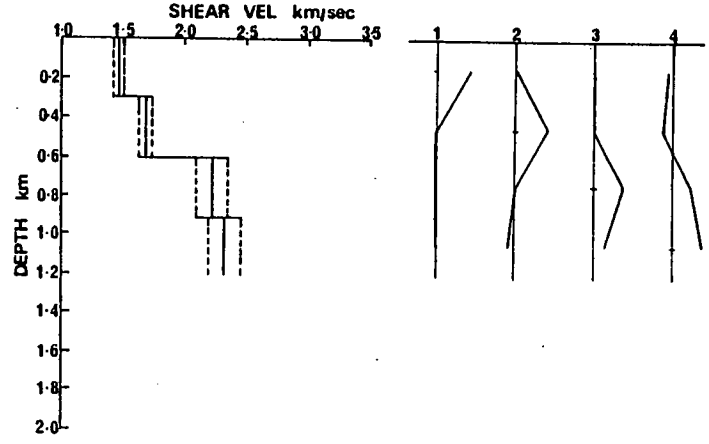

(a) Shear velocity models with bounds obtained by linearized inversion of the observed group velocity and standard deviations.

(b) Resolution kernels associated with this inversion - kernels are normalized with respect to their individual maximum, and horizontal ticks mark the centre of the corresponding layer.

Figure 4.8. Group velocity inversion results for paths to LOWNET stations EDI and EAU.

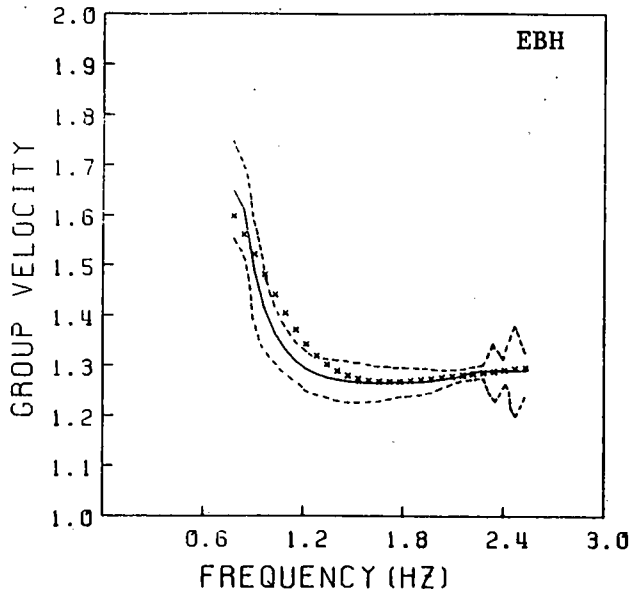

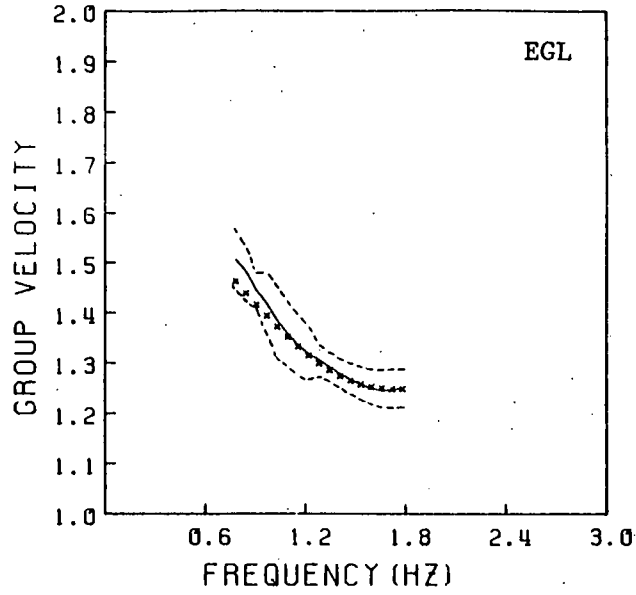

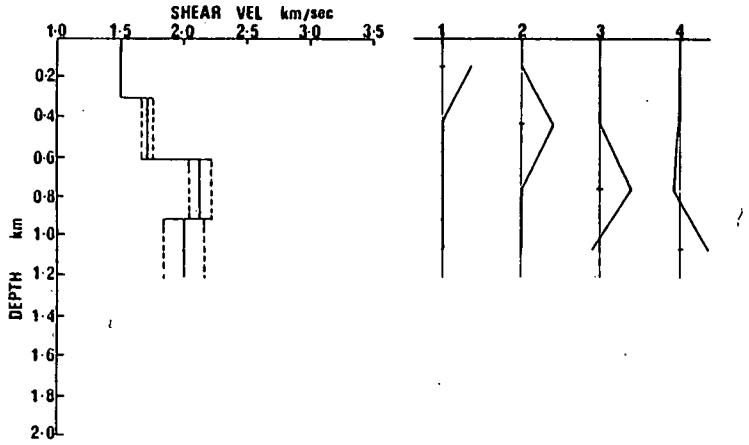

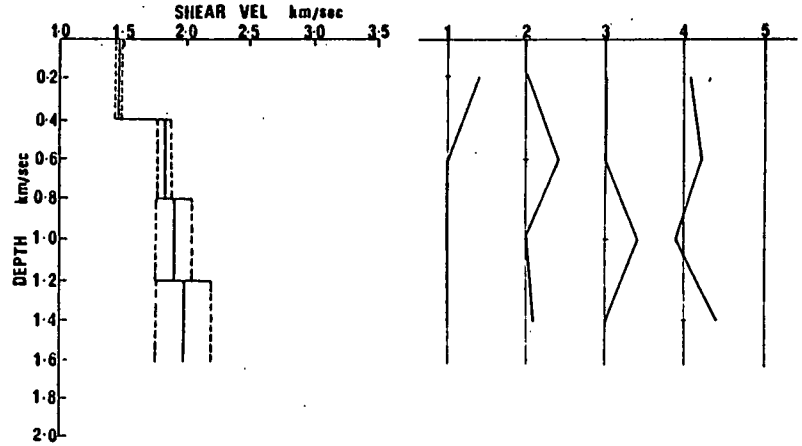

Figure 4.9. Group velocity inversion results for paths to LOWNET stations EBH and EGL.

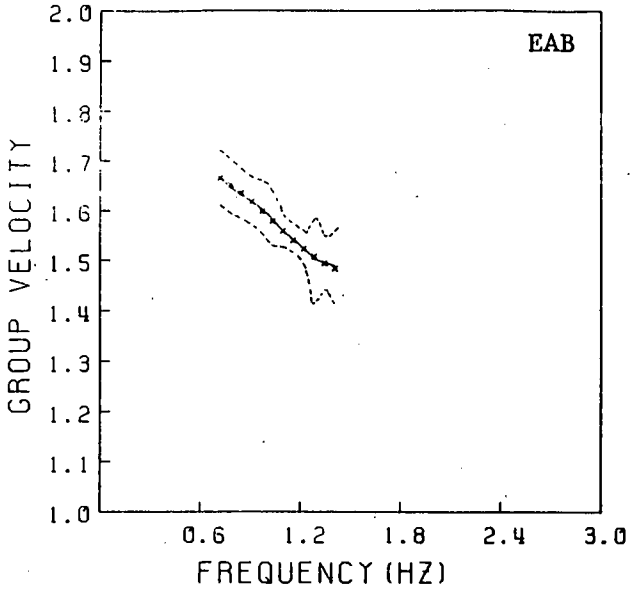

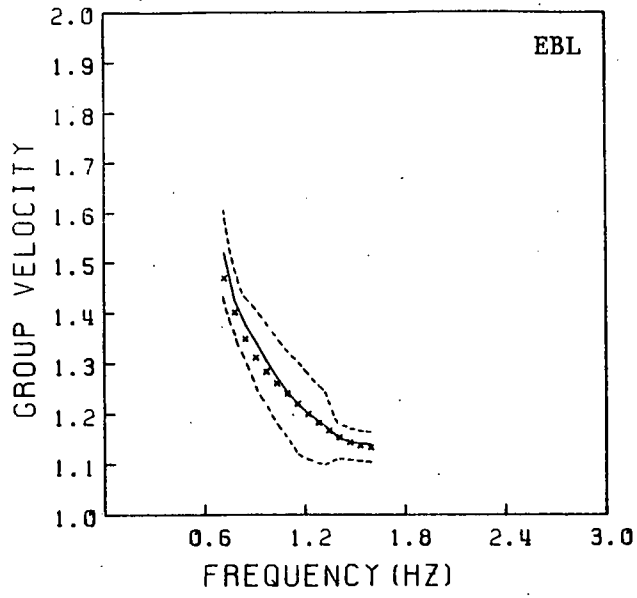

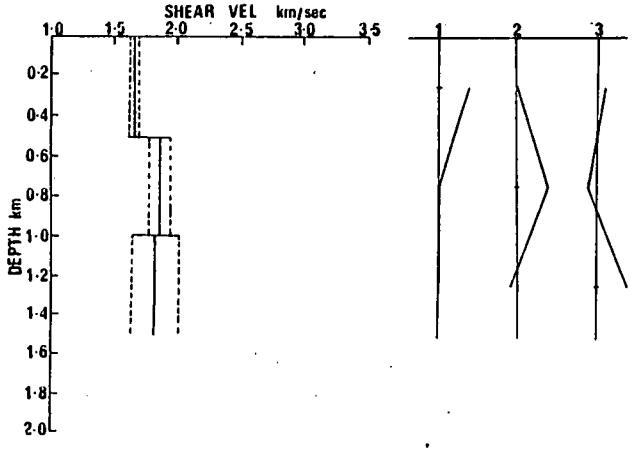

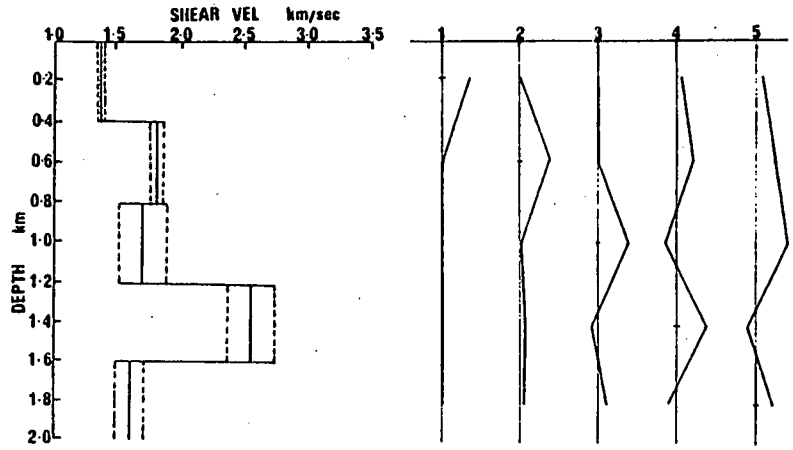

Figure 4.10. Group velocity inversion results for paths to LOWNET stations EAB and EBL.

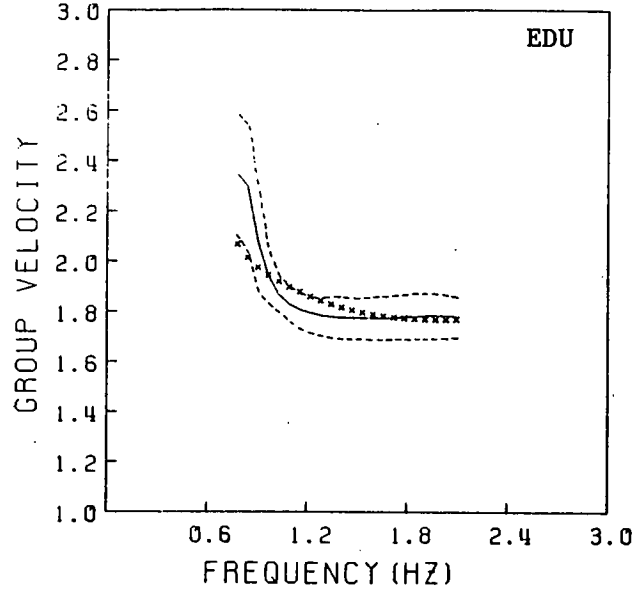

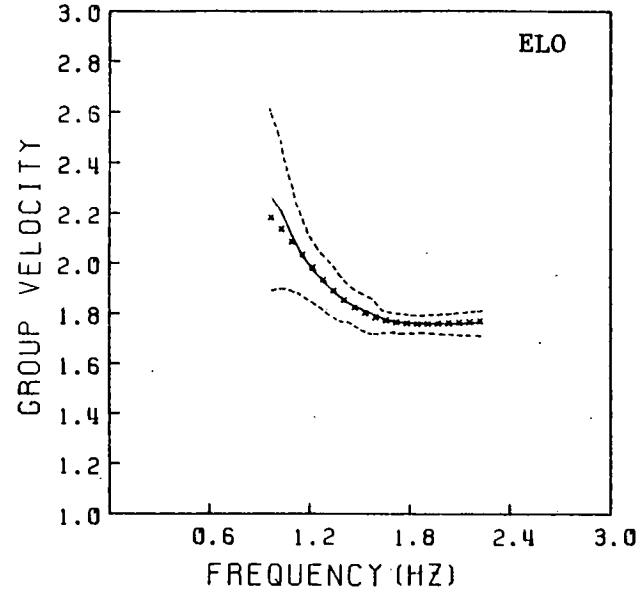

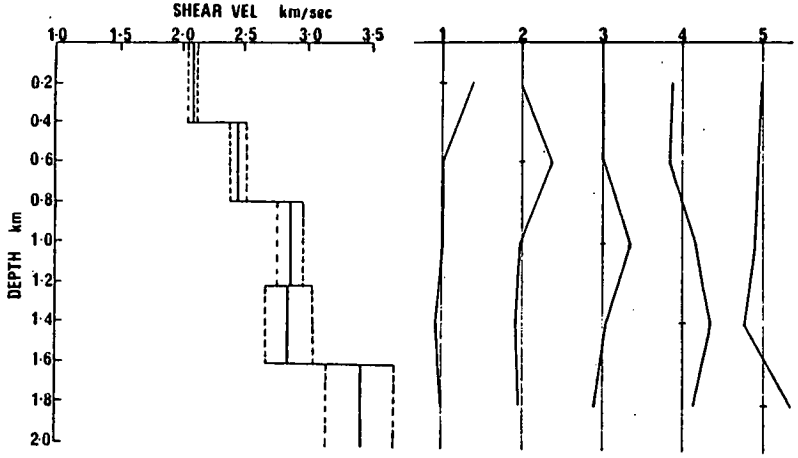

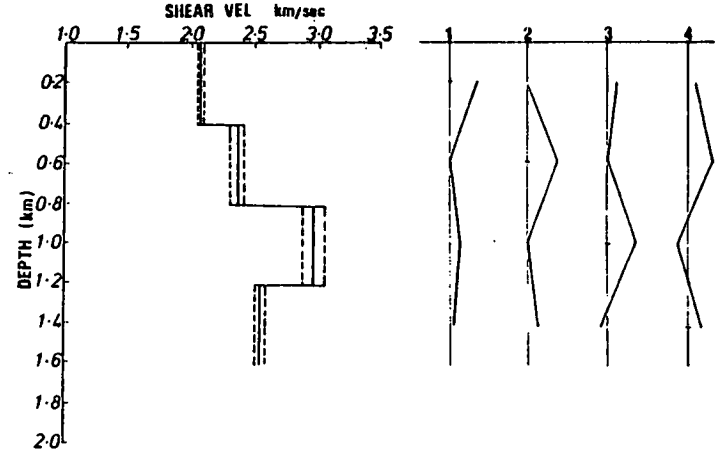

Figure 4.11. Group velocity inversion results for paths to LOWNET stations EDU and ELO.

set to equal thicknesses. However, if the layers are too thin (for a particular set of velocities and frequencies) the inversion process becomes unstable, and if too thick the resolution potential is decreased. Thus the layer thicknesses are adjusted until an optimum between stability and resolution is attained. This point varies for different stations, and so the models are not completely uniform across the array. For example, the model for EDI has 300m thick layers whilst those for EAB have a thickness of 500m.

The bounds on each estimated layer velocity increase with depth, as expected for a Rayleigh wave of finite penetration. In cases where this does not occur, the resolution kernels increase in width. The majority of shear velocities are less than 3.0 km/sec, which is the limit set by the cross-section of Bamford et al. (1976) and Evans (1981) for this region. In the lower layers, there is an undesirable correlation between negative side-lobes of the resolution kernel and low velocities. This spurious effect is particularly noticeable for stations EBH, EAB, EBL and ELO, and decreases the reliability of these estimates.

The profiles from the inversions are assessed collectively in Figure 4.12. The most distinctive feature of these depth distributions is the contrast between the shear velocity of 2.1 km/sec in the top layers of the models for the paths to stations EDU and ELO, with the lower velocities of around 1.5 km/sec for the paths to the other stations. This is to be expected as the paths to the former two stations cross a greater proportion of the high velocity Old Red Sandstone province (Figure 4.2). Although the path to the station EAB traverses this formation, this represents only a very small fraction of the total path length, the major part of which

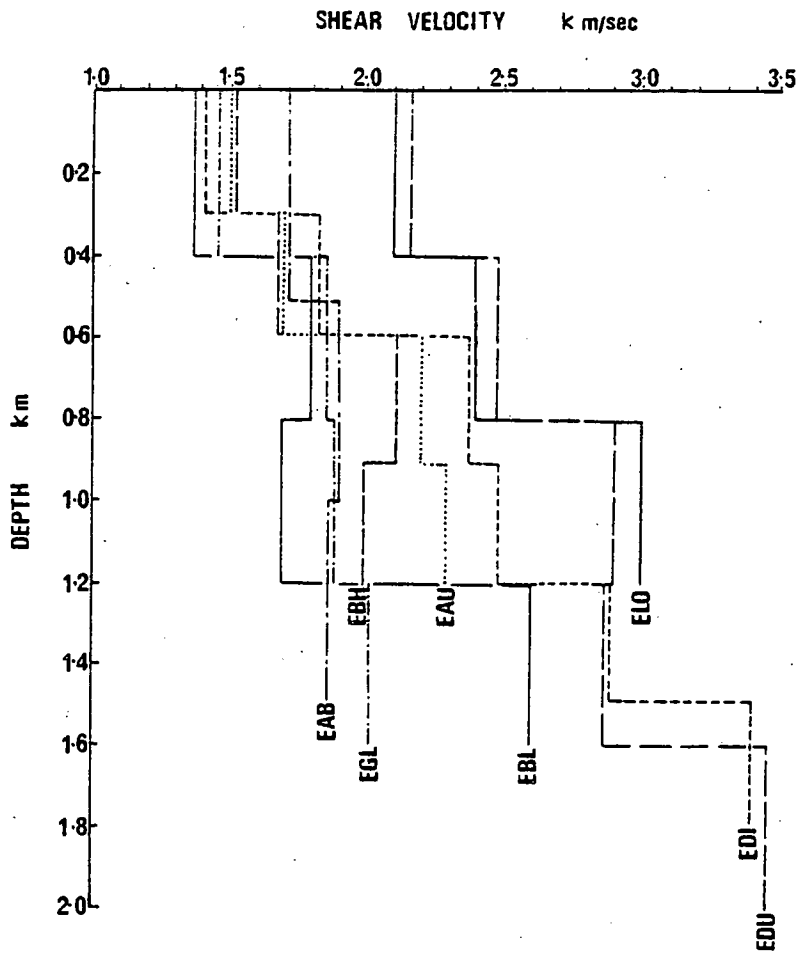

Figure 4.12. Summary of the shear wave velocity profiles obtained by inversion of the group velocity data corresponding to the eight LOWNET stations.

crosses the lower velocity Carboniferous sediments. A shear velocity of 1.7 km/sec for this station is in correspondence with this observation. The top layer velocities at stations EDI, EAU, EBH, EGL, and EBL are all grouped around 1.45 km/sec. There is a general increase in shear velocity with depth for all models, and there appear to be no significant low velocity regions excepting the spurious values described above. Below a depth of 400m, the models for stations EGL and EAB have an approximately constant velocity of 1.8 km/sec, which extends down to a depth of 1.5 km. In spite of the variation in depth penetration for stations EDI, EAU, EBH, and EBL, the profiles match each other well, this is expected for all except station EBH as each path samples a similar surface geology (see Figure 4.2). EGL should conform with this group also, but does not. The models for stations EDU and EDI show a shear velocity of 3.5 km/sec at a depth of 2 km. At this depth there are wide differences in the velocities, ranging from 1.9 - 3.5 km/sec, due to the pronounced decrease of resolution with depth.

Calculations of the phase velocity curves corresponding to these single-station shear velocity models for stations EDI, EAU, EBL, and EGL elucidate an interesting feature concerning propagation of the surface waves in the Firth of Forth. The velocities are less than the velocity of sound propagation v in the water at the frequencies 1.0 - 1.4 Hz. For a pure Rayleigh wave in a solid overlain by a water layer this cannot occur, and consequently indicates the existence of a Stoneley wave (these can always exist between a solid and a liquid layer) at these frequencies. The transition region between the two types of surface wave corresponds to the point at which $c \simeq v$. Around this frequency an interaction between pure

Stoneley and pure Rayleigh waves occurs (Biot, 1952).

These observations suggest that the explosion initially generates a mixture of Stoneley and Rayleigh waves which propagate along the water-solid, or sediment-solid interface. At the sea-land boundary the waves are converted into fundamental and higher Rayleigh modes. The transmission coefficient between Stoneley and Rayleigh modes at this boundary could partly account for the appearance of the waves and the higher mode energy.

4.3.5 Pure Provincial Velocity Structure

The events and stations give an azimuthal coverage in three quadrants of the eastern section of the Midland Valley. The paths to each station are generally through a mixture of Old Red Sandstone, Devonian Lavas, Low velocity Carboniferous sediments, and the Firth of Forth (Figure 4.2). The sea-bed deposits are mainly a silty-clay facies, but this unconsolidated material has a thickness of only a few centimetres. The more solid quaternary deposits can reach a thickness of between 20 - 60m in the epicentral area according to the isopachs of Thomson (1977).

The general qualitative trend of group slowness (inverse of velocity) corresponding to the single-station group velocity data above, is shown in Figure 4.13a. These curves agree with the conclusions of Evans (1981) that the provincial slownesses increase in the order:- Devonian Lavas, Old Red Sandstone, and Carboniferous sediments. The propagation paths to stations EDI, EAU, EGL, EBL and EBH, which are mainly within the Carboniferous

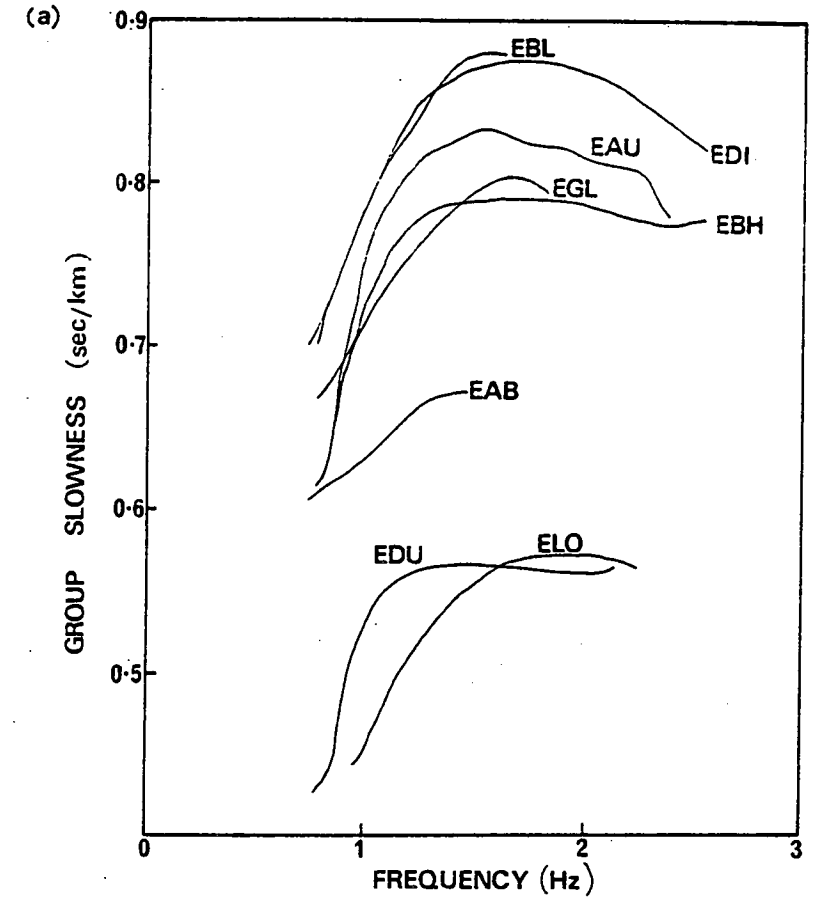

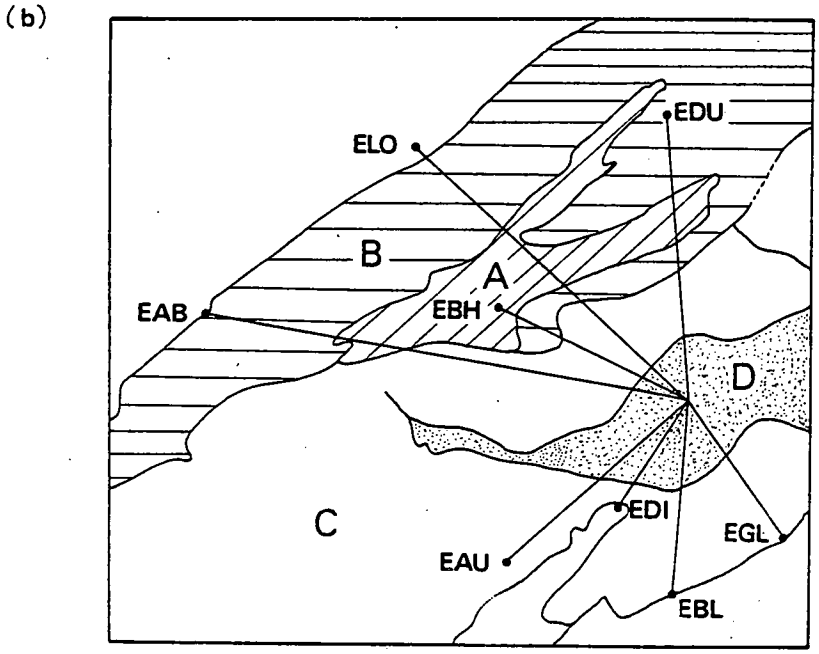

Figures 4.13. (a) Group slownesses corresponding to the averaged group velocities of Figures 4.6 and 4.7.

(b) Provincial division of the Midland Valley for pure-provincial inversion study.

province, have the highest slownesses. The slowness curve for EBH is the lowest of this group, as the path crosses a small fraction of the higher velocity Devonian Lavas and Old Red Sandstone. The path to EAB crosses a larger fraction of these formations and consequently records a lower slowness. The paths to both EDU and ELO sample a relatively larger fraction and are grouped together below EAB. The group velocity inversion profiles also show this trend. It is expected that the path to EDI should record the highest slowness as a consequence of the large proportion of the Firth of Forth which it intersects, however the curve for EBL is coincident with this.

To obtain pure provincial group slownesses we divide the Midland Valley into four regions containing Devonian Lavas A, Old Red Sandstone B, Carboniferous sediments C, and the Firth of Forth Estuary D (Figure 4.13b). The proportion of each path through these provinces is determined from this diagram, and the matrix of fractional path lengths is given in Table 4.2. The matrix shows that EDU and ELO contribute about the same information from the four provinces, the slowness curves being consistent with this. EBL is again inconsistent, as it should record a similar slowness to EAU. Therefore in the scheme for provincial inversion, data from this station is excluded. The curve for EDU is also excluded as the low frequency gradient is unreliable (Section 4.3.4).

The solution of the equation relating provincial velocities to mixed path velocities at each frequency (Equation 1.18) is obtained by the method of least squares inversion used to invert group velocities (Section 4.3.4). Only one iteration of this procedure is necessary as the equation is linear. Province A is not

	PROVINCE			
	A	B	C	D
EDI	0.00	0.00	0.25	0.75
EAU	0.00	0.00	0.55	0.45
EBH	0.13	0.26	0.37	0.24
EGL	0.00	0.00	0.61	0.39
EAB	0.14	0.29	0.45	0.12
EBL	0.00	0.00	0.57	0.43
EDU	0.19	0.36	0.24	0.21
ELO	0.22	0.38	0.27	0.13

A - Old Red Sandstone

B - Devonian Lavas

C - Carboniferous

D - Firth of Forth

TABLE 4.2. Matrix of fractional path lengths through the four different provinces in the Midland Valley.

resolved (Figure 4.13b clearly shows the reason for this), and a pure provincial velocity cannot be obtained. Provinces C and D are well resolved as every path passes through them. The results for C and D are quite stable, even when data from stations are excluded or included in the scheme. The corresponding pure provincial velocities with standard deviations obtained by inversion of the slowness data from the six stations, and the fit of the theoretical mixed path slownesses to the observations are shown in Figures 4.14a and b respectively. The narrow frequency range of the inversion solutions is due to an inexact matching of the frequency limits at each station. The pure-provincial group velocities have large standard deviations of around 0.2 km/sec, which are anti-symmetric about the mean curve as the inversion results are in terms of slowness. Group slownesses for provinces C and D are not significantly different and show a smooth decrease from 1.4 to 1.1 km/sec with frequency. This confirms that the 30m water layer and the sediments in the Firth of Forth do not noticeably influence the velocity of propagation. The theoretical curves for EDI, EAU, and EAB match the observations, whereas the observed slownesses for stations EBH and ELO are not well modelled. Lateral refraction of the wavefronts and phase delays at boundaries or other associated effects may cause differences. As the overall fit is poor at these latter stations, further inversion of the provincial velocity curves to shear velocity depth models is not undertaken.

More reliable inversions of this nature obtained with a greater station density and wider frequency range could provide important information regarding lateral variations in velocity in a region and the propagation of waves from underwater explosions.

(a)

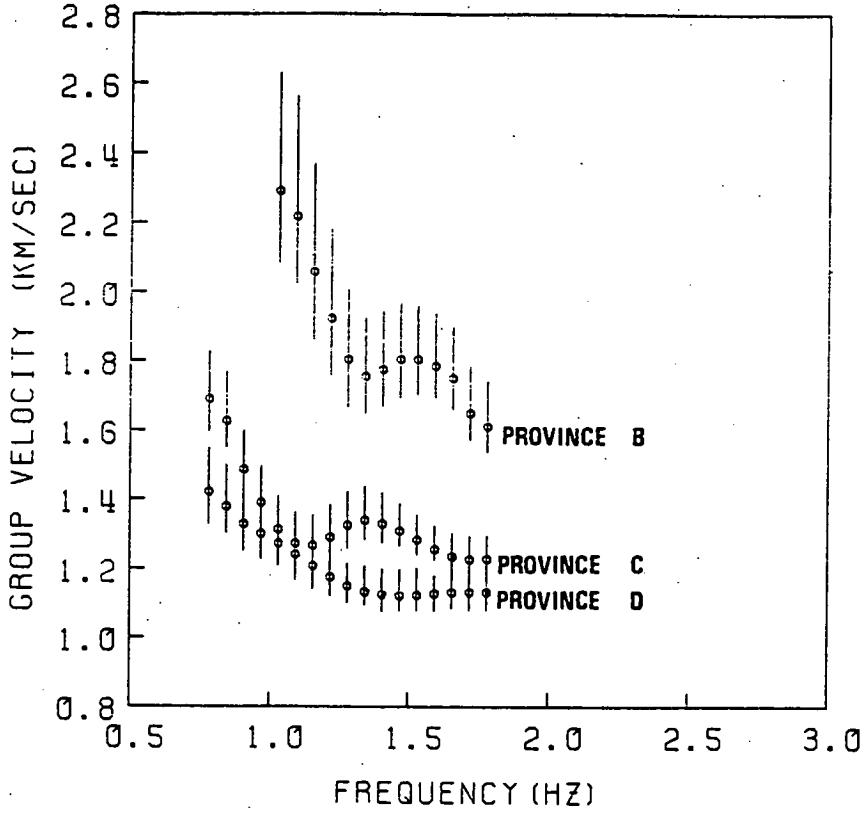

(b)

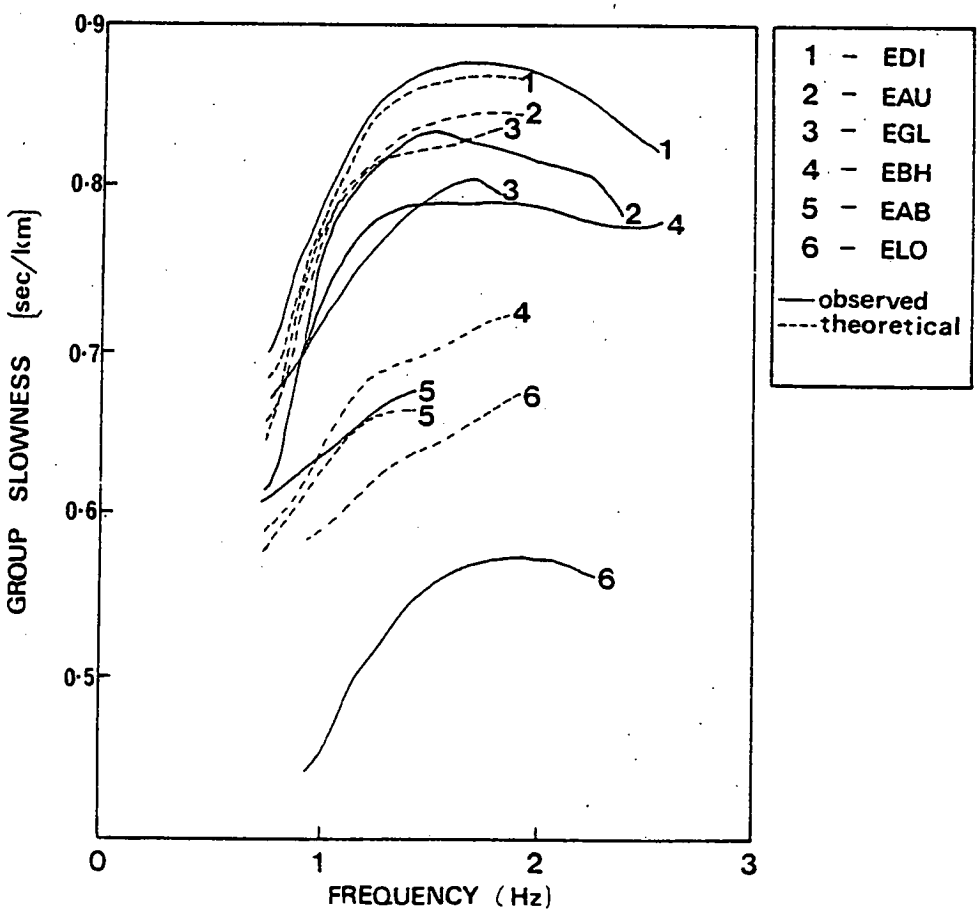

Figure 4.14. (a) Pure provincial group velocities for provinces B, C and D of Figure 4.13 obtained by least squares inversion (province A being unresolved).

(b) The fit of the theoretical slowness curves generated by the inversion compared to the corresponding observations.

4.4 Kyle Earthquake Data

4.4.1 Description of Seismograms

The earthquake KEQ of surface wave magnitude 3.7 generated Rayleigh waves which were recorded on the ALPHA and BETA segments of the LISPB line (Section 1.3). Figures 4.15 - 4.17 show the Rayleigh waves for the complete set of vertical component recordings, azimuth and station code for each being marked. Dotted lines indicating velocities of 3.5 km/sec, 3.0 km/sec, and 2.5 km/sec are shown for guidance.

Inspection of the seismograms reveals three distinct portions corresponding to strong first and second higher mode arrivals, and a very weak apparent fundamental mode arrival. The identity of the latter portion of the surface wave train is uncertain. It could be coda from the other two arrivals, but it is definitely not a lateral refraction as it occurs at the same position for the majority of seismograms.

As the focal depth of KEQ is much larger than the expected wavelength (0.5 - 4 km) of fundamental mode surface waves recorded within the frequency range of the seismometers, it is not surprising that higher mode energy is preferentially excited. The factor $\exp(-mh)$ roughly determines the decay of the fundamental mode energy with depth (Appendix A.2). This has a value of $\approx 10^{-4}$ at a depth of 11 km, frequency of 1 Hz, and for a phase velocity of 3.5 km/sec. Higher modes have critical depths at which they are excited most efficiently, and frequencies at which they are not excited at all. Modes with non-zero depth eigenfunctions at the earthquake focus

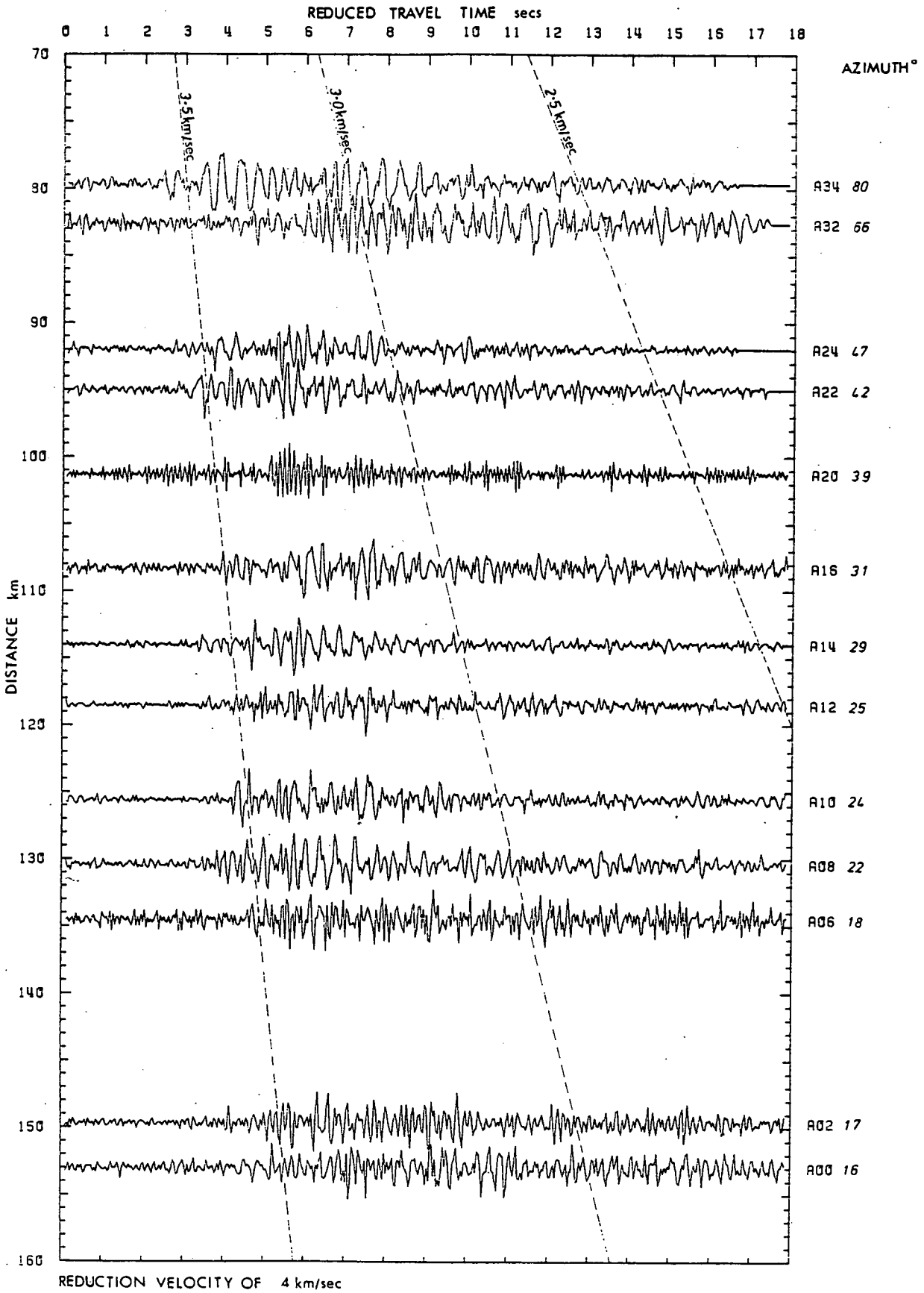

Figure 4.15. Vertical component recordings of KEQ along the first section of the ALPHA line.

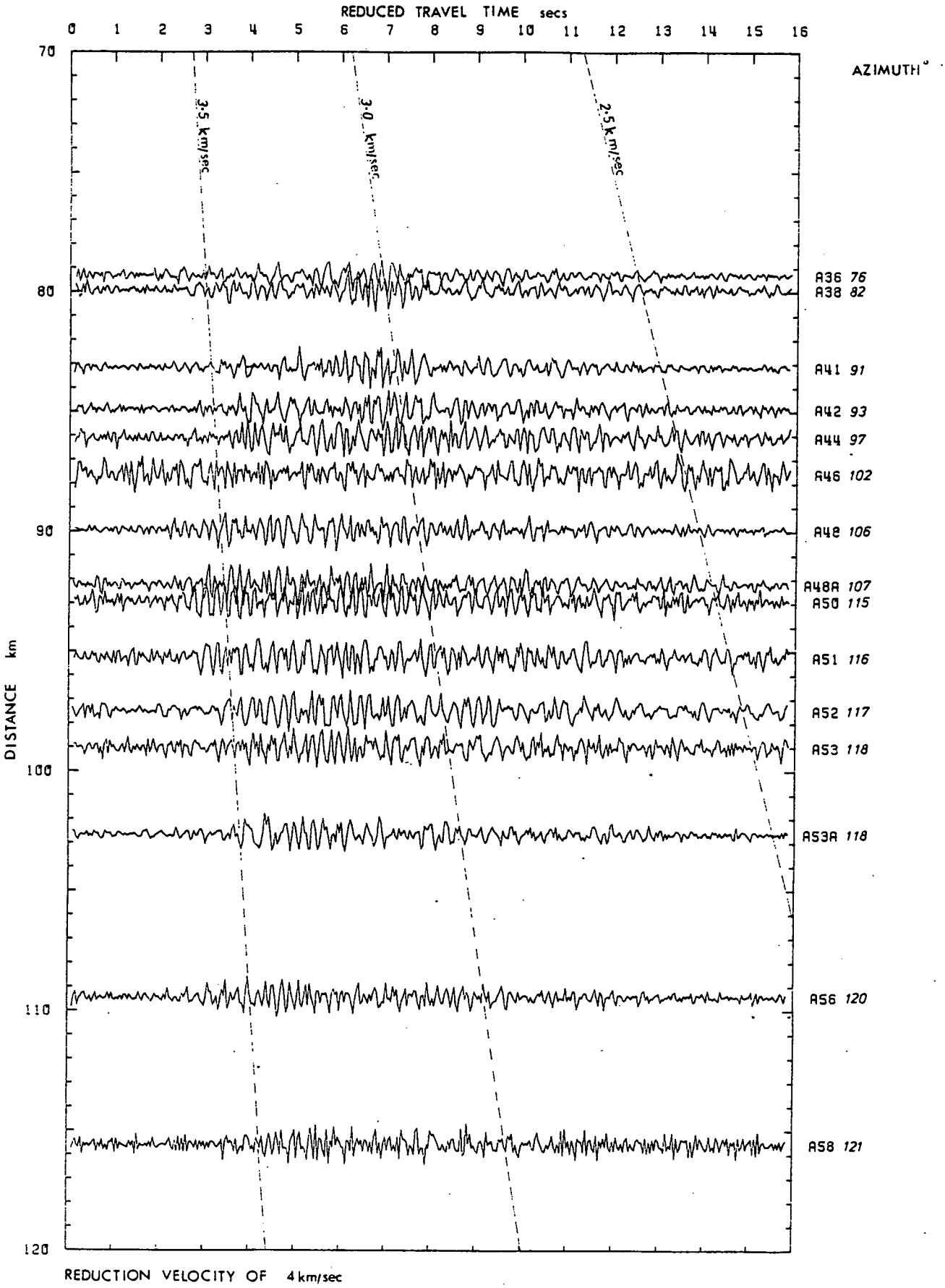

Figure 4.16. Vertical component recordings of KEQ along the remaining segment of the ALPHA line.

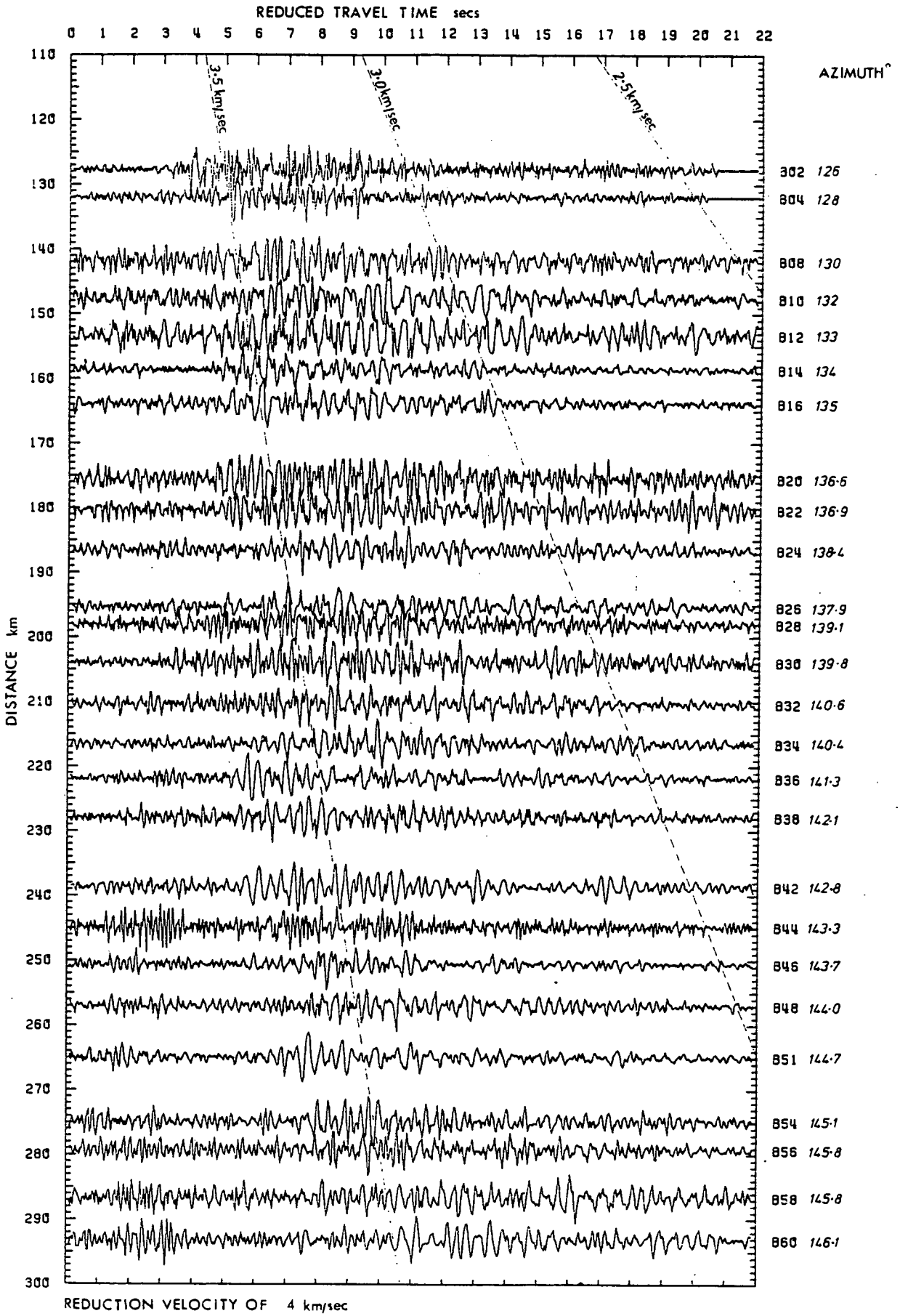

Figure 4.17. Vertical component recordings of KEQ along the BETA line.

will be excited. This is illustrated schematically in Figure 4.18. A similar phenomenon has been observed for deep earthquakes (Okal, 1979).

In an attempt to emphasize that only fundamental Rayleigh waves in the range 0.5 - 5.5 Hz are weak, long period seismograms are examined. No recordings of KEQ are available, however a recording of the main shock, with a focal depth of 10 km, at the WWSSN station VAL revealed a fundamental Rayleigh wave of 0.1 Hz with an estimated wavelength of 35 km.

The relative amplitudes of the modes recorded at each station do not directly reflect the relative excitation at the source. Each successive higher mode has a higher frequency content and is more susceptible to scattering and energy loss by attenuation than the lower modes. Calculations indicate that the third and fourth higher modes are probably preferentially excited at frequencies of 0.5 - 5.5 Hz for KEQ, but are rapidly attenuated.

The surface waves generated by KEQ and recorded on the LISPB short period instruments have energy up to 5.5 Hz, with a dominant frequency of about 2 Hz. On average, the second higher mode arrives at 3.5 km/sec and the first higher mode at 3.1 km/sec. The smaller amplitude waves arrive with a velocity of 2.9 km/sec or less. There is considerable variation in the velocity of arrival from station to station along the ALPHA line, which reduces towards the latter half of the BETA line as the propagation paths cover a narrower azimuthal range.

The data for the BETA line is generally of a much poorer quality than that for the ALPHA line and has a much smaller signal to noise

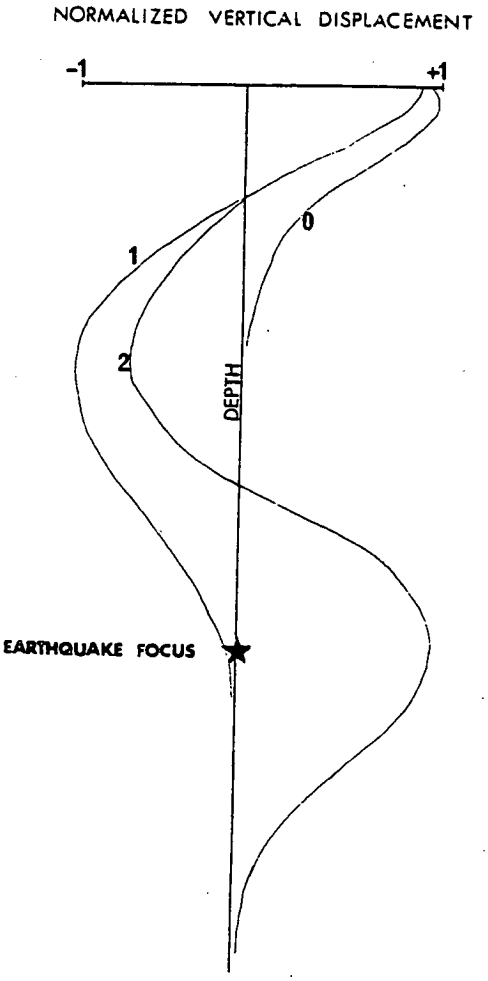

Figure 4.18. Schematical illustration of the depth dependence of the eigenfunctions corresponding to fundamental (0), first (1), and second (2) higher modes at a fixed frequency. The second higher mode will be preferentially excited from an earthquake source at this frequency as it possesses an anti-node at the event focus.

ratio. This cannot be accounted for on the basis of greater path lengths. The separation between the first and second higher modes, and the interfering S-wave and second higher mode, is greater for the BETA line, and this helps to isolate the individual signals.

4.4.2 Observed Group Velocities

A typical contour diagram of instantaneous amplitude in the group velocity - frequency plane is shown for the recording at station A34 in Figure 4.19. The higher modes are well separated along the velocity axis, but the main energy peaks have a similar frequency content. The lower frequencies of the first higher mode interfere with the second higher mode, and automatic following of the ridge crest is inhibited. The group velocities are again obtained by visual inspection of the contour diagram. In some cases the mode energy overlaps making discrimination difficult. Shear waves interfere mainly with the second higher mode, but are clearly separated on the contour diagrams for the majority of seismograms due to their higher frequency content and small dispersion. Possible S-wave energy is shaded in Figure 4.19. No special techniques are used to obtain the higher mode spectra. The mode energy is selected on the basis of a simple time window around the seismogram.

The combined effect of Assumpção's (1981) new epicentre and origin time is to increase the Rayleigh wave group velocities, particularly at the closest stations, relative to the Kaminski et al. (1976) solution. The increase ranges from 0.2 km/sec at

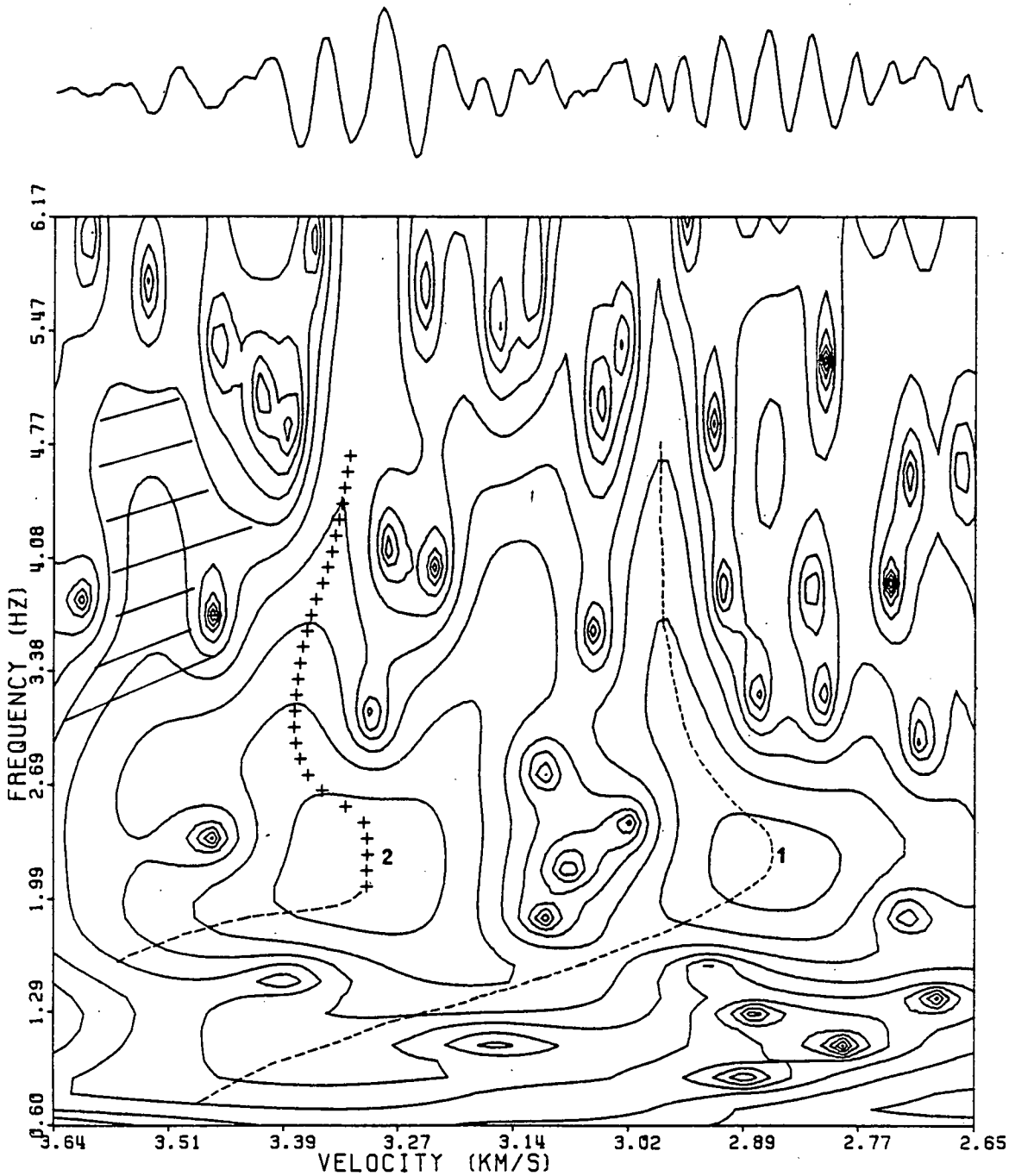

----- group velocity inferred from contours.

+ + + group velocity picked automatically by the analysis algorithm.

Figure 4.19. Contour diagram of first (1) and second (2) higher modes for station A 34. Shaded regions correspond to possible SV energy.

at the closest stations to 0.01 km/sec at the outermost.

The data are averaged every four frequency harmonics, thus increasing the separation between the spectral estimates to 0.098 Hz. To increase the precision and reliability of each group velocity observation, and for the purposes of computing standard deviations on each datum, adjacent group velocities showing similar dispersion characteristics are averaged and then smoothed. Seven sets are obtained, the regions covered are labelled A - G, and are shown in Figure 4.20. Table 4.3 shows the stations in each group. The regions represent relatively homogeneous provinces with respect to wave velocity.

The smoothed sample averages and standard deviations are shown in Figures 4.21 - 4.24, and given numerically in Appendix C.2. The second higher mode group velocity curve lies above the first higher mode curve in all cases. The frequency range for the higher of the two modes is 1.8 - 4.3 Hz, while it is 0.8 - 4.3 Hz for the lower one. The standard deviations for the second higher modes are generally smaller than those of the first higher mode, which could indicate a more homogeneous earth structure at greater depth in the crust. The number of stations contributing to each group varies along the line. Along the BETA line the group velocities are very similar, and group G contains 25 stations. Group D, on the other hand, covers a large azimuthal range with 3 stations.

4.4.3 Lateral Variation of Velocity

The higher modes penetrate into the crust on average between 6 - 17 km. This should be compared with only 2 km for the fundamental Rayleigh waves generated by the Kirkcaldy Bay shots. Therefore only the high frequency group velocity can be influenced by the

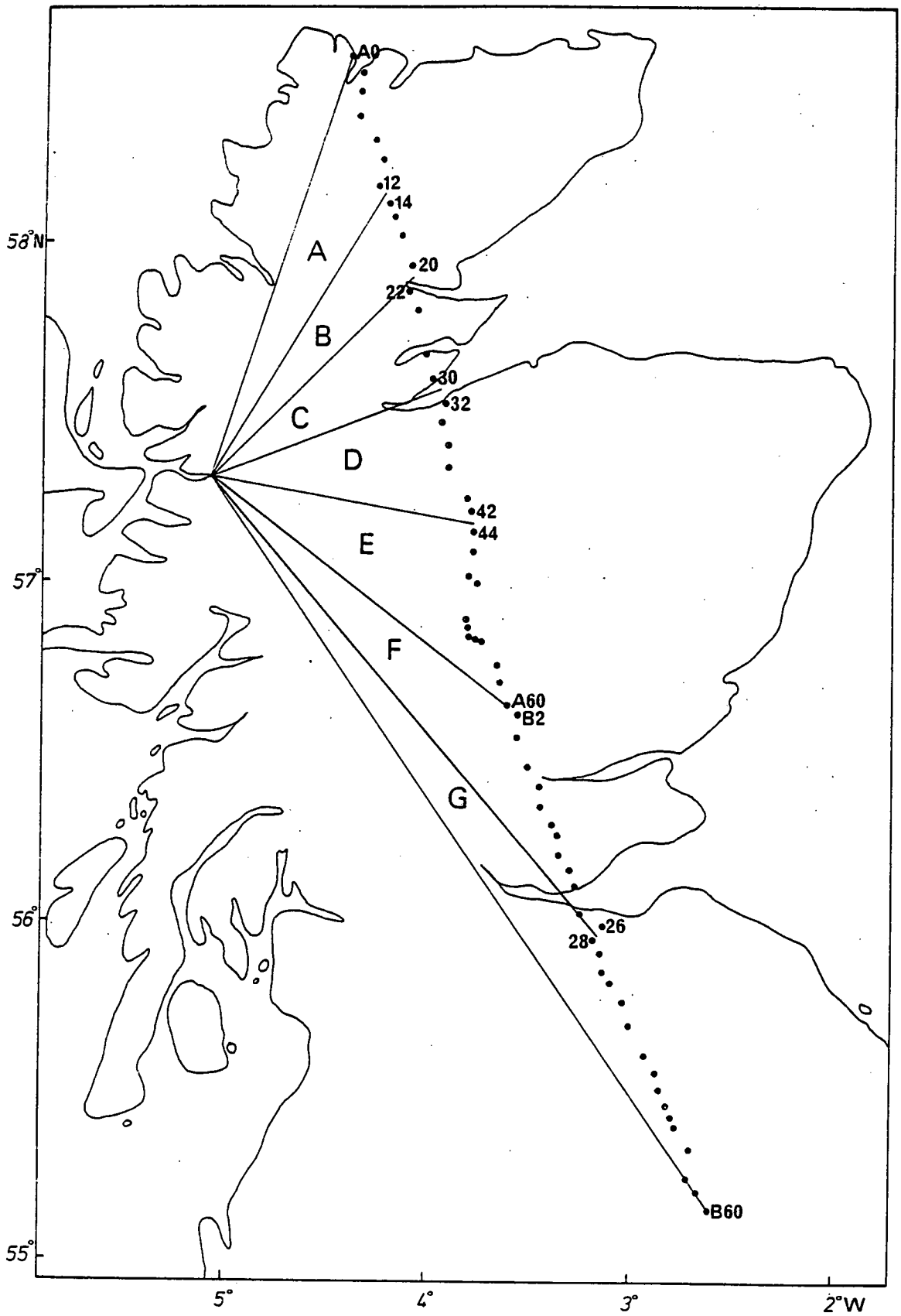

Figure 4.20. Regionalization of Scotland based on the group velocity dispersion characteristics of first and second higher Rayleigh modes generated by the earthquake KEQ.

VELOCITY DISPERSION GROUPINGS

	FIRST HIGHER MODE	SECOND HIGHER MODE
A	A00, A02, A06, A08, A10, A12	A00, A02, A06, A08, A10, A12
B	A14, A16, A20	A14, A16, A20
C	A22, A24	A22, A24, A30
D	A32, A34, A36, A38, A41, A42	A32, A34, A36, A38, A41, A42
E	A44, A48, A50, A51, A52, A53 A53A, A56, A58	A44, A48A, A48, A51, A53 A53A, A56, A58
F	B02, B04, B08, B10, B12, B14 B16, B20, B22, B24, B26	B02, B04, B08, B10, B12, B14 B16, B20, B22, B24, B26
G	B28, B30, B32, B34, B36, B38 B42, B44, B46, B48, B51, B54 B56, B58, B60	B28, B30, B32, B34, B36, B38 B42, B44, B46, B48, B51, B54 B56, B58, B60.

TABLE 4.3. Grouping of stations along the LISPB line, which yield dispersion curves with similar characteristics.

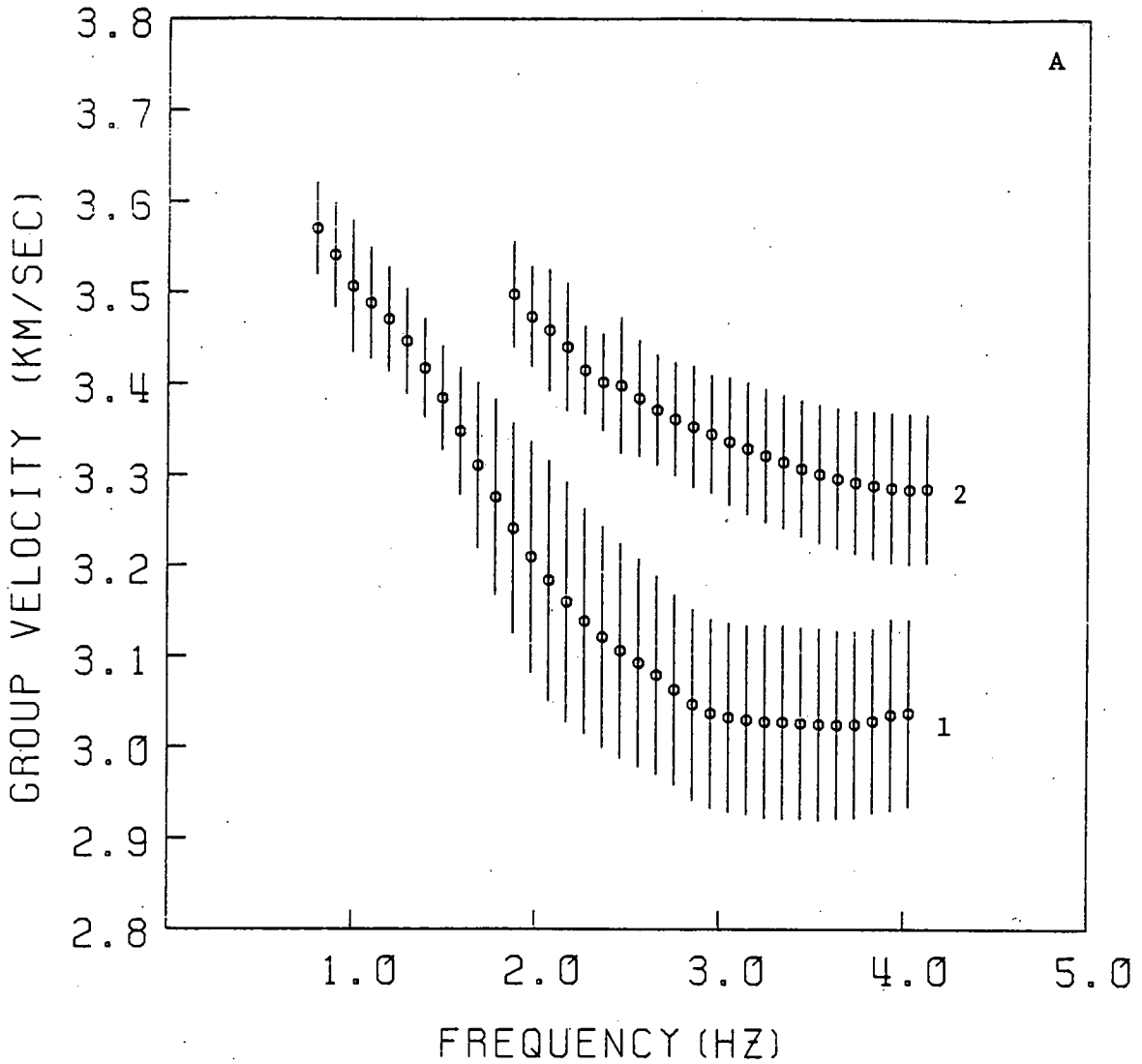

Figure 4.21. Smoothed and averaged first (1) and second (2) higher mode group velocities and corresponding standard deviations for region A.

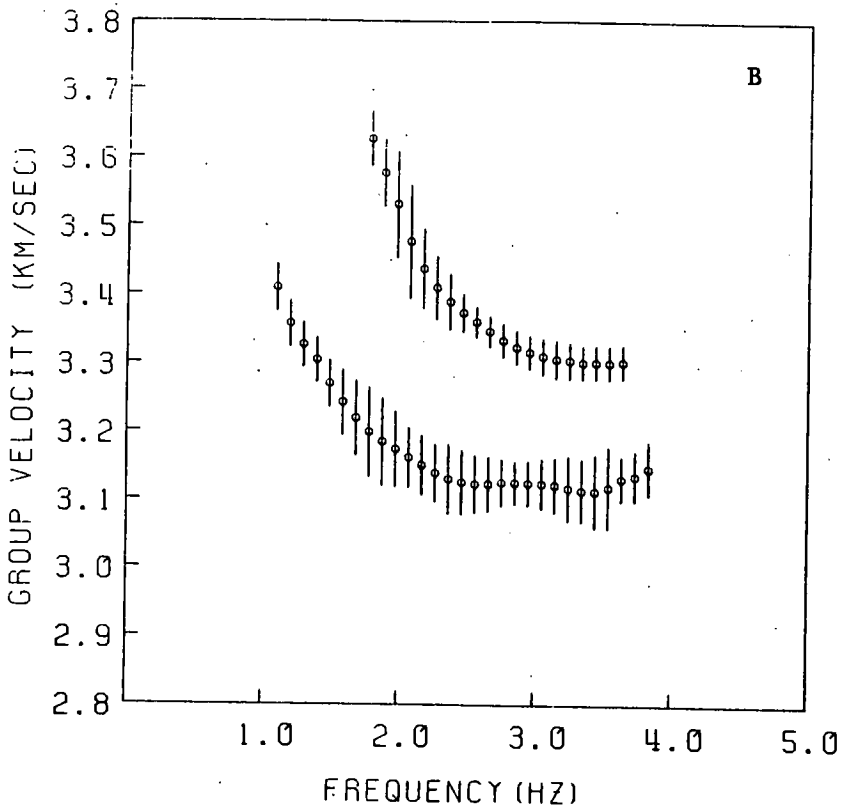

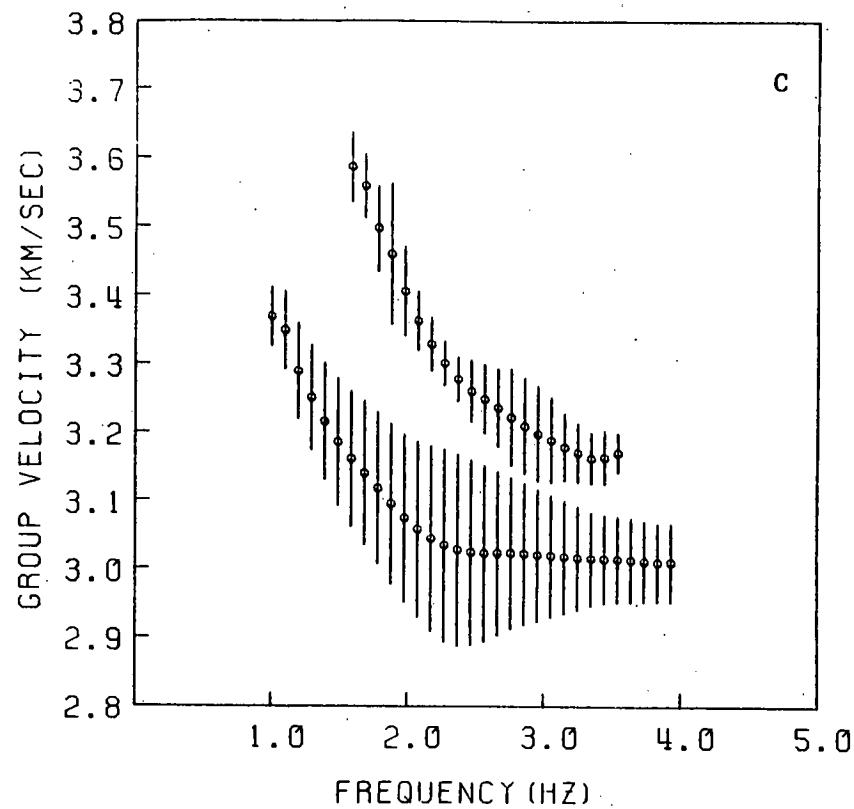

Figure 4.22. Rayleigh wave higher mode group velocity data, generated by the earthquake KEQ, for regions B and C.

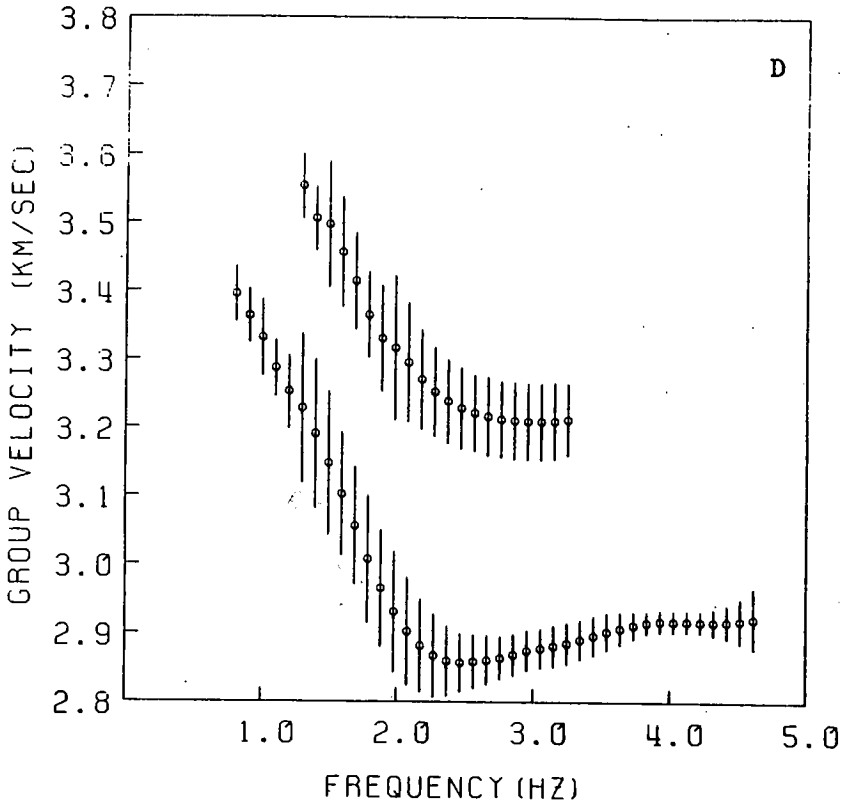

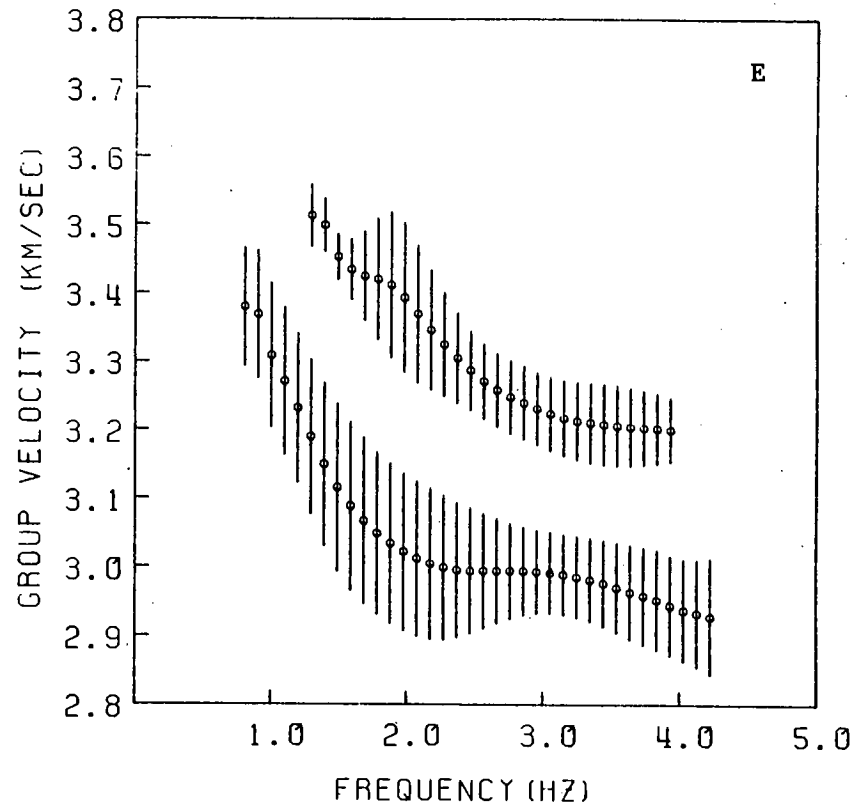

Figure 4.23. Rayleigh wave higher mode group velocity data, generated by the earthquake KEQ, for regions D and E.

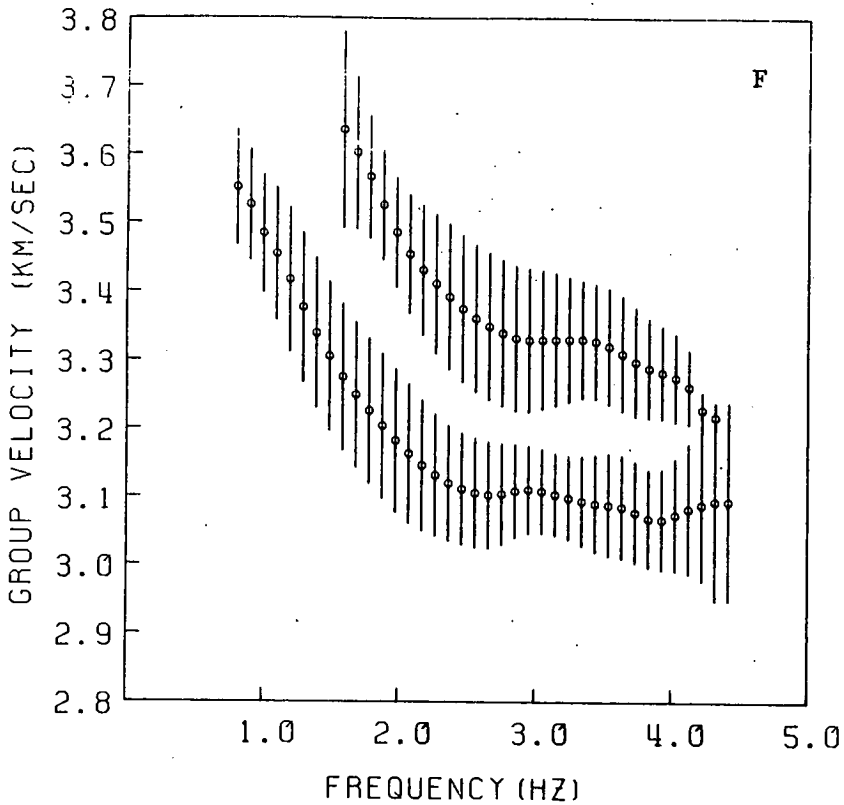

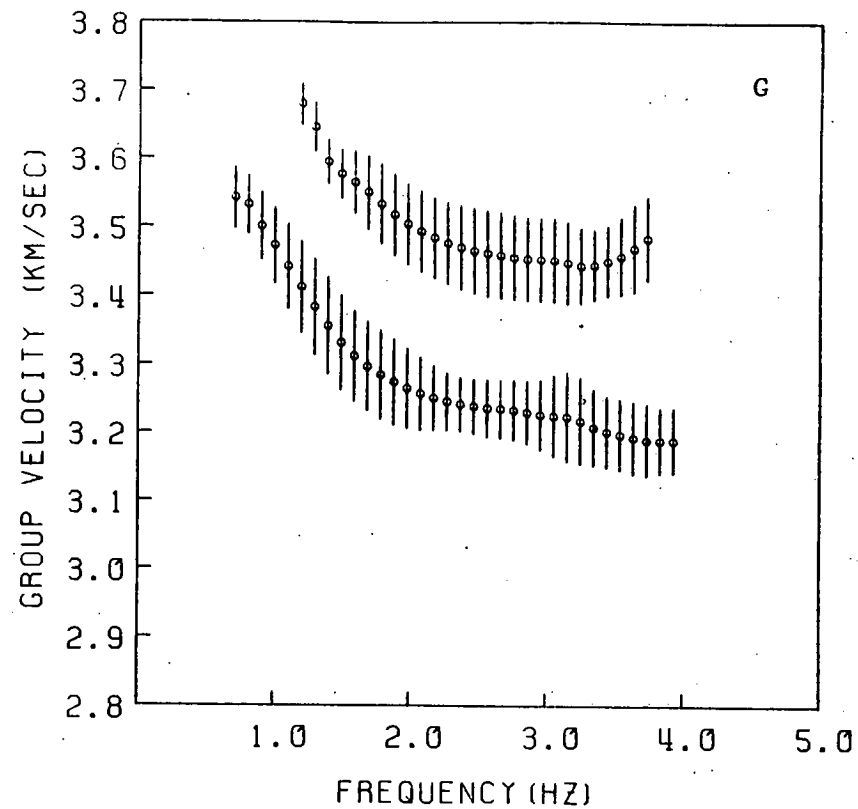

Figure 4.24. Rayleigh wave higher mode group velocity data, generated by the earthquake KEQ, for regions F and G.

surface geology, as it is an expression of the lithology in the upper few kilometres of the crust. Figure 4.25 displays a sketch map of the surface geology of Scotland. The paths in groups A - E are through the high velocity Moine province. Paths in groups F and G are through the slower Carboniferous and Old Red Sandstone rocks of the Midland Valley. The expected trend of the high frequency group velocity is not evident in Figures 4.21 - 4.24. There is instead a noticeable decrease of the high frequency group velocity for groups C, D and E, with the lowest at group D, being particularly clear in the first higher mode. Groups B and F have similar dispersion characteristics, and group G has the largest high frequency velocities, this again being more noticeable for the first higher mode. This lateral variation in group velocity across Scotland amounts to 0.4 km/sec. As there is no noticeable correlation between the group velocity and the surface geology, this method of interpretation was not pursued further.

4.4.4 Check on Mode Identification

Theoretical group velocity dispersion curves for the fundamental, first, and second higher modes, are computed using Evans' (1981) northern and southern Moine province models, obtained by the inversion of fundamental mode Rayleigh wave data. These are superimposed upon the averaged curves for both modes from each group, and are compared in Figure 4.26. The theoretical fundamental mode velocities do not come close to any of the curves. The gradients of the theoretical curves are much larger than those of the observations,

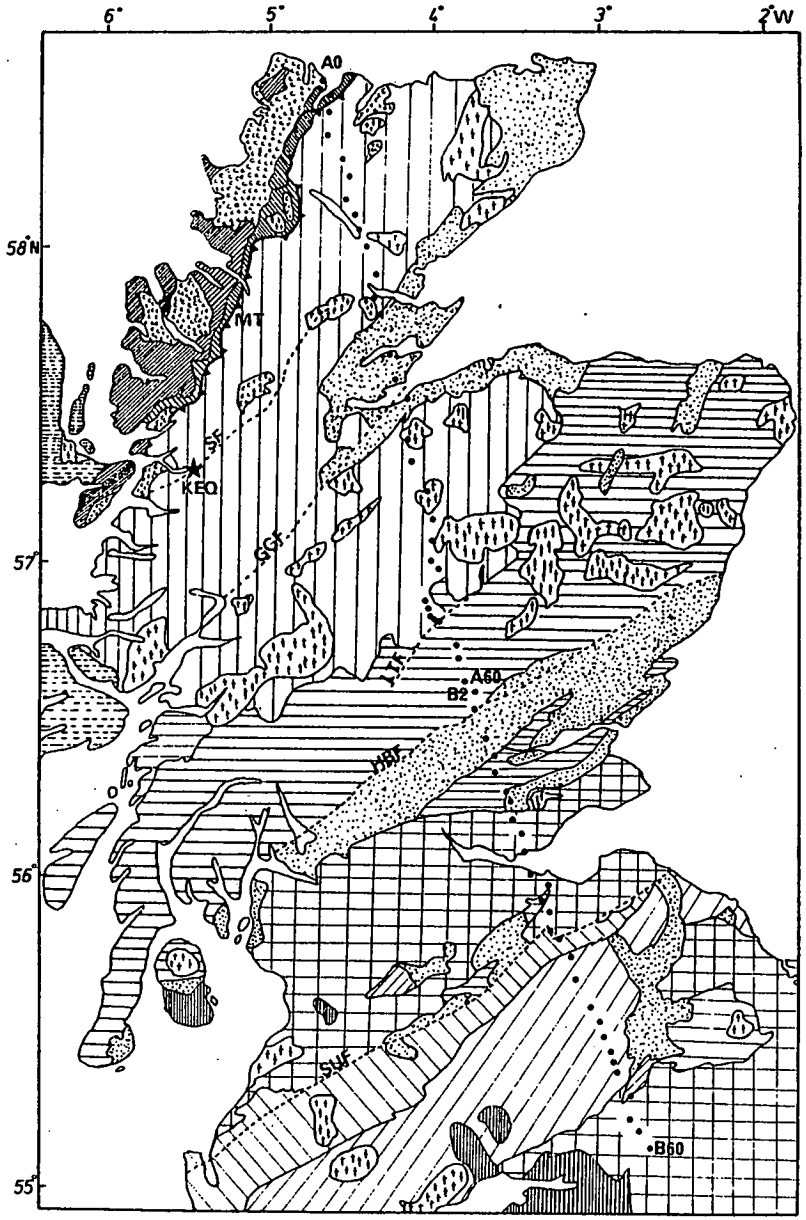

Figure 4.25. Sketch map of surface geology in Scotland and relative position of LISPB ALPHA and BETA lines, and KEQ.

Key to Geology sketch map

- New Red Sandstone
- Carboniferous
- Old Red Sandstone
- Silurian
- Ordovician
- Cambrian
- Torridonian
- Tertiary
- Devonian Lavas
- Igneous Intrusive
- Dalradian
- Moine
- Lewisian Complex

MT Moine Thrust
SF Strathconan Fault
GGF Great Glen Fault
LTF Loch Tay Fault
HBF Highland Boundary Fault
SUF Southern Uplands Fault

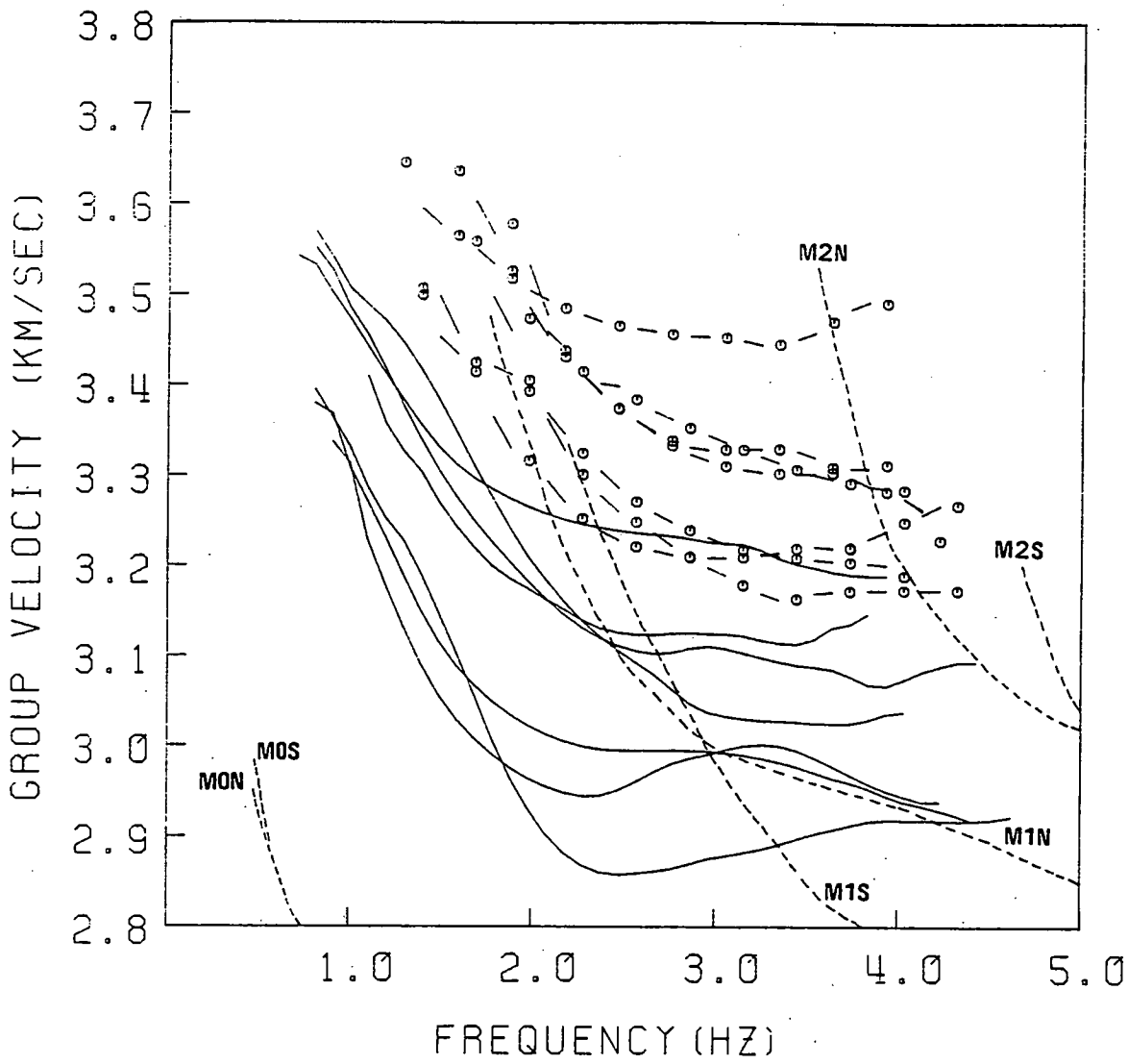

M0N - fundamental mode
M1N - first higher mode
M2N - second higher modes
] Northern Moine model

M0S - fundamental mode
M1S - first higher mode
M2S - second higher mode
] Southern Moine model

——— first higher modes from groups A-G

—o— second higher modes from groups A-G

Figure 4.26. Comparison of observed first and second higher mode group velocities for the regions A-G with the theoretical fundamental, first and second higher mode dispersion derived from the high frequency Moine models of Evans (1981).

and the high frequency velocities are lower. However it is clear that one must identify the second arrival as the first higher mode, and the first arrival as the second higher mode.

4.4.5 Particle Motions

The theoretical ellipticity and sense of rotation in the sagittal plane are computed using the Thomson-Haskell matrix method implemented in program 'MLR' of Appendix D.3 and the northern Moine province model used above. $E(\omega)$ for the fundamental, first, and second modes is shown in Figure 4.27, for the frequency range 0.5 - 5.0 Hz. The first and second mode cut-offs are at 1.8 and 3.4 Hz respectively. The velocity model has smaller velocity contrasts than the Carboniferous model used in Section 4.3, and so the higher mode ellipticities are retrograde for all frequencies.

Only one three component set is available, that from the LISPB station A52 in the Atholl net. These seismograms are rotated and filtered around the dominant frequency of 2 Hz using a Martin-Graham filter. The particle motions are averaged over the windows of 0.63 sec. The orbitals in Figure 4.28 again show considerable fluctuation about the ideal elliptical shape. The average retrograde ellipticities for the two wavepackets are 0.3 and 0.5 respectively, and are plotted in Figure 4.27. From measurements of particle motions alone, one cannot accurately distinguish between the two modes. It may have been possible to discriminate the modes at low frequencies where there is a chance of prograde motion, however there is very little higher mode energy at such frequencies.

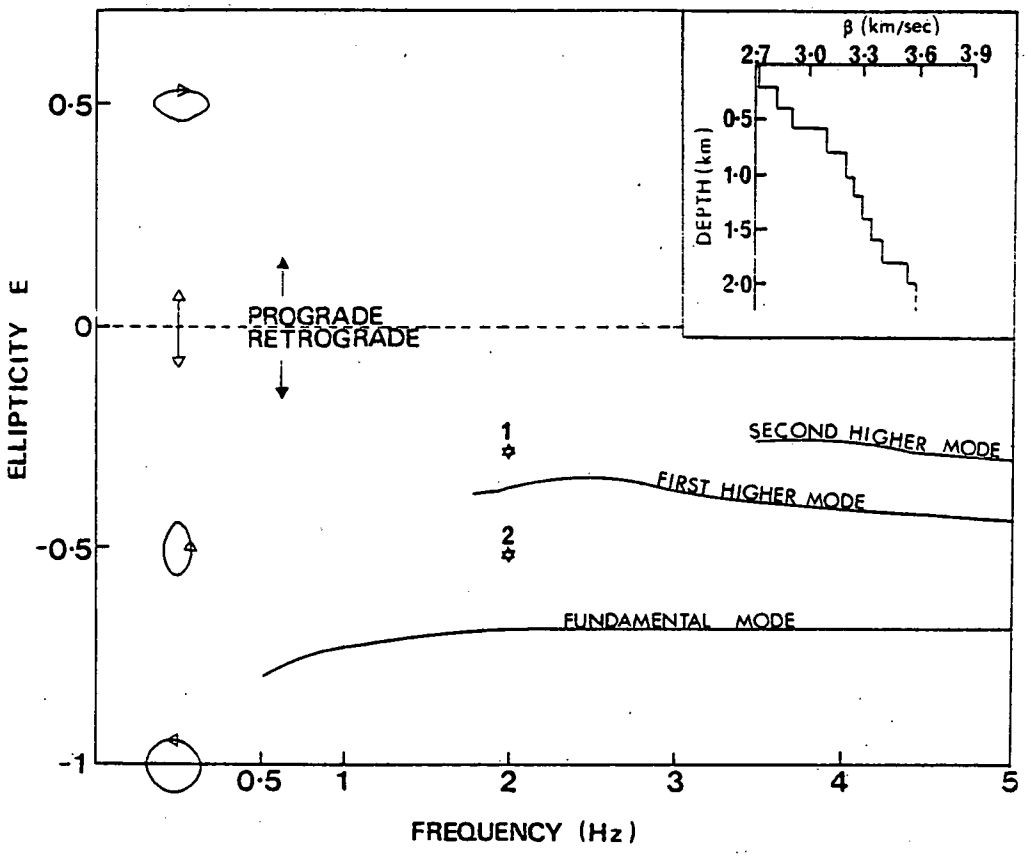

Figure 4.27. Theoretical frequency dependent ellipticity for the first three Rayleigh wave modes computed using Thomson-Haskell matrix theory and Evan's (1981) northern Moine province model (shown inset). Points '1' and '2' correspond to values of ellipticity for first and second higher modes respectively, estimated from observed particle motion plots.

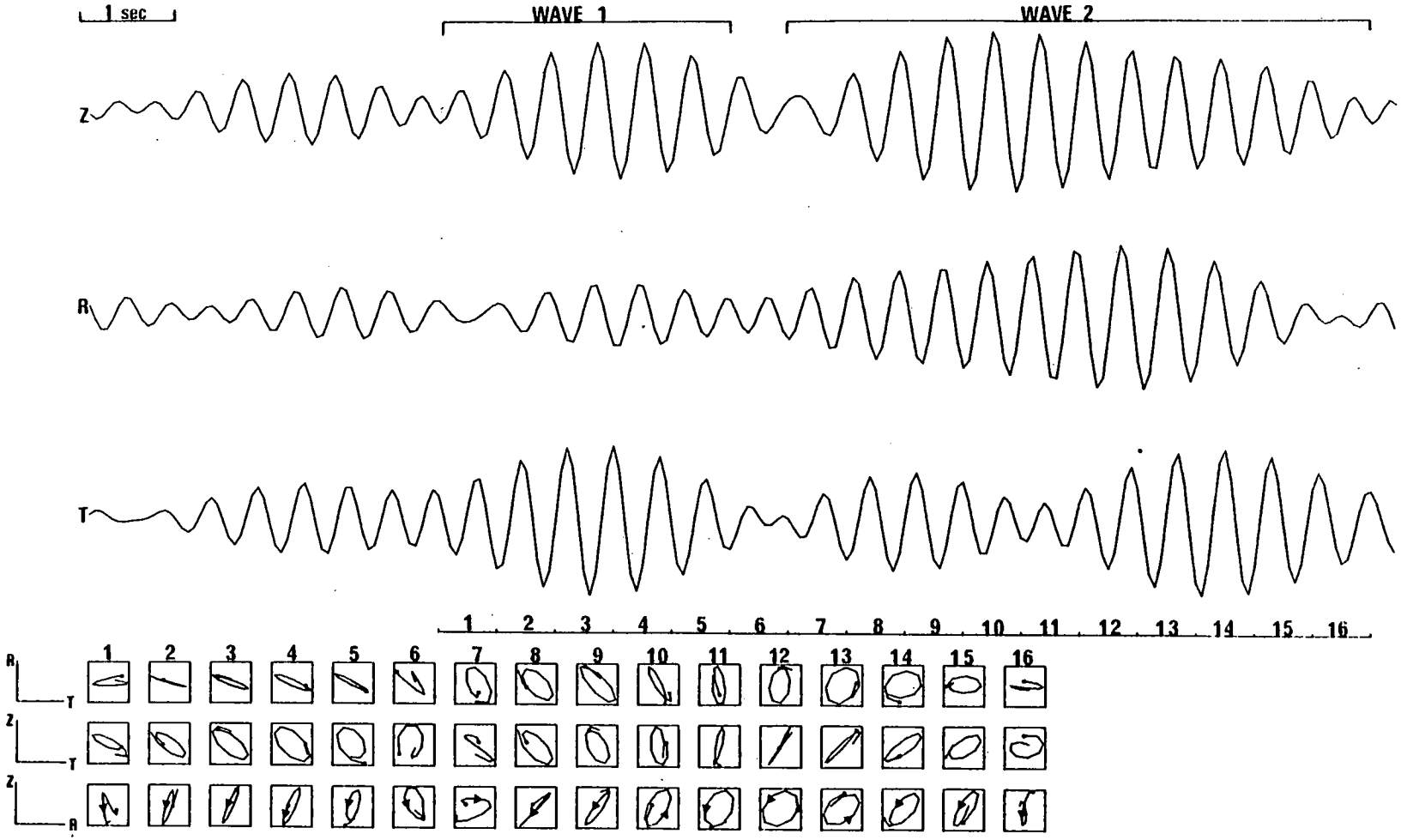

Figure 4.28. Rotated three component recording of KEQ at station A52 in Atholl Net, band-pass filtered around 2.0 Hz using a Martin-Graham filter. Particle motions were averaged over a 0.63 second window. Average ellipticity of waves 1 and 2 are evaluated and plotted in Figure 4.27.

4.4.6 Regional Velocity Structure

It was illustrated in Figure 4.18 that the depth distributions of the first and second higher mode energy at a particular frequency are markedly different. The second higher mode will sample rocks at certain depths in the earth to a different extent from the first higher mode. Therefore a particular velocity structure will influence different portions of the dispersion curve of each mode, and there may also be depths at which the rock velocity affects only one or other of the modes. Simultaneous inversion of the multimode group velocities will therefore result in a more reliable and accurate determination of the common structural parameters, considerably better than that of independent inversions.

Examination of partial derivatives of group velocity with respect to shear velocity in a given layer, provides a physical insight into the inversion problem. They display the dependence of the observations on the model at particular frequencies, and can be used to compare the different information contributed by the two higher modes. Good resolution in all layers is possible if each layer independently influences part of the first and second higher mode data.

The partial derivatives for a typical shear velocity model (Figure 4.29a) used in the regional inversion are shown in Figure 4.29b as a function of depth for frequencies of 0.8, 1.88, 2.76, and 4.0 Hz. The partial derivatives for the second higher mode are not shown at 0.8 Hz as this frequency is below the cut-off frequency for this mode and structure. Similarly, the 4 Hz derivatives for the first higher mode are not shown. The curves clearly demonstrate that the first and second higher mode group velocities at the same

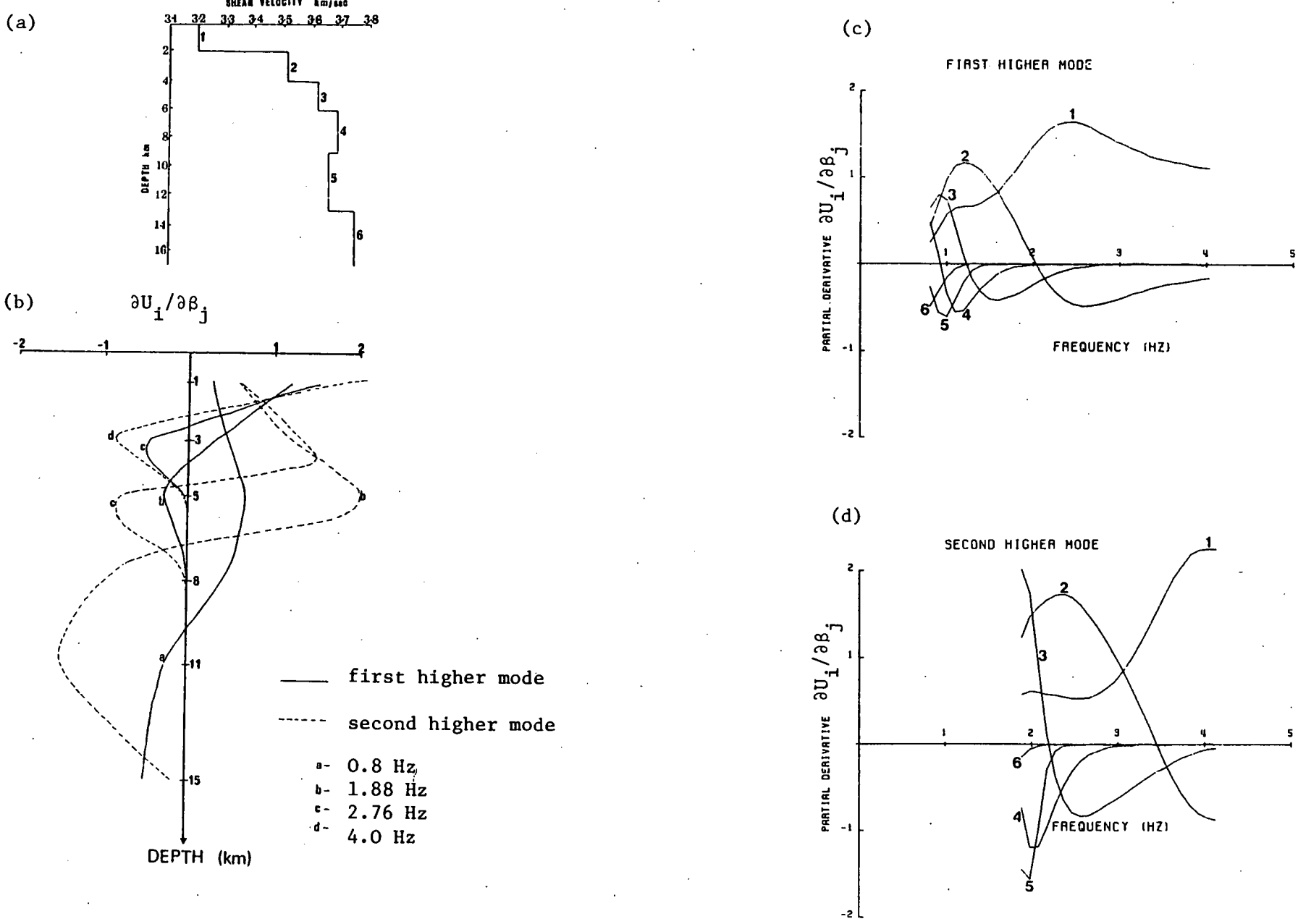

Figure 4.29. Higher mode partial derivatives of group velocity with respect to shear velocity ($\partial U_i/\partial \beta_j$) for a typical LISPB KEQ shear velocity model shown in (a), as a function of depth (b), and frequency (c) and (d).

frequency are affected to different extents by the same layer. A noticeable feature is that the high frequency partial derivative of the second mode matches the lower frequency derivative curve of the first higher mode. This implies an overlap of the information contributed by the higher frequency group velocities of the second higher mode with the mid frequency range of the first higher mode.

Partial derivatives as a function of frequency and for particular depths in the earth are shown in Figures 4.29c and d. From these, it appears that the main mode energy is confined to the upper 6 km of the crust, although the second higher mode penetrates slightly further into the earth.

To implement the simultaneous inversion we combine the two equations connecting the observations to model parameters (Equation 4.1) for each mode. This gives

$$\begin{bmatrix} \underline{y}_1 \\ \underline{y}_2 \end{bmatrix} = \begin{bmatrix} A_1 \\ A_2 \end{bmatrix} \underline{x} \qquad (4.3)$$

where $\underline{x}$ is a column vector of first order perturbations in the common model layer velocities, $\underline{y}_1$ and $\underline{y}_2$ are column vectors of the differences between the observational and theoretical curves, A_1 and A_2 are matrices of first order partial derivatives for the two modes. The iterative scheme described in Section 4.3.4 is again utilized to obtain shear velocity models with depth.

The bandwidth for higher mode propagation through an elastic structure is limited by the high and low frequency cut-offs. These are determined by the depth to the model half-space and the thickness of the top layer of the model respectively. In choosing a suitable

velocity model for inversion the low frequency limit is satisfied by trial and error. Instabilities, which govern the choice of the minimum layer thickness, oppose the high frequency cut-off effect, which is set at 2 km for this data. The thickness of each layer is increased with depth to compensate for the decrease of resolution with depth. This reduces the unwanted negative side-lobes in the resolution kernels and provides a more definitive interpretation of the results. Each group is given the same layering, with thicknesses of 2, 2, 2, 3, and 4 km, overlying a half-space. Initial velocity models for the inversion are based on an average of the Moine province models above for the upper 2 km of the crust (3.2 km/sec), and the P-wave cross-sections of Bamford et al. (1976) which suggested an increase to 3.7 km/sec at a depth of 17 km. The inversions utilize the Poisson's ratio distribution of Assumpção and Bamford (1978).

The measure of fit between the observations and theoretical curves is monitored by the combined χ^2_ν function (Equation 4.2) for both modes. It is more difficult to satisfy individual mode fits using the same model. An attempt is made to invert the combined data sets to a 5% significance level, only group B failing to meet this requirement and being fitted to a 10% significance level.

The results of the inversions are shown in Figures 4.30 - 4.33. Each diagram compares the observed group velocities and associated standard deviations with the theoretical velocities. It is decided to compute the errors on the model parameters, corresponding to the standard deviations on the observations, for maximum deltaness in the resolution matrix. This provides a more quantitative evaluation

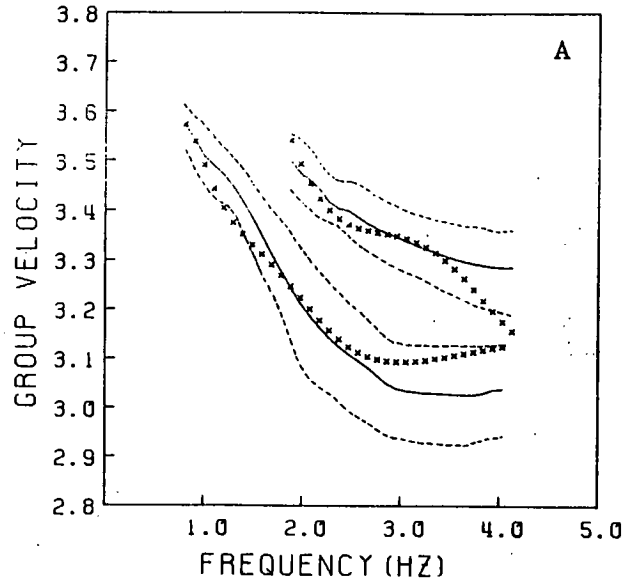

Comparison between theoretical higher mode group velocity points generated by the shear velocity model found by simultaneous inversion (x x x), and observed curves (——). Dotted lines indicate standard deviations on the observations.

(a) (b)

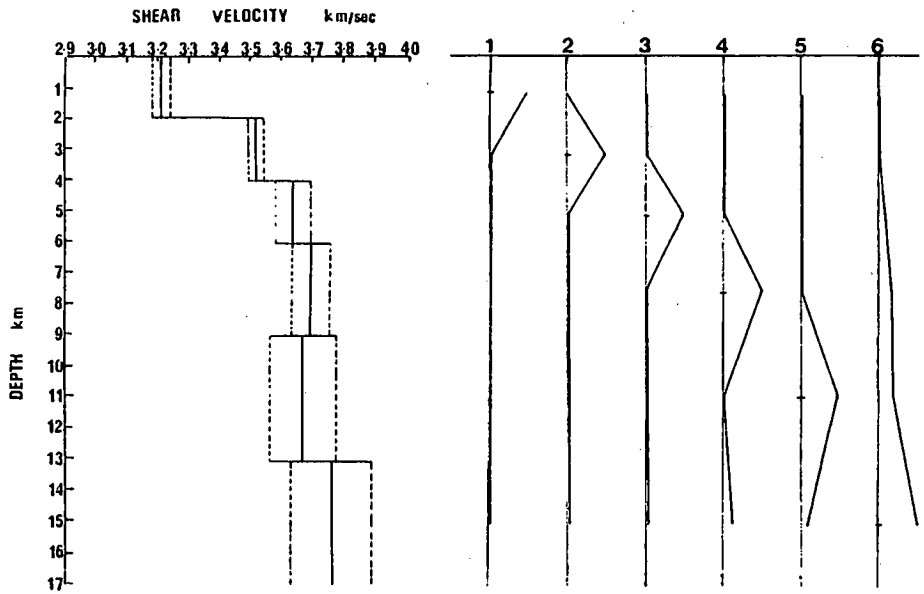

(a) Shear velocity model with bounds obtained by simultaneous inversion of observed first and second higher mode group velocities and standard deviations.

(b) Resolution kernels associated with this inversion - kernels are normalized with respect to their individual maximum, and horizontal ticks mark the centre of the corresponding layer.

Figure 4.30. Simultaneous linearized inversion results for group velocity dispersion data from first and second higher mode Rayleigh waves in Region A.

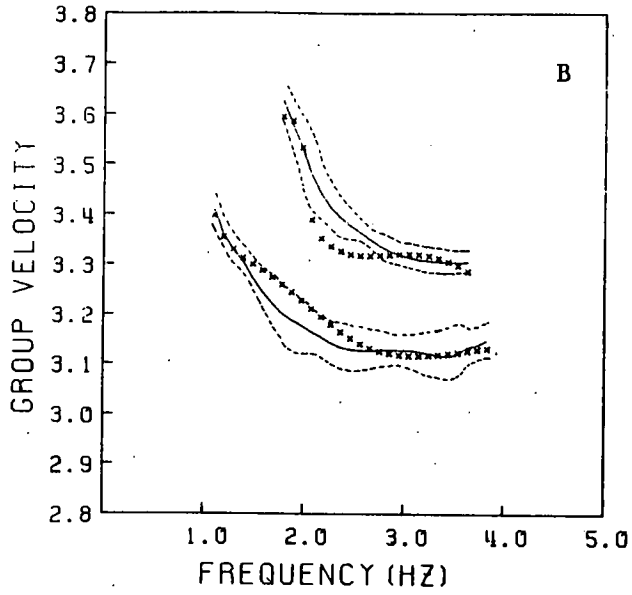

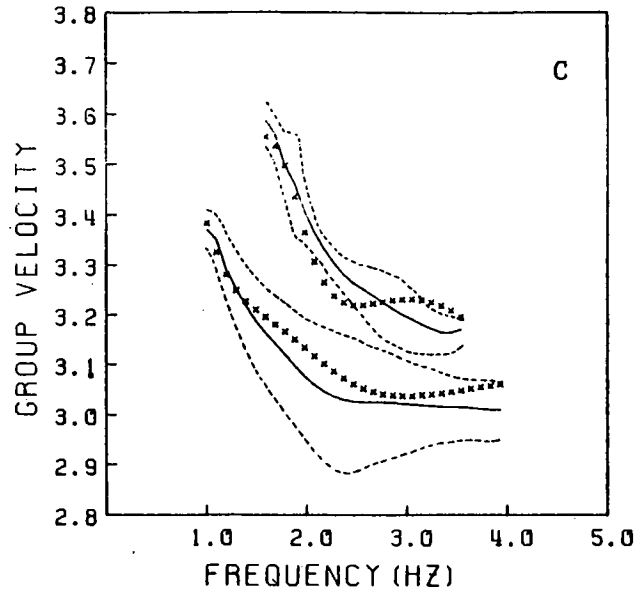

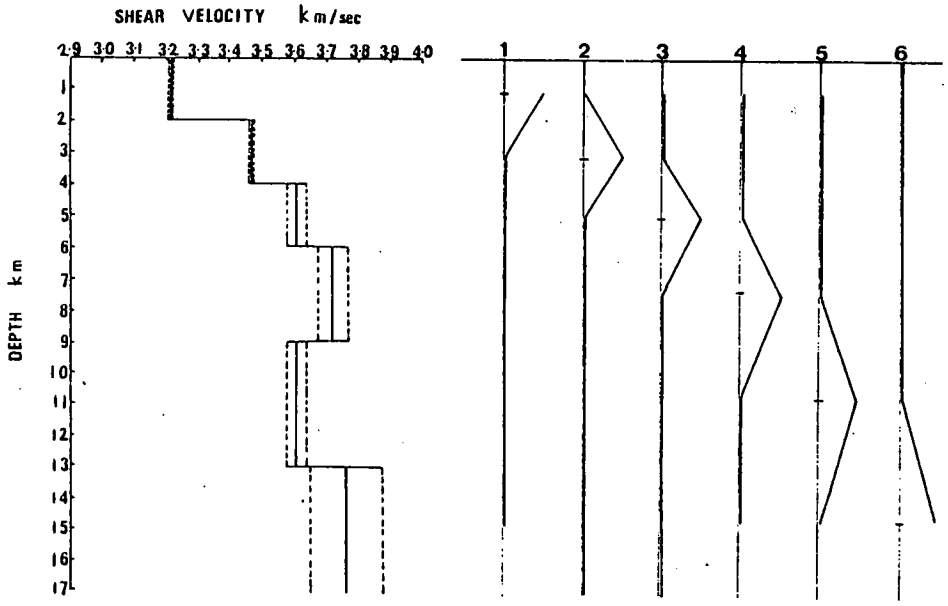

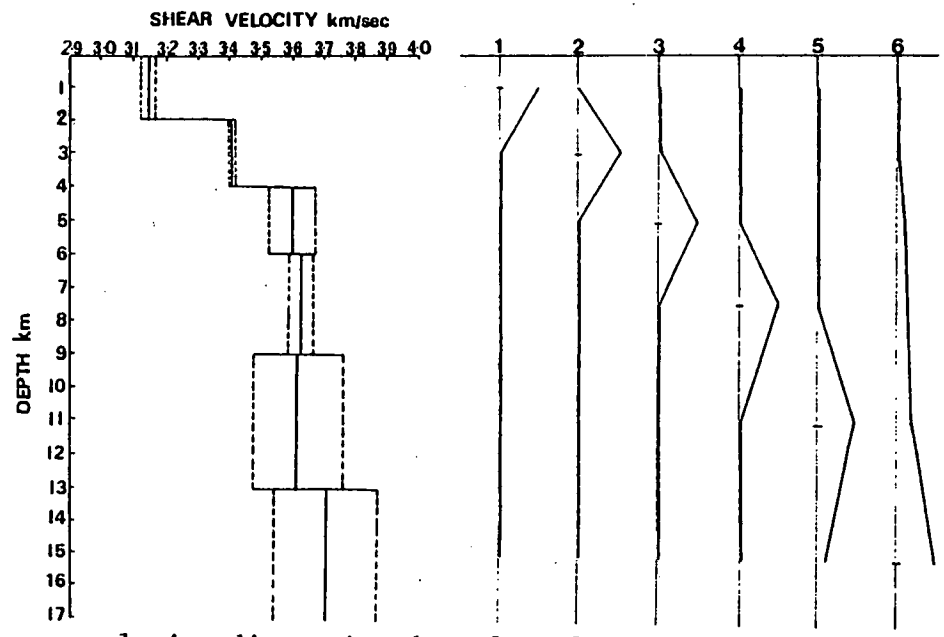

Figure 4.31. Simultaneous linearized inversion results for group velocity dispersion data from first and second higher mode Rayleigh waves in regions B and C.

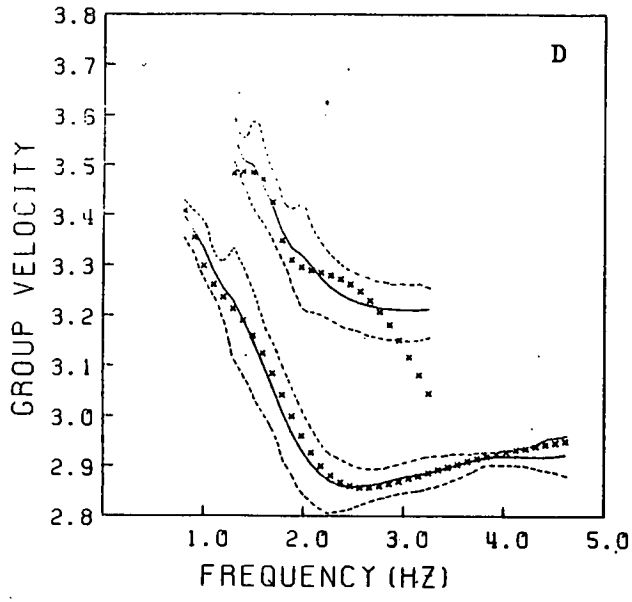

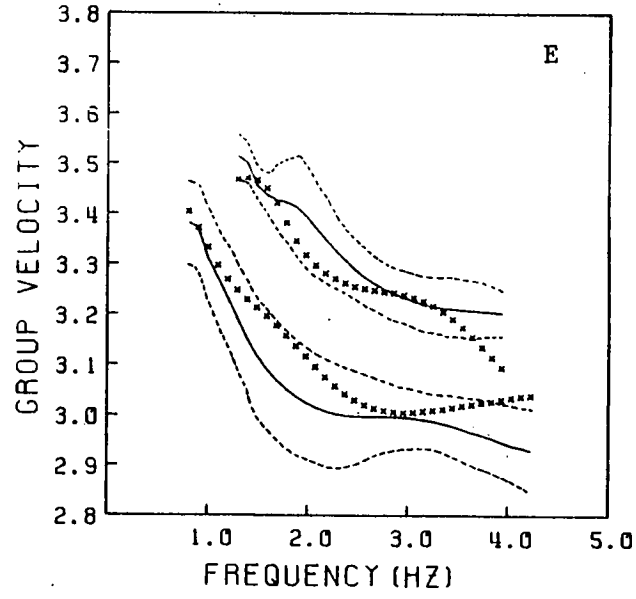

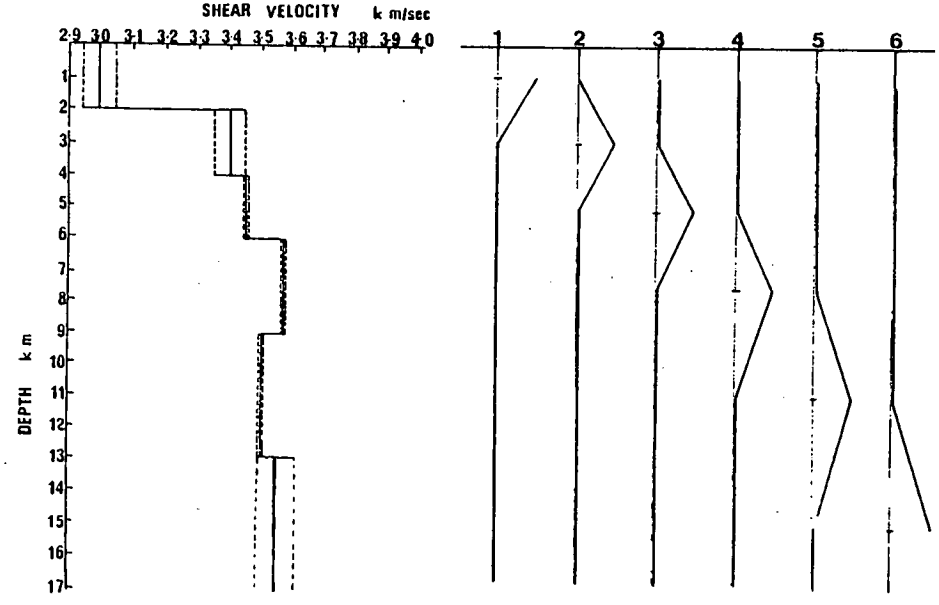

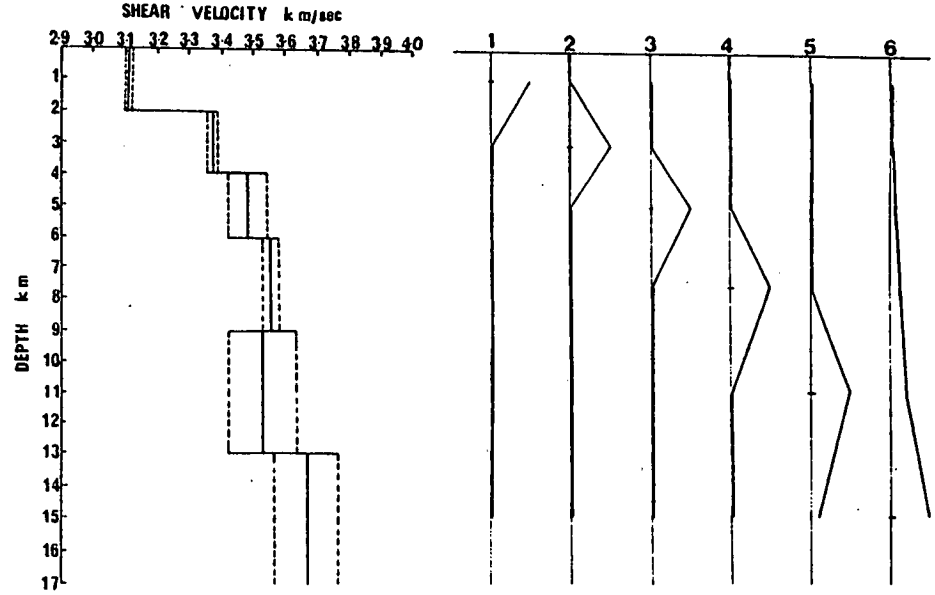

Figure 4.32. Simultaneous linearized inversion results for group velocity dispersion data from first and second higher mode Rayleigh waves in regions D and E.

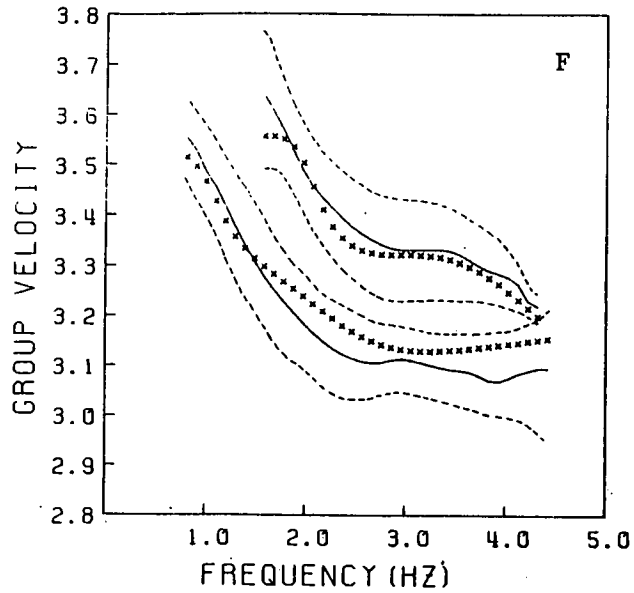

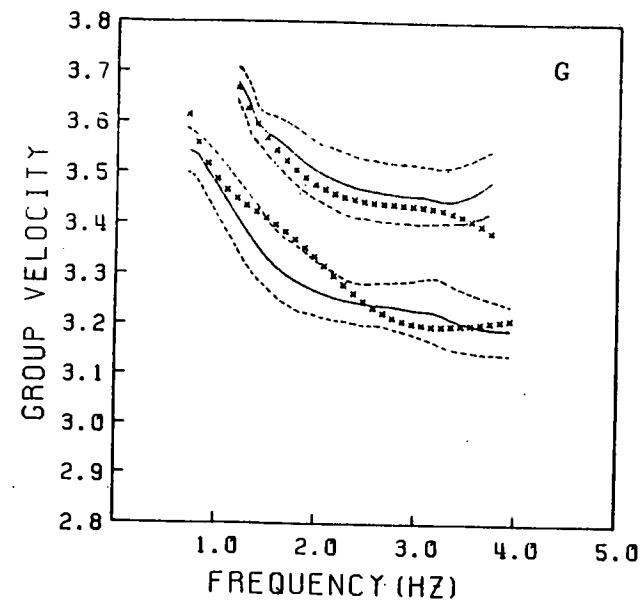

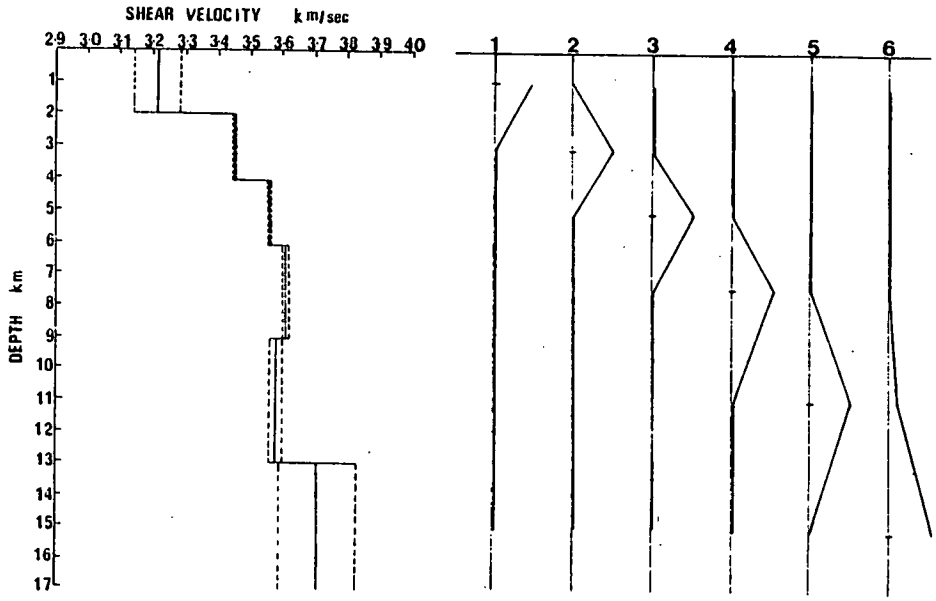

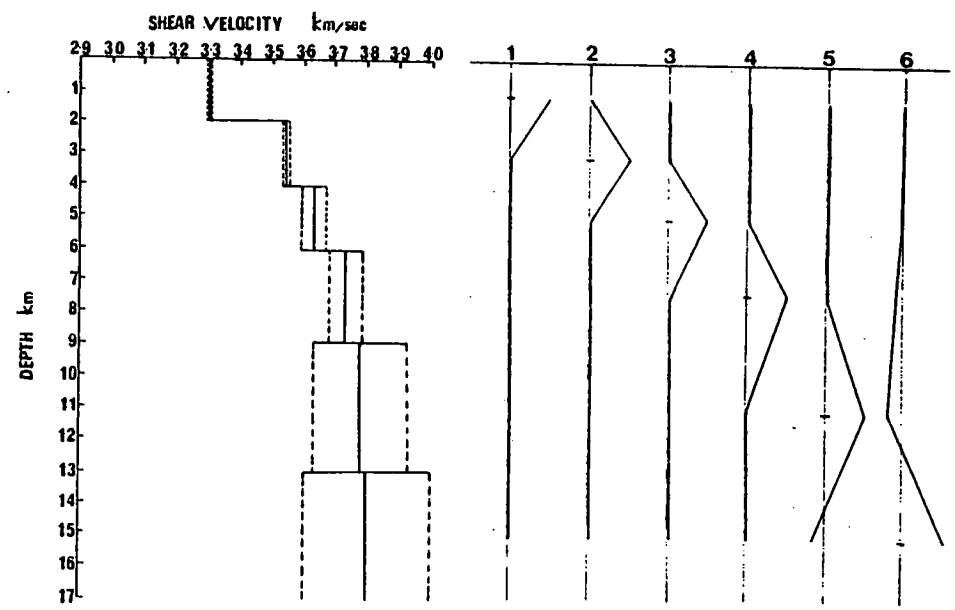

Figure 4.33. Simultaneous linearized inversion results for group velocity dispersion data from first and second higher mode Rayleigh waves in regions F and G.

of the errors on the solution, and permits a comparison with local fluctuations in the structural properties.

In the majority of inversions the high frequency theoretical group velocity for the second mode is an underestimate of the observed dispersion, and the velocity for the first higher mode is an overestimate. A possible cause of this could be S-wave interference with the higher modal frequencies. The shear velocity in each model increases with depth. There is a distinctive jump in the shear velocity between the top layer of the models (with a mean of 3.1 km/sec) and the lower layers (with a mean of 3.6 km/sec). All of the profiles are consistent with this apparently low velocity in the upper 2 km of the crust. The standard deviations on the model velocities generally increase with depth, although for several models the smallest uncertainty occurs in a layer other than the deepest. This is due to the particular energy distribution of the higher modes (this contrasts with the results of Figures 4.8 - 4.11). The inversions of the group velocities for regions D and F have very tight bounds of about ±0.01 km/sec on the shear velocity models.

The shear velocity profiles are plotted together in Figure 4.34, in addition to a profile obtained by averaging each layer velocity. This clearly shows the discontinuity in the velocity at 2 km depth. The average profile shows an increase in shear velocity with depth, with a slight decrease in velocity between 9 to 13 km. The shear velocity gradient is a consistent 3.4 - 3.8 km/sec increase within a depth range of 2 - 17 km in the upper crust. At a depth of 13 km there is another increase in velocity, but in this case it is only by about 0.15 km/sec. Although the shear velocities

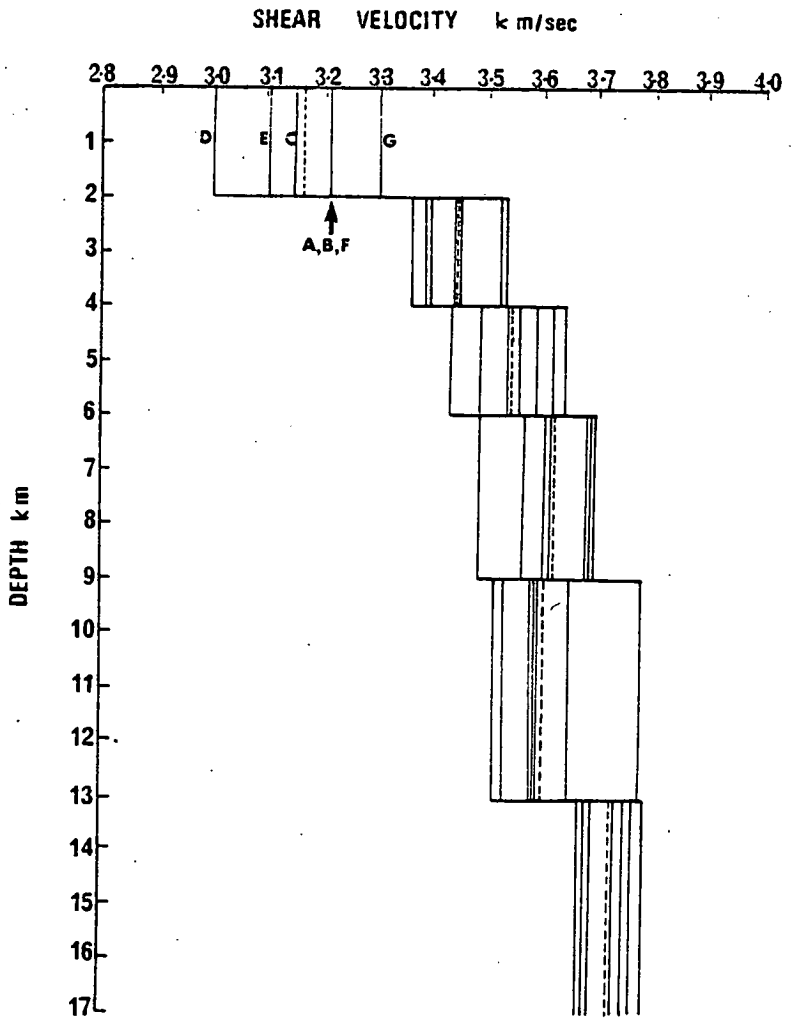

Figure 4.34. Summary of shear velocity-depth profiles for regions A-G, obtained by simultaneous inversion of first and second higher mode group velocity data. The dotted lines indicate the average velocity in each layer taken over all regions. As the profiles group closely, only the top layer velocities are marked for the different regions.

for the bottom layer (corresponding to the effective depth limit) have the largest bounds, the estimates are closely grouped. The profiles here show less variation than the corresponding plot of Figure 4.12 for the Kirkcaldy Bay data, implying a decrease of lateral inhomogeneities with increasing depth.

4.5 Summary

The main emphasis in this chapter has been to establish a reliable and accurate set of profiles for the shear wave velocity structure in Scotland. To obtain these, Rayleigh wavepackets were identified and extracted from the seismograms, and analysed in the frequency-group velocity plane. The derived group velocity dispersion curves were averaged, smoothed and inverted to yield shear velocity models with depth for single-station paths (Kirkcaldy Bay) and regions (KEQ) in Scotland.

In the process of analysing the seismograms, some important features regarding the use of particle motions to discriminate between fundamental and higher mode Rayleigh waves were elucidated. Such a technique appeared to be only possible for low frequency Rayleigh waves traversing a structure with large velocity contrasts. Other features of the wavetrains were related to the effects of the source and the propagation path.

Single-station fundamental mode group velocity data generated by underwater explosions in Kirkcaldy Bay and recorded on the LOWNET array were inverted to give velocity models to depths of 1.2 - 2 km for each path. These velocities were clearly influenced by the surface geology and showed a shear velocity variation of 1.5 - 2.1 km/sec in

the upper 400m of the crust.

The first and second higher mode group velocity data generated by the earthquake KEQ and recorded on LISPB were grouped into approximately homogeneous regions within Scotland. The structures show a distinct lateral variation across the country, but this does not correlate with the surface geological expression. The top layer of the models (giving an average down to a depth of 2 km) has a mean velocity of 3.1 km/sec, and for depths between 2 - 17 km there is a mean velocity of 3.6 km/sec.

The shear velocity models reduce the number of parameters which describe the Rayleigh wave amplitude spectrum for our particular data sets. This reduction will facilitate the complete development and application of the single-station attenuation technique in Chapters 5 and 6.

CHAPTER 5

SINGLE-STATION ATTENUATION METHODS FOR RAYLEIGH WAVES

5.1 Introduction

The objective of the work covered in the previous chapters was to obtain a simple parameterized description of the amplitude spectrum of a Rayleigh wave. This was achieved by factorizing the spectrum into a number of spectral functions, each representing the effect of different phenomena on the wavepacket (Chapter 1). On making simple assumptions and approximations regarding the spectral effects of the seismic source and the propagation medium (Chapters 1, 2 and 3), expressions can be written which describe the spectra of the signals generated by an underground explosion, underwater explosion, and an earthquake using a small number of simple parameters. This parameter set was further reduced by deriving shear wave velocity models for our data from the inversion of group velocity dispersion curves (Chapter 4). The final parameterization can be used to develop the method of measuring single-station attenuation.

This chapter will describe the development of the technique for measuring the depth-distribution of shear wave specific attenuation along an event-station path, from a single Rayleigh wave amplitude spectrum. The explicit expression for each of the functions which combine to form the theoretical spectrum will be examined to evaluate

which physical parameter, or set of parameters, will be the most 'important' in determining the overall spectrum. This analysis will identify those spectral effects for which the observations can be corrected. Two different inversion techniques will then be discussed which can be used to obtain estimates of the remaining parameters by mapping the expected functional form onto the corrected observations. The procedure will be developed for all three seismic sources.

As an introduction, a simple technique will be described which can be used to obtain an approximate half-space attenuation value by measuring the frequency at which the spectrum peaks. This will rely on only the rough trend of the spectral functions.

5.2 Rough Estimate of Attenuation using the Peak Frequency Method

Most seismic spectra possess a distinct peak due to a combination of the factors in Equation 1.5. If we correct for the instrument response $I(\omega)$ and the spectrum still possesses a peak, then because attenuation acts as a low pass filter, the source-dependent function $S(\omega) = S_o S_T(\omega) S_F(\omega) M_z(\omega)$ must either increase with frequency, or have a peak. The explicit form of the attenuation function in Equation 1.2 and the condition for a maximum in the amplitude spectrum at $\omega = \omega_m$, lead to an equation which relates the specific attenuation $Q_\gamma^{-1}(\omega)$ to the source function and the group velocity

$$\frac{dQ_\gamma^{-1}}{d\omega} + Q_\gamma^{-1}\left(\frac{1}{\omega} - \frac{1}{U}\frac{dU}{d\omega}\right) = \frac{2U}{\omega r}\frac{1}{S}\frac{dS}{d\omega}\bigg|_{\omega=\omega_m} . \qquad (5.1)$$

To determine an estimate of attenuation based on the discrete peak frequency observation, the spectral characteristics of the source, group velocity dispersion, and the frequency dependence of Q_γ^{-1} must be known.

As we are taking only one measurement from the spectrum it is reasonable to approximate the attenuation model by a half-space. Using this approximation, Equation 5.1 now reduces to

$$Q_\gamma^{-1} = \frac{2U}{\omega r}\frac{1}{S}\frac{dS}{d\omega}\left(\frac{1}{\omega} - \frac{1}{U}\frac{dU}{d\omega}\right)^{-1}\Bigg|_{\omega=\omega_m} . \qquad (5.2)$$

The attenuation value is thus independent of variations in the absolute amplitude of the spectrum as the scaling factor S_o cancels in the term $\frac{1}{S}\frac{dS}{d\omega}$. Another advantage of this equation is that measurements can be made from stations with a low signal-to-noise - the peak amplitude being the most uncontaminated part of the spectrum. Zhadin and Devagachev (1973) estimated specific attenuation factors, using body waves generated from micro-earthquakes, by employing a similar technique. If the combined function $S_o S_T(\omega) S_F(\omega) M_z(\omega)$ increases monotonically with frequency, then it can be approximated by a power law in frequency, that is $S(\omega)\alpha\omega^q$ where q is some real number. Equation (5.2) can now be replaced by

$$Q_\gamma^{-1} = \frac{2qU}{\omega^2 r}\left(\frac{1}{\omega} - \frac{1}{U}\frac{dU}{d\omega}\right)^{-1}\Bigg|_{\omega=\omega_m} . \qquad (5.3)$$

Q_β^{-1} is obtained from Q_γ^{-1} using Burton's (1973) expression

$$Q_\gamma^{-1} = Q_\alpha^{-1} + Q_\beta^{-1} \qquad (5.4)$$

for a half-space, and Equation 1.8 which relates Q_α^{-1} to Q_β^{-1}. A constant group velocity of 2.5 km/sec, $q = 1$, and $Q_\gamma^{-1} = 0.04$ gives a 1.6 Hz change in the peak frequency for an increase in distance from 10 to 50 km. Thus, according to this approximation the maximum of the amplitude spectrum is very sensitive to attenuation.

For events such as underwater explosions with bubble oscillations and most earthquakes, the source has a natural peak. In this case, Equation 5.2 must be used and the specific form of $S(\omega)$ considered. The sharper the peak in the source function, the smaller the change in peak frequency. Therefore, for accuracy, the method is best restricted to sources for which $S(\omega)$ is a power law function.

5.3 Identification of the Most Important Parameters Shaping the Theoretical Spectrum of a Rayleigh Wave

5.3.1 Introduction

To obtain a single-station measurement, we must ideally isolate the attenuation function from the other phenomena composing the spectrum. This can be achieved by obtaining estimates for the parameters which describe the source and propagation path effects, and then dividing the observed spectrum by their corresponding spectral functions (Section 1.2). However, this correction procedure is only justified if these functions do not have a strong influence on the amplitude spectrum. In practice, it is likely that only a partial isolation is possible, and so one must be content to estimate the attenuation parameters along with other parameters. It is the purpose of this section to ascertain the identity of those parameters which

only weakly influence the amplitude spectrum. The relative importance of each spectral parameter is defined as the extent by which the theoretical spectral amplitude changes as a result of an a priori perturbation on that particular parameter. This perturbation represents a realistic error on an estimate of the parameter. This is quantified using the fractional change in the spectral amplitude. For example, a finite perturbation δp of some parameter p describing the function $X(\omega;p)$ leads to a fractional change in $A_z(\omega)$ given by

$$F(\omega) = \frac{\delta A_z}{A_z} = \frac{\delta X}{X} = \frac{X(\omega;p + \delta p) - X(\omega;p)}{X(\omega;p)} \quad . \qquad (5.5)$$

This quantity is independent of the other functions contributing to the shape of $A_z(\omega)$, and reduces to $(\frac{\partial X}{\partial p})\frac{\delta p}{X}$ in the limit of a small perturbation δp, which is similar to the standardized partial derivative used by Burkhard and Jackson (1976) in their resolution analyses. The advantages of this expression are that the influence of each spectral function is compared on a common basis and the parameters are described in terms of perturbations with equal a priori probability. Simultaneous fluctuations in different spectral parameters are not considered.

5.3.2 Strength of the Source Action

The strength of the source action S_o generated by an explosion can be computed from the explosive yield and the constitutive properties of the material surrounding the charge (Chapter 2), and for earthquakes

it can be related to the surface wave magnitude (Chapter 3). There are however many unpredictable effects which contribute to a scatter of the absolute spectral amplitudes recorded at different geographical locations, the spectral shape being quite stable (Der et al., 1982). Båth (1974) confirms that the absolute level is usually the most uncertain spectral parameter, and it is difficult to compute exactly. However special features such as peaks, troughs, and slopes have more significance. Consequently, S_o must be considered as an unknown parameter.

5.3.3 Source Spectral Functions

The spectrum of the source time action $S_T(\omega)$ for the underground explosion is uncertain, as we do not know whether the time history is dominantly Dirac impulsive or step-like (Section 2.2.5). As the spectra of these two extremes differ by a factor of ω, this uncertainty cannot be ignored in spectral calculations. Therefore we must regard the underground explosion source function as an unknown.

$S_T(\omega)$ for earthquakes is known with much more certainty than in the above case, and it can be represented by the spectrum of the exponential ramp function of Ben-Menahem and Toksöz (1962) and Marshall (1970) (Section 3.2.5). The inverse time constant ω_T specifying this function cannot be measured directly, but must be estimated from other measurable source parameters. Thus, to ascertain the sensitivity of the overall amplitude spectrum to the earthquake source function, a nominal value of 20 rad^{-1} with errors as large as $\pm$ 15 rad^{-1} is considered. The fractional change in the spectral amplitude for these

fluctuations taken in steps of 5 rad^{-1} is plotted in Figure 5.1. There is an increase in $F(\omega)$ with frequency, the maximum change being 0.3.

The source spectral signature for an underwater explosion can be written as

$$S_T(\omega) = S_r(\omega;d,h)S_b(\omega;W,d) \qquad (5.6)$$

where W is the yield of the explosive, d is the depth of the explosion in the water, and h is the thickness of the water layer (Section 2.3.4). These functions represent the reverberation response and the bubble spectra respectively. As the effect of explosive yield on the bubble spectrum produces a similar effect on the spectrum to that of depth (both related to the bubble frequency in Equation 2.6), then the former parameter can be excluded. Consequently, only two degrees of freedom are needed to specify the source spectral function. If the exact water thickness has not been measured, it can generally be estimated to an accuracy of ± 10m using bathymetric data, as was the case for the Kirkcaldy Bay explosions. This is taken as the uncertainty on the shot depth also.

The dependence of the spectrum on the thickness of the water layer is contained in the reverberation response. To investigate the influence of this parameter the fractional change $F(\omega)$ is computed for a shot of yield 155 kg at depths of 15m and 80m (similar to underwater explosions in Kirkcaldy Bay and for LISPB). The water thicknesses are varied between 25 ± 10m and 90 ± 10m respectively, in steps of 5m. The effects of these variations are shown in Figures 5.2a and 5.2b. For the first model, $F(\omega)$ has the same sign as the change in the

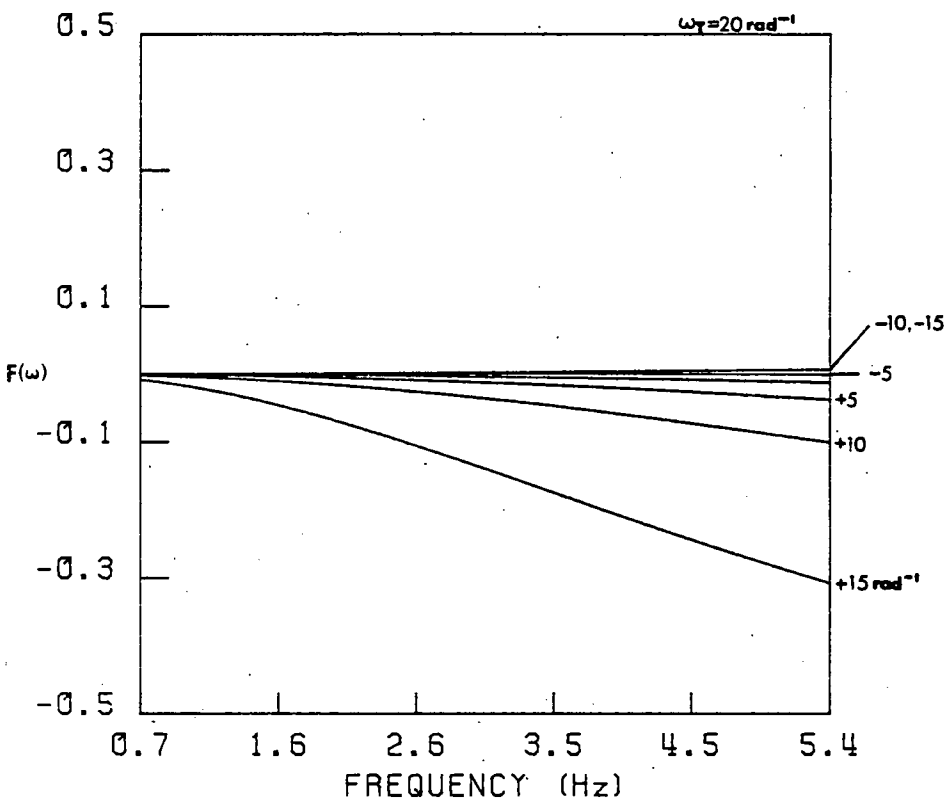

Figure 5.1. Fractional change $F(\omega)$ in the spectral amplitude of an earthquake for perturbations in the inverse time constant ω_T of ±5 rad^{-1}, ±10 rad^{-1}, and ±15 rad^{-1} about a model with ω_T = 20 rad^{-1}.

(a)

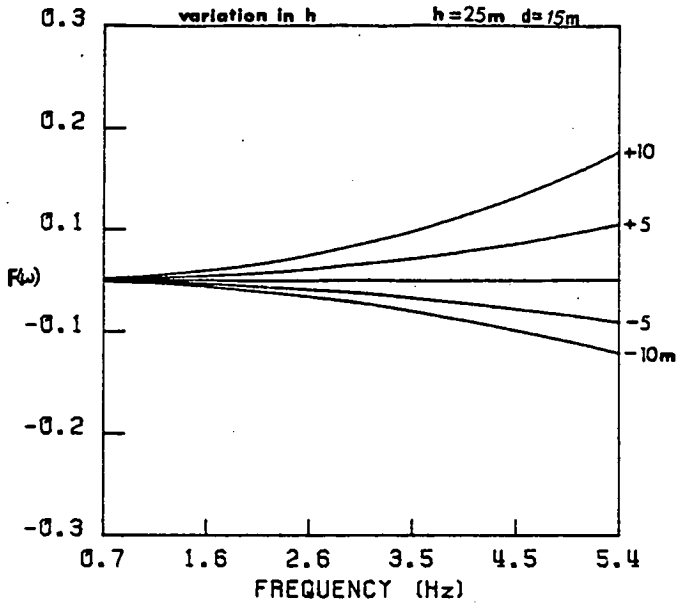

(b)

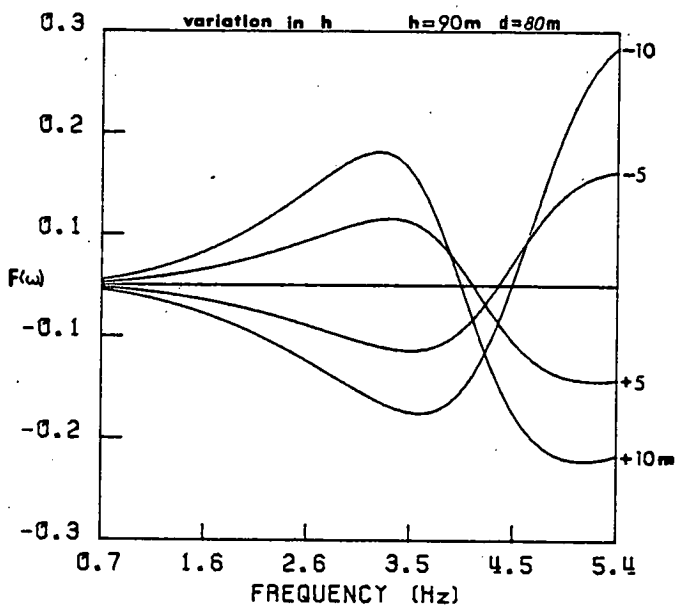

Figure 5.2. Fractional change $F(\omega)$ in the spectral amplitude of an underwater explosion for ±5m and ±10m perturbations in the water layer thickness h about a model with a yield of 155 kg of TNT at a depth d of:

(a) 15m in a water layer thickness of 25m

(b) 80m in a water layer thickness of 90m.

thickness and increases steadily with frequency to reach a maximum of 0.16. The explosion at the larger depth displays similar characteristics, however $F(\omega)$ now changes sign for frequencies beyond 4.2 Hz, this corresponding to a peak in the reverberation response.

The reverberation response and the bubble spectrum are both dependent on the shot depth, and in addition the latter depends on the number of bubble pulses. The fractional changes in spectral amplitude for a source with no bubble pulses, water thickness of 35m, and a water shot depth of 25 ± 10m taken in steps of 5m, are plotted in Figure 5.3a. In this case $F(\omega)$ possesses deep oscillations of magnitude around 0.4. The curves for a model with identical shot parameters, but now including one bubble pulse are more sensitive to the shot depth by a factor of roughly ten (Figure 5.3b). Although the maximum fluctuation is now 3.5, the mean effect is only 0.5.

The effect of low velocity sediments at the sea-bottom would be to concentrate the Rayleigh wave energy into that layer. This would produce a strong peak in the spectral amplitude at a frequency related to the wave velocity and thickness of the layer (Hudson and Douglas, 1975). There is not enough reliable information available to consider this effect fully.

5.3.4 Source Finiteness

The finiteness factor $S_F(\omega)$ for explosions is a function of frequency and the elastic radius of the source. This has a negligible influence on the spectrum of intermediate and small explosions in the

(a)

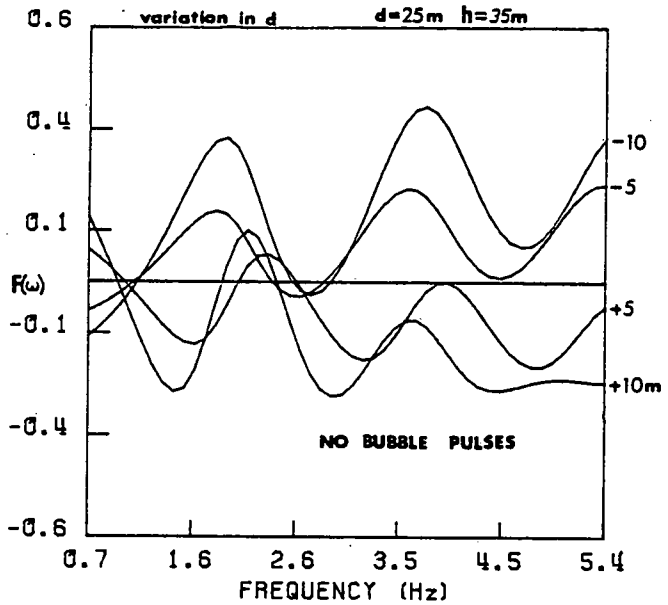

(b)

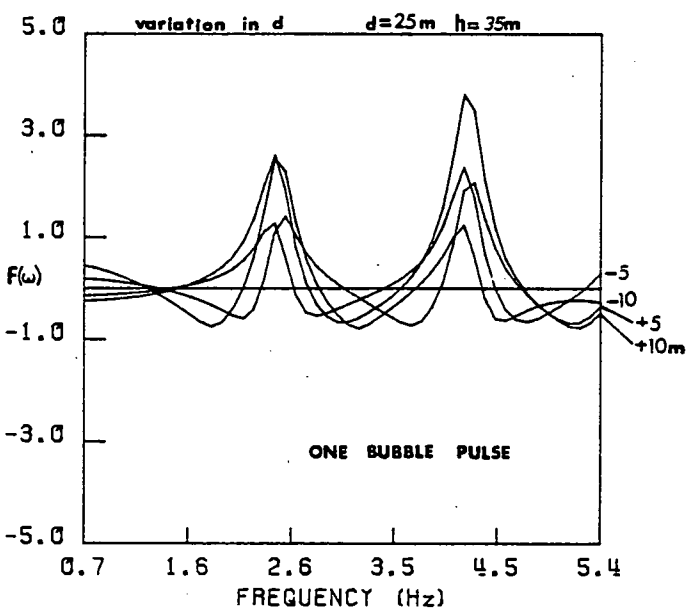

Figure 5.3. Fractional change $F(\omega)$ in the spectral amplitude of an underwater explosion at a depth d of 25m in a water layer with a thickness h of 35m, for perturbations in the depth of ±5m and ±10m about this model. Source functions correspond to a model with no bubble pulses and one bubble pulse respectively.

frequency range 0.7 - 5.5 Hz. This statement is verified for the underground shots recorded on the LISPB array in Section 6.2.1.

The finiteness factor $S_F(\omega)$ for an earthquake is a function of frequency, phase velocity, rupture length and azimuth of the observer. The phase velocity is not considered further as it can be determined using the velocity structure of the medium. The fault length is usually measured indirectly using relationships with other measurable quantities, particularly earthquake magnitude. The estimate of rupture length varies from place to place, and formula to formula, for a particular magnitude, and there could be as much as a factor of ten variation (for example, contrast values calculated for a particular magnitude using formulae given by Kanamori and Anderson (1975), Ohnaka (1978), Wyss (1979) and Singh and Havskov (1980)). Uncertainties in azimuth are most important when the ratio of phase velocity to fault rupture velocity is $\simeq 1$. The error in azimuth depends mainly on the uncertainty in the determination of the strike of the fault. This is usually the most accurate focal parameter, and can be estimated to an accuracy of less than $\pm 15^{\circ}$ (Tsai and Aki, 1970). The fractional changes in the spectral amplitude for an earthquake model with a rupture length of 1 km observed at azimuths of 0° and 45°, are shown in Figures 5.4a - 5.4d for fluctuations in the fault length of $\pm$ 0.5 km in steps of 0.25 km, and fluctuations in the azimuth of $\pm 15^{\circ}$ in steps of 5°. Figures 5.4a and 5.4b show $F(\omega)$ for an azimuth of 45° with fluctuations in the length and azimuth respectively. The fractional changes are similar in character for both diagrams. A decrease in the length or azimuth tends to increase/decrease the spectral amplitude. Above 3 Hz the absolute magnitude of $F(\omega)$ is 0.5, for higher frequencies it becomes very

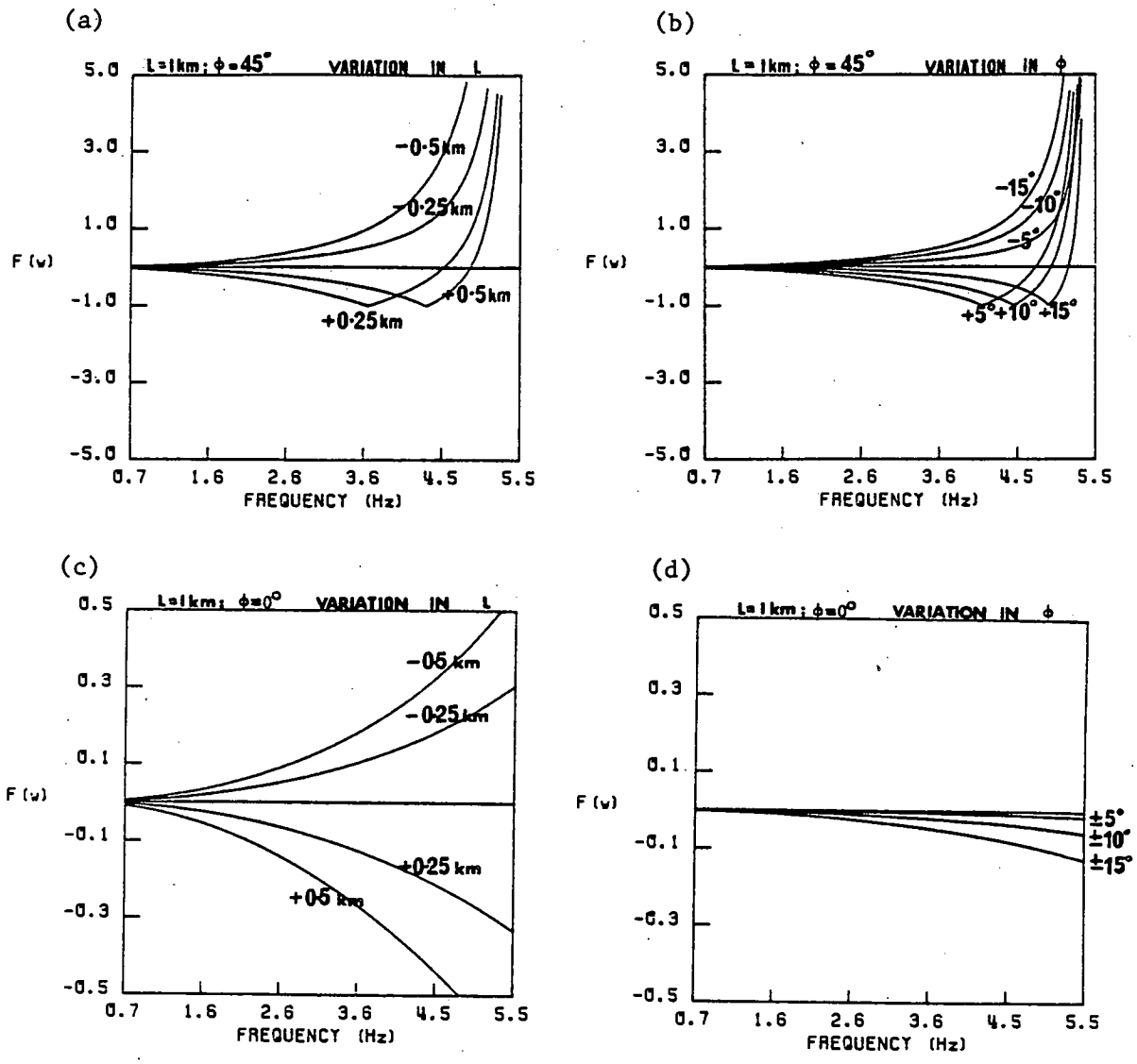

Figure 5.4. Fractional change $F(\omega)$ in the spectral amplitude of an earthquake, arising from the finiteness function, due to perturbations in the length L and azimuth ϕ of the fault about a model with L = 1 km and $\phi = 0^{\circ}$ or 45°.

(a), (c) perturbations of ± 0.5 km in the length, taken in steps of 0.25 km.

(b), (d) perturbations of $\pm 15^{\circ}$ in the azimuth, taken in steps of 5°

large ($\simeq$ 5.0) for both positive and negative parameter changes, due to a minimum in the finiteness function.

Figures 5.4c and 5.4d show $F(\omega)$ for the earthquake model observed at an azimuth of 0^{o} and fluctuations in the length and azimuth respectively. In this case, the greatest change in the spectral amplitude corresponds to variations in the rupture length. $F(\omega)$ again increases with frequency, however there are no minima in the finiteness factor at these azimuths and it rises to a maximum of 0.5 at 5 Hz. The values of $F(\omega)$ corresponding to changes in the azimuth are very small (< 0.1), and both positive and negative fluctuations produce a decrease in the spectral amplitude.

5.3.5 Spectral Response of Medium

The underground explosions in this thesis are essentially surface sources. Therefore the Rayleigh wave medium response is only dependent on the distribution of shear wave velocity with depth. The group velocity inversion procedures of Chapter 4 estimated this velocity structure to an accuracy of $\pm$ 0.2 km/sec. The three layered model shown in Figure 5.5a is chosen as representative of the velocities encountered in the shallow crust of Scotland. The multi-layered medium response for each model is computed using the program 'MLR' which is listed in Appendix D.2. The fractional change in the spectral amplitude for a variation of the shear velocity in each layer by $\pm$ 0.2 km/sec, taken in steps of 0.05 km/sec, is shown in Figures 5.5b, c, and d. The medium response increases for a decrease in the shear velocity for the top layer of the model, for which the fractional

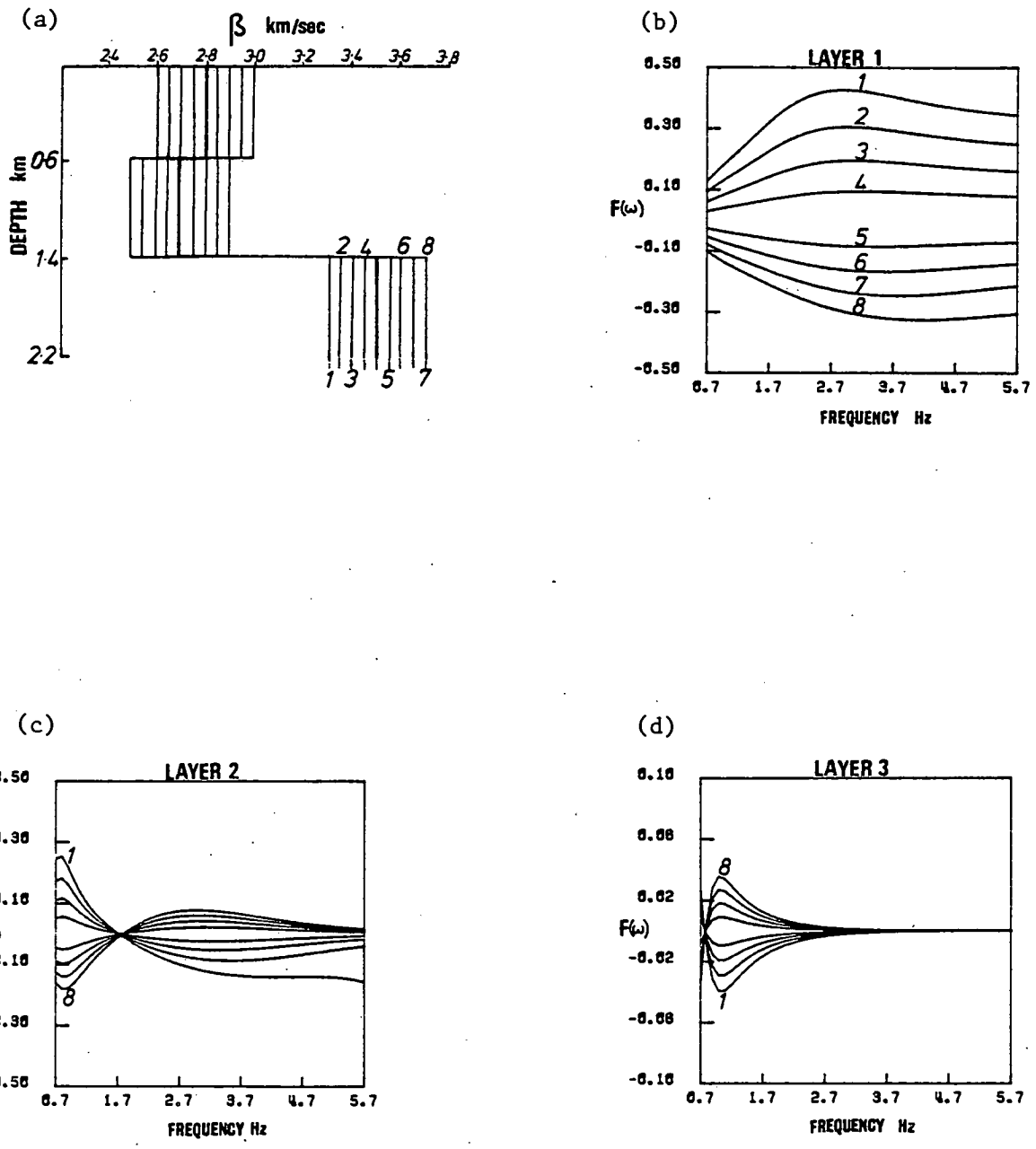

Figure 5.5. Fractional change $F(\omega)$ in the spectral amplitude of an underground explosion due to perturbations in the shear velocity β in each layer of a two-layer plus half-space model (bold line in (a)) of ± 0.2 km/sec taken in steps of 0.05 km/sec.

(b) perturbations in the upper velocity layer
(c) perturbations in the second layer
(d) perturbation in the lowest layer

change reaches a maximum of 0.4. For layers 2 and 3 $F(\omega)$ is much smaller, and reverses sign above 1.7 Hz and 0.75 Hz respectively. As the medium responses for an underground explosion, underwater explosion, and earthquake can be expressed in terms of the same basic function of the medium properties (Douglas et al., 1971), then there is no reason to believe that these should not yield similar results to the above. As a half-space is a specific case of a multi-layered medium, then the results apply to this also.

The response of a multi-layered medium excited by a general earthquake source at depth is dependent on frequency, source depth, and orientation of the fault plane, in addition to the elastic parameters of the medium (Section 3.2.3). The three orientation parameters of dip δ, rake λ, and strike azimuth ϕ, can usually be determined within errors of $\pm 15^{\circ}$ or less (Tsai and Aki, 1970). The focal depth h can be estimated to within $\pm$ 1 km for earthquakes with a similar size to KEQ (inferred from Bulletins of International Seismological Centre). To test the effect of uncertainties in these parameters we consider a vertical strike-slip and a horizontal dip-slip earthquake model at a depth of 5 km in a typical crustal model derived from figure 4.34. The azimuth of the observing station with respect to the source is taken as 45°. Variations in the amplitude spectrum of the first higher mode Rayleigh wave are investigated (the second higher mode amplitudes being very similar) as the earthquake KEQ generated only higher modes.

$F(\omega)$ is calculated for perturbations in the three orientation parameters of $\pm 5^{\circ}$, $\pm 10^{\circ}$ and $\pm 15^{\circ}$, and perturbations in the focal depth of $\pm$0.5 km and $\pm$ 1 km - the results being shown in Figure 5.6. Fluctuations in the rake of the strike-slip model, and

Figure 5.6. Fractional charge $F(\omega)$ in the spectral amplitude of an earthquake for perturbations in the dip δ, rake λ, strike azimuth ϕ, and depth h of the fault. Unperturbed models are horizontal dip-slip and vertical strike-slip faults at a depth of 5 km in a crustal velocity model derived from the group velocity inversion results of Chapter 4, and observed at an azimuth of 45°. Perturbations in ϕ for the dip-slip model, and in λ for the strike-slip model, are omitted for convenience as the effects are identical to perturbations in λ for the dip-slip model. The maximum variation in the angular parameters δ, λ and ϕ is $\pm 15^{\circ}$, taken in steps of 5°, and in depth it is ± 1 km taken in steps of 0.5 km.

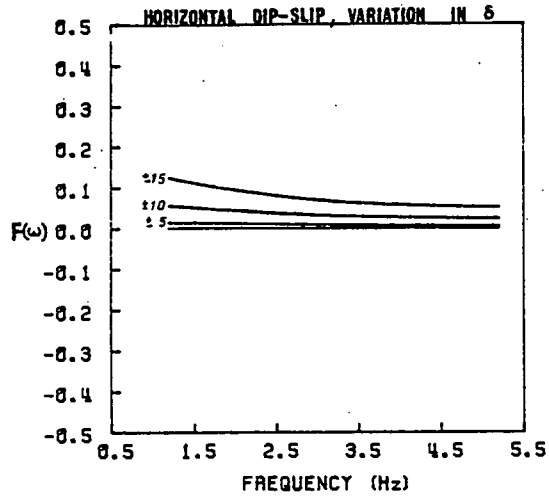
HORIZONTAL DIP-SLIP, VARIATION IN δ
F(ω)
FREQUENCY (Hz)
±15
±10
± 5

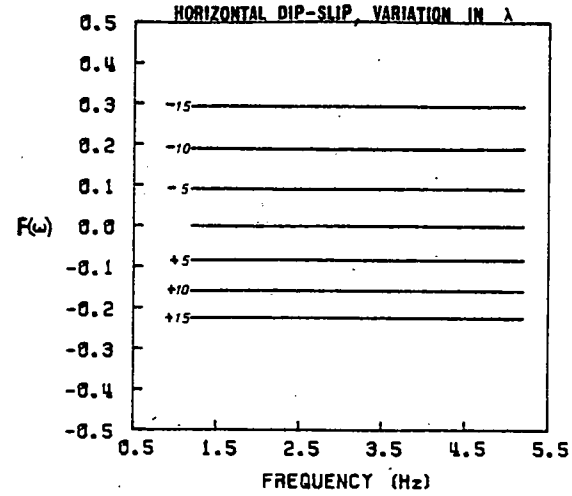
HORIZONTAL DIP-SLIP, VARIATION IN λ
F(ω)
FREQUENCY (Hz)
-15
-10
- 5
+5
+10
+15

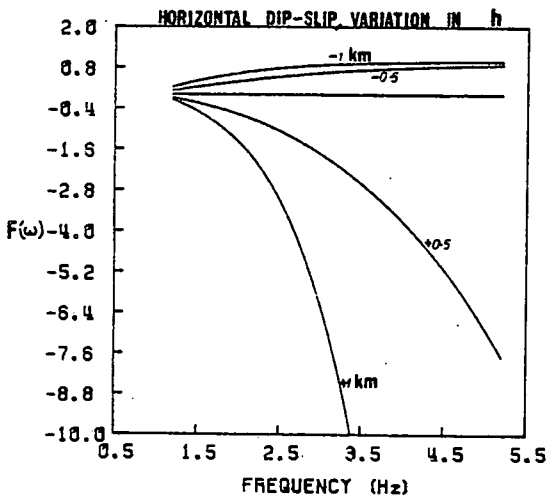
HORIZONTAL DIP-SLIP, VARIATION IN h
F(ω)
FREQUENCY (Hz)
-1 km
-0·5
+0·5
+1 km

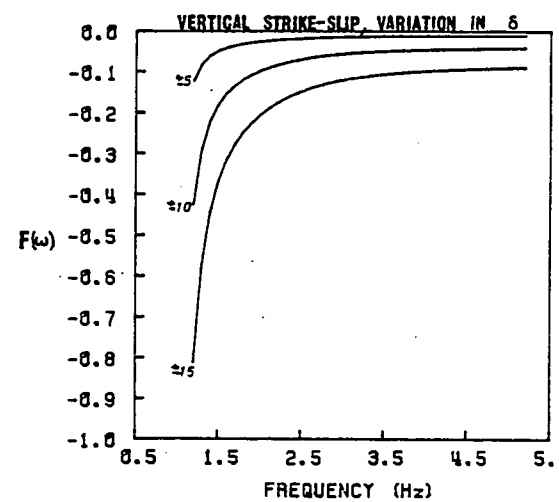
VERTICAL STRIKE-SLIP, VARIATION IN δ
F(ω)
FREQUENCY (Hz)
±5
±10
±15

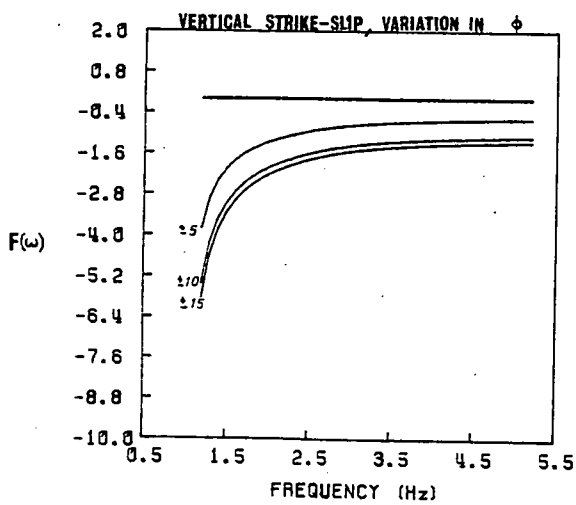
VERTICAL STRIKE-SLIP, VARIATION IN ϕ
F(ω)
FREQUENCY (Hz)
±5
±10
±15

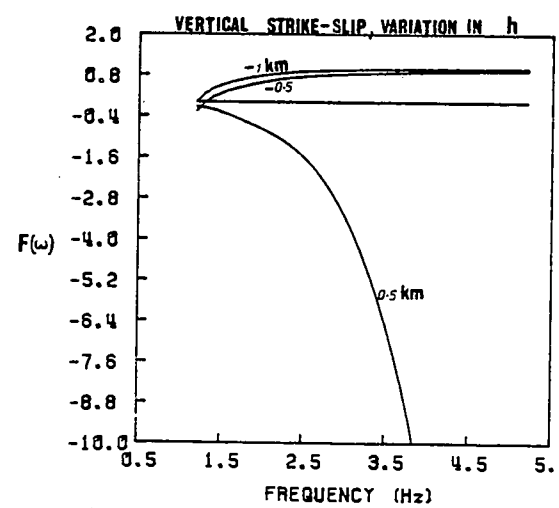
VERTICAL STRIKE-SLIP, VARIATION IN h
F(ω)
FREQUENCY (Hz)
-1 km
-0·5
0·5 km

strike azimuth of the dip-slip model produce identical spectral effects to changes in the rake of the dip-slip model, and are therefore not shown. The effect of this variation is to scale the spectrum by only a constant factor, the maximum value of $F(\omega)$ being $\simeq 0.3$. The variation in dip angle for the dip-slip models results in a small change of 0.1 maximum; $F(\omega)$ having the same sign for both negative and positive perturbations. Due to the presence of a spectral minimum in the low frequency spectrum of the strike-slip fault, $F(\omega)$ has values of between 0.1 and 0.8, and 1.6 and 6.4 at frequencies of < 1 Hz, for perturbations in both δ and ϕ respectively. There is a decrease in the amplitude spectrum for both negative and positive changes in these parameters. The most influential parameter is clearly the depth of the earthquake, especially for an increase in focal depth, for which $F(\omega)$ can reach values of 10.0 or more.

5.3.6 Attenuation Function

The attenuation function $D(\omega)$ decreases exponentially with distance from the source, and is strongly frequency dependent. It is expected to find variations of up to $\pm$ 0.02 in the Q_β^{-1} models measured using high frequency Rayleigh waves (Evans, 1981). The shallow crustal velocity model of the above section is chosen to compute the frequency dependent weighting functions for each Q_β^{-1} (Equation 1.9). A typical upper crustal three layered Q_β^{-1} model (Figure 5.7a) is inferred from Evans (1981). The fractional change in the spectral amplitude is computed for $\pm$ 0.01 and $\pm$ 0.02 variations

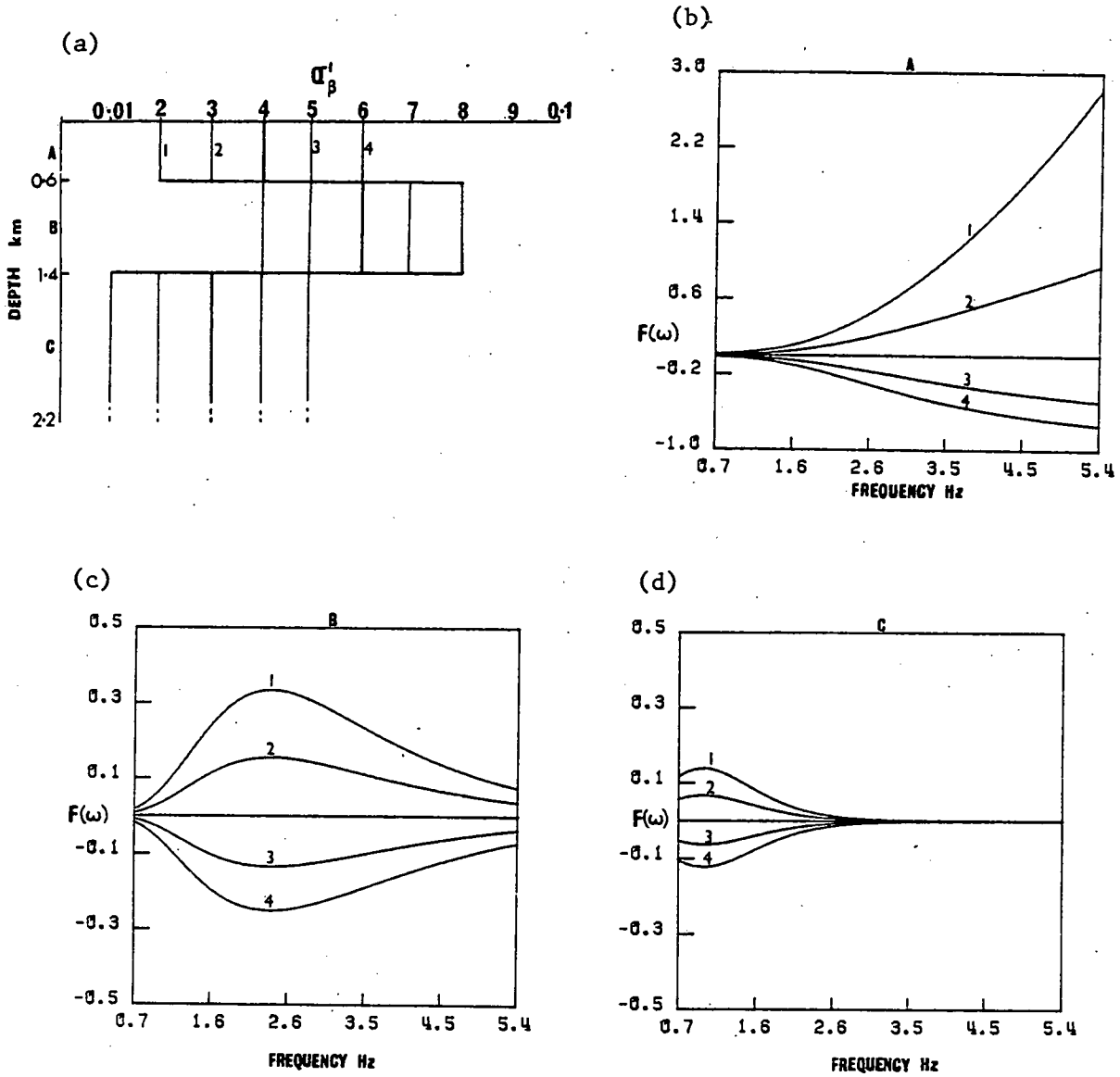

Figure 5.7 Fractional change in spectral amplitude for Q_β^{-1} perturbations in each layer of a typical upper crustal attenuation model. The epicentral distance is 30 km.

(a) unperturbed Q_β^{-1} model with perturbations of ±0.01 and ±0.02

(b), (c) and (d) fractional changes in spectral amplitude corresponding to perturbations in upper, middle, and lower layer of attenuation model.

in the Q_β^{-1} of each layer, and this is shown in Figures 5.7b,c, and d for a distance of 30 km. In calculating these values, it is discovered that $F(\omega)$ scales approximately linearly with distance. The largest values for $F(\omega)$ are in the top layer, where the error increases steadily with frequency from 0.0 to 2.8. The attenuation parameter in the second layer is less effective by a factor of 9, and in the third layer by a factor of 28. Larger Q_β^{-1} values result in a greater change than lower values.

5.3.7 Instrument Response

The instrument response was discussed in Section 1.3. In practice one might expect ± 10% deviations in the seismometer gain. This produces a frequency independent fractional error of ± 0.1. Errors in the damping constant of the seismometer distort the theoretical spectral amplitude, and usually have a magnitude of ± 10%. Fractional changes in the spectrum for those fluctuations in the damping constant are shown in Figure 5.8 for the velocity transducers used in the LISPB and LOWNET arrays (Willmore Mk. II and HS10/FS60 seismometers). The most noticeable feature of the curves is the maximum fractional change of 0.1 at the natural frequency of the instruments.

5.3.8 Comparison of All Effects

The preceding sub-sections have shown the effect of a priori uncertainties in the series of parameters representing the theoretical amplitude spectrum. To compare these results it must be emphasized

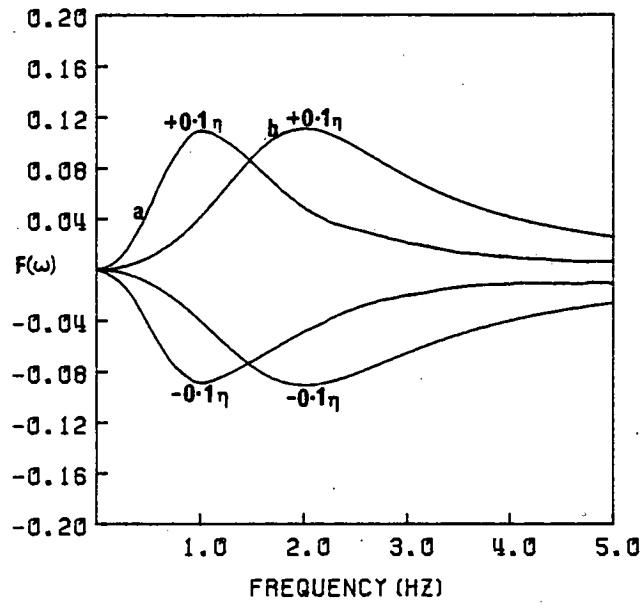

Figure 5.8. Fractional change $F(\omega)$ in spectral amplitude corresponding to ±10% perturbations in the damping constant η of the three typical instruments used in LOWNET and LISPB arrays.

a - Willmore Mk II, $\eta = 0.7$

b - HS 10/FS60, $\eta = 0.6$.

that the most important parameters are those which yield the largest variation in the amplitude spectrum per a priori uncertainty. Using this definition, there is a clear categorization of the spectral functions examined above into those that produce weak and strong effects. The weak functions are:- medium response $M_z(\omega)$ (for underground explosions, underwater explosions, and earthquakes) with respect to perturbations in shear velocity depth distribution, earthquake source function $S_T(\omega)$ with respect to the inverse time constant, earthquake medium response with respect to rake angle, underwater explosion source function with respect to the thickness of the water layer, underwater explosion source function for no bubble pulses with respect to the depth of the shot, and instrument response with respect to the damping constant and gain factor. All these effects produce fractional variations in the spectral amplitude of $\lesssim 0.4$. The stronger functions are:- attenuation, underwater explosion source function for one bubble pulse with respect to perturbations in the depth of the shot, the earthquake medium response with respect to focal depth, dip and azimuth, and the earthquake finiteness function with respect to rupture length and azimuth. From the latter group, all but the attenuation effect are important as a result of the characteristic functions forming a minimum in the amplitude spectrum. The source function $S_T(\omega)$ and the source strength S_o for underground explosions group with these functions as they are regarded as unknowns.

The effect of attenuation is only important for the top layer of the Q_β^{-1} model. However, $F(\omega)$ scales with distance and we generally cannot neglect any of the Q_β^{-1} values in the lower layers.

This distance variation results in an interesting feature regarding the resolution of the attenuation effects from the spectrum. Close to an event, the influence of the attenuation is weak, and the other phenomena strongly influence the spectrum. At large distances the attenuation is dominant. There is therefore an optimum distance at which various properties can be extracted with equal importance as the attenuation. Simple calculations achieved by scaling the curves of Figure 5.7b show that this point for the focal depth is at a distance of 300 km, whereas for the earthquake inverse time constant it is 7 km.

5.4 Single-station Attenuation Measurements

5.4.1 General Methodology for Different Source Types

The analysis above has shown that the attenuation function cannot be completely isolated in the amplitude spectrum as other functions also play an important role. The identification of these strong functions is now utilized in designing a procedure for measuring single-station attenuation. The single-station technique consists of correcting each observed amplitude for the functions which have a weak effect on the spectrum, and obtaining estimates for the remaining parameters which describe the strong or unknown effects by mapping the expected functional form onto the corrected observations. As the most important phenomena shaping the theoretical spectrum of underground explosions, underwater explosions, and earthquakes are different, then these sources are considered separately below.

The observed spectrum from an underground explosion is corrected

for the medium response and the instrument response, and the finiteness effect is ignored. The strength and the spectrum of the source time action are unknown, and attenuation strongly influences the amplitude spectrum. Thus, the remaining function is parameterized by S_o, the inverse time constant, and the Q_β^{-1} model (specified by $Q_{\beta\ell}^{-1}$: $\ell = 1,m$)

$$A_z(\omega) = S_o S_T(\omega;\omega_T) D(\omega;Q_{\beta\ell}^{-1}) \quad . \tag{5.7}$$

The observed spectrum from an underwater explosion is corrected for the medium response and instrument response, while the water thickness at the shot point is calculated using bathymetric data. The remaining function is then parameterized by S_o, shot depth, and the Q_β^{-1} model

$$A_z(\omega) = S_o S_r(\omega;d) S_b(\omega;d) D(\omega;Q_{\beta\ell}^{-1}) \quad . \tag{5.8}$$

The observed spectrum from an earthquake source is corrected for the spectrum of the source time action and the instrument response. The rake of the earthquake fault is determined using other data. Thus the remaining amplitude is parameterized by S_o, focal depth, dip angle, strike azimuth, rupture length, and the Q_β^{-1} model

$$A_z(\omega) = S_o S_F(\omega;\phi;L) M_z(\omega;\phi;h,\delta) D(\omega;Q_{\beta\ell}^{-1}) \quad . \tag{5.9}$$

Having reduced the set of variables specifying the theoretical spectrum to a minimum, the individual parameterized functions above are now fitted to the corrected amplitude spectra to obtain estimates

for each variable, and particularly for attenuation. As we expect an average of 20 - 30 evaluations of the spectral amplitude at discrete frequency harmonics per station, then this problem is clearly over-determined provided the attenuation model has only several layers. In choosing the number of layers for the attenuation model we are guided by the following:

(a) it is not realistic to have models with finely divided layers which match the smaller fluctuations in spectral amplitude

(b) the number of parameters describing the spectrum must not approach or exceed the number of frequency points (for good resolution, stability of inversion procedures, or a unique solution)

(c) the speed of the inversion decreases as the number of descriptive parameters increases.

On the basis of the above factors we restrict the Q_β^{-1} model to three layers. Later, when the single-station method is applied to the data, the limitations and advantages of this assumption will become apparent.

As the single-station procedure will be applied to a large number of amplitude spectra, it is advantageous to choose an inversion procedure that produces a quick solution. Constraints on the solution region expedite a fast inversion, and ensure physically reasonable estimates of the spectral parameters. Accordingly, the bounds on Q_β^{-1} in each layer are set a priori to $0.0 \leq Q_{\beta\ell}^{-1} \leq 0.1$ for all ℓ. The magnitude of the source time action S_o is completely uncertain, and must therefore be treated as unconstrained. The constraints on the other function parameters depend on the specific source, but no difficulty is envisaged in obtaining these.

5.4.2 Hedgehog Method

The Hedgehog method (Keilis-Borok and Yanovskaja, 1967; Valyus, 1968) has often been used in inversion problems (Burton, 1974; Stuart, 1978; Clark, 1983). In this method, the unknown parameters describe a multi-dimensional hyperspace, in which each dimension corresponds to a particular parameter. The constraints on the parameters specify a volume in this space. This region is then discretized by inscribing a regular network of knots or set of coordinate points with a constant spacing along each coordinate axis. One may visualize a selected combination of variables (a particular model) as a vector drawn to one of these knots. The Hedgehog method used here initially starts as a Monte-Carlo procedure, in which these vectors are generated in a pseudo-random fashion. The theoretical curve corresponding to each vector is computed, and this is compared with the observations in the context of certain pre-specified constraints. If the solution is accepted, this primary vector is then used as a basis of systematically generating further vectors satisfying the criteria. The search is continued until all of the particular neighbours have been tried, and thus delineates an acceptable region from the bad solutions. To reduce the time taken to fill the region, only neighbours corresponding to a certain symmetry or rank are tried (Valyus, 1968). The algorithm then switches back to the Monte-Carlo procedure and attempts to locate another solution which does not lie within this connected region. The procedure has an advantage over the deterministic inversions in that it is easy to apply to both linear and non-linear problems alike. However, a disadvantage of the technique is the time taken to 'satisfactorily' define the connected region. Acceptable

solutions are chosen on the basis of two criteria:

(a) the shape of the theoretical curve must fit within the envelope defined by the uncertainty estimate δA^o_{zi} on each observed spectral point at the ith frequency (these are evaluated in the following section). To implement this we use the condition

$$A^o_{zi} - \delta A^o_{zi} \leq C_q A^t_{zi} \leq A^o_{zi} + \delta A^o_{zi} \qquad (5.10)$$

for all i. This set of constraints must be satisfied for one particular value of $q = -5$ to $+5$. A^o_{zi} is the corrected spectral amplitude, A^t_{zi} is the theoretical spectral amplitude at the ith frequency, and $C_q = (A^o_{zi} + q/5\delta A^o_{zi})/A^t_{zi}$.

This constraint can be visualized as scaling the low frequency end of the theoretical curve in increments between the upper and lower limit, the remaining theoretical points following in correspondence. For each step, a check is applied to ascertain if the spectrum now lies within the error envelope on the observations. Ten steps were chosen as a sufficient compromise between speed and accuracy of discrimination.

(b) models are accepted which yield a χ^2_ν-value which is smaller than some threshold value (this is defined in Equation 4.2, the amplitude spectrum replacing the group velocity in this case).

In the Hedgehog inversion, a special feature can be employed for tackling the unknown parameter S_o. According to Tsai (1972), the value of S_o which minimizes χ^2_ν, for any particular parameter set specifying this function, is given by

$$S_o = \frac{\sum_{i=1}^{n} A_{zi}^t \, A_{zi}^o}{\sum_{i=1}^{n} A_{zi}^t \, A_{zi}^t} \quad . \tag{5.11}$$

This is calculated for each selected set of spectral parameters, and thus need not be considered as a variable in this inversion procedure.

5.4.3 Fast Optimization and Boundary Evaluation (FOB)

5.4.3a Optimization

The problem of computing the parameter estimates and uncertainties can be approached using a less time-consuming method than the Hedgehog inversion. In this technique, all the source parameters excluding the magnitude of the source action, are discretized on a grid with extremes corresponding to the physical limits of each quantity. Each grid point is selected in turn, and the corresponding spectral source functions deduced. Theoretically, if the corrected spectrum $A_z(\omega)$ at each station is divided by these functions, the remaining spectrum is described by the factor S_o and the attenuation function $D(\omega)$. The parameters of the remaining function are now obtained by minimizing the quantity

$$\chi^2_{FOB} = \frac{1}{(n-4)} \sum_{i=1}^{n} \left(\frac{\ell n A_{zi} - \ell n A_{zi}^t}{\delta \ell n \, A_{zi}^o} \right)^2 \tag{5.12}$$

with respect to S_o and the Q_β^{-1} values. $\delta \ell n A_{zi}^o$ is the maximum standard deviation on the observed logarithmic spectrum at the ith frequency.

The χ^2_{FOB} function appears to be more sensitive to the attenuation parameters when the logarithmic spectral amplitudes are used. This differs from MacBeth and Burton (1983) who used a correlation coefficient in an attempt to fit only to the spectral shape. This coefficient appeared to be relatively insensitive to the attenuation.

The minimization of χ^2_{FOB} is achieved using a quasi-Newtonian procedure (Gill and Murray, 1976; Appendix B.1), which is basically a second order gradient-search method. The algorithm to implement this technique is available from the ERCC (Edinburgh Regional Computing Centre) 'NAG' library as an easy-to-use 'black-box' routine (E04JAF). This method is chosen, in particular, as it operates on constrained function variables. If the limits on the source strength are set sufficiently large that they may be regarded as infinite bounds, the inversion can now be thought of as fitting to the shape of the spectrum. The values of Q_β^{-1} and S_o at each optimum point (minimum in χ^2_{FOB}) are stored. The process of selecting a new grid point, and correcting for the source functions is then repeated. On completion, the χ^2_{FOB} is examined as a function of the grid coordinates, and the set of parameters with the smallest χ^2_{FOB} value is selected. This procedure is extremely fast as only several source parameters (one in the case of an underground explosion) need be considered.

The resolving power of each parameter in Equations 5.7, 5.8, and 5.9 for this inversion is directly related to the importance of each spectral parameter as defined in Section 5.3. Therefore we expect the attenuation parameters to be well resolved for the explosion data. With the earthquake source, in addition to a large number of parameters

to estimate (relative to the other sources) there are many strong effects, and we expect a smaller potential resolution of Q_β^{-1} from the amplitude spectra.

5.4.3b Bounds on Estimates

Once the parameters corresponding to the best grid point are obtained from the optimization procedure the observations are again corrected for the source functions, but now the optimum values are used. Taking the natural logarithm of the remaining expression separates S_o from the specific attenuation values and gives

$$\ell n(A_{zi}^t) = \ell n(S_o) + \gamma_i r = \ell n(S_o) + r \sum_{\ell=1}^{3} K_{i\ell} Q_{\beta\ell}^{-1} \qquad (5.13)$$

for the ith frequency. This is a linear equation in the three unknown $Q_{\beta\ell}^{-1}$'s and $\ell n(S_o)$. The envelope of error around the observations defines an acceptable region in the hyperspace of these parameters

$$\ell n(A_{zi}^o - \delta A_{zi}^o) \leq \ell n(A_{zi}^t) \leq \ell n(A_{zi}^o + \delta A_{zi}^o) \qquad (5.14)$$

for all i. The Simplex linear programming method (Garvin, 1960; Dantzig, 1963; Johnston, 1972) can be adapted to obtain upper and lower bounds on the parameters at each station corresponding to this inequality equation. The bounds on each parameter correspond to the range of possible parameter values for which the difference between the theoretical and observed points is smaller than the observed standard errors. This technique and its application to this problem

is fully described in Appendix B.2. The algorithm to implement this procedure uses the ERCC routine H01ADF.

The technique totally defines an acceptable region within solution space, and produces boundaries on the parameter values which can be interpreted like those for Hedgehog. The process is extremely fast because the search is done over a series of points, unlike the multi-dimensional search of the Hedgehog method. The optimization and boundary evaluation techniques are implemented in the program 'SSQ' which is listed in Appendix D.3.

5.4.4 Uncertainties in the Rayleigh Wave Amplitude Spectrum

The output from the inversion procedures described above will be estimates of the unknown parameters involved in Equations 5.7 - 5.9, and also bounds on these values corresponding to errors on the observations and the inherent non-uniqueness of the inversion procedure. The latter effect is dependent on the number of constraints imposed on the solution, the number of parameters which define the model, and the formulation of the problem. The evaluation of the spread of each model parameter in the inversion is as important as the method itself, for if these uncertainties exceed local fluctuations in structural properties, then the estimates cannot be used to discern physical mechanisms relating to the wave properties. In order to compute these bounds in the inversion procedures, one must assign a realistic set of errors to each isolated amplitude spectrum. For this, we assume the uncertainties arise from two dominant sources:- scattering of Rayleigh waves

from lateral heterogeneities and microseismic noise.

Scattering is a difficult phenomenon to quantify as there is no way at present of accurately measuring the scale-length of an inhomogeneity or the number of potential scatterers. The Rayleigh waves arriving at different stations will have experienced a variety of interactions with scatterers of unknown size or quantity. However, Aki and Richards (1981) and Aki et al. (1972) quote a rule of thumb viz.: 'inhomogeneities are likely to become important when the propagation path exceeds 50λ'. A given wavelength of radiation has a greater probability of being influenced by inhomogeneities the greater the distance from the source. On the other hand, for the same epicentral distance higher frequencies travel more wavelengths and therefore have a greater probability of interaction. To compute the error in the amplitude spectrum a nominal fractional error of 0.3 is chosen for a path length 50λ. Thus the fractional error in $A_z^o(\omega)$ for a path length r and at a particular frequency ω is given by $r\omega/c(\omega)\ 10^{-3}$, where $c(\omega)$ is the phase velocity of the Rayleigh wave.

Ambient noise, defined as the continuous background of seismic activity which is monitored at a station before a significant disturbance such as an explosion or earthquake, limits the frequency range and the dynamic range of a signal from which one wishes to extract information. The noise level represents a frequency dependent uncertainty on the recorded amplitude spectrum. Short period noise is usually caused by cultural activities, or by local natural phenomena such as wind (Frantti, 1963). The noise level is affected by topographic shielding (Robertson, 1965), local geology and the surface sediments upon which the seismometer is

placed (Frantti et al., 1962). The cultural and local phenomena in the frequency range (0.7 - 5.5 Hz) are unpredictable, and vary from place to place. Therefore, the effect of this disturbance on the signal must be estimated by analysing the microseismic activity preceding each event, using time windows with identical lengths to the signal wavepacket.

The two sources of error are combined by adding the noise spectrum $N(\omega)$ to the error on the spectral amplitude due to lateral inhomogeneities, giving

$$\delta A_z^o(\omega) = N(\omega) + \frac{r\omega}{c(\omega)} A_z^o(\omega) 10^{-3} . \qquad (5.15)$$

5.5 Summary

In this chapter, the explicit form of each function which combines to synthesize the theoretical amplitude spectrum of a Rayleigh wave was examined to identify the most important parameters in determining the spectral shape. This was ascertained using the fractional change in the spectrum corresponding to an a priori uncertainty in the particular spectral parameter. Applying this procedure to underwater explosions, underground explosions, and earthquake sources, we discovered:

(a) the underground explosion spectrum can be corrected for the medium response and the instrument distortion.

(b) the underwater explosion spectrum can be corrected for the medium response and instrument distortion, and the thickness of the water layer set to a constant.

(c) The earthquake spectrum can be corrected for the source function $S_T(\omega)$ and the instrument distortion, and the shear wave velocity distribution in the earth and rake set to values obtained from other data.

The single-station procedure consisted of correcting the observed spectrum for the above weak functions. The theoretical spectrum was then specified by the few remaining parameters, and mapped onto the corrected observations. Estimates for these parameters and their bounds can be obtained using two inversion methods - one of which was a Hedgehog technique. Although the details of the procedure applied to underground explosions, underwater explosions, and earthquakes were similar in methodology, they differed as the most important phenomena shaping the spectrum were not the same. Uncertainties in the observed spectra can be deduced from the effect of lateral heterogeneities and noise spectra.

A peak frequency method, which relates the frequency at which the spectrum peaks to an approximate half-space attenuation value, was described initially. This will hopefully produce a Q_β^{-1} value which can be used to obtain a rough order of magnitude guide for a region.

The techniques above will be applied in Chapter 6 to the specific examples of amplitude spectra generated from the underground explosions, underwater explosions, and earthquake source, which were described in Chapters 1 and 4.

CHAPTER 6

APPLICATION OF SINGLE-STATION ATTENUATION METHODS TO 0.7 - 5.5 HZ RAYLEIGH WAVES IN SCOTLAND

6.1 Introduction

In the preceding chapter, the methodological results of the first four chapters of this thesis were collated leading to a technique for modelling the average Q_β^{-1} depth distribution within the crust along a single event-station path. The method consisted of correcting the observed spectrum for less important functions, and then obtaining estimates for the remaining parameters specifying the theoretical curve by inversion procedures.

Here, this single-station technique will be applied to the spectral data generated by the underground explosions, underwater explosions, and KEQ earthquake which were fully discussed in Chapters 1 and 4. The scheme for obtaining the single-station attenuation will follow different routes for the three sources, as each has a particular set of strong or weak effects. The earthquake source will have the largest number of residual parameters to be determined along with the specific attenuation.

The data will be presented in increasing degrees of complexity with regard to the source and event-station configuration. The first set of amplitude spectra will be derived from the LISPB recordings of the underground explosions L1 and L2, and the underwater explosions N1 and N2 (Figure 1.1). The line of stations intersects a variety of relatively homogeneous geological provinces to which the fundamental

mode Rayleigh waves are sensitive. Previous work by Evans (1981) has exploited this simple arrangement to obtain estimates of the average dissipative properties in each formation. These values will be used to corroborate the single-station measurements of attenuation. The underwater explosions shot in Kirkcaldy Bay generate fundamental mode Rayleigh waves which are recorded on the LOWNET array over a range of different azimuths covering three quadrants. Each path intersects a variety of different geological formations. The final complexity will be the earthquake KEQ which generates first and second higher mode Rayleigh waves, these being recorded on the LISPB array at a variety of azimuths distributed over two quadrants. The higher mode waves have been shown to be sensitive to the crustal structure down to depths of 17km. The geometric event-station arrangements for the Kirkcaldy Bay and KEQ data sets are good examples of situations in which the single-station techniques are most appropriate.

Each section follows roughly the same format. The source effects for the specific event/s will be examined using the theory outlined in Chapters 2 and 3. Next, the observed spectra will be described with particular emphasis on the change in the shape of the curves with distance. After a preliminary study of the peak frequencies of the spectra, each amplitude spectrum will be analysed to obtain a single-station Q_β^{-1} profile with depth. Finally, the results of the analysis will be compared with the expected results obtained using simple assumptions regarding the lateral variations in the dissipative properties (Section 1.5) and pure-provincial attenuation models.

6.2 Underground and Underwater Explosions Recorded on the LISPB Array

6.2.1 Underground Explosion Source Effects

The shot line consisted of six bore-holes spaced 31m apart and around 46m deep. A cylindrical package of 227kg of SG90 explosive (90% nitroglycerine) was placed in each. The charges were on average one-third of the length of the enclosures. The dispersed shot configurations were arranged with their longitudinal axes normal to the direction of observation. Calculations based on Equation 2.14 indicate that there is no significant change in the theoretical Rayleigh wave spectral amplitude for a variation in the orientation of the shot line of up to $\pm 10^{\circ}$.

Using Equation 2.1 the explosion cavity radius r_c is estimated at between 1.2 - 3.1m. This gives an elastic radius in the range 5.4 to 14m, which is smaller than the spacing between the shots, and consequently the explosions act as independent emitters. The natural undamped frequency of each explosion, corresponding to the elastic radius (Section 2.2.4), is between 90-250 Hz for a shear wave velocity of 2.5 km/sec in the source region, implying that the source finiteness function can be neglected. The shortest seismic wavelength is 200m compared to a charge length of 15m and a borehole radius of 7.5cm. Therefore the longitudinal extension of the source does not effect the Rayleigh wave spectra, and the equivalent seismic radiator surface will be spherical in the frequency range 0.7-5.5 Hz. Consequently, each explosion can be represented by a body force system consisting of three orthogonal couples without moment acting on the surface of an earth model.

Each bore-hole was tamped with gravel chippings and was heavily waterlogged. During detonation this tamping was rapidly ejected from

the majority of the holes by the expanding gaseous by-products. No attempt is made here to model this first order effect as this would increase the number of parameters describing the source to an unacceptable level.

The fundamental mode Rayleigh waves from the underground explosions are generated initially in the Dalradian province. The energy propagates in a northernly direction up the ALPHA line into the Moine province, and in a southern direction the paths intersect Old Red Sandstone and the Devonian Lavas. Before applying the single-station methods, the observations must be corrected for the frequency dependent effects of transmission across the boundary between two adjacent geological formations. An analytic expression for the transmission coefficient $P(\omega)$ has been obtained by many authors (Bache et al., 1978; McGarr, 1969a) by assuming constant energy flux during transmission, normal incidence at the boundary, and no mode conversions or lateral reflections. For a wave travelling from medium 1 into medium 2

$$P_{1\rightarrow 2}(\omega) = \left[\frac{c_2(\omega)\, M_{z2}(\omega)}{c_1(\omega)\, M_{z1}(\omega)}\right]^{1/2} \qquad (6.1)$$

where $c(\omega)$ is the phase velocity and $M_z(\omega)$ the spectral medium response in each environment. The medium response functions for an underground explosion in stratified media corresponding to the Dalradian, Old Red Sandstone, Moine, and Devonian Lava provinces, in addition to a half-space with a shear velocity of 2.5 km/sec, are shown in Figures 6.1a and c. These are computed using the Thomson-Haskell technique described in Appendix A.4 for the frequency range 0.4 - 4.8 Hz, implemented using the program 'MLR' (listed in Appendix D.2), and the shear velocity models of Evans (1981) for each province (displayed

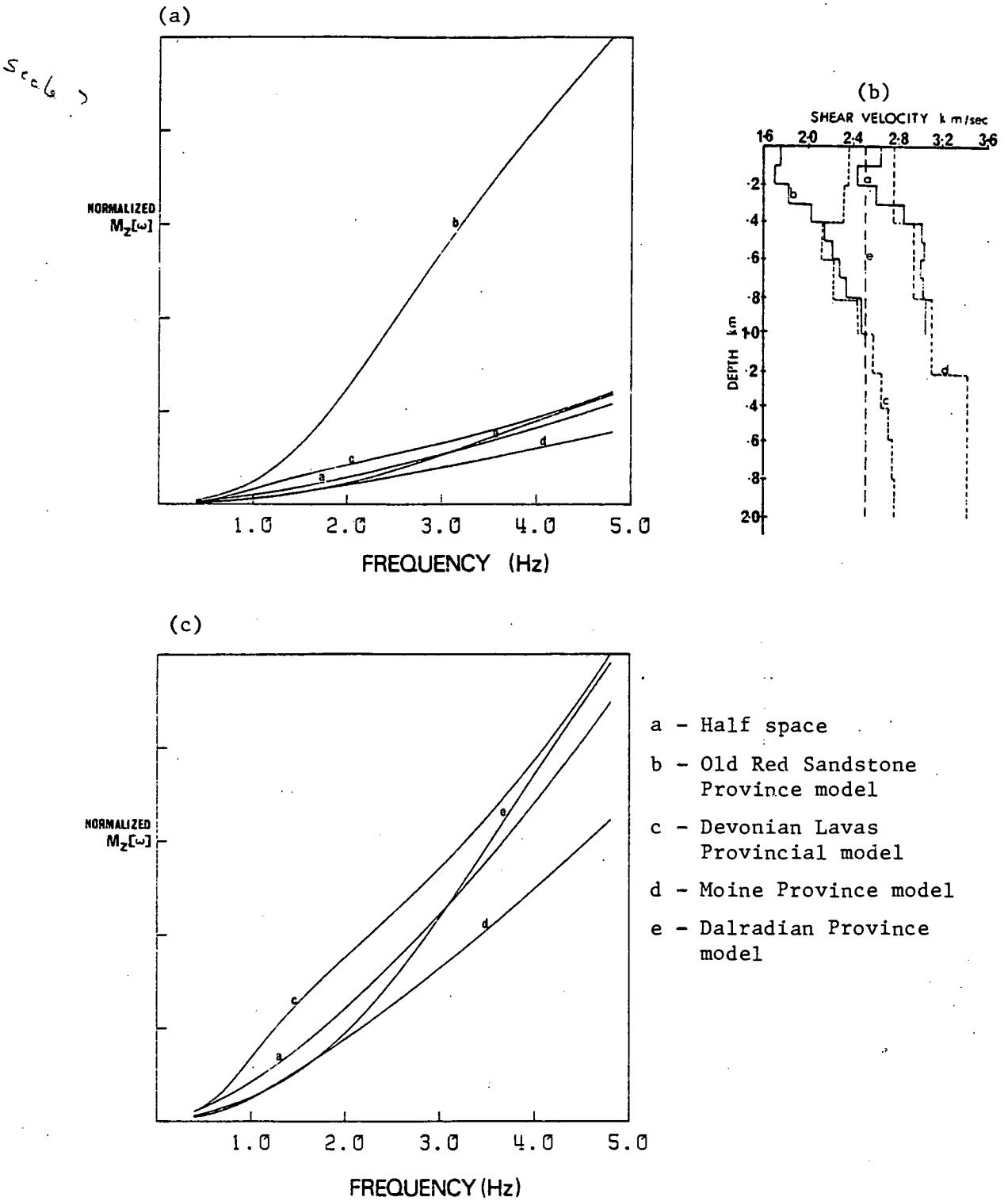

Figure 6.1. Spectral medium responses $M_z(\omega)$ corresponding to LISPB multi-layered velocity model (after Evans, 1981) and a half-space model with a shear velocity of 2.5 km/sec.
(a) Medium responses for Dalradian, Old Red Sandstone, Devonian Lava and Moine provinces and the half space.
(b) LISPB velocity models (from Evans, 1981).
(c) Medium responses drawn again, but excluding the Old Red Sandstone function for clarity.

in Figure 6.1b). All the functions are monotonically increasing with frequency, the Dalradian medium response having the steepest gradient. The Old Red Sandstone model, with the lowest velocities, has clearly the largest medium response for these frequencies. The phase velocities corresponding to these models are computed using the theory of Schwab and Knopoff (1972) (see Appendix A.4).

The transmission coefficients corresponding to waves from the Dalradian into Moine and Old Red Sandstone provinces, and Old Red Sandstone into the Devonian Lava province are shown in Figure 6.2. The highest and lowest values are for Rayleigh wave propagation into and out of the Old Red Sandstone, due to the low wave velocities in this rock. The coefficients are roughly constant over the frequency range of interest and therefore we use only the frequency averaged values in further calculations. The correction of the observations for these effects is considered in the description of the single-station analysis in Section 6.2.5.

6.2.2 Underwater Explosion Source Effects

The underwater explosion charge size was limited by the necessity to fire at optimum depth and near the tip of the LISPB line in shallow water. The shots were therefore dispersed into three packages with an individual yield equivalent to 203 kg of TNT, and separated by 40m. Again, calculations based on Equation 2.14 show that the length of this line has a negligible effect on the spectral amplitude. The explosives were fired simultaneously at an optimum depth of 95m. The depth of water for shot-point N1 was 115m, whereas N2 was bottom-fired. Consequently, the source functions for the two events are different.

Equations 2.7 and 2.8 imply a maximum bubble radius of 5.4m and a

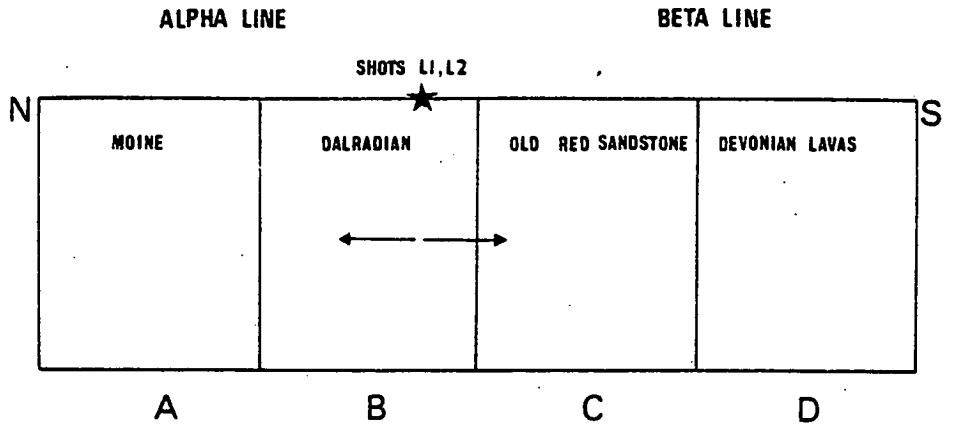

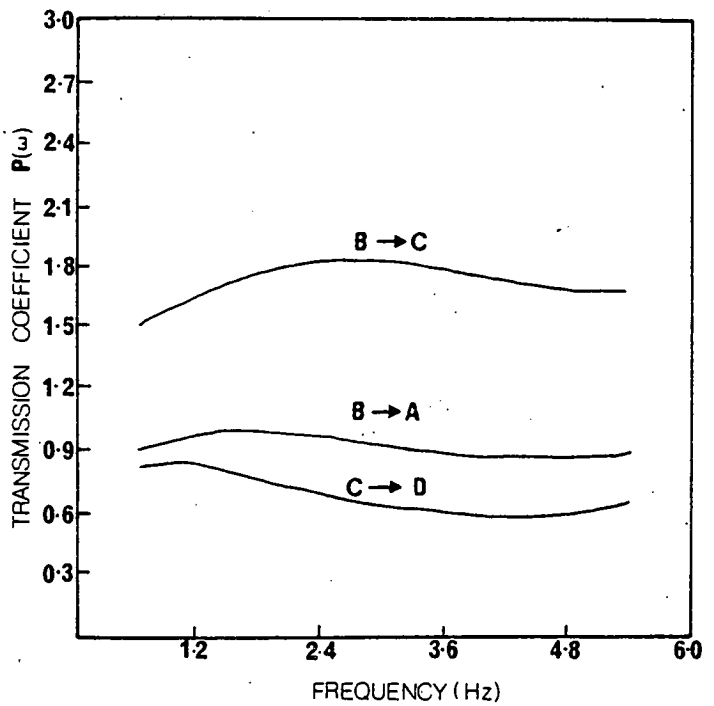

Figure 6.2. Frequency dependent transmission coefficients, for Rayleigh waves generated by underground explosions, between the geological provinces intersected by the LISPB line.

vertical rise in depth between the time of initiation and the first bubble pulse of 3m. These values imply that the bubble of gaseous by-products from both N1 and N2 will probably complete one oscillation before reaching the water surface. An additional problem for N2 however is that interaction with the sea-bottom sediment will reduce the energy in the bubble pulse, and therefore the shock wave will predominate. The theoretical functions which combine to shape the overall source spectrum of the explosions N1 and N2 are shown in Figure 6.3. The curves display the following characteristics:

(a) the bubble spectrum $S_b(\omega)$ for N2 exhibits a steady linear increase from zero frequency and tends to a constant value, with a slight oscillation about this value. The spectrum for N1 shows a distinct peak of constructive interference slightly below the natural bubble frequency of 3.9 Hz.

(b) the sharp reverberation spectrum $S_r(\omega)$ of N1 confirms that the shot is at optimum depth, as the peaks of the bubble spectrum and reverberation spectrum are at 3.5 Hz. The effect of setting the water thickness and charge depth to the same value for shot N2 is to shift the reverberation peak to 4.1 Hz.

(c) the composite spectrum $S_b(\omega)S_r(\omega)M_z(\omega)$ for shot N1 is narrower than that of N2 and peaks at a lower frequency.

6.2.3 Description of Observed Rayleigh Wave Spectral Amplitudes

The observed amplitude spectra for this data set, compensated for the instrument response and geometric spreading, are displayed in Figures 6.4, 6.5, and 6.6 as a function of epicentral distance and frequency. The underwater explosion spectra in Figure 6.4 have a

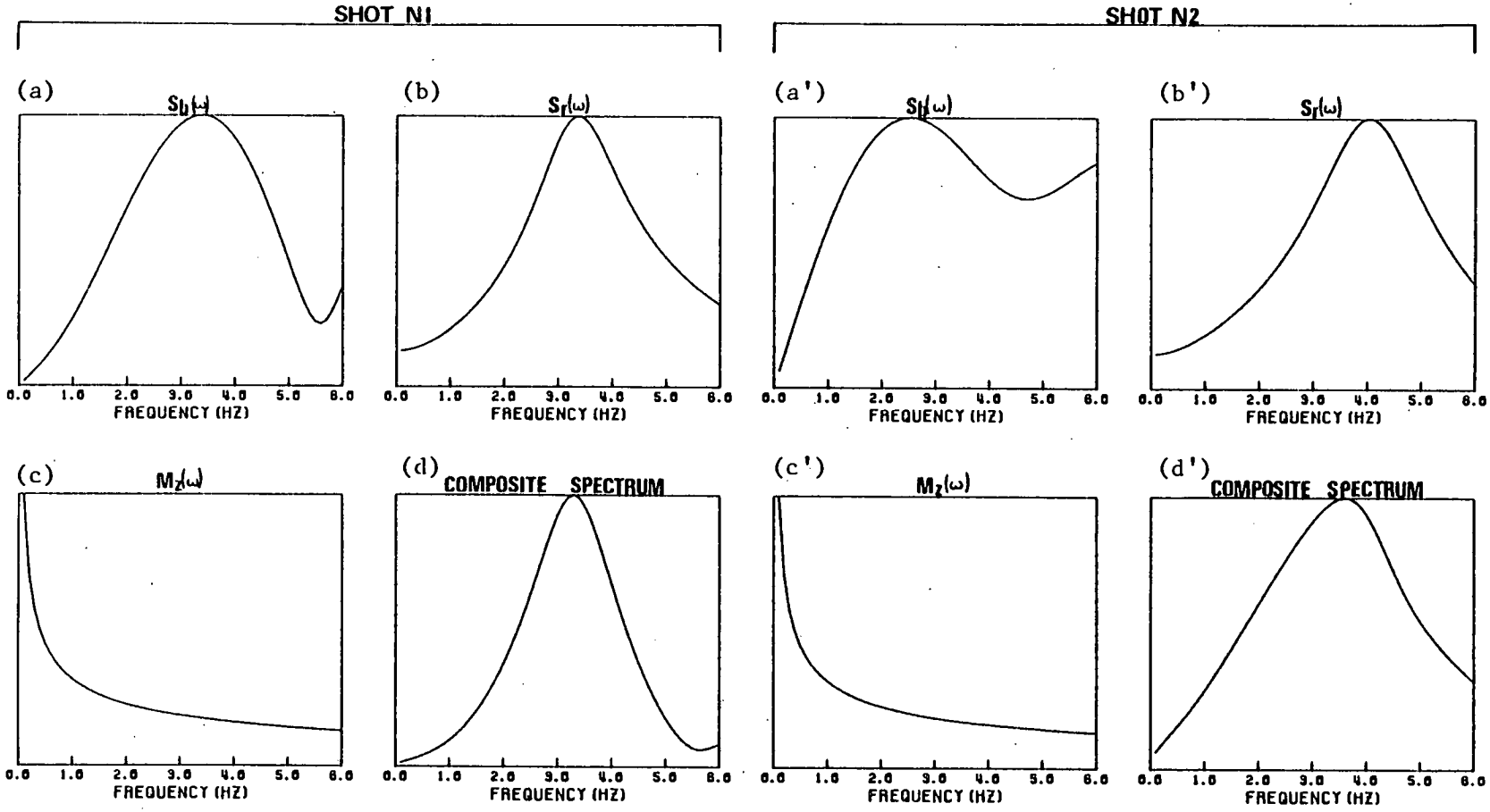

Figure 6.3. Functions which combine to form the complete unattenuated theoretical spectral shape from the underwater explosions recorded on the LISPB array. The curves are normalised with respect to their maximum amplitude in the frequency range 0.1 - 6.0 Hz.

(a) spectrum of bubble pulse oscillations for shot N1 (a') spectrum of shock wave for shot N2

(b),(b') reverberation spectrum

(c),(c') spectral medium response

(d),(d') composite spectrum $S_r(\omega)\ S_b(\omega)\ M_z(\omega)$

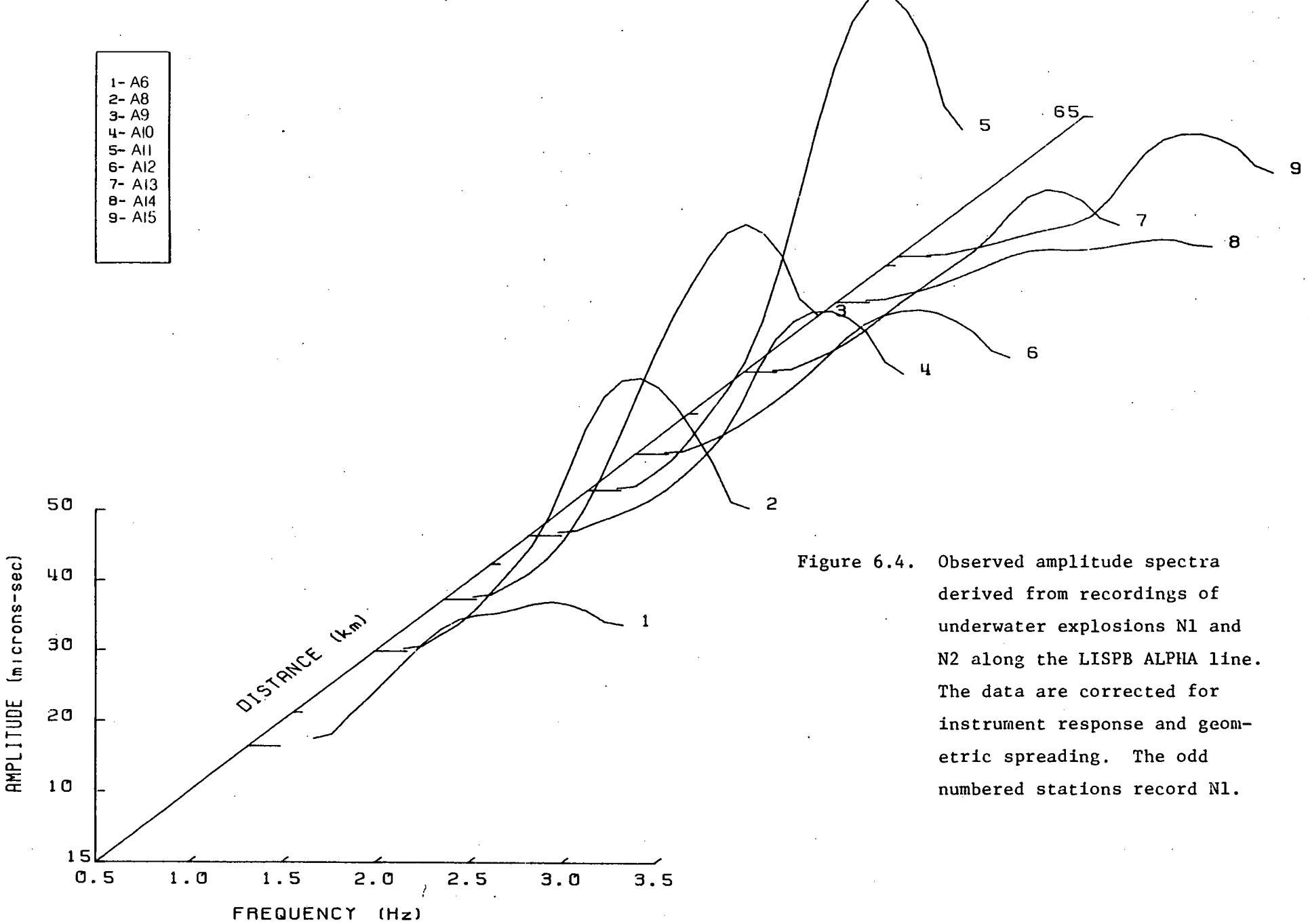

Figure 6.4. Observed amplitude spectra derived from recordings of underwater explosions N1 and N2 along the LISPB ALPHA line. The data are corrected for instrument response and geometric spreading. The odd numbered stations record N1.

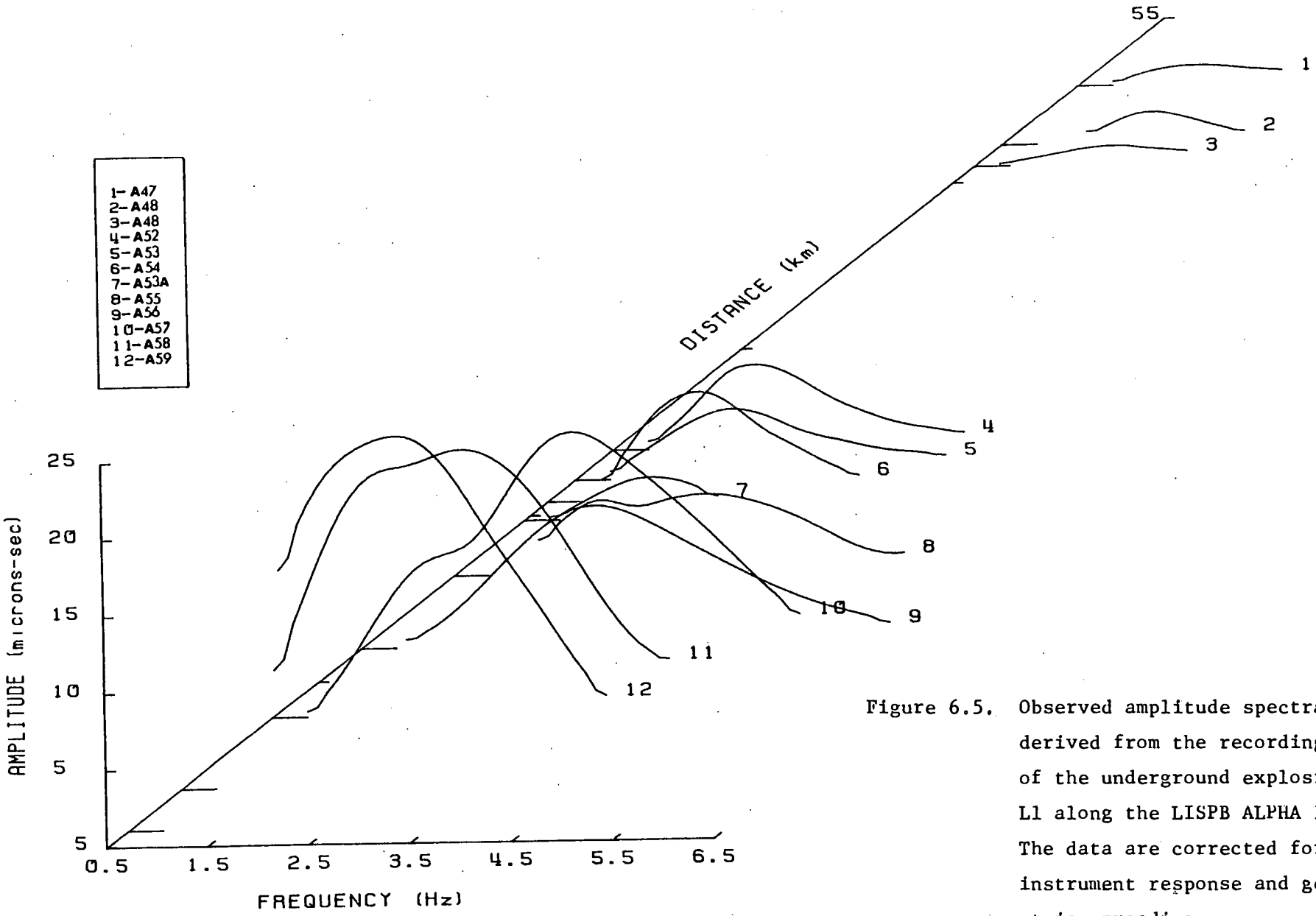

Figure 6.5. Observed amplitude spectra derived from the recordings of the underground explosion L1 along the LISPB ALPHA line. The data are corrected for instrument response and geometric spreading.

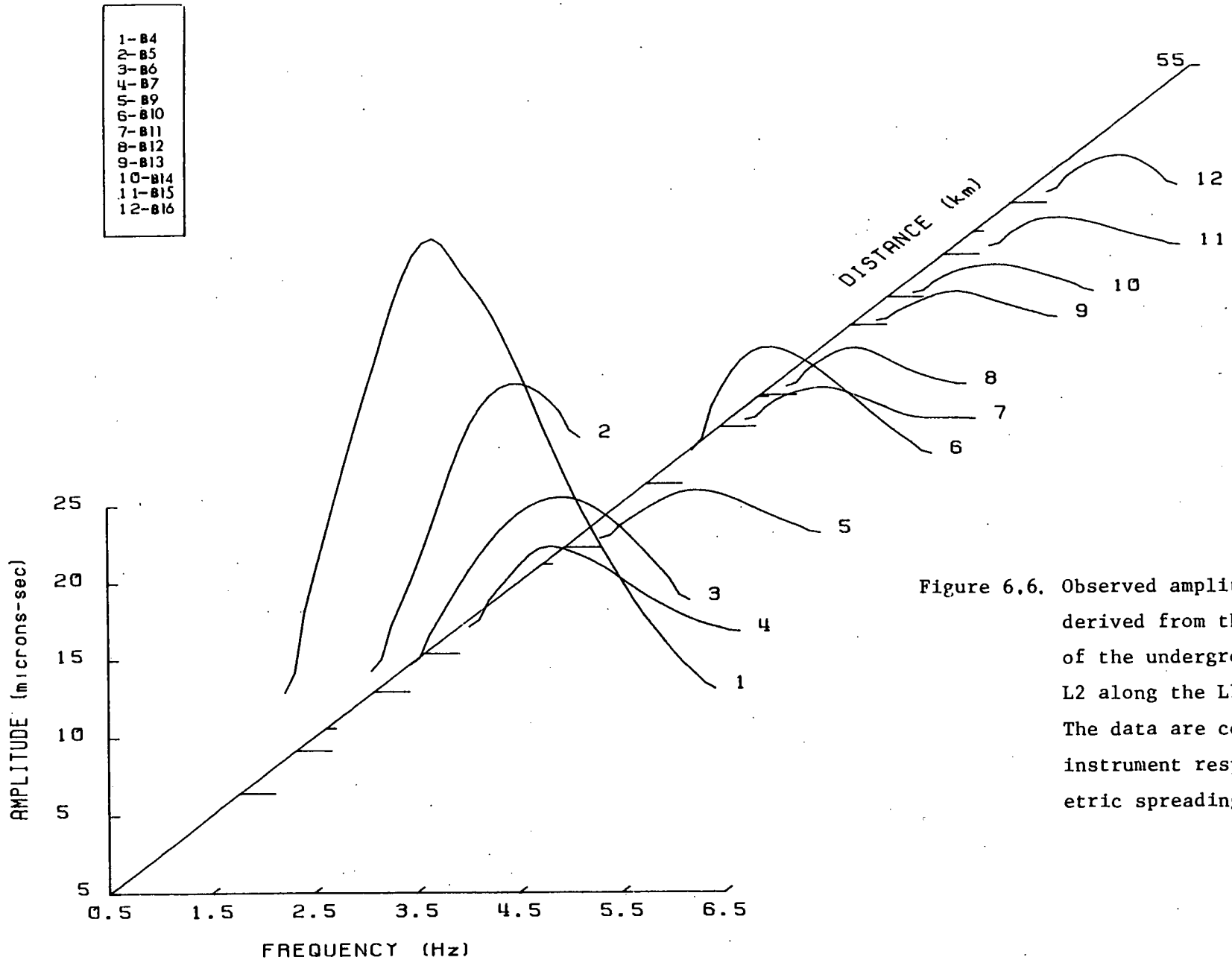

Figure 6.6. Observed amplitude spectra derived from the recordings of the underground explosion L2 along the LISPB BETA line. The data are corrected for instrument response and geometric spreading.

narrow band-width of about 1.5 Hz and the general spectral shapes do not show the trend with distance normally attributed to attenuation. The underground explosion spectra in Figures 6.5 and 6.6 display entirely different characteristics. These have large bandwidths of up to 4 Hz wide and absolute amplitudes that clearly decrease with distance. There is also a noticeable shift of the dominant frequencies to lower values, but this is not pronounced for stations greater than 35km from the source. The features of the latter two sets of spectra look promising for the application of the single-station methods.

6.2.4 Preliminary Study by the Peak Frequency Method

The peak frequency of each digital spectrum from the underground explosion and underwater explosion data, is read directly from the instrument corrected spectral amplitudes. In situations where it is difficult to take a singular reading, the spectra are smoothed and the peaks re-picked. The measurements are plotted against distance from the source in Figure 6.7a. The theoretical variations of peak frequency with distance for a power law source function $\omega^{\frac{1}{2}}$, and an anelastic half-space with shear velocity of 2.5km/sec and attenuation specified by a Q_β^{-1} of 0.01 and 0.06 are superimposed on this diagram for comparison with the observations. The peaks corresponding to the underground explosions show the expected shift to lower frequencies with increasing distance, ranging from 3.8 Hz down to 1.5 Hz; although, for distances greater than 35km the frequencies are approximately constant. All the underwater explosion spectra peak at frequencies of approximately 2Hz. This invariance with distance suggests either a very sharp source function or that the spectral content of the Rayleigh

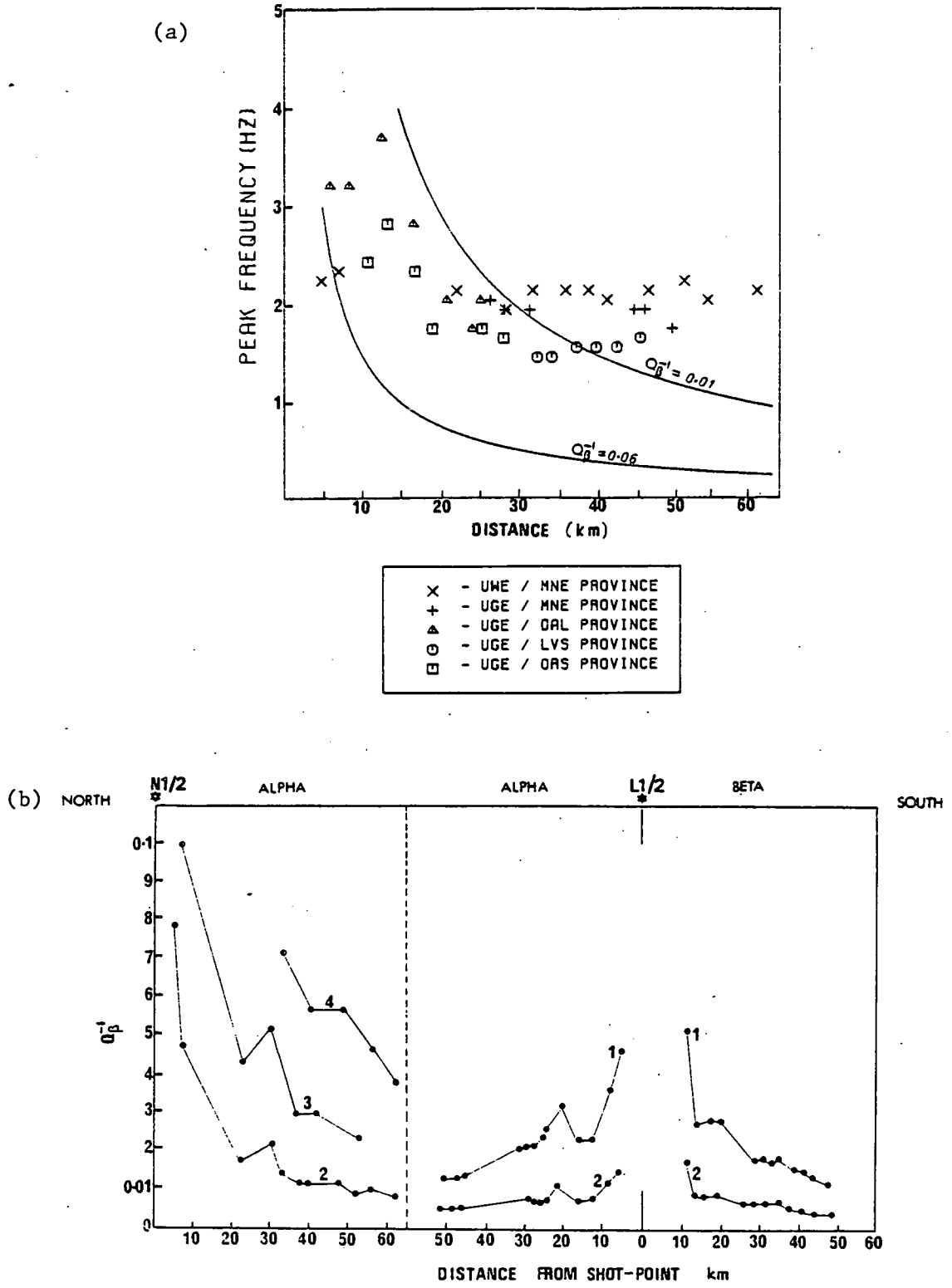

Figure 6.7, (a) Peak frequency of each Rayleigh wave spectral amplitude versus distance for all LISPB recordings. The solid lines indicate the theoretical variation of peak frequency with distance for an anelastic half-space with β = 2.5 km/sec , Q_β^{-1} = 0.01 and 0.06, and a power law source function $\omega^{\frac{1}{2}}$.

(b) Half-space Q_β^{-1} values estimated from the peak frequencies using:
1 - power law source function $\omega^{\frac{1}{2}}$ for underground explosion
2 - power law source function $\omega^{\frac{1}{2}}$ for underwater explosion
3 - underwater explosion source model with no bubble pulses (shot N2)
4 - underwater explosion source model with one bubble pulse (shot N1).

waves is dominated by the earth structure near the recording site and/or the instrument.

Q_β^{-1} is calculated for each peak frequency using Equations 5.2 and 5.3. This requires values for the gradient of the source function and group velocity at the peak frequency. The gradient of the group velocity is calculated at this point using the central difference formula:

$$\left.\frac{dU}{d\omega}\right|_{\omega=\omega_m} \simeq \frac{U_{m-1} - U_{m+1}}{\Delta\omega} \qquad (6.2)$$

where U_{m+1} and U_{m-1} are discrete measurements at the frequency points either side of the peak frequency, and $\Delta\omega$ the frequency difference between these values. The half-space medium response $M_z(\omega)$ for underground explosions is $\alpha\ \omega^{3/2}$, (Appendix A.2). The source time action is uncertain (Section 2.2.5), however the behaviour is either a step or a delta function, implying that $S_T(\omega)$ lies between $1/\omega$ and a unit constant. As the finiteness effect is unimportant for these events, the source function $S(\omega) = S_o S_T(\omega) S_F(\omega)$ $M_z(\omega)$ can be represented by the power law function ω^q, where q is 1/2 or 3/2, and estimates of attenuation can be obtained using Equation 5.3. The simplified medium response appropriate to the underwater explosions is proportional to $\omega^{-\frac{1}{2}}$ (Appendix A.3). The spectrum of the source action $S_T(\omega) = S_b(\omega)S_r(\omega)$ is proportional to ω for measurements taken below the peak in the bubble spectrum (Section 2.3.3), this giving $S(\omega)\ \alpha\ \omega^{\frac{1}{2}}$. For measurements close to the natural frequencies of the source one must consider the specific form of $S(\omega)$ and obtain a Q_β^{-1} measurement from Equation 5.2. In this case the

gradient of the source function can be calculated using an identical formula to that of Equation 6.2. As it is difficult to choose the category to which the underwater explosion data belong, both approaches are used in the Q_β^{-1} calculations.

The Q_β^{-1} values corresponding to the peak frequencies of the underwater and underground explosion spectra are shown in Figure 6.7b. They are calculated using the two possible source functions for the underground explosions, and both the power law and full source functions for N1 and N2 which are described in Section 6.2.2. Using the delta function source for the underground explosions gives a Q_β^{-1} ranging from 0.05 at distances close to the shot, down to 0.01 at a distance of 50km. Q_β^{-1} also decreases with distance for the step function case, but the values are smaller by a factor of 3. The higher Q_β^{-1} solutions and hence the delta function source are favoured, these being more in agreement with previous measurements of upper crustal Q_β^{-1}. There is a rapid decrease of Q_β^{-1} with distance for the underwater explosions - this is expected because of the constant peak frequencies. The Q_β^{-1} values for the power law source function range from 0.01 to 0.08, with the highest values at the closest stations. Realistic bubble pulse models for N1 and N2 give higher values, ranging from 0.02 to 0.1.

Using the peak frequency results it is not possible to detect differences in attenuation along various paths as these are totally obscured by the distinct decrease of Q_β^{-1} with distance. However, the measurements do provide a rough order of magnitude ($\simeq$0.02) for the specific attenuation Q_β^{-1} of the region, and suggest a delta-like source time action for the underground explosions. The results are more reliable for underground explosions than for underwater explosions.

6.2.5 Application of Single-Station Attenuation Methods

6.2.5a Introduction

In this section the underwater explosion and underground explosion spectra are analysed according to the single-station attenuation scheme described in Chapter 5. Following this method, the observed spectra for the explosion sources are smoothed and then corrected for the medium response $M_Z(\omega)$ and the instrument distortion. The underwater explosion medium response corresponds to a semi-infinite fluid overlying a half-space (Appendix A.3), whereas the medium response for the underground explosions is chosen on two levels of approximation:- the response of a half-space medium (Appendix A.2) and a multi-layered source medium. The basic multi-layered medium response is computed using the shear velocity model for the Dalradian province which was shown in Figure 6.1b. To take account of transmission across the boundaries between geological formations, the response function is multiplied by the appropriate transmission coefficient for each boundary crossed along the path. This is unnecessary for the Rayleigh waves generated by the underwater explosions as the paths are entirely within the northern Moine province.

As an indication of the possible effect of using a half-space medium response instead of a multi-layered medium response for the underground explosions on the single-station measurements, the source function $S_T(\omega)$ is combined separately with these responses in the Figures 6.8. The spectrum of an exponential step was chosen in Chapter 2 to represent $S_T(\omega)$. An inverse time constant of $8 rad^{-1}$ is calculated from O'Brien (1967b) assuming cube root scaling. The corresponding source function $S_T(\omega)$ and the medium responses are shown

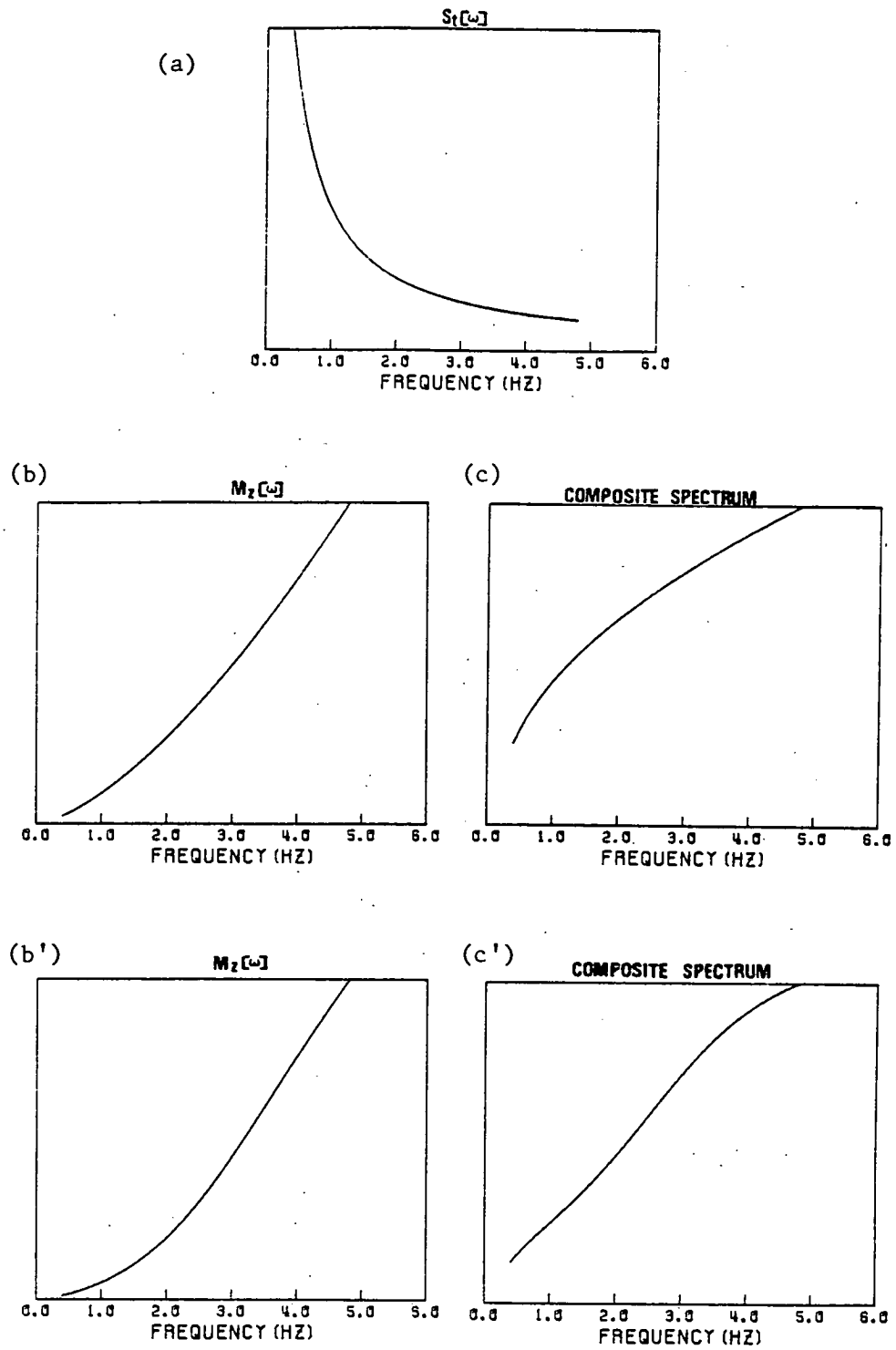

Figure 6.8. Comparison of the different theoretical spectra obtained using a half-space and a multi-layered medium response. All the functions are normalized with respect to their maximum amplitude in the frequency range 0.4 - 4.8 Hz.

(a) spectrum of source time action $S_T(\omega)$ estimated for underground explosions with an inverse time constant of .8 rad^{-1}.

(b) half-space medium response (β = 2.5 km/sec.)

(b') multi-layered medium response $M_z(\omega)$ corresponding to the Dalradian province model of Figure 6.1b.

(c), (c') composite spectrum $S_T(\omega)\ M_z(\omega)$.

in Figures 6.8a, 6.8b and 6.8b' respectively. The composite spectra $S_T(\omega)M_z(\omega)$ are displayed in Figures 6.8c and c'. The source spectrum for the half-space case has a smaller low frequency content, whilst both functions are similar at high frequencies. We therefore expect the difference between the single-station solutions to lie in the attenuation properties of the deeper layers.

The corrected spectra are specified by the source strength, spectrum of the source time action and the attenuation function. The latter is not only a function of the Q_β^{-1} depth distribution, but also of the velocity structure of the propagation path via the frequency dependent weights which describe the relative effect of each Q_β^{-1} value in a layered model on the amplitude spectrum. These are related to the partial derivatives of the Rayleigh wavenumber k(w) with respect to body wave velocity (Equation 1.9). k(w) is readily computed for each geological province using the theory of Schwab and Knopoff (1972) and the multi-layered models of Figure 6.1b, and the derivatives are calculated using first order differences. However, all the Q_β^{-1} depth models used in this analysis consist of only three layers, compared to the many layers of the velocity models. To obtain weights corresponding to each Q_β^{-1} of the three layered model, we use the property that the weighting functions between adjacent layers of a particular velocity model can be summed if the same value of Q_β^{-1} is used for these two layers. This process is repeated until only three weighting functions remain. The layers are combined with regard to the objective that each Q_β^{-1} influences discrete portions of the data to similar extents, this corresponding to equal resolution of all three values.

To correct for the change from one velocity profile to another along the paths from the underground explosions, the layers in the

adjacent velocity models are first reduced using the technique described above, with the aim in this case, of obtaining layers at coincident depths in each three layered model. If these requirements are met, the velocity models can now be amalgamated by averaging the weighting functions over each corresponding layer. The relative contribution of a particular profile to the overall average is related to the proportion of the total path which crosses the province. This method has a disadvantage in that the restrictions imposed on the possible combinations of the layers limits the potential resolution capability of each Q_β^{-1} value. Two typical sets of specific attenuation weighting functions for stations B6 and A59 are shown in Figure 6.9.

Noise samples of approximately similar duration to the Rayleigh waves are extracted from portions of the record at stations A12, A47, and A52 on the ALPHA line just before the arrival of the body waves. The restriction to stations along the ALPHA line is due to the difficulty in obtaining noise of sufficient duration at the other stations, as the data had been trimmed either side of the body and surface waves to reduce storage space on magnetic tape. The noise spectra are shown in Figure 6.10a for the approximate frequency range 0.5 - 5.0 Hz. The average ambient level is about 0.025 microns-sec, however to account for variations above the mean amplitude the level is chosen as 0.04 microns-sec. To calculate the standard deviations on the amplitude spectra we use the theory of Section 5.4.4 which takes account of noise and scattering from lateral inhomogeneities. A typical set of errors combining these effects are shown in Figure 6.10b for stations B4 and B14. These diagrams demonstrate the increase in the pseudo-standard deviations with distance and frequency, which is expected of observed errors on the spectra.

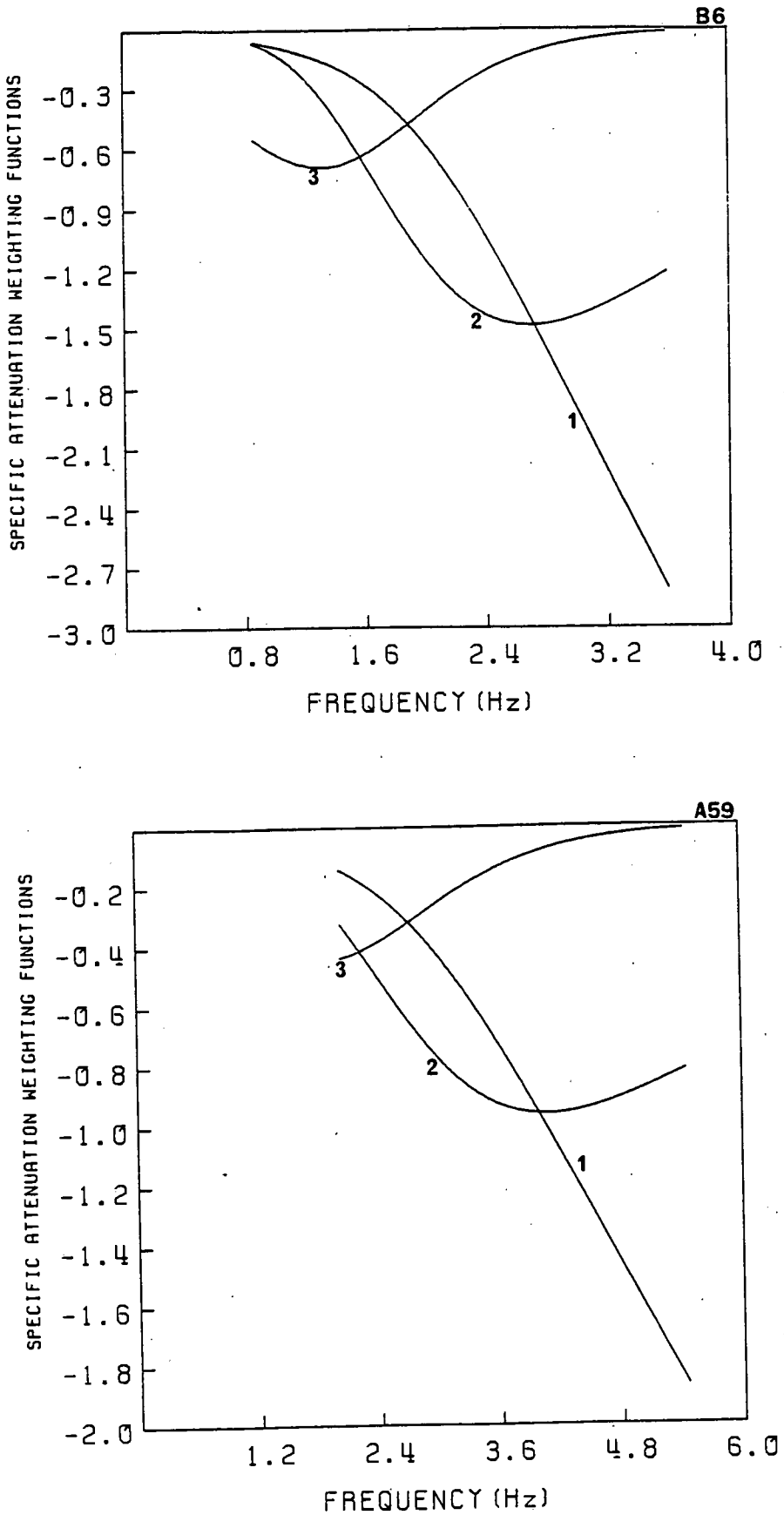

Figure 6.9. Shear wave specific attenuation weighting functions versus frequency for the Q_β^{-1} values in a three layered anelastic model corresponding to paths to stations B6 and A59. 1, 2 and 3 refer to top, middle and half-space layers of the model.

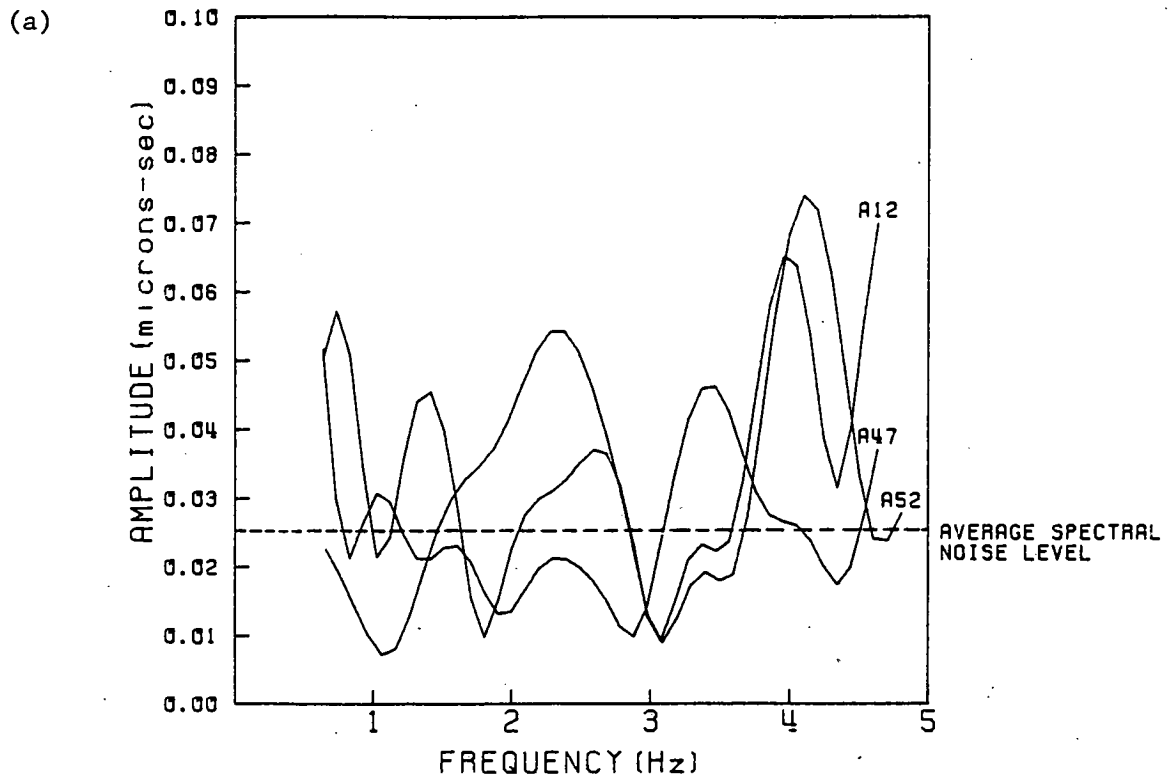

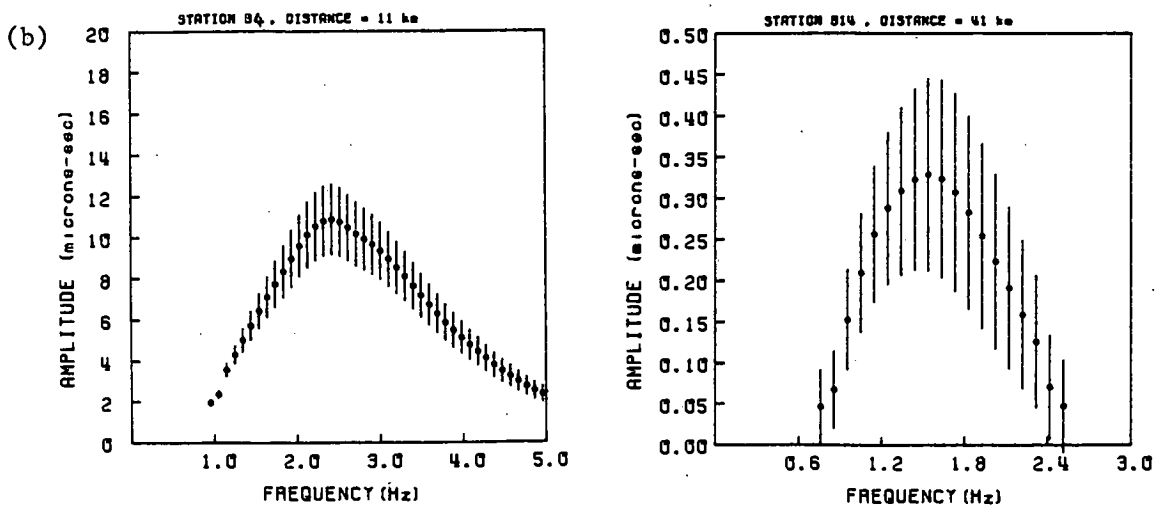

Figure 6.10. (a) Amplitude spectra of noise samples from stations A12, A47 and A52 on the ALPHA line.

(b) Estimated standard deviations, allowing for both noise and lateral inhomogeneities, corresponding to stations B4 and B14 on the LISPB line. Notice the increase of the standard deviations with distance and frequency.

6.2.5b FOB Inversion of Underground Explosion Spectra

Having corrected for the medium response, transmission coefficients, instrument distortion, and computed the specific attenuation weighting functions, the remaining spectral parameters of source strength factor, inverse time constant, and the specific Q_β^{-1} values now completely specify the amplitude at each frequency (Equation 5.7). For every station there are two spectra, corresponding to correction by the half-space and multi-layered medium response. The FOB inversion technique is now applied to each set of spectral data. In this procedure, the inverse time constant ω_T is increased from 0 to 240 rad^{-1} in steps of 2.4 rad^{-1} (the source action is like a step or delta function at the extremes). For each value of ω_T the spectrum is divided by $S_T(\omega)$, and estimates of S_o and the Q_β^{-1} depth distribution which produce a good fit between the theoretical curve and the corrected observations are computed. Consequently χ^2_{FOB} is obtained as a function of the inverse time constant for each station along the array. Curves of χ^2_{FOB} versus ω_T for two typical stations A58 and B4 are shown in Figure 6.11. The spectra at both stations corrected for the corresponding multi-layered medium response are fitted better than those corrected for the half-space medium response model. The value of χ^2_{FOB} decreases sharply with ω_T up to 25 rad^{-1}, at which point the function becomes roughly constant. The closest stations display a shallow minimum at this corner, but this becomes less pronounced with increasing distance (degradation of source information). The average inverse time constant at which this occurs, for amplitudes corrected by the multi-layered medium response, is 25 ± 8 rad^{-1} for the ALPHA line, and 23 ± 5 rad^{-1} for the BETA line. The explosion L1 is therefore not statistically different from L2 and we can assume a common source

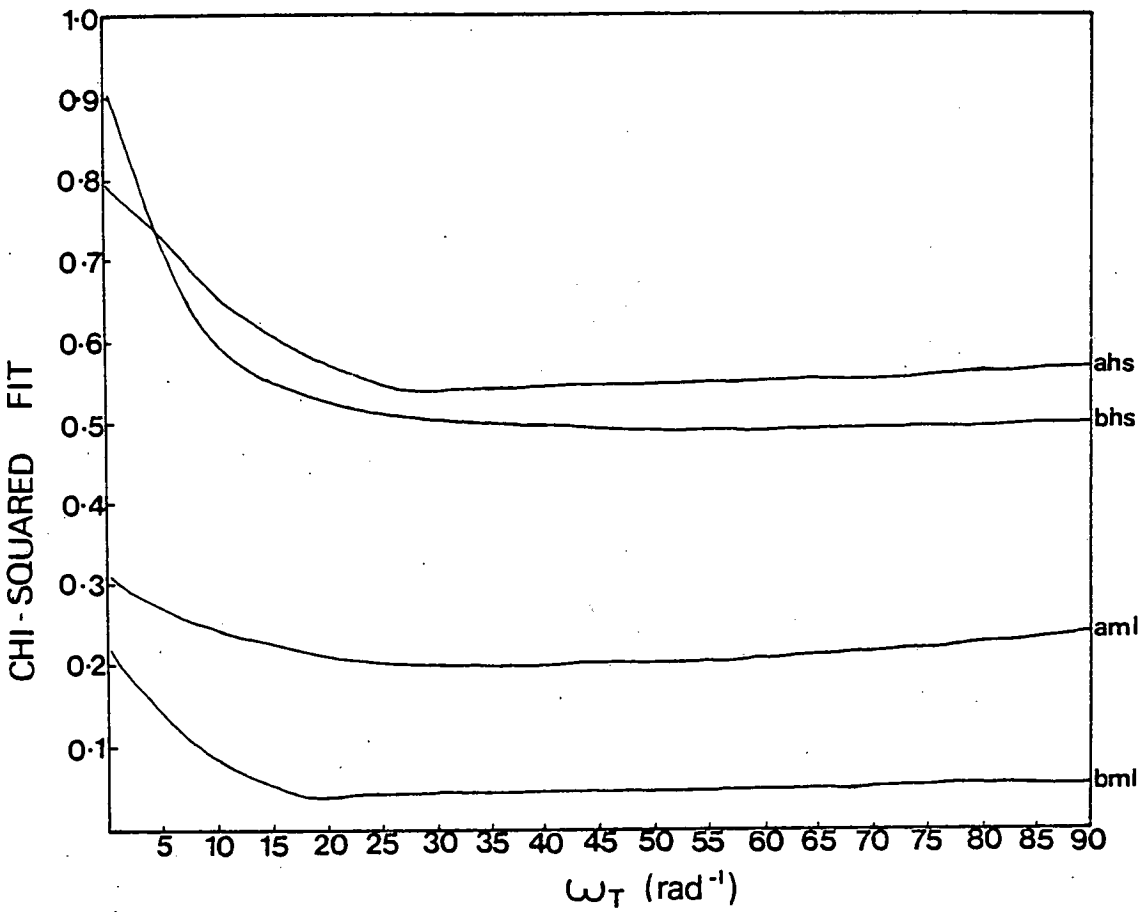

ahs	half-space source medium model	– station A58
aml	multi-layered source medium model	
bhs	half-space source medium model	– station B4
bml	multi-layered source medium model	

Figure 6.11. χ^2-fit functions versus inverse time constant ω_T for typical stations B4 and A58 recording the LISPB underground explosions.

function with an inverse time constant of 24 rad^{-1} (which is predominantly Dirac impulsive, being consistent with the conclusions of the peak frequency analysis). The shallow minima reflect the extent to which ω_T can be resolved. The corners/minima are much more scattered for the data corrected by the half-space medium response.

Proceeding with the second step in the FOB inversion, the spectra are corrected again for the source function $S_T(\omega)$ corresponding to the optimum inverse time constant of 24 rad^{-1}. The bounds on the source strength and the shear wave specific attenuation (which correspond to the errors on the spectral amplitude at each station) are now computed for the spectra which have been corrected by the multi-layered medium response. Statistically, the solution bounds represent the range of possible parameter values for which the difference between the theoretical and observed points is insignificant, at a particular level of confidence. For a confidence level of C%, the computed standard deviations are multiplied by the Student's t-value $t(C,\nu)$, where ν is the number of degrees of freedom.

The solution bounds for two or three stations on the ALPHA line cannot be computed unless the observed spectral errors are substantially increased, this being due to the difficulty in modelling either the sharp low frequency drop-off or very gentle high frequency slope. To obtain bounds for the stations at which this occurs, several outlying points are excluded from the low frequency or high frequency end of the spectrum, and the parameter estimates are re-computed. For many other stations in this line the bounds on the Q_β^{-1} solutions are very small. It is difficult to obtain a uniform representation of the confidence bounds on the estimated Q_β^{-1} values for the spectra observed along the ALPHA and the BETA lines. Using the same trend in the

computed standard deviations for the BETA line, the Q_β^{-1} bounds are found to be effectively unresolved (filling the full range of Q_β^{-1}), and it was necessary to reduce the errors by a factor of 0.674, corresponding to a pseudo-50% confidence level. The limits for the ALPHA line correspond to a confidence level of 66%. This demonstrates the quality of the data recorded along the BETA line compared to that for the ALPHA line.

Complete inversion results for stations A53, B4, and B9 are shown in Figures 6.12, 6.13a and 6.13b. These display the derived Q_β^{-1} models and values of S_o with uncertainties corresponding to errors on the observations at the confidence levels mentioned above, and also the match between the observed and theoretical amplitude spectra (both corrected for instrument; the theoretical spectrum including the effects of transmission between geological structures). The complete theoretical spectra corresponding to the half-space and multi-layered medium responses are shown for comparison. It is particularly noticeable that the theoretical curve assembled with the half-space response often lies outside the error envelope on the observations (see Figure 6.13a). The bounds on the Q_β^{-1} values occasionally fill the full range (being effectively unresolved at this confidence level on the observations) for the deep layers. During the inversions it is found that at several stations two or all of the Q_β^{-1} estimates are equal to either the upper or lower limits set on the parameter. This is related to a distortion of the spectral shape by some effect other than attenuation. The problem is circumvented by successively reducing the number of layers in the Q_β^{-1} model and re-inverting until specific attenuation values that lie between the physical boundaries are obtained. Under the worst circumstances a half-space Q_β^{-1} value

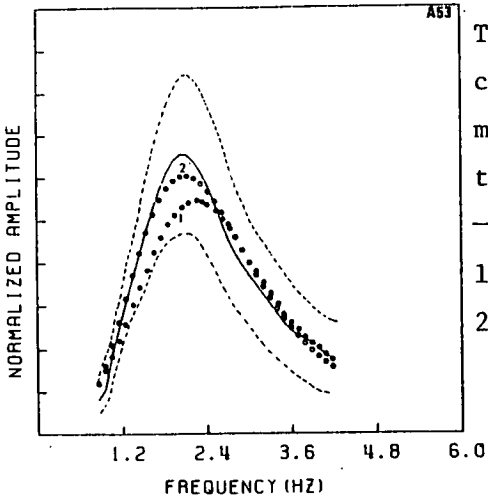

The fit between observed amplitude spectrum and theoretical spectrum (both corrected for instrument response) corresponding to optimum values of Q_β^{-1} model and S_o from the FOB inversion. The theoretical spectrum includes the transmission coefficients between provinces

——— observed spectrum ----- estimated errors on observed spectrum.

1 - theoretical spectrum assembled using half-space medium response

2 - theoretical spectrum assembled using multi-layered velocity model of Dalradian province (see Figure 6.1b).

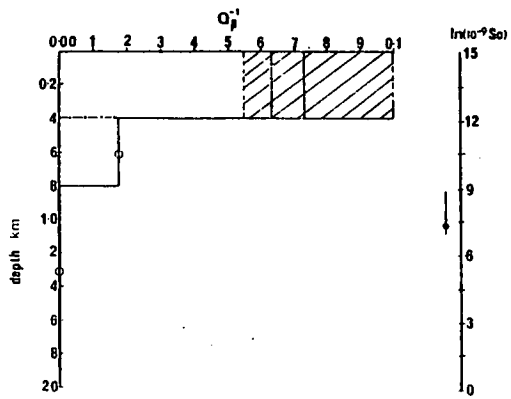

Optimum Q_β^{-1} and S_o solutions with bounds corresponding to the pseudo-standard deviations on the observations.

——— optimum Q_β^{-1} model corresponding to the multi-layered medium response.

----- bounds on Q_β^{-1} model corresponding to estimated errors in observed spectrum

-·-·- optimum Q_β^{-1} model corresponding to the half-space medium response

O - unresolved solution

Figure 6.12. Single-station Q_β^{-1} and S_o solutions obtained using the FOB inversion technique and the corresponding fit between theory and observations for the spectrum at station A53.

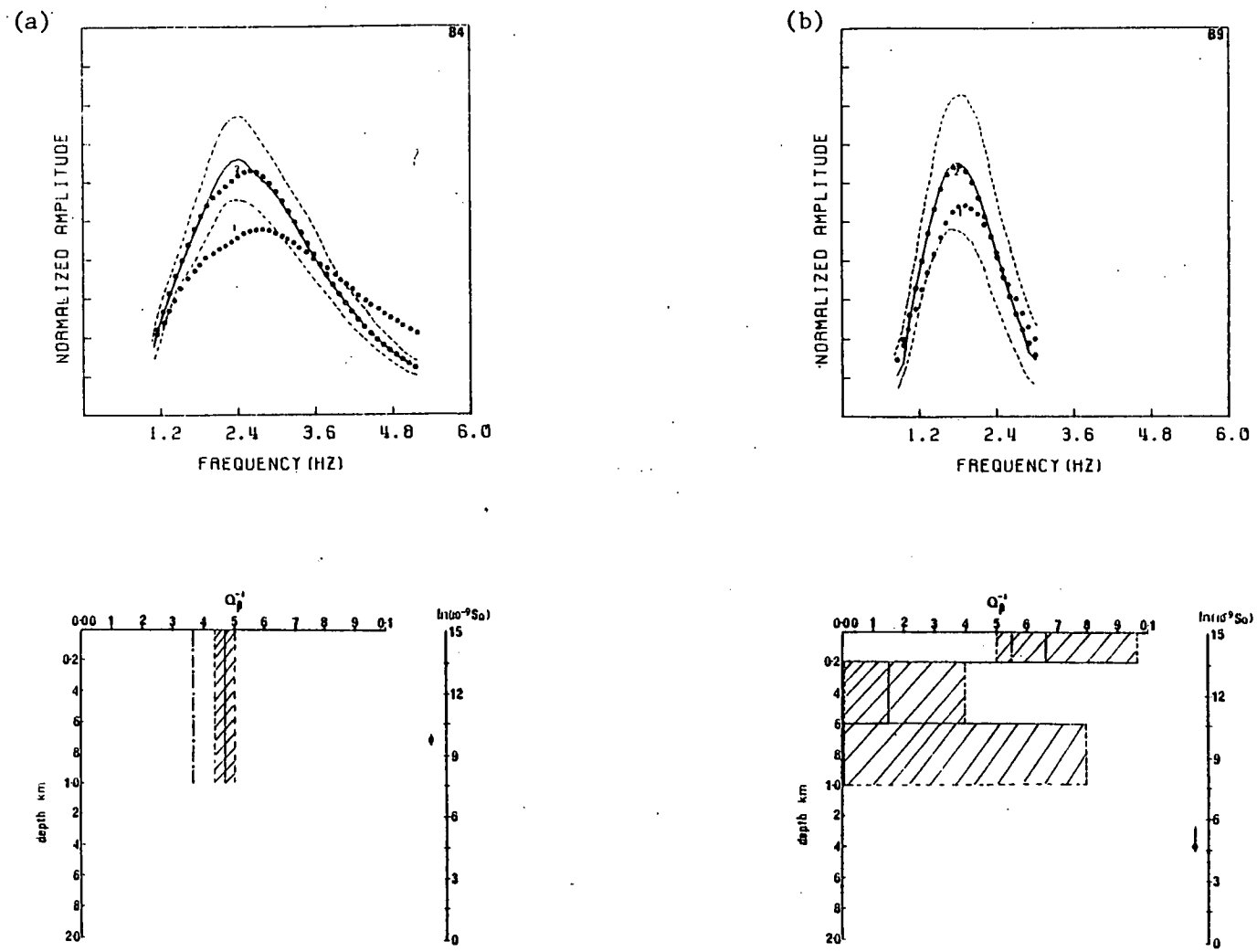

Figure 6.13. Single-station Q_β^{-1} and S_o solutions obtained using the FOB inversion technique and the corresponding fit between theory and observations for the spectra at stations B4 and B9 (see Figure 6.12 for details). The bounds for these solutions correspond to the pseudo-standard deviations on the observations multiplied by a factor of 0.674.

could still be obtained, effectively giving an average in the upper 1km of the crust (Figure 6.13a). The bounds on the specific attenuation value are very narrow in this case as we have reduced the number of parameters with which we are modelling the spectrum.

Q_β^{-1} solutions with corresponding error bounds for all the stations along the ALPHA and BETA lines are shown in Figure 6.14. As the layering in the attenuation models along each segment of the station line does not match, the crust is split into five different depth ranges down to the limit of penetration so that the profiles can be uniformly presented. The limit of penetration depends on the frequency range and wave velocities at each station, but is typically between 1 - 2 km. The mutually consistent Q_β^{-1} values of the BETA line (with a mean of 0.045 in the top layer) contrast with the generally higher and scattered values from the ALPHA line (ranging from 0.02 to 0.09 in the top layer), along which the parameter uncertainties vary considerably. The uncertainties on the Q_β^{-1} values in the top layer of the models generally increase with distance from the explosion, corresponding to the decrease in signal-to-noise. The effect is particularly noticeable at the stations A47 and A48A, for which the Q_β^{-1} values in the top layer are unresolved for a 66% confidence level on the observations. There is also a decrease in the resolution of Q_β^{-1} with depth, especially for the BETA line, and this trend implies that only attenuation in the top 400m of the crust can be accurately resolved by the single-station technique at these frequencies and these particular confidence levels on the observations.

Each Q_β^{-1} value in Figure 6.14 represents an average of the Q_β^{-1} depth distribution between event and station. Each successive point corresponds to the average dissipation along the path from the event to the preceding station and the extra path to this station. Therefore

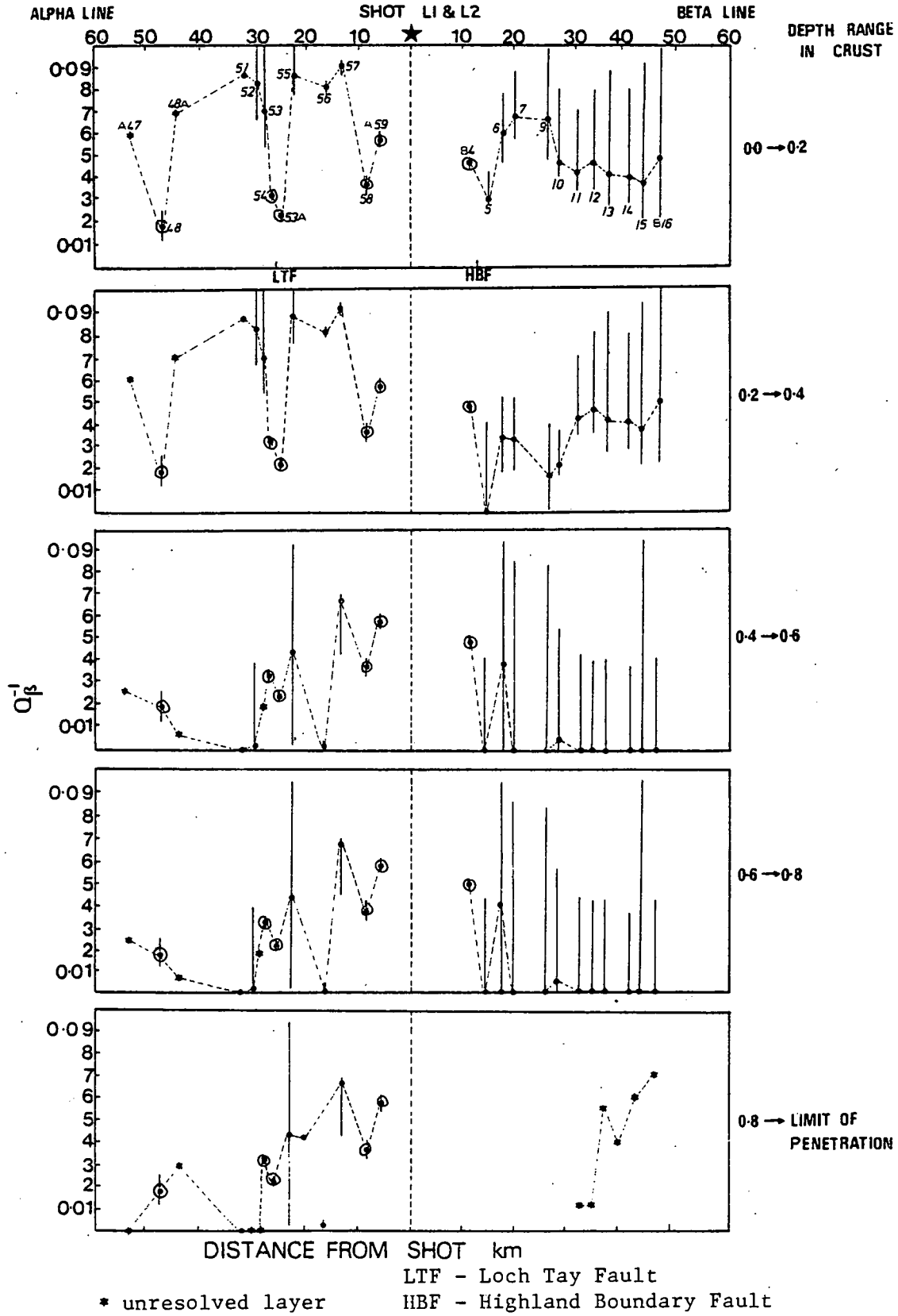

Figure 6.14. Q_β^{-1} values and bounds inferred for a variety of different depths within the crust from three layered single-station profiles. These are obtained by analysing the spectra derived from recordings of the underground explosions L1 and L2 along the LISPB line using the FOB inversion technique. The bounds on the Q_β^{-1} values for the BETA line correspond to the pseudo-standard deviations on the observations multiplied by a factor of 0.674.

⊙ Q_β^{-1} values which are more unreliable than others as they correspond to an attenuation half-space

the Q_β^{-1} values should fluctuate very slowly from station to station within the computed uncertainties. In this respect the stations A58, A59, A53A, A48, B4 and B5 imply a rapid increase or decrease of Q_β^{-1}, these values being incompatible with an average of Q_β^{-1} over the provinces. A physical explanation for such rapid fluctuations is not apparent.

The source strength values with corresponding uncertainties are shown in Figure 6.15. The solutions are approximately constant (within the error bounds) over the Moine, Dalradian and Devonian Lava provinces, with the lowest values being in the Old Red Sandstone (corresponding to a slight increase in the top layer Q_β^{-1} of the profiles). Stations A58, A59, and B4 display inconsistently large amplitudes. The Loch Tay fault appears to have no effect on the source strength factor. Averaging S_o over all the stations gives a value of 10^{12} N m. Using Equation 2.5 and taking the cavity radius of the explosion as 2m gives a theoretical estimate of the same order of magnitude.

The source strength values for the half-space attenuation solutions tend to be large, and the Q_β^{-1} values and the error bounds small - this is exemplified at station A53A. Evans (1981) notes that the seismogram amplitude at this station is very much reduced due to destructive interference at the Loch Tay fault. However our analysis does not show the effects of this scattering. In contrast, the instrument drop-off at station A51 is shown in the plot of the S_o values. In this case, the single-station method is successful in obtaining a Q_β^{-1} model, implying that this malfunction influenced only the absolute amplitude of the record.

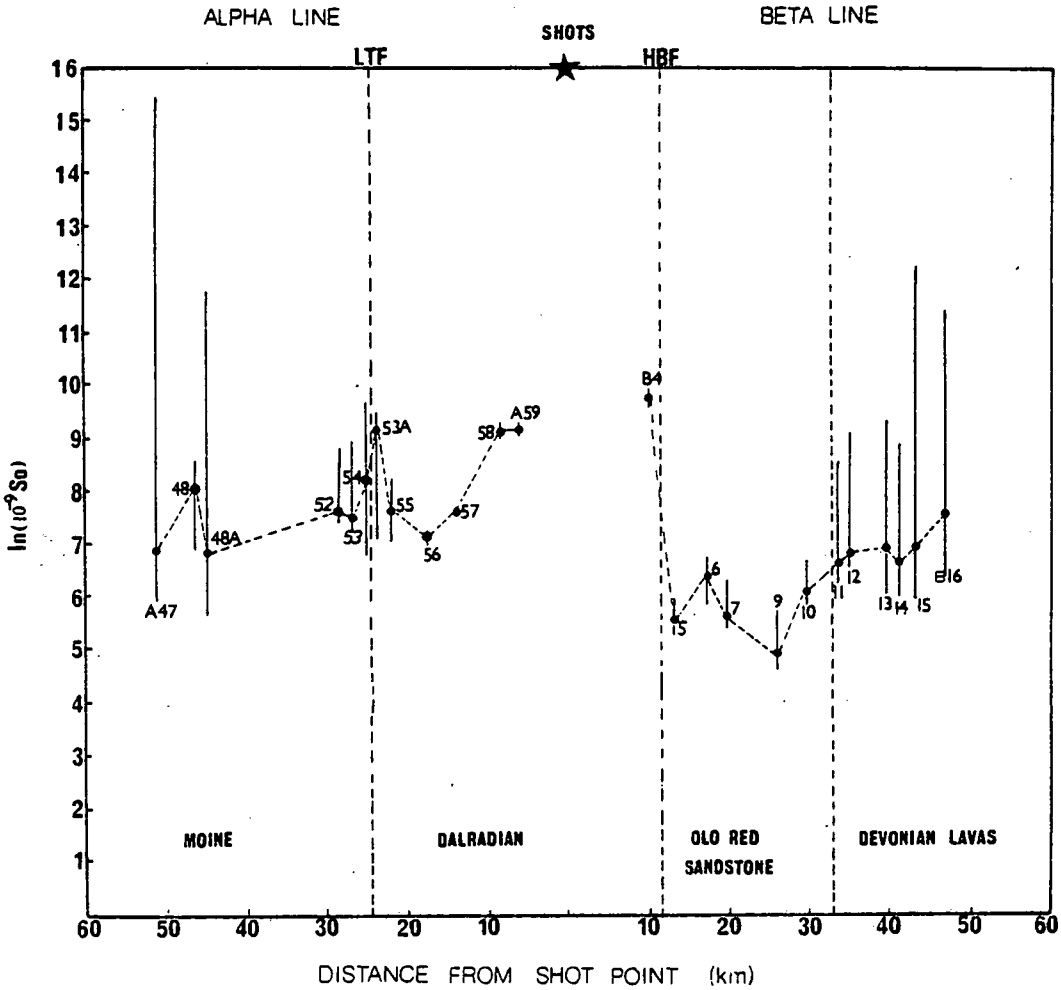

LTF - Loch Tay Fault HBF - Highland Boundary Fault

Figure 6.15. Source strength factor S_o and bounds corresponding to the spectral amplitudes and calculated errors, derived from the LISPB recordings of underground explosions L1 and L2 using the FOB inversion technique. The bounds on the S_o values for the BETA line correspond to the pseudo-standard deviations on the observations reduced by a factor of 0.674.

6.2.5c FOB Inversion of Underwater Explosion Spectra

The corrected underwater explosion spectra are parameterized by shot depth, water thickness, source strength and the Q_β^{-1} values. The thickness of the water layer is fixed at 115m for shot N1. The shot depth and water thickness are set equal for the bottom-fired N2. The explosions are analysed using a grid of the source depths in the range 1.0 - 500m taken in steps of 5m, and for source models consisting of the shock wave alone, then one, and finally two bubble pulses. The results for both shots give optimum source depths between 150 and 250m. Moreover, the Q_β^{-1} models are unrealistic and have values of less than 0.001. The spectral model we are using cannot match the shape of the observations with physically reasonable values for the spectral parameters. For this reason the underwater explosions are not considered further, and excluded from the Hedgehog inversion below.

6.2.5d Hedgehog Inversion of Underground Explosion Data

In this section the inversion of the corrected underground explosion spectra is re-considered using the Hedgehog technique. The source spectral function used above, which changes slowly between the spectrum for an impulse and a step is impracticable for a Hedgehog inversion as it generates too many solutions. We therefore choose a simple source which can switch between the two extremes

$$S_T(\omega;i) = \delta_{1i} + \frac{\delta_{2i}}{\omega} \qquad (6.3)$$

where $\delta_{ki} = 1$ for $i = k$, $\delta_{ki} = 0$ for $i \neq k$, and $i = 1,2$. A grid of Q_β^{-1} values is selected in the range $0.0 \leq Q_\beta^{-1} \leq 0.1$ for each layer, with a uniform spacing of 0.005. The maximum χ_ν^2 is set at 0.12 for the BETA line and 0.60 for the ALPHA line corresponding to a greater than 99%, and 98% confidence level respectively. Again, the computed standard deviations on the spectra from the BETA line must be reduced by a factor of 0.674, implying the envelope test of Equation 5.10 is performed at a 50% confidence level.

It is apparent on a cumulative basis that the number of Hedgehog solutions for the delta source outweigh those for the step, although the step-like source function is preferred for the closer stations. In fact only a step function fits the closest station A59 on the ALPHA line. This situation quickly changes for distances greater than 15km, and the delta function then becomes the better model. A58 has an equal number of solutions from both types of source, and A54 gives a purely delta-type source. This will be discussed further in Chapter 7.

The solution with the lowest χ_ν^2 is selected for each station to represent the best estimate, and this is plotted with the bounds on each Q_β^{-1}, obtained as the width of the Hedgehog regions, in Figure 6.16. The results compare closely with the solutions for the FOB inversion despite the different assumptions used in each procedure. There are no Hedgehog solutions for stations A57, A53A or A51 as the constraint of a pure step or delta function source is too restrictive in these cases.

The inversion profiles produced by the FOB and Hedgehog inversion technique indicate a high specific attenuation Q_β^{-1} value with a mean of about 0.05 in the upper 200m of the crust in Scotland. There is a decrease in Q_β^{-1} between the depths of 200-400m (particularly for

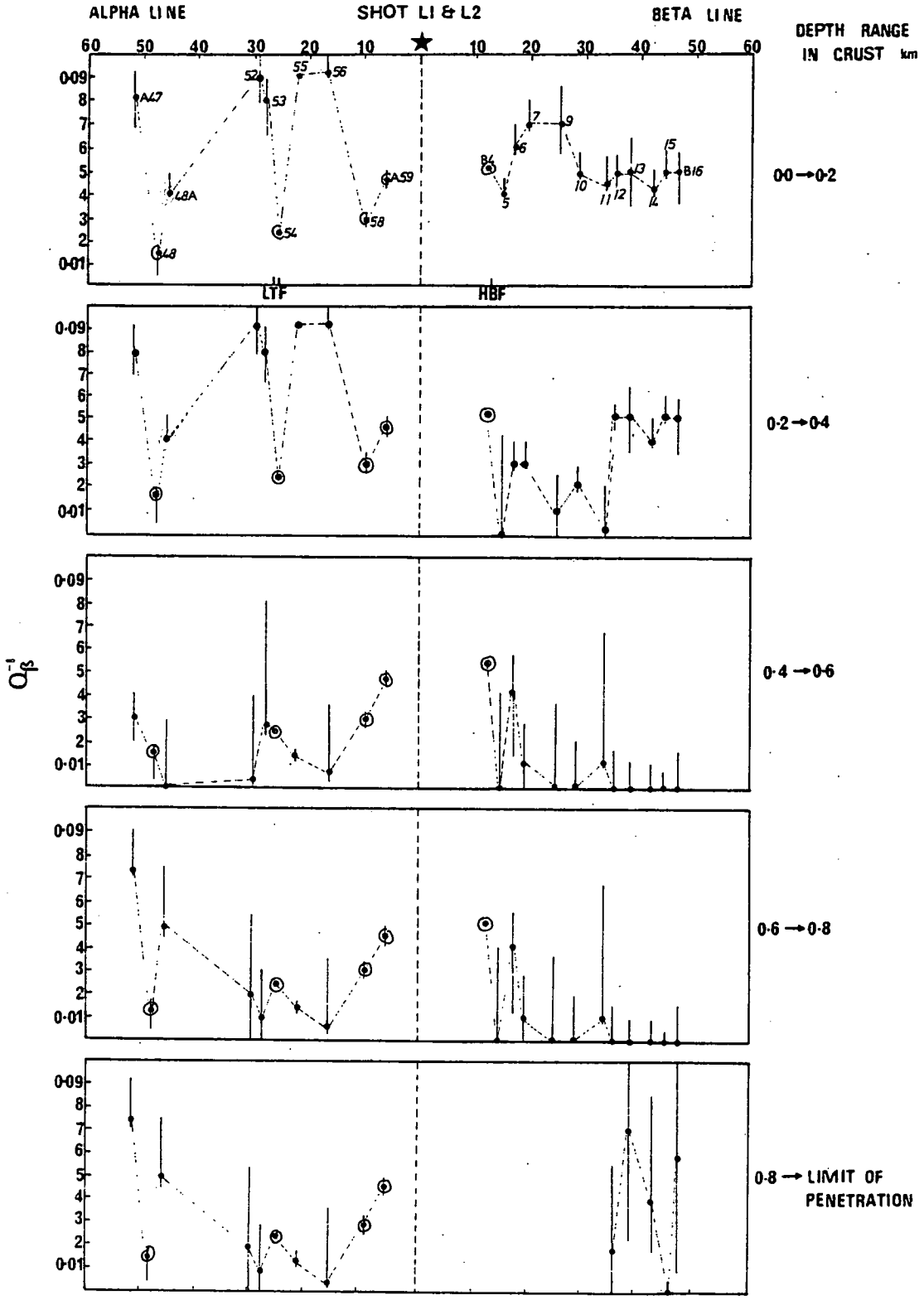

Figure 6.16. Single-station Q_β^{-1} solutions for stations along the ALPHA and BETA line using the Hedgehog inversion procedure. The diagram is interpreted in a similar fashion to Figure 6.14. The bounds on the Q_β^{-1} values for the BETA line correspond to the pseudo-standard deviations on the observations reduced by a factor of 0.674.

⊙ Q_β^{-1} values which are more reliable than others as they correspond to an attenuation half-space.

stations B4 - B11 which are mainly in the Old Red Sandstone), and between 400m and 800m Q_β^{-1} is less than 0.01. Below 800m Q_β^{-1} increases again to around a mean of 0.04. The Q_β^{-1} distribution with depth shows the same general trend as the pure provincial profiles obtained by Evans (1981).

6.2.5e Comparison of Single-Station Results with Station-averaged Results

An attenuation coefficient for each station is computed using the Q_β^{-1} depth models obtained from the single-station methods above and using Equation 1.9. These are compared with the two available pure provincial attenuation coefficients, corresponding to the Dalradian and Old Red Sandstone formations, in Figure 6.17. Each single-station value represents an average of the attenuation over the provinces through which the waves have propagated; this is expressed mathematically in Equation 1.19. Accordingly, if the dissipative properties of the Rayleigh waves are sensitive to the surface geology the attenuation coefficients for the stations along the ALPHA line should lie between the coefficients for the Dalradian and Moine provinces, and similarly the BETA line values should lie between those for the Old Red Sandstone and Devonian Lavas. In the absence of station-averaged Q_β^{-1} models for the Moine and Devonian Lava provinces, the comparison is not complete. However Figure 6.17 can be used to obtain an indication of whether the measurements are consistent with the station-averaged attenuation coefficients for the upper crust in Scotland. The single-station curves fall between the two pure provincial attenuation coefficient curves, but tend to cluster closer

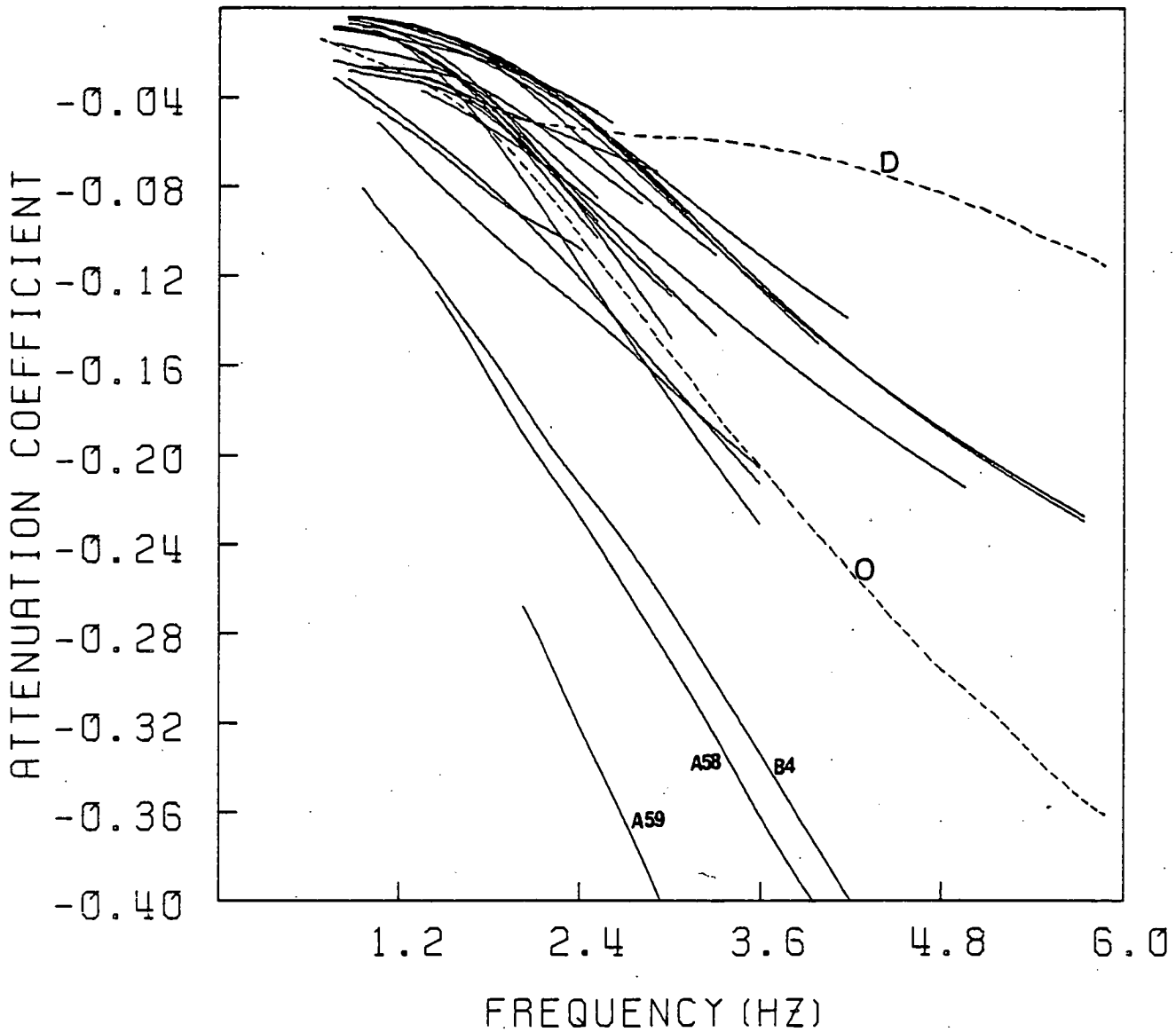

D Dalradian

O Old Red Sandstone

Figure 6.17. Single-station attenuation coefficients compared with provincial attenuation coefficients derived from Evans (1981) for the Dalradian and Old Red Sandstone formations.

to the curve for the old Red Sandstone. There are three outliers not conforming to this, corresponding to stations A59, A58, and B4. These also produce the inconsistent values of Q_β^{-1} and S_o above.

6.3 Underwater Explosions in Kirkcaldy Bay Recorded on the LOWNET Array

6.3.1 Source Effects

Calculations based on Equations 2.7 and 2.8 show that the bubble of gaseous explosion by-products from the Kirkcaldy Bay shots rises to the surface by a vertical distance of 8m in the time interval between the shock wave and first expected bubble pulse, this being slightly greater than the maximum bubble radius of 7m. As mentioned in Section 2.3.1, these migration effects imply that the bubble spectrum of the source is dominated by the shock wave and the ensuing negative pressure. This is further ensured as the charge is fired on the sea-bottom which reduces any primary bubble contributions. The bubble spectrum $S_b(\omega)$ for this case (Figure 6.18a) has an initial linear increase but tends to a constant value at higher frequencies, with a slight oscillation about this value. For comparison, the spectra for one bubble pulse and two bubble pulses are shown in Figures 6.18 a' and a", and they possess deep oscillations. The first peak for the spectrum corresponding to one bubble pulse is slightly lower than the natural bubble frequency of 1.67Hz.

The thickness of the water layer at the source is about 1/10 of the minimum seismic wavelength. Therefore the reverberation response $S_r(\omega)$ (Figure 6.18b), which has a first harmonic at 19 Hz, may be

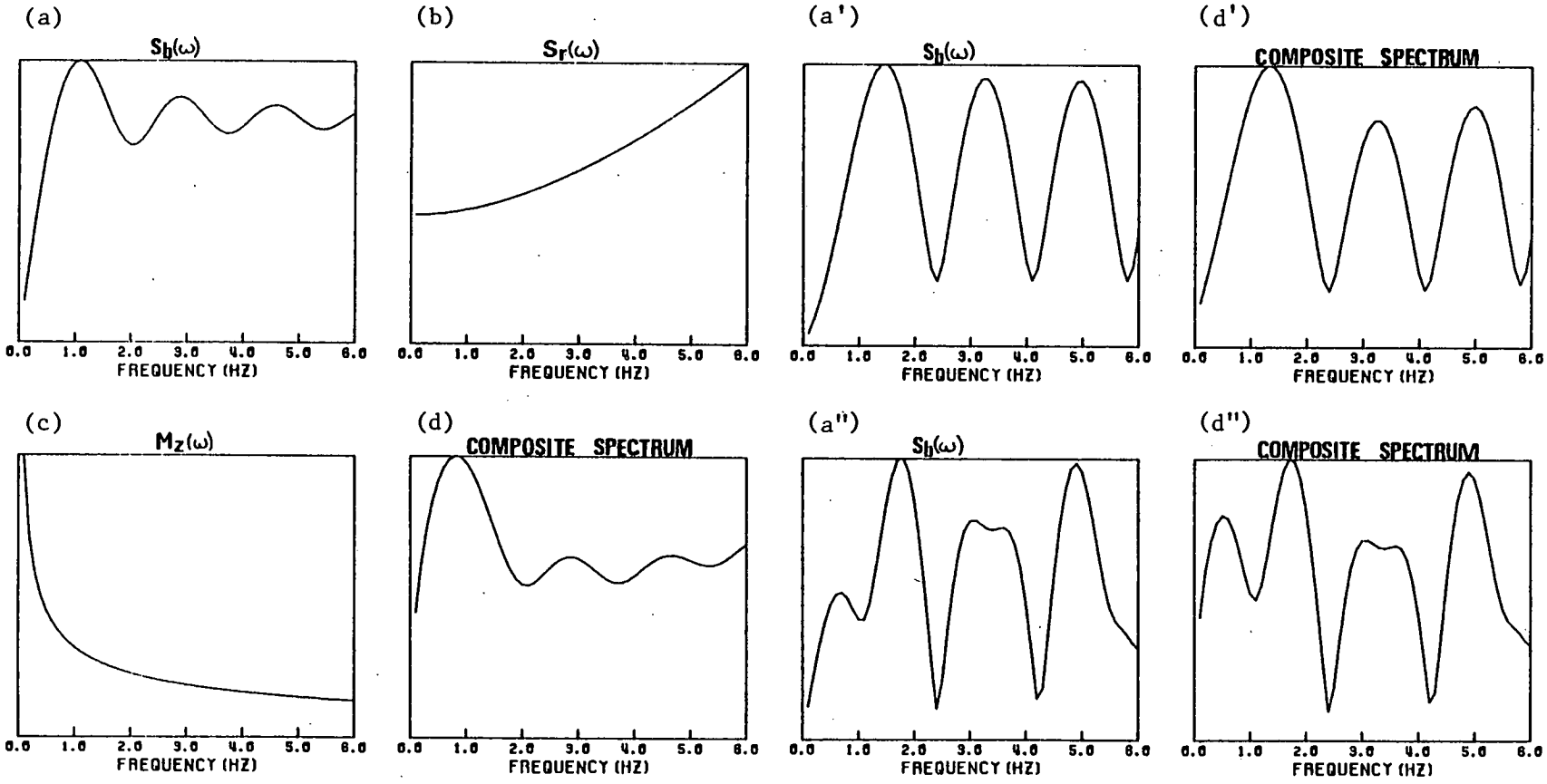

Figure 6.18. Functions which combine to form the complete unattenuated theoretical spectral shape from the Kirkcaldy Bay underwater explosions. All the functions are normalized with respect to their maximum amplitude in the frequency range 0.1 - 6.0 Hz.

(a),(a'),(a") spectrum of bubble oscillations for none, one and two bubble pulses.

(b) reverberation spectrum

(c) spectral medium response

(d),(d'),(d") composite spectrum $S_r(\omega)\ S_b(\omega)\ M_z(\omega)$ for the different bubble pulse models.

regarded as a constant. Due to the difficulties associated with defining the exact nature of the Rayleigh wave excitation, we do not attempt to model the source medium as a multi-layered half-space. Instead, we use the results of Appendix A.3 for the spectral response dilatational source in a fluid overlying a solid elastic half-space (Figure 6.18c). The composite spectra $S_b(\omega)S_r(\omega)M_z(\omega)$ for the source models corresponding to the shock wave alone, then one bubble pulse, and finally two bubble pulses, are shown in Figures 6.18d, d' and d" respectively.

6.3.2 Description of Observed Spectral Amplitudes

The amplitude spectra derived from recordings of the eight underwater explosions are averaged to produce one spectral curve at each station. This procedure increases the signal to noise ratio. Anomalously large or small spectra are subjectively rejected. The events and stations included in the averaging scheme are shown in Table 6.1. The instrument corrected and event - averaged amplitude spectra with the observed standard deviations are shown in Figures 6.19 - 6.20. The standard deviations are of comparable magnitude to those estimated for LISPB by taking account of the noise level and scattering from inhomogeneities. Thus, the results of Section 6.2 correspond to realistic errors on the spectra. The amplitudes are corrected for geometric spreading and displayed as a function of distance in Figure 6.21.

The spectra have a narrow band-width of between 0.6 - 1.7 Hz, the smallest being for the furthest station EAB. The peak frequencies are all approximately 1 Hz, thus showing an inconsistency with the notion

	1	2	3	4	5	6	7	8
EDI	D	D	D	-	D	D	D	D
EAU	-	D	D	D	D	-	D	D
EBH	D	-	D	-	D	D	-	-
EGL	-	D	D	D	D	-	D	D
EAB	D	D	-	D	D	D	-	D
EBL	N	D	-	-	D	D	D	N
EDU	D	D	-	D	D	D	N	-
ELO	D	N	N	D	D	D	D	D

D data used

\- data excluded

N no seismogram

Table 6.1 Events and stations used to compute the event-averaged amplitude spectra

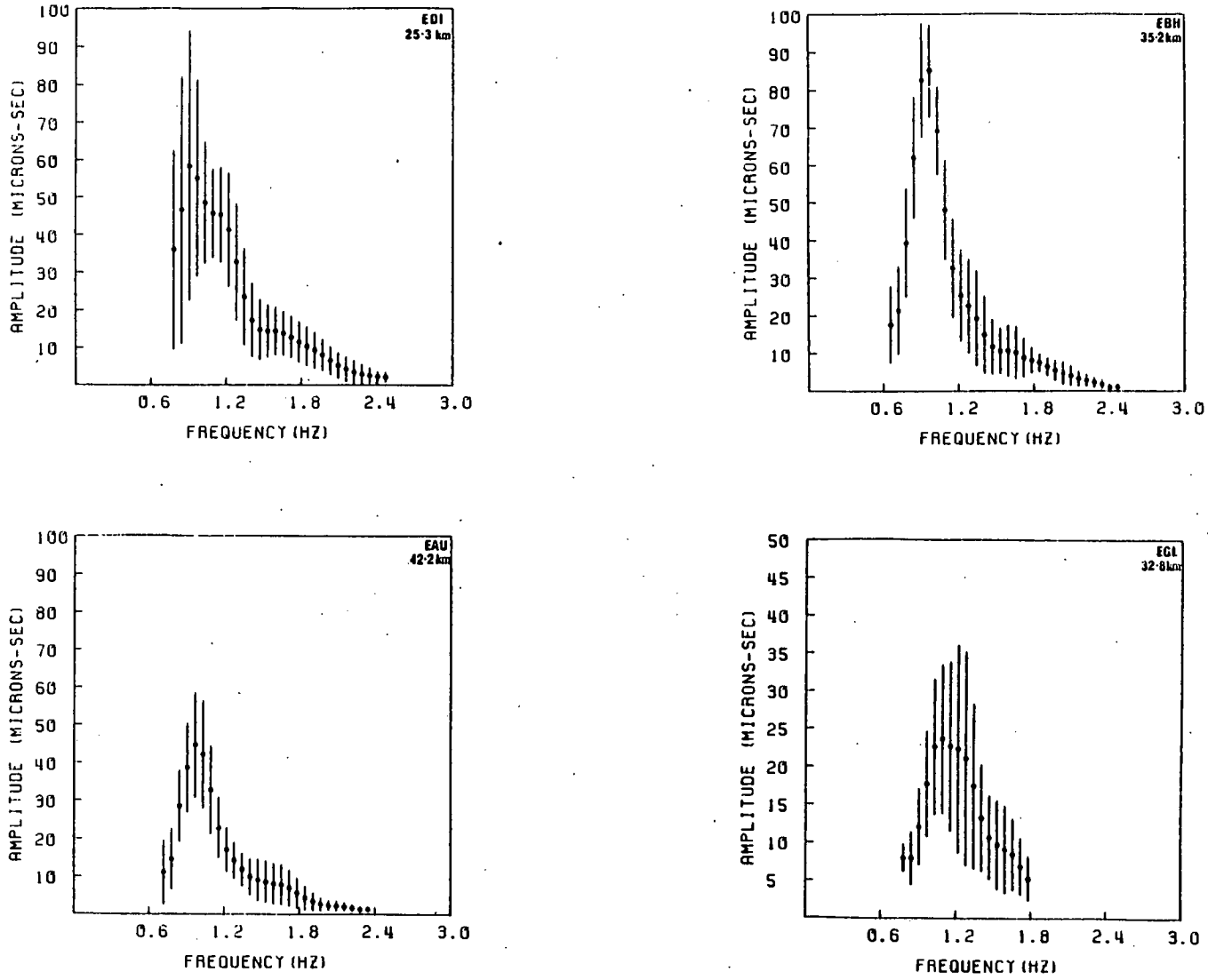

Figure 6.19. Event-averaged spectra and standard deviations for LOWNET stations EDI, EAU, EBH and EGL.

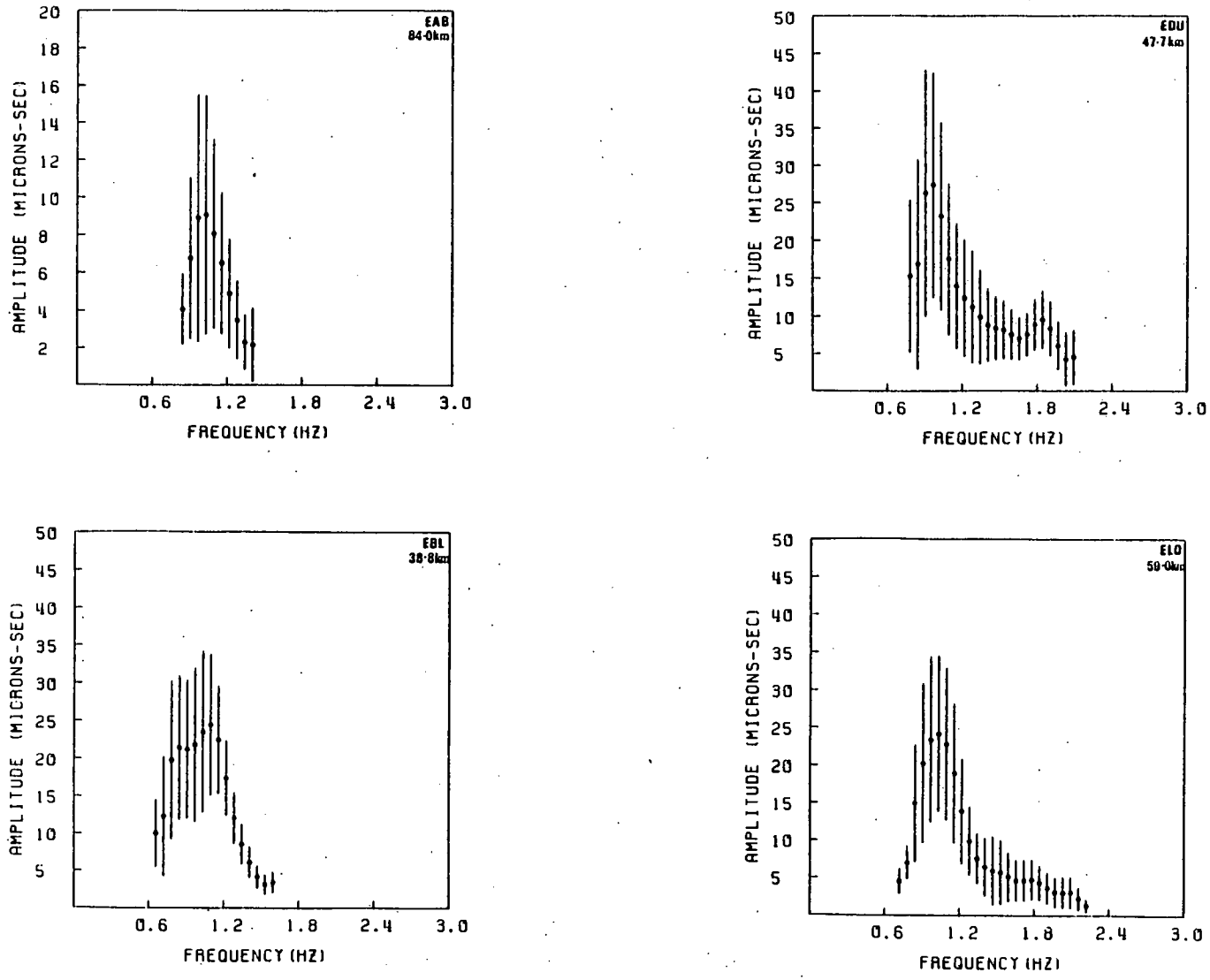

Figure 6.20. Event-averaged spectra and standard deviations for LOWNET stations EAB, EBL, EDU and ELO.

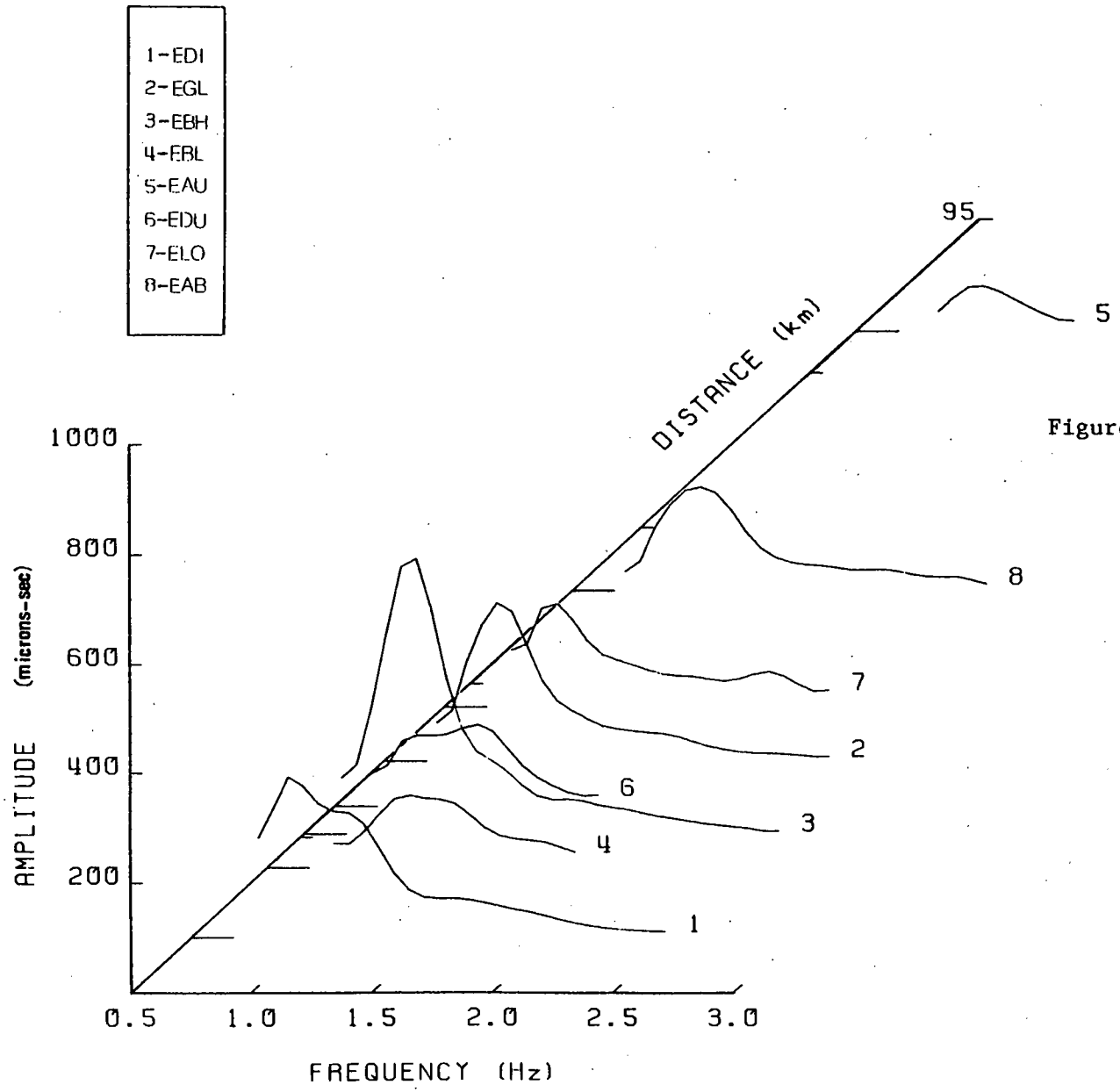

Figure 6.21. Event-averaged spectra derived from the LOWNET recordings of the underwater explosions in Kirkcaldy Bay. The data are corrected for geometric spreading and instrument response.

of a shift in relative energy concentration to lower frequencies with increasing distance. The spectrum at station ELO has a second smaller peak at 1.8 Hz. It is interesting to note that the features of these spectra are shared with the spectra from the LISPB recordings of the underwater explosions N1 and N2. This comparison suggests the shape of the spectra is governed by the source. A further characteristic of these spectra is the rapid low frequency decrease in amplitude, spanning no more than four frequency points in the spectrum. The expected general trend of a decrease in amplitude with distance is not followed.

6.3.3 Measurement of the Average Regional Attenuation

The Rayleigh wave attenuation coefficient $\gamma(\omega)$ is obtained for all the stations in the LOWNET array by fitting a straight line to the decay of logarithmic amplitude with distance (Equation 1.11), Figure 6.22a shows the resulting function. As expected, there are broad standard deviations on $\gamma(\omega)$, presumably due to the heterogeneities, scattering, boundary transmission, and other azimuthally dependent effects. The mean value of $\gamma(\omega)$ is around 0.01 km^{-1}. Applying the analysis again to stations EDI, EAU, EGL and EBL, with corresponding propagation paths mainly within the Carboniferous province, $\gamma(\omega)$ has a narrower bandwidth than in the previous diagram (Figure 6.22b), and drops below zero at frequencies less than 1Hz. Deletion of the furthest station (EAB) from the analysis does not seem to affect the results.

An estimate of the source spectrum $S_b(\omega)S_r(\omega)M_z(\omega)$ of the Kirkcaldy Bay events is also obtained from the above calculations by

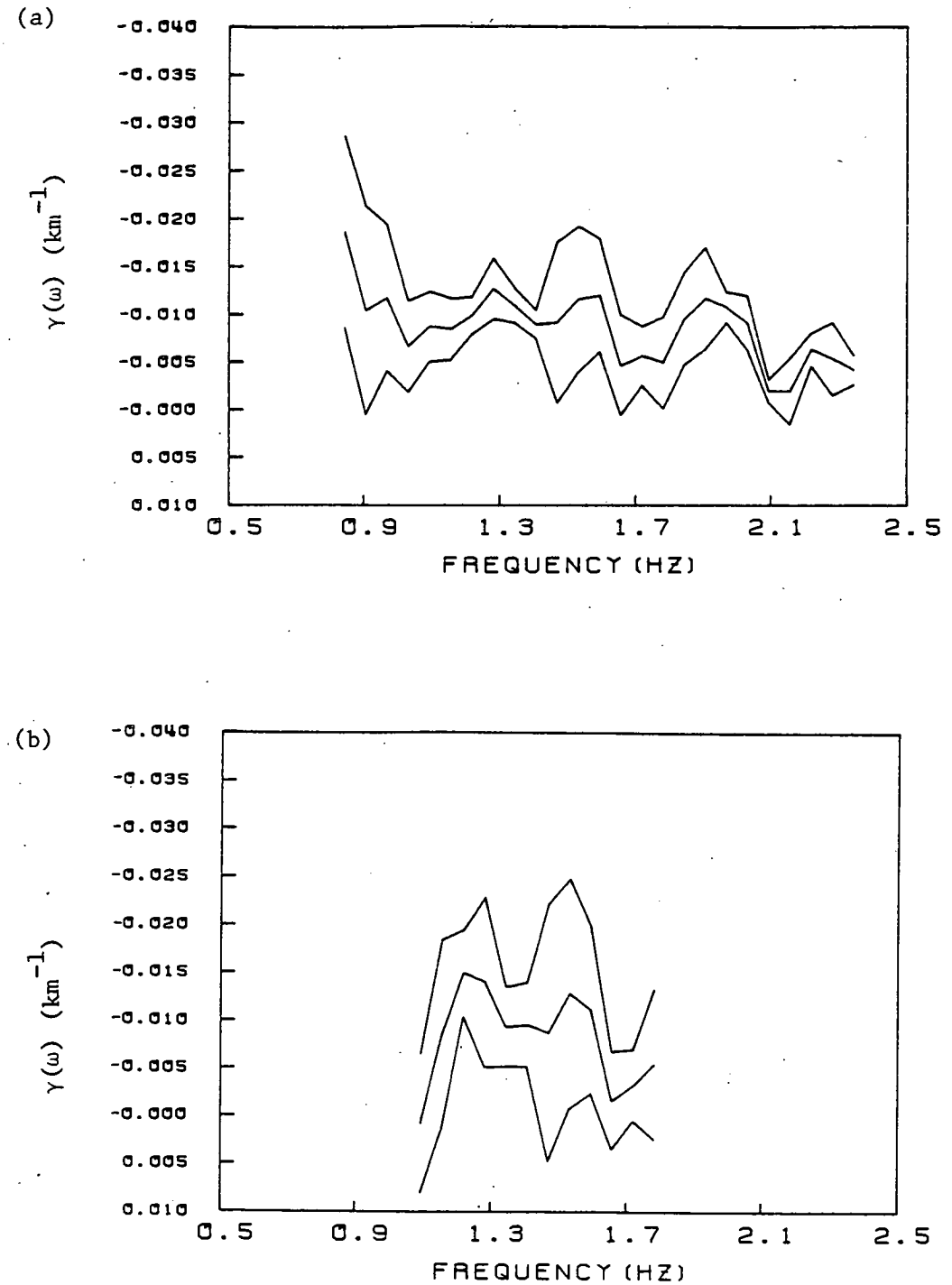

Figure 6.22. (a) Rayleigh $\gamma(\omega)$ calculated using all the event-averaged amplitude spectra derived from the LOWNET recordings of the Kirkcaldy Bay underwater explosions.

(b) Rayleigh wave $\gamma(\omega)$ calculated using the amplitude spectra from the LOWNET stations EDI, EAU, EBL and EGL whose event-station paths lie within the Carboniferous province.

measuring the ordinate intercept of the line fit to the decay of the logarithmic amplitude at each frequency. Taking the result derived using all stations as being most representative, the source function with standard deviations is shown in Figure 6.23. The spectrum has a peak frequency at 1Hz and displays some of the characteristics of the theoretical spectra of Figure 6.18 and the observed spectra in Figure 6.21.

6.3.4 Preliminary Study by the Peak Frequency Method

Peak frequencies at each station for the event-averaged and individual spectra are read directly from the instrument-corrected digital amplitudes. The frequencies are plotted in Figure 6.24a as a function of distance, together with the theoretical trend of peak frequency with distance for anelastic half-spaces with a Q_β^{-1} of 0.005 and 0.01. To draw these curves we assume a shear velocity half-space of 1.5 km/sec and a source function of $\omega^{\frac{1}{2}}$ (see Section 6.2.4 for reasoning behind this choice). The results imply a very low shear wave specific attenuation factor (< 0.01) for all the paths to LOWNET (if the power law source function is a reasonable representation).

Using Equation 5.2, a half-space Q_β^{-1} value corresponding to each peak frequency measurement is calculated, the gradient of the group velocity and source function $S(\omega) = S_T(\omega)M_z(\omega)$ being computed using Equation 6.2. Evaluating the full source function using Equations 2.10 and 2.11 for the signal generated using only the shock wave, it is found that the gradient of $S(\omega)$ becomes negative at certain frequencies, there are thus no solutions for this model. Consequently, the source model with one bubble pulse is considered. The computed Q_β^{-1}

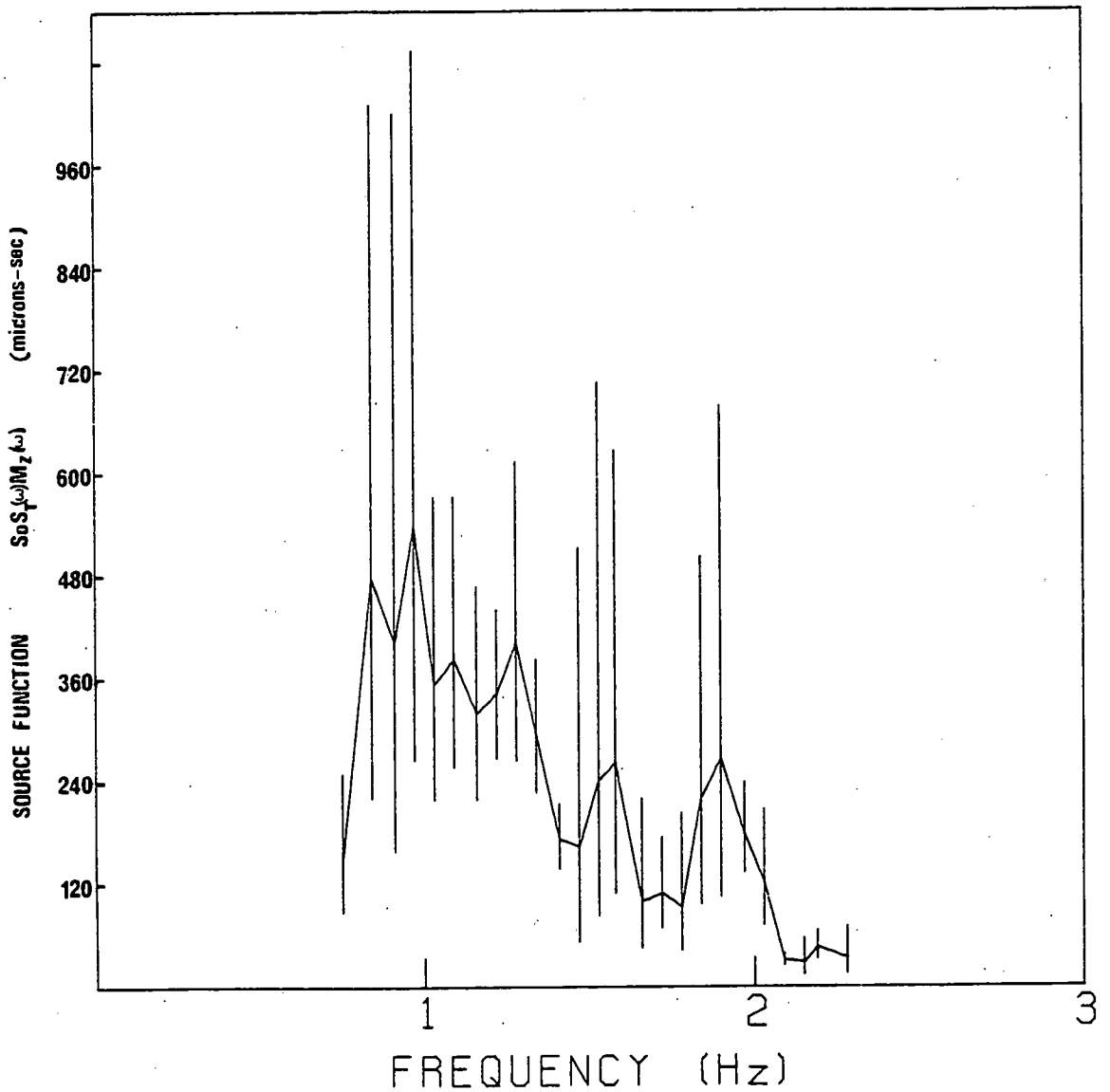

Figure 6.23. Empirical source function and standard deviations obtained in addition to the Rayleigh wave $\gamma(\omega)$ when the amplitude spectra at all the LOWNET stations are analysed with respect to the decay with distance.

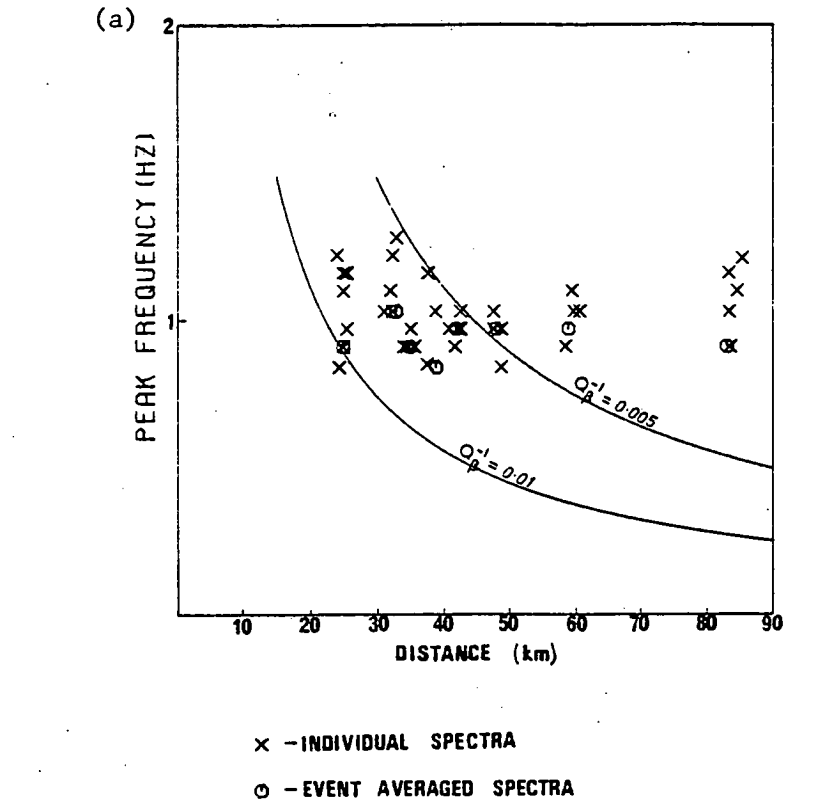

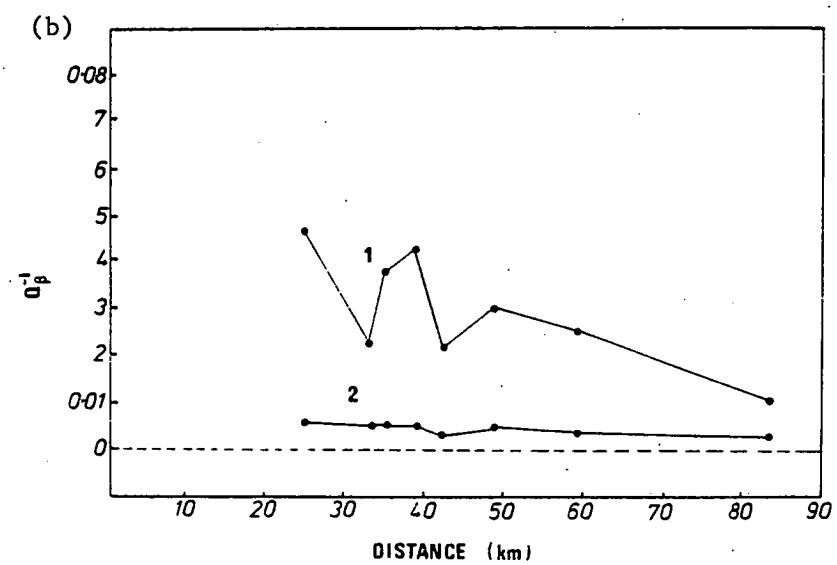

Figure 6.24. (a) Peak frequencies of the individual and event-averaged amplitude spectra, derived from the Kirkcaldy Bay underwater explosions recorded on LOWNET, as a function of distance.

(b) Q_β^{-1} values corresponding to peak frequency measurements for the event-averaged spectra. 1-source model with one bubble pulse; 2-power law source function $\omega^{\frac{1}{2}}$.

values are shown as a function of distance in Figure 6.24b. The values for the power law source function $S(\omega) \alpha \omega^{\frac{1}{2}}$ are also shown here for comparison. The Q_β^{-1} values obtained using the source with one bubble pulse decrease with distance, ranging from 0.05 at 25km to 0.01 at 85km. For the power law source function the attenuation is smaller, being between 0.003 and 0.01. From the previous calculations of Q_β^{-1} in the upper crust these values seem less realistic, and therefore it appears that the power law source function is not appropriate for these events.

6.3.5 Application of Single-Station Attenuation Methods

6.3.5a Introduction

The event-averaged and individual spectra are corrected for the half-space medium response of Appendix A.3, and have been corrected for the instrument response. The data are now specified by the shot depth, thickness of water layer, source strength, and the Q_β^{-1} values. Following the single-station scheme of Section 5.4, the thickness of the water layer is set equal to the shot depth (as the explosion is fired at the sea-bottom). Bathymetric chart data (Thomson, 1977) indicate that the epicentral region lies between depth contours of 20m and 30m, with a maximum depth of 60m for the Firth of Forth area. This places a physical constraint on the source depth d of $0 \leq d \leq 60$m.

The frequency dependent weights which describe the relative effect of the Q_β^{-1} in each layer of the attenuation model are calculated for an equivalent three-layered velocity model as in Section 6.2.5a. The multi-layered shear velocity models of Figures 4.8 - 4.11, representing each event-station path, are used for this purpose. Again, the layers

are grouped with the aim of achieving equal resolution of each Q_β^{-1} value. The set of frequency dependent weights at station EDI is shown in Figure 6.25.

6.3.5b FOB Inversion of Underwater Explosion Data

A grid of depth values is established which runs from 0 to 60m in increments of 1m. The observed spectra are corrected for the source function corresponding to each grid point in turn. Estimates of S_o and the specific attenuation Q_β^{-1} values are then found which minimize the χ^2_{FOB} function defining the fit between the theoretical curve and the corrected observations at each point. Three curves of χ^2_{FOB} versus shot depth are generated using this procedure, corresponding to the three different source models described above. The curves obtained using the event-averaged spectra are averaged over all the stations in the LOWNET array, and are shown in Figure 6.26. The source model with no bubble pulses produces only one shallow minimum at about 14m. The model with one bubble pulse leads to two minima in the fit function:- a sharp minimum at 10m and a much wider minimum at about 32m. The model with two bubble pulses generates depth minima in similar positions, but the wider minimum is at 42m and is generally clearer. For the latter two models, the two troughs are probably caused by the competing bubble and reverberation functions. These general features are observed on the χ^2_{FOB} curves for all the individual spectra.

The fit between the observed and the theoretical spectra (both instrument corrected), corresponding to each minimum in the χ^2_{FOB} function, is shown in Figures 6.27 and 6.28 for the event-averaged

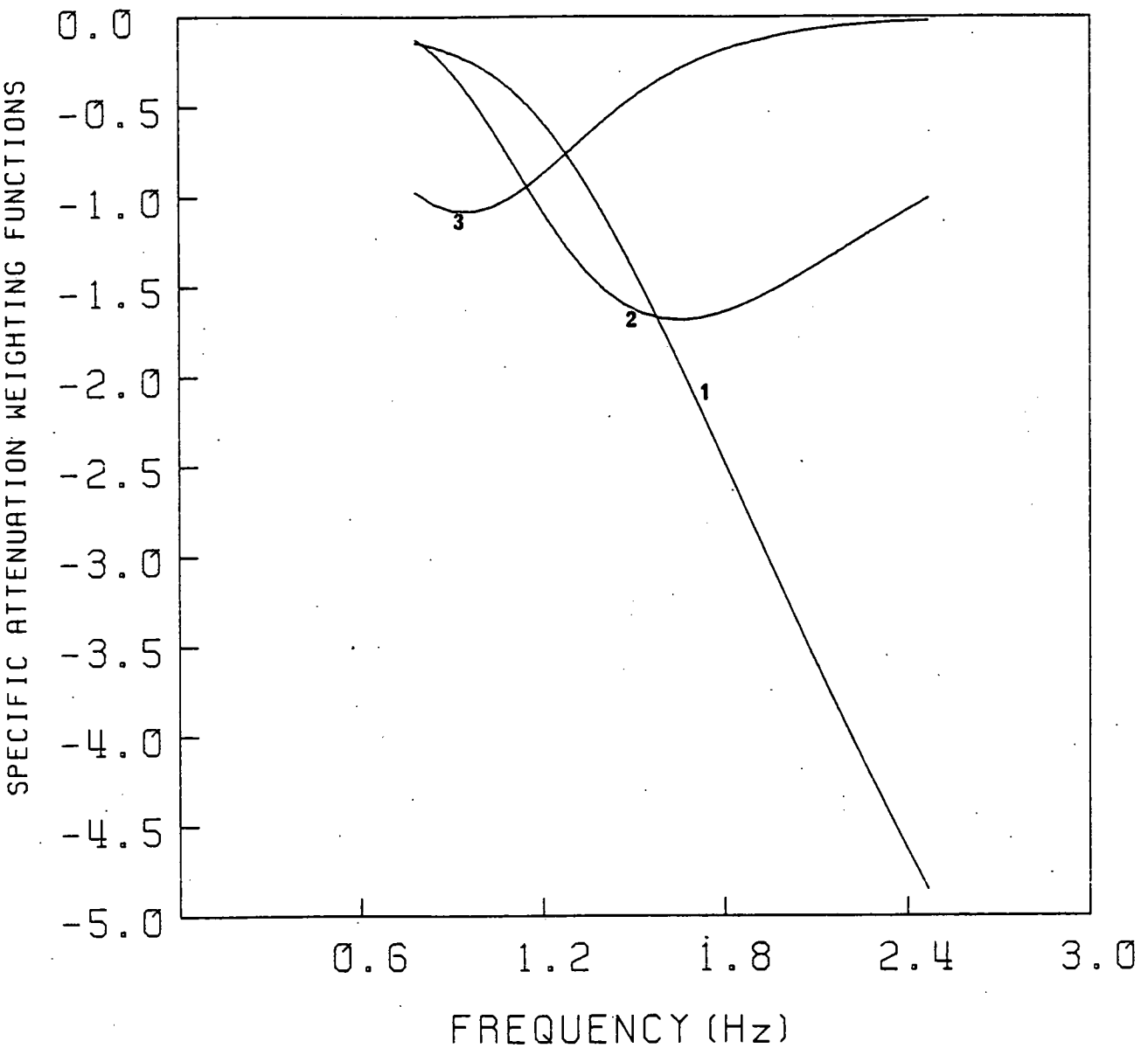

Figure 6.25. Typical set of weighting functions for station EDI corresponding to a three layered equivalent velocity model.

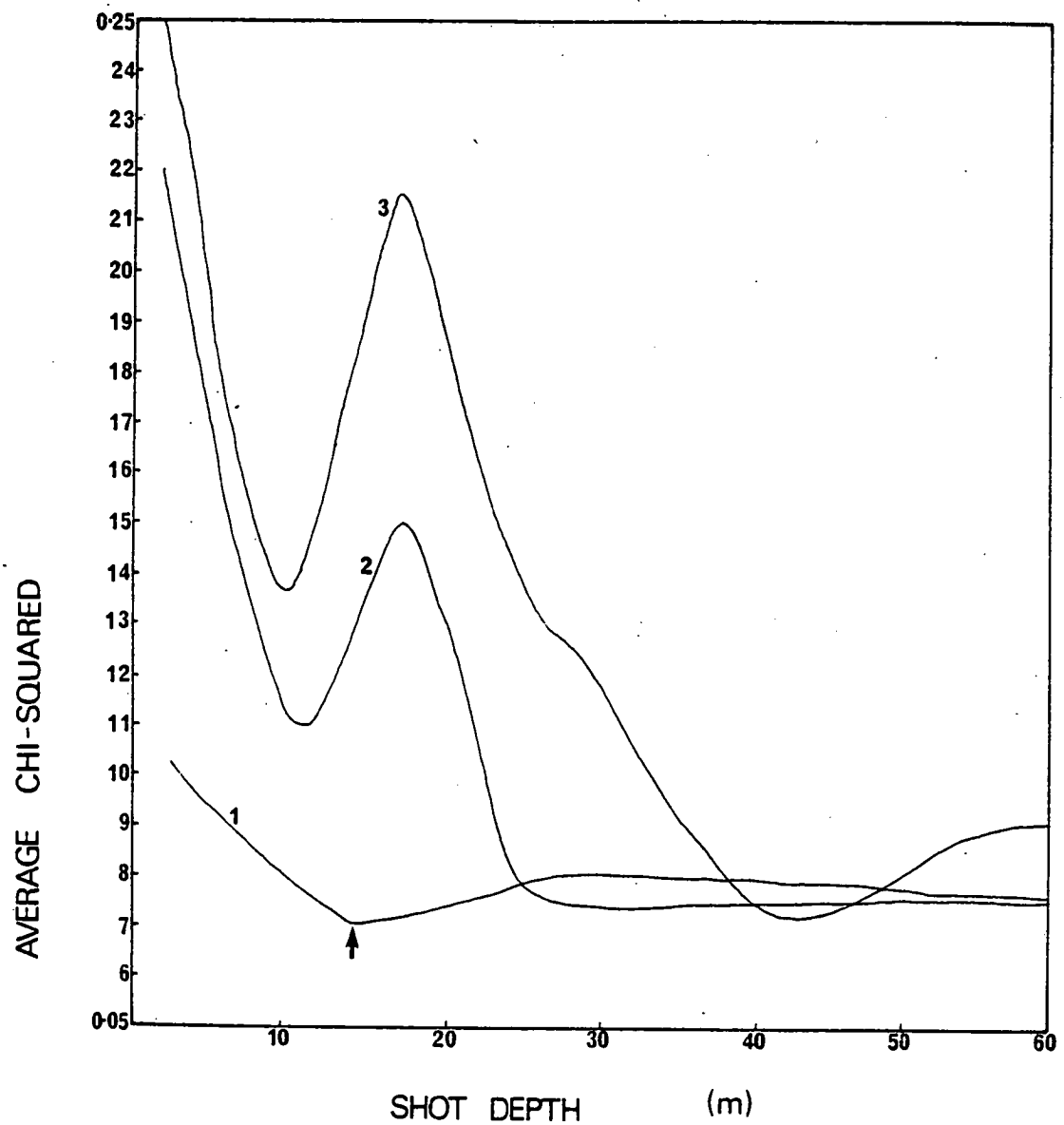

Figure 6.26. Average of χ^2_{FOB} fit function, obtained from the event averaged spectra, over all stations and for different source bubble models. Preferred minimum is marked with an arrow (see explanation in text).

Model 1 - shock wave only

Model 2 - one bubble pulse

Model 3 - two bubble pulses

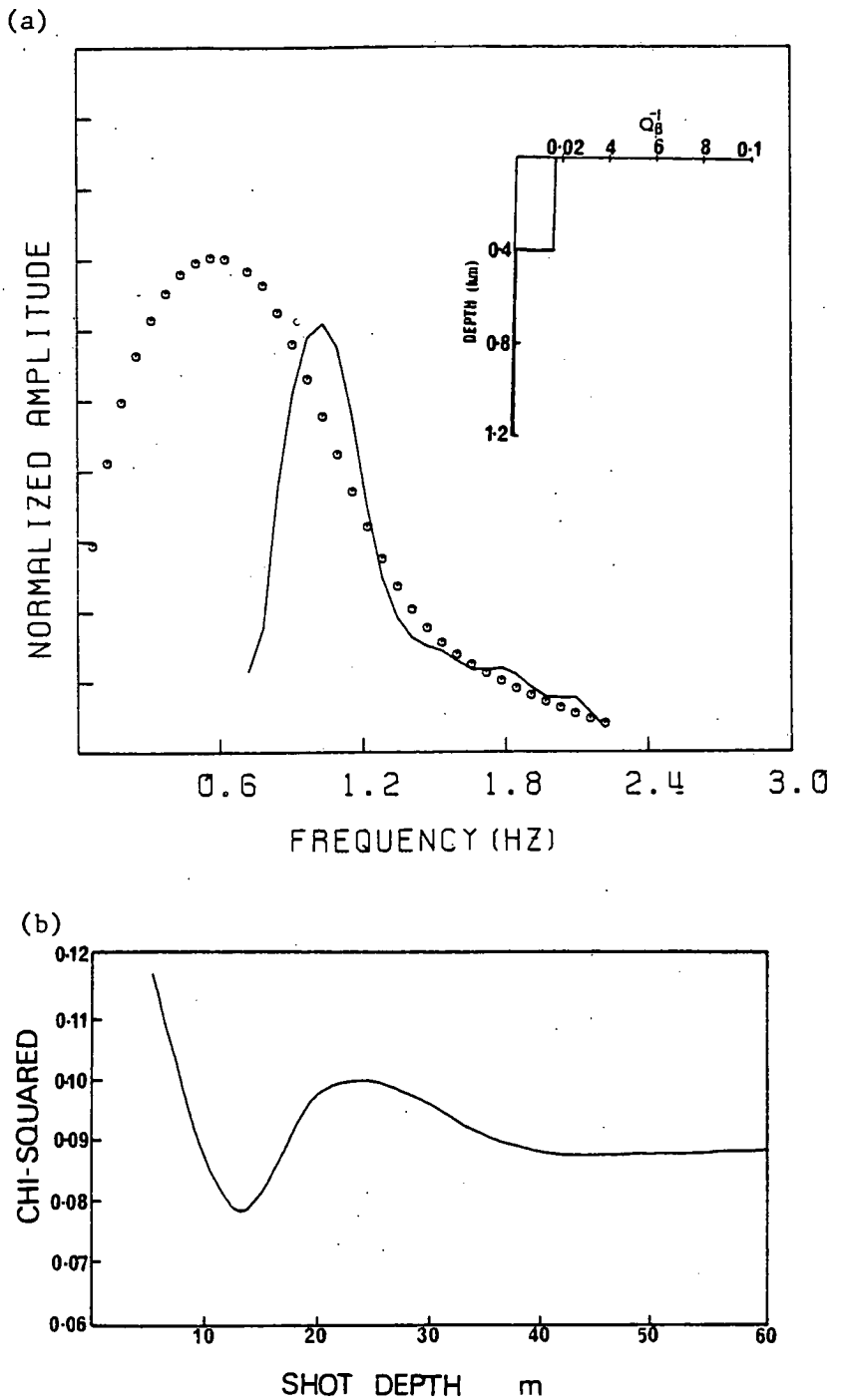

Figure 6.27. (a) Comparison of 'best-fit' theoretical spectrum with event-averaged spectrum at station ELO. Q_β^{-1} solution corresponds to the minimum of χ^2-fit function and source model has no bubble pulses.

(b) χ^2-fit function versus shot depth for station ELO and this particular source model.

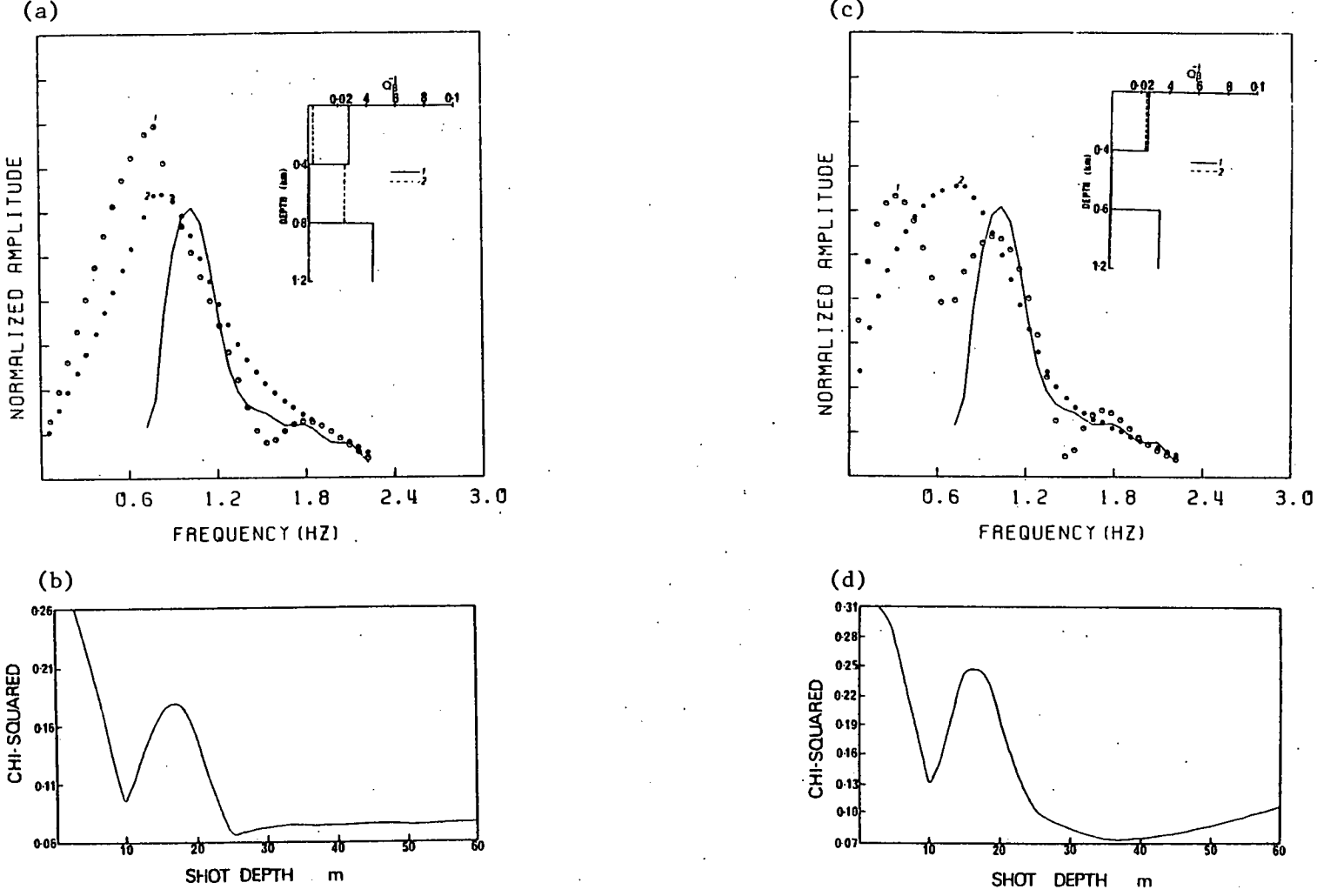

Figure 6.28 (a),(c) Comparison of 'best-fit'theoretical spectrum with event-averaged spectrum at station ELO. Q_β^{-1} solutions correspond to minima of χ^2-fit function and source model has one and two bubble pulses respectively.

(b),(d) χ^2-fit function versus shot depth for station ELO and these particular source models.

spectrum at station EL0. The specific attenuation Q_β^{-1} model obtained for each $\chi^2_{FOB}(d)$ minimum is displayed inset. Figure 6.27a compares the theoretical spectrum produced by a source model with only the shock wave, and Figures 6.28a and 6.28c show theoretical spectra for the source models with one and two bubble pulses. The Q_β^{-1} values in the upper layer of the profiles are about 0.02 for each source model, although Q_β^{-1} in the lower layers is more dependent on the particular source function and the choice of the shot depth. The physical constraints on the shot depth and Q_β^{-1} values restrict the theoretical curves to fit only the high frequency slope of the observations. The low frequency drop-off in all cases is too sharp to be modelled. The closest low frequency fit is for the theoretical spectrum corresponding to the first depth minimum of the source model with two bubble pulses. This spectrum has a similar peak frequency to the observed spectrum. Unfortunately the fit is relatively poor elsewhere along the curve and consequently χ^2_{FOB} is larger than for the second minimum. The depth values corresponding to the minima in χ^2_{FOB} for each event and particular source model are averaged over all stations. The averages with standard deviations are shown for each specific event, minimum, and model in Figures 6.29a, b, and c. Averaged depth values for the event-averaged spectra (denoted 'AV') are also shown. As the explosion events are apparently identical we would expect the depths to be statistically similar. Within the range given by the standard deviations, only the points and bounds corresponding to the model with no bubble pulses are consistent in this respect. The depth measurements must also be compared by examining the magnitude of the standard deviations. If the averages and standard deviations are drawn

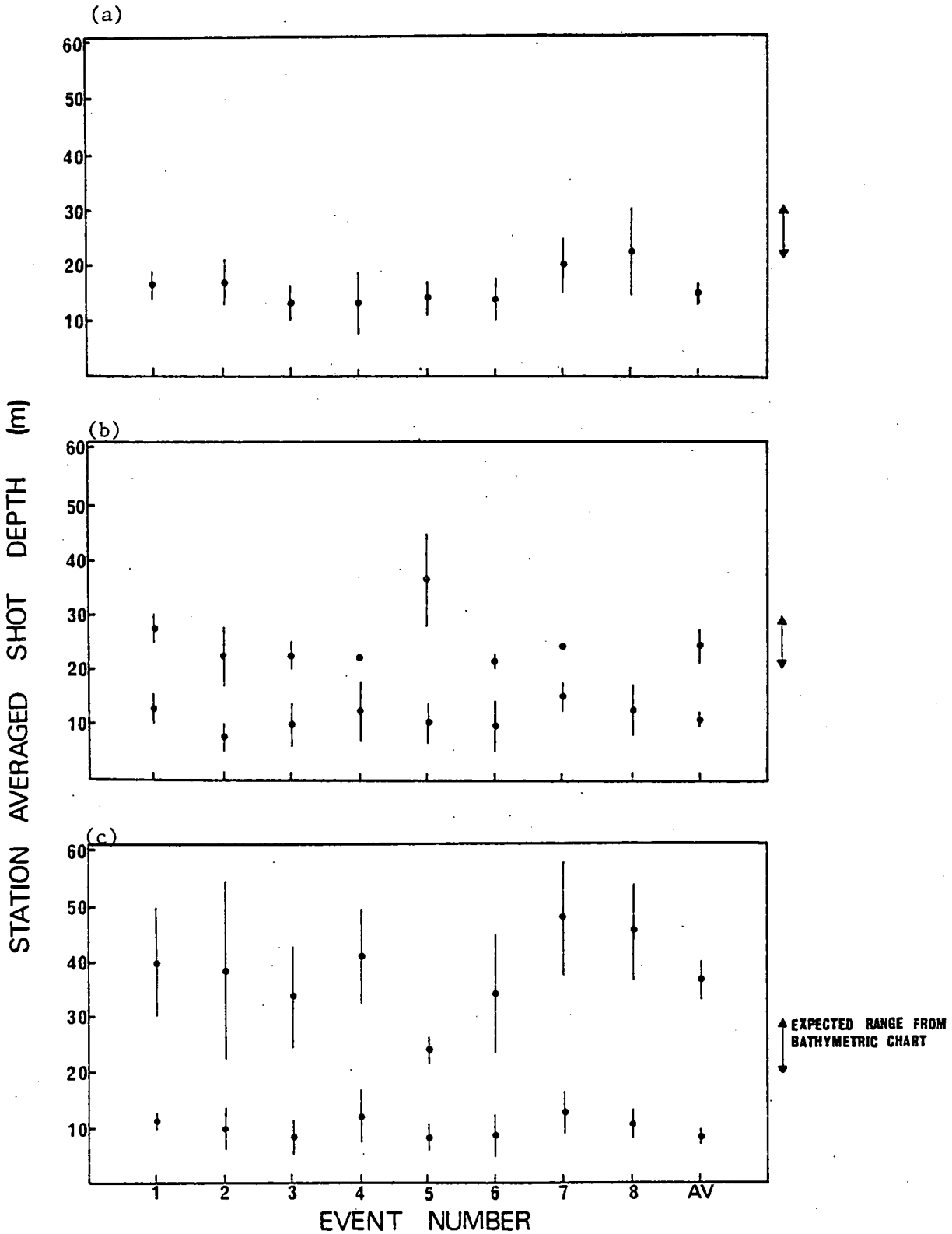

Figure 6.29 Station averaged shot depths corresponding to each minimum of the χ^2-fit functions for source models with:

(a) no bubble pulses
(b) one bubble pulse
(c) two bubble pulses.

from the same common parent distribution, then the standard deviations must be comparable. The standard deviations of the higher minima in Figures 6.29b and 6.29c vary widely in the magnitude, whereas those for the lower minima for all three source models are uniform over most events. Thus although the depth value of the second minimum in the χ^2_{FOB} curve corresponding to the model with two bubble pulses, fits the data to a similar extent as the source model with only the shock wave, the latter gives more consistent depth values. Consequently, the optimal depth is chosen as 14m. The discrepancy between the shot depth obtained from the bathymetric data and this depth value is probably due to the explosion bubble rising to the surface of the water. The optimal depth value should therefore be related to the residual negative pressure field, and implies that it persists for 0.8 secs.

The Q_β^{-1} and S_o parameters corresponding to the chosen source function and the event-averaged spectra are shown in Figures 6.30 - 6.33 with the match between the high frequency shape of the theoretical amplitude spectrum and the observed spectrum. The bounds on each parameter, corresponding to the observed standard deviations on the amplitude spectra, are also shown. The standard deviations on the amplitude spectra at stations EGL and EAB are multiplied by a factor of 0.674 in order that the bounds lie within the physical range of Q_β^{-1}, and thus the uncertainties are reduced to a 50% confidence level. The natural logarithm of the source strength solutions and their corresponding uncertainties for all stations are shown together in Figure 6.34. The estimates are practically constant on this scale, and have a mean of 10^7 Nm. This value is one order of magnitude different from the 10^8 Nm predicted using Equation 2.9 with the pressure data of Weston (1960). The value for station EAB has extremely large bounds, even at a 50% confidence level on the

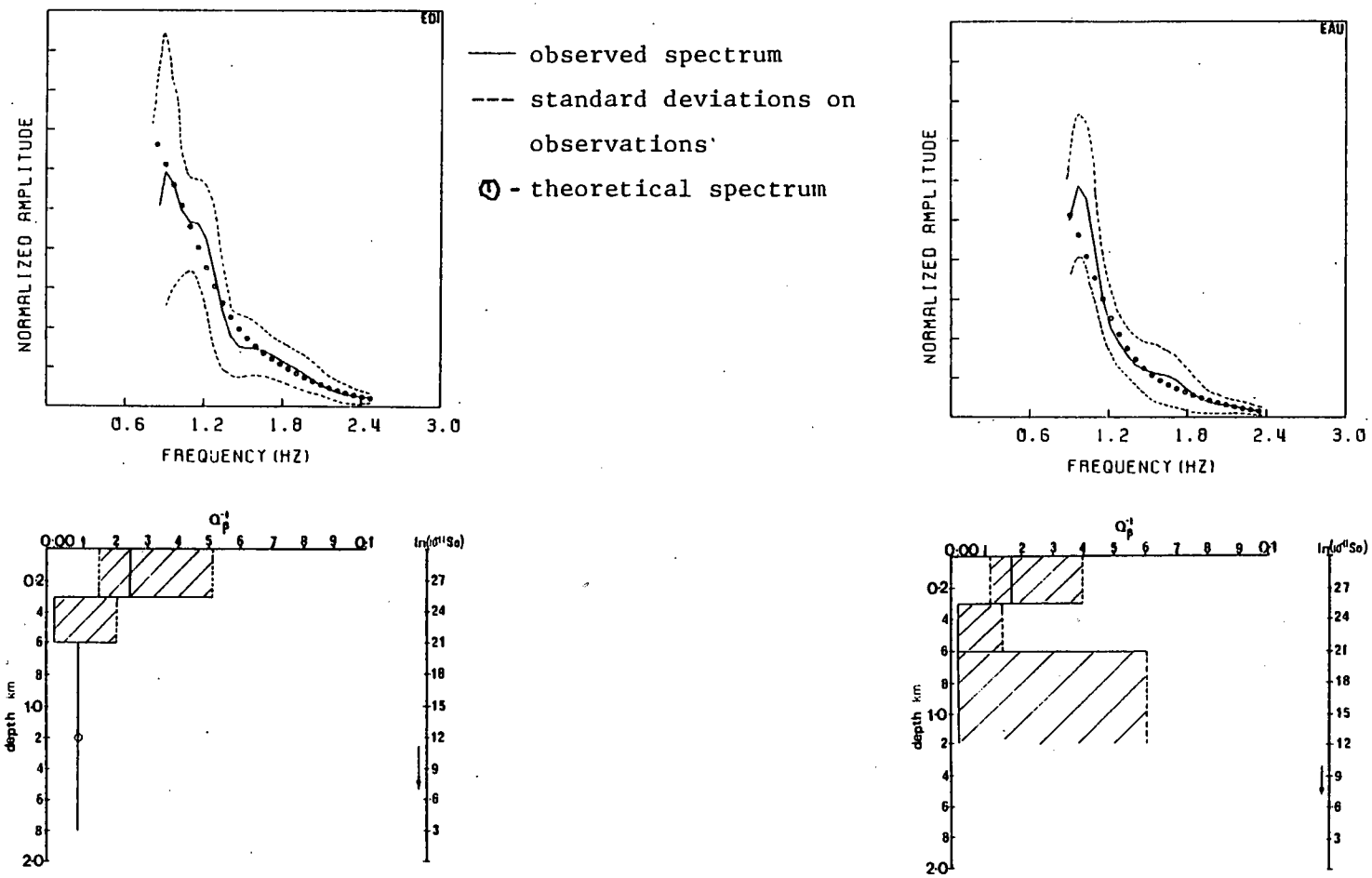

Figure 6.30. The fit between observed and theoretical amplitude spectra corresponding to optimum values of Q_β^{-1} model, S_o, and the source function from the FOB inversion. The source model has a depth of 14m and no bubble pulses.

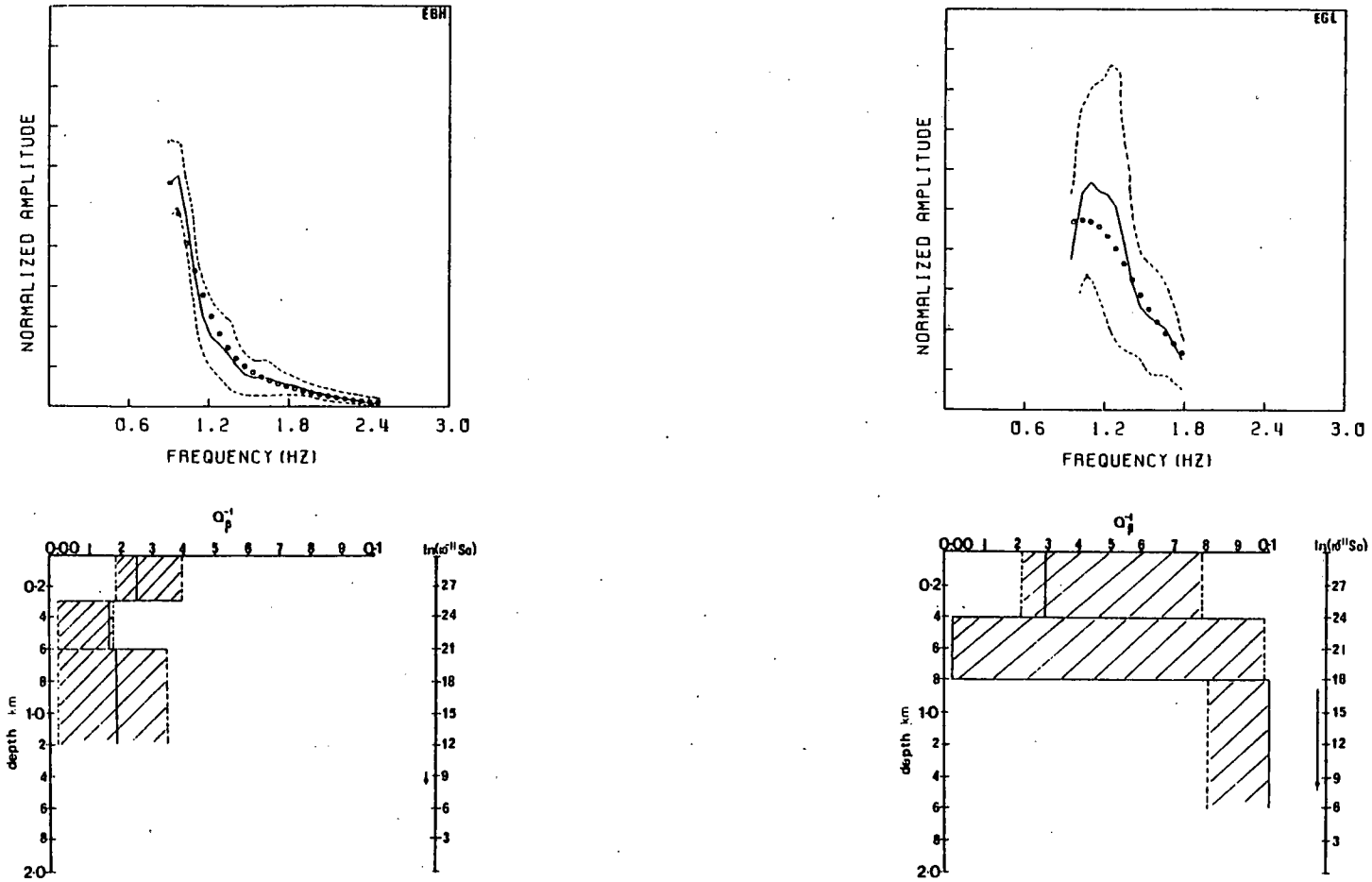

Figure 6.31 Single-station solutions at stations EBH and EGL

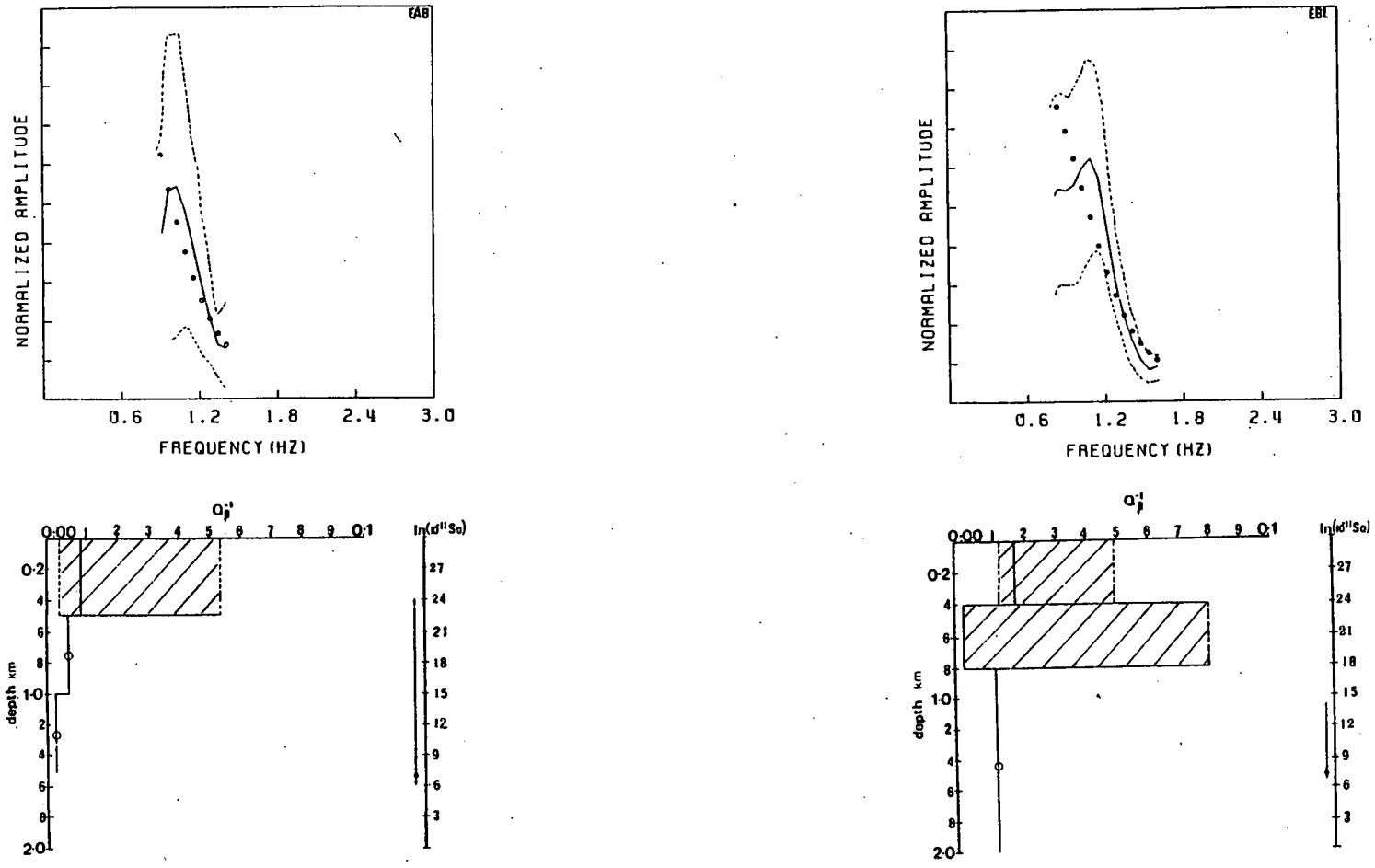

Figure 6.32. Single-station solutions at stations EAB and EBL.

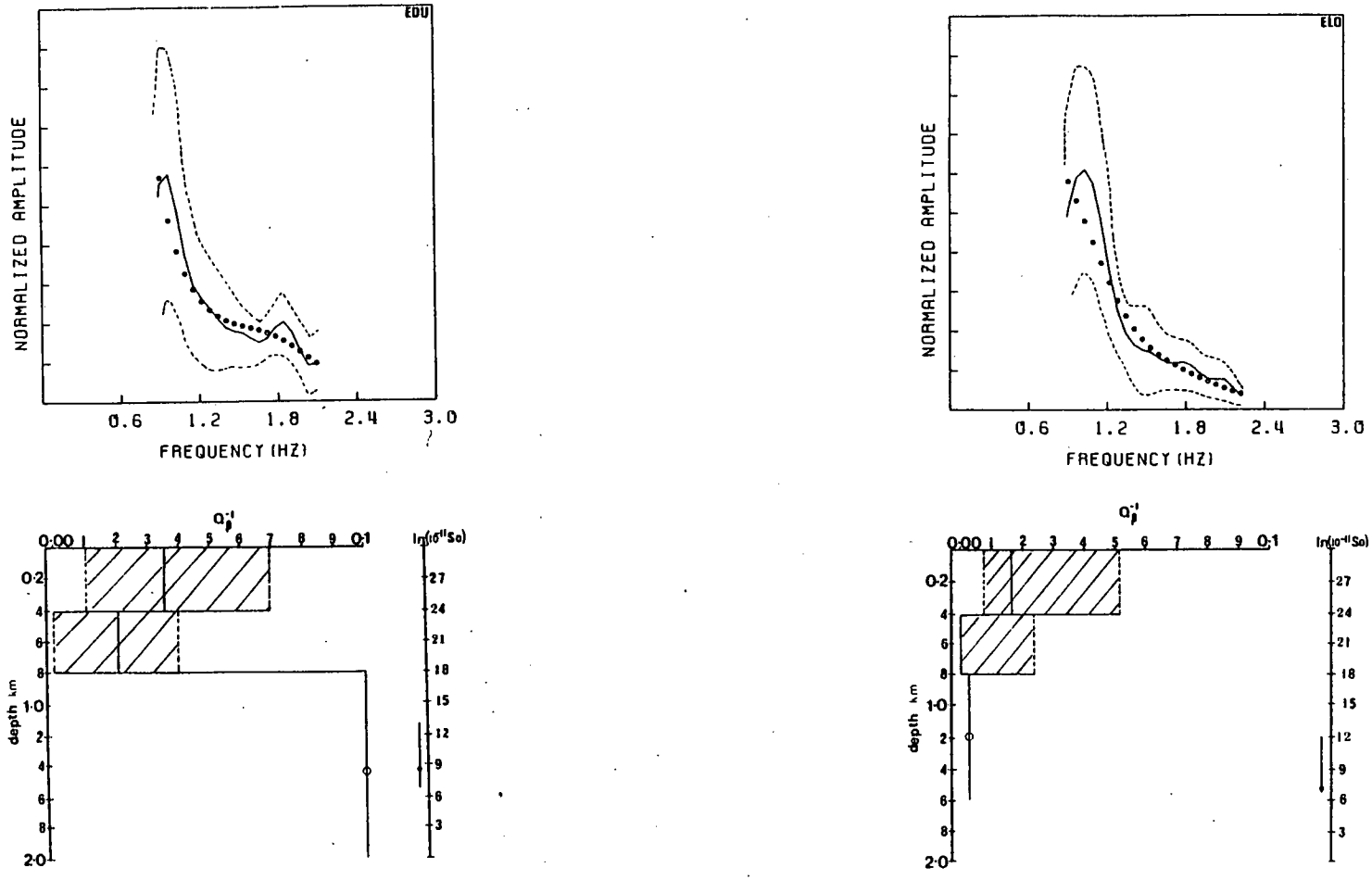

Figure 6.33. Single-station solutions at stations EDU and ELO.

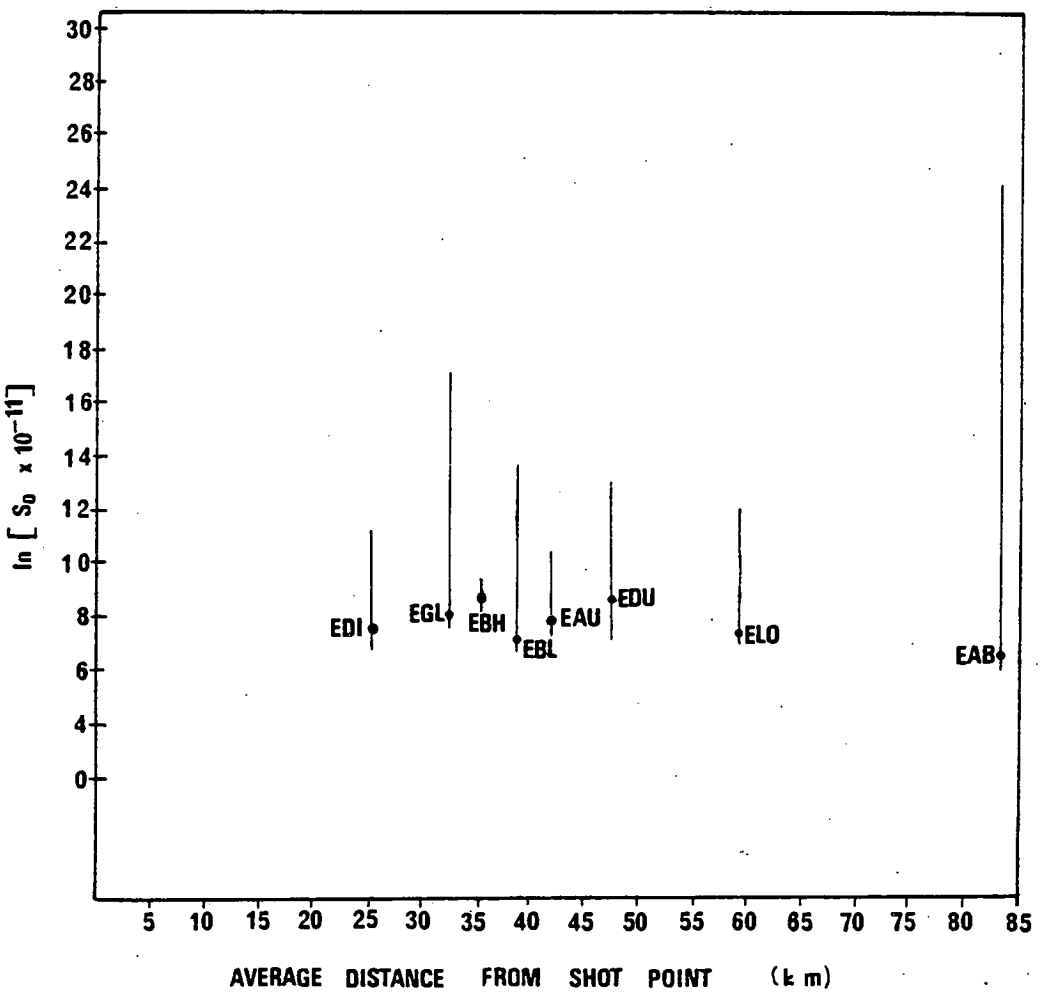

Figure 6.34. Estimates and bounds for the source strength factor S_o corresponding to the optimum solution of the source function for the Kirkcaldy Bay underwater explosions.

observations, resulting from a decrease in the signal to noise ratio.

6.3.5c Hedgehog inversion of Underwater Explosion Data

Another estimate of the Q_β^{-1} and source depth values for the event-averaged spectra is obtained by inverting using the Hedgehog method. Here, the search of parameter space is carried out over a grid Q_β^{-1} values with a spacing of 0.005 for each layer, and depth limits of $0 \leq d \leq 60$m with a spacing of 1m. The limit on the maximum permitted χ^2_ν - value is set at approximately 0.12, corresponding to a confidence level greater than 99%, and only the source model with no bubble pulses is considered.

The Q_β^{-1} solutions with bounds for both the FOB and Hedgehog inversions are compared in Figure 6.35, and the Hedgehog range of depth values is shown in Figure 6.36. The uncertainties for stations EGL and EAB again correspond to errors on the amplitude spectra at a 50% confidence level. Although only three layered models are obtained at each station, each model has different layer thicknesses. Therefore, to present a uniform picture of the distribution of Q_β^{-1} with depth, the penetration into the crust is split into a number of different depth ranges. The results agree quite closely, despite the different assumptions used in the two inversion techniques. The solutions show that Q_β^{-1} in the top 400m of the crust remains around 0.02. Between 400 and 800m the attenuation decreases (but not at station EDU) to less than 0.01, and the bounds on Q_β^{-1} increase. In the deeper layers Q_β^{-1} begins to increase again, reaching an average of 0.04 (this is partly biased by two anomalous values of 0.1).

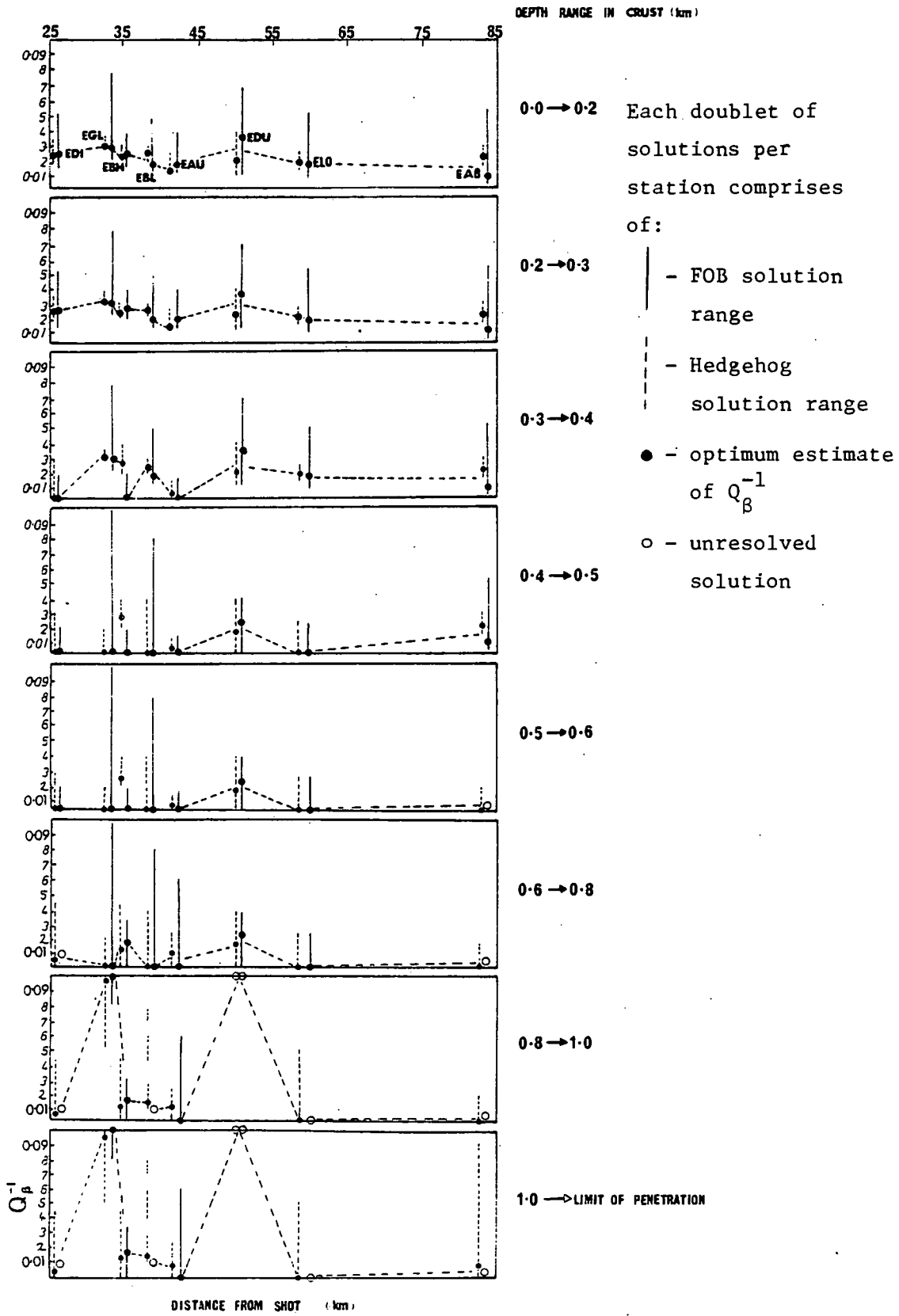

Figure 6.35. Q_β^{-1} solutions and bounds inferred for a variety of different depths within the crust from the three-layered single-station profiles estimated using the FOB and Hedgehog inversion techniques. The bounds on the solutions for stations EGL and EAB correspond to the standard deviations on the observations reduced by a factor of 0.674.

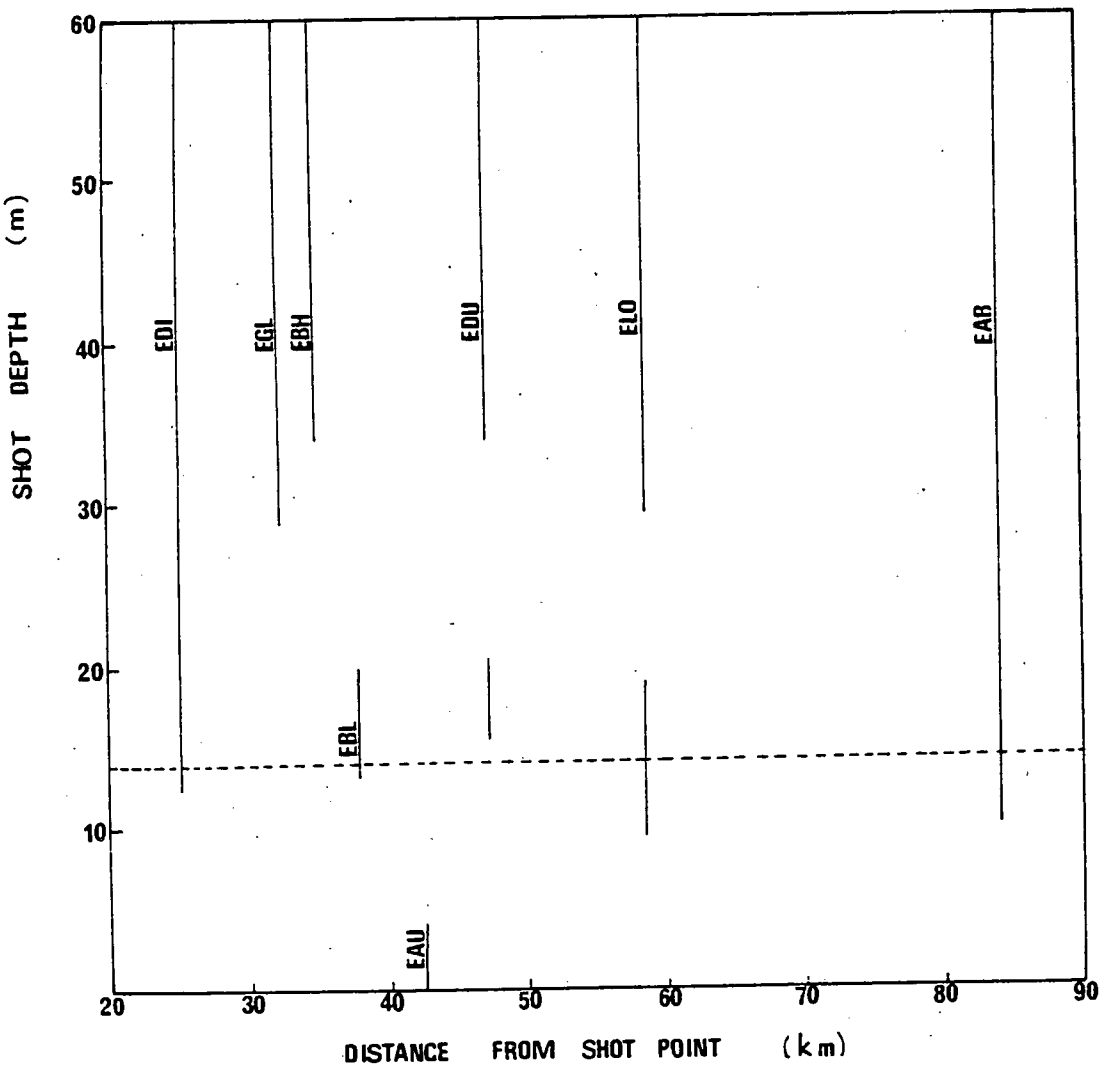

Figure 6.36 Range of shot depths which satisfy the constraints on the Hedgehog inversion of the underwater explosion spectra derived from the LOWNET recordings.

The spread of shot depth values for the Hedgehog technique (see Figure 6.36) covers a large proportion of the constrained range, and only four stations include the optimum value of 14m obtained using the FOB inversion technique. As the Q_β^{-1} solutions are similar to those obtained using the FOB technique, the values thus appear to be insensitive to the shot depth.

6.3.5d Comparison with Station-averaged Attenuation Values

Single-station attenuation coefficients are computed at each station using the single event-station Q_β^{-1} models of Figure 6.35. These are compared in Figure 6.37 with the multi-station attenuation coefficient for the Carboniferous and Old Red Sandstone formations, which dominate the Midland valley, derived from the profiles of Evans (1981). The attenuation coefficients should lie between those for the two pure provinces if the dissipative properties are dependent on surface geology. The curves compare quite closely, but they are mostly grouped around the Old Red Sandstone coefficient. The attenuation coefficients for stations EGL and EDU lie close to the curve for the Carboniferous formation. This distribution suggests that the single-station values are not sensitive to the geological provinces in the same way as we found the group velocities to be in Chapter 4. However, it is interesting to note that the group velocity dispersion measured at station EGL is also inconsistent with the general trend of provincial velocities (Section 4.3.4).

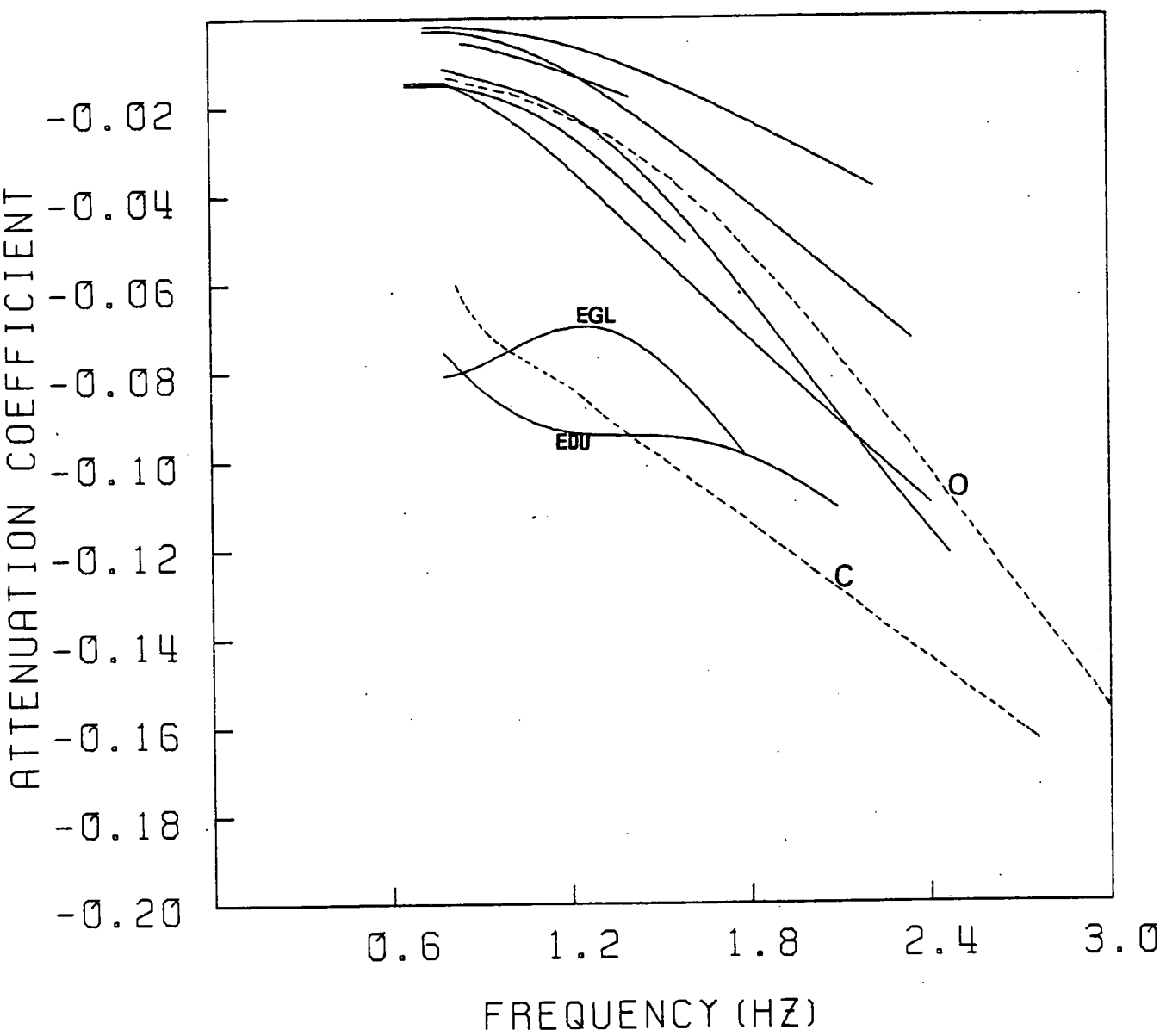

C Carboniferous province

O Old Red Sandstone Province

Figure 6.37. Single-station attenuation coefficients compared with the 'pure-provincial' attenuation coefficients for the Carboniferous and Old Red Sandstone formations.

6.4 KEQ Recorded on the LISPB Array

6.4.1 Source Effects

This earthquake represents the most complicated source which we will use in our study. Variables related to the effects of source finiteness, focal depth, strike azimuth and dip angle, in addition to attenuation must be specified to determine the amplitude spectrum. Some of these parameters can be roughly determined using formulae connecting them to the surface wave magnitude. The dimensions of the earthquake are estimated using the empirical relation of Ohnaka (1978)

$$\log (\Delta\sigma\, A) = 1.07 M_L + 12.81$$

for moderate local shocks ($2.0 \leq M_L \leq 6.8$). $\Delta\sigma$ is the stress drop in bars, A is the area of the fault in m^2, and M_L the local magnitude. A stress drop of 30 bars for the U.K. gives $L \simeq 0.8$km for KEQ, assuming a circular fault. The rupture velocity for KEQ was calculated as 2.59 km/sec using the formula in Section 3.2.4 and the shear velocity models of Chapter 4. A typical phase velocity for the region was computed using Figures 4.30 - 4.33. Calculations based on Equation 3.3 indicate that we cannot ignore the effect of source finiteness at the frequencies 1 - 6 Hz. The finiteness function $S_F(\omega)$ is plotted in Figures 6.38c, 6.38e, 6.38 c' , and 6.38e' for the first and second higher mode respectively, and for observation azimuths of 45° and 90°. The functions at an azimuth of 90° have a noticeable minimum associated with the fault length. The effect of finiteness on the spectrum for both modes is almost identical.

The source time history $s_T(t)$ can be represented by an exponential

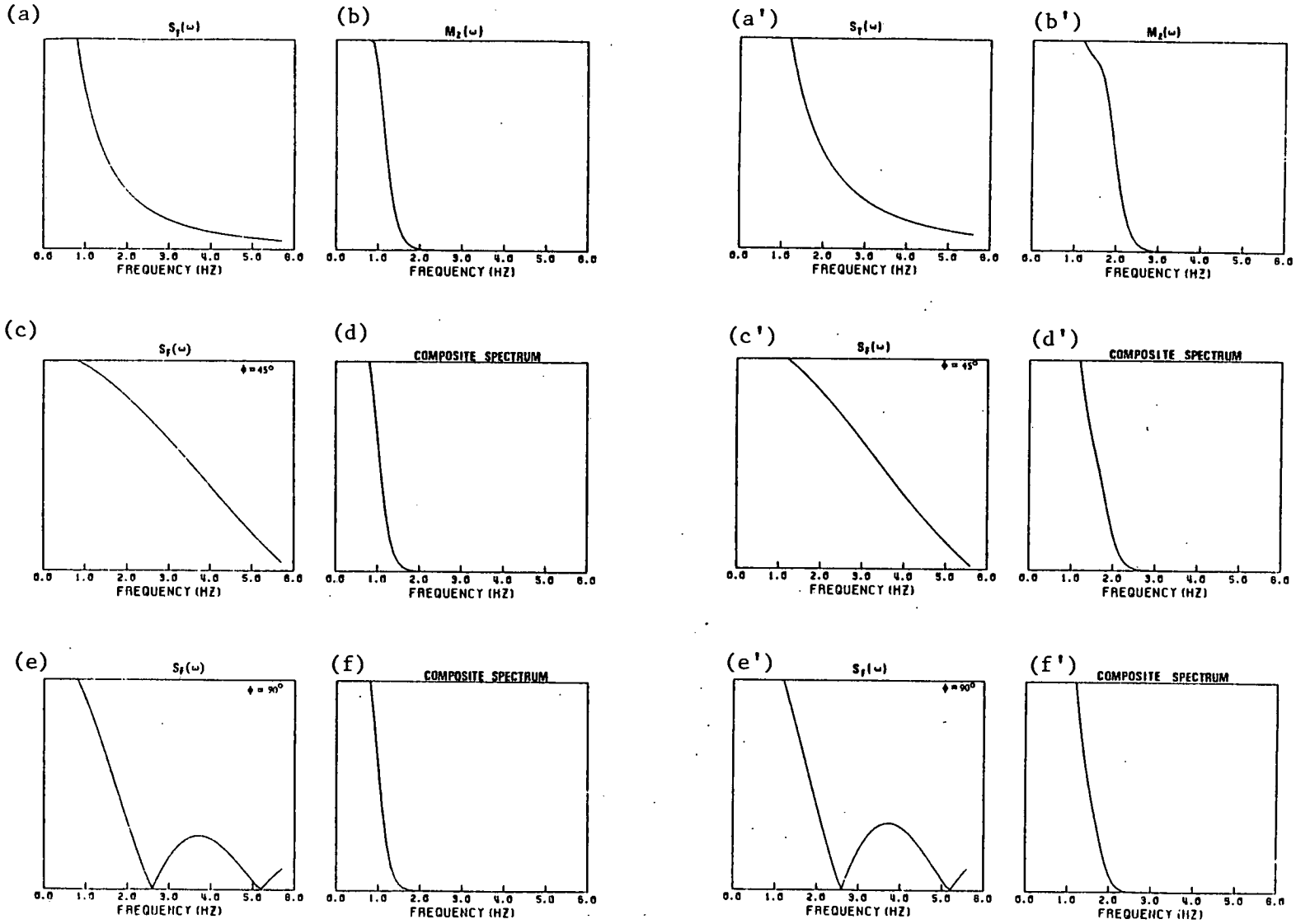

Figure 6.38. Functions which combine together to form the complete unattenuated theoretical spectral shape of the first and second higher mode Rayleigh waves. The curves are normalized with respect to their maximum amplitude in the frequency range 1.0 - 5.5 Hz.

(a), (a') spectrum of source time action

(b),(b') spectral medium response

(c), (c') source finiteness effect at an azimuth of 45^o

(d),(d') composite spectrum $S_T(\omega)$ $S_F(\omega)$ $M_z(\omega)$ at an azimuth of 45^o.

(e), (e') source finiteness effect at an azimuth of 90^o

(f),(f') composite spectrum $S_T(\omega)$, $S_F(\omega)$ $M_z(\omega)$ an azimuth of 90^o.

ramp function (Section 3.2.5). This is characterized by the inverse time constant ω_T. Tsai and Aki (1970) considered the spectral effect of this earthquake source function, and although no data on the rise time of small earthquakes was found, they thought an earthquake with a magnitude < 6 should have an inverse time constant ω_T of greater than 6 rad^{-1}. Geller (1976) derived a relation between inverse rise time and fault area:

$$\omega_T = 7\beta_s/8A$$

for a circular fault. β_s of 3.7 km/sec yields an inverse time constant of 10 rad^{-1}. $S_T(\omega)$ for this value is shown in Figures 6.38a and 6.38a'.

Assumpção obtained a well resolved depth of 10.6 ± 2km and a focal solution for KEQ. Using these values the medium response $M_z(\omega)$ can be computed for an azimuth of 45°. This function has an extremely strong drop-off for both modes between 2.5 and 3 Hz (Figures 6.38b and b'), and dominates every factor which combines to form the composite spectrum $S_T(\omega)S_F(\omega)M_z(\omega)$ (Figures 6.38 d,f,d' and f'). Even a very long fault of about 20km can only produce a narrow spectral peak in the final composite spectrum.

6.4.2 Description of Observed Spectral Amplitudes

The spectra for the first and second higher modes are grouped together using the same regional areas as in the group velocity studies (see Figure 4.20). The amplitude spectra for groups A, B and C are shown in Figure 6.39, these representing typical spectral shapes at all stations. The spectra are quite complicated, having an oscillatory

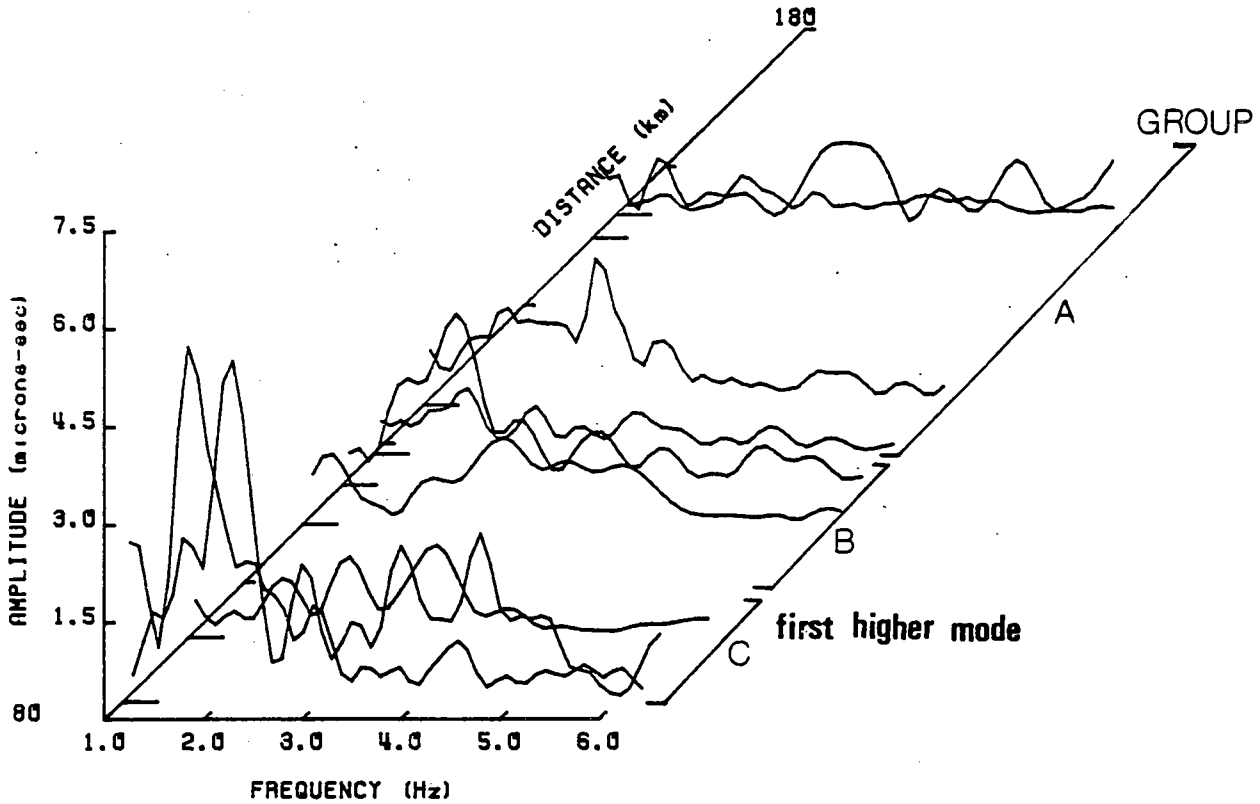

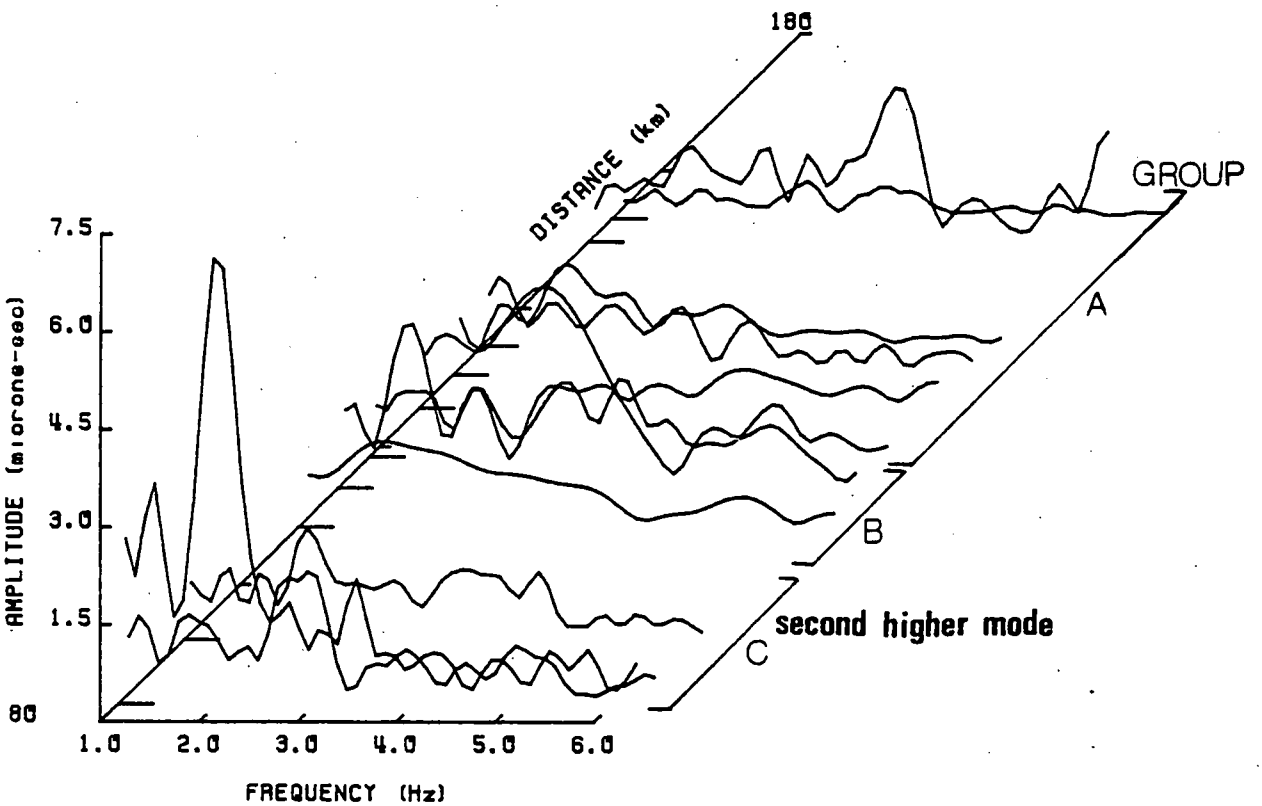

Figure 6.39 Amplitude spectra of first and second higher order mode Rayleigh waves derived from recordings of the earthquake KEQ. The data are corrected for the instrument response and geometric spreading.

character with many peaks and troughs. This particular feature could be due to finite energy outside the chosen time window, or interference between modes. The low frequency limit for both higher modes is 1.0 - 1.5 Hz, and the high frequency limit on the spectrum is between 4 - 5 Hz. The major energy is concentrated in a peak at 2.0 - 2.5 Hz.

The energy in the range 2.5 - 5.5 Hz is not predicted by the theoretical spectra of Figures 6.38, and within the framework of the spectral analysis utilized here and the limits placed on the spectral parameters, there is no phenomenon which could be invoked to take account of this disparity. The main contributing factor to this difference is the focal depth of the earthquake. To illustrate this point the spectral medium response is plotted as a function of frequency for a variety of focal depths, and for the first and second Rayleigh modes in Figure 6.40. A depth of 3 - 5 km could account for the observed spectrum if it were not well determined at 10.6 km. Consequently, the possibility of obtaining attenuation by using the single-station spectral techniques is not considered further, and the radiation pattern at specific frequency values is now examined as an alternative.

6.4.3 Attempted Measurement of Attenuation by Correcting for the Radiation Pattern

In an attempt to derive an attenuation value for each region, a simple approximation for the medium response as a function of azimuth and frequency is used

$$M_z(\omega;\phi) \simeq X(\phi)M_z(\omega)$$

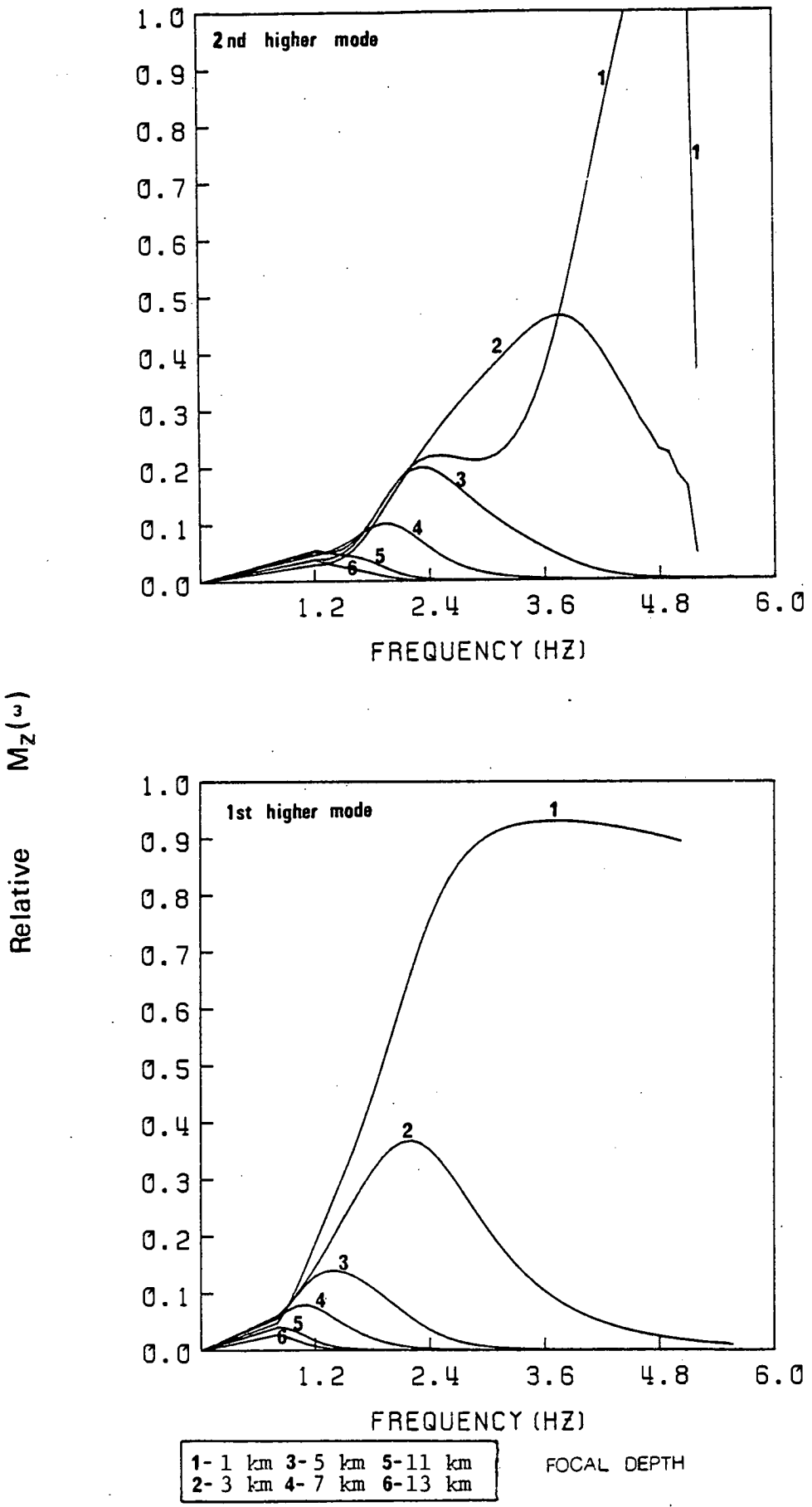

Figure 6.40. First and second higher mode medium responses as a function of frequency for the KEQ fault model at various focal depths in the crust.

where X is only a very weak function of frequency - this approximation is well justified for KEQ in Figure 6.41. The spectral amplitude $A_z(\omega)$ can now be written as a function of azimuth

$$A_z(\omega;\phi) = S(\omega)S_F(\omega;\phi;L)X(\phi;h;\lambda,\delta)D(\omega;\phi)$$

where $S(\omega) = S_o S_T(\omega)M_z(\omega)$ is a constant to be determined at each frequency. The rake of the fault is well determined and the focal depth h is not considered as a parameter as it is well resolved. The radiation pattern is therefore specified by the rupture length L and the dip δ of the fault (the latter is not well constrained in Assumpção's (1981) solution).

Utilizing the general single-station methodology of Chapter 5, the following approach is adopted:-

(a) set up a grid of L and δ values

(b) step along the grid, and at each point evaluate $S_F(\omega;\phi)$ and $X(\phi)$; $X(\phi)$ is computed using the program 'MLR' listed in Appendix D.2.

(c) correct the smoothed spectra at each station for these functions

(d) use Equation 1.11 to obtain the attenuation coefficient $\gamma(\omega)$ and source function $S(\omega)$ by fitting a least squares regression line to the decay of logarithmic amplitude with distance at each frequency point. The scatter about the least squares line is monitored using the standard errors on the ordinate intercept and gradient averaged over all frequencies. These quantities are compared with similar errors obtained by applying Equation 1.11 directly to the spectra without correction for the source directivity.

The amplitudes are divided into three groups for the application of this scheme, corresponding to the group velocity regions A - C, D - E, and F - G, this division being based mainly on station density and

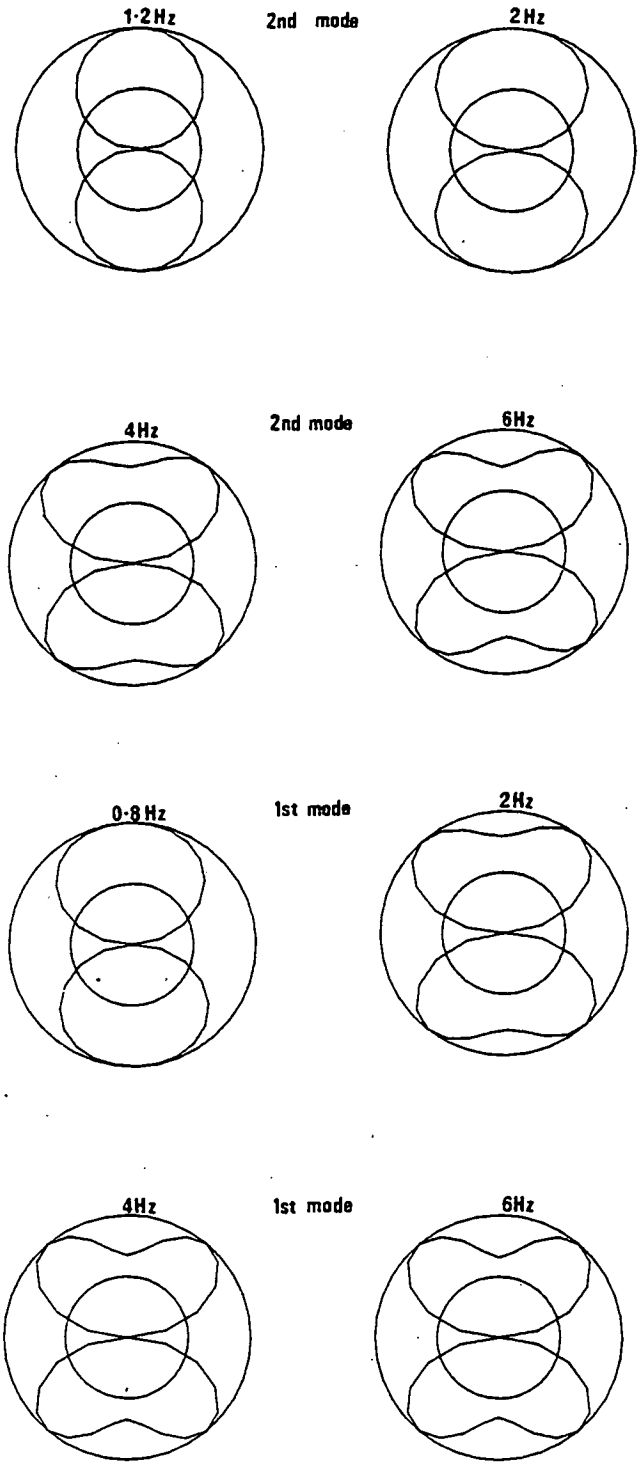

Figure 6.41. Theoretical radiation patterns given by the medium response function $M_z(\omega;\phi)$ at different frequencies for the KEQ earthquake model, and for the first and second higher modes. Note that there is little variation in the radiation pattern across this particular frequency range.

distance range in each region. L is varied from 0 to 10km in steps of 0.1km, and δ from 54° to 94° in steps of 1°. The results are poor, and no combination of δ or L can reduce the scatter for any group to below that for the amplitudes uncorrected by the azimuthal variation in amplitude. Re-grouping the data does not alleviate this problem. In particular, the results for the BETA line yield negative attenuation values for all δ and L. Similar conclusions are reached for both higher mode spectra. It is not possible to discern values of δ and L using this method. Figure 6.42 shows the observed amplitudes as a function of azimuth at a frequency of 2Hz for both modes. Theoretically the radiation pattern possesses a node at group G. The second higher mode observations do not show this feature. When stations close (±1°) to the theoretical node of the radiation pattern are rejected, the attenuation coefficients for the BETA line still yield negative attenuation coefficients. A further azimuthal coverage extending into the second quadrant would perhaps have yielded a better resolution for the rupture length and revealed the true nodes in the pattern.

As the source spectral parameters cannot be resolved, we correct the amplitude spectra for a fixed radiation pattern with L = 0.0km and δ = 74°, and evaluate $\gamma(\omega)$ and $S(\omega)$. The errors on the resulting attenuation coefficient and source function for groups D-E are very large. Only the results for the first group (A-C) display reasonable values; these being shown with corresponding errors in Figure 6.43. The coefficients, with a mean of $0.02km^{-1}$, show a slight decrease of attenuation with increasing frequency, however the errors on the curves are too large to be inverted to a well constrained Q_β^{-1} depth structure.

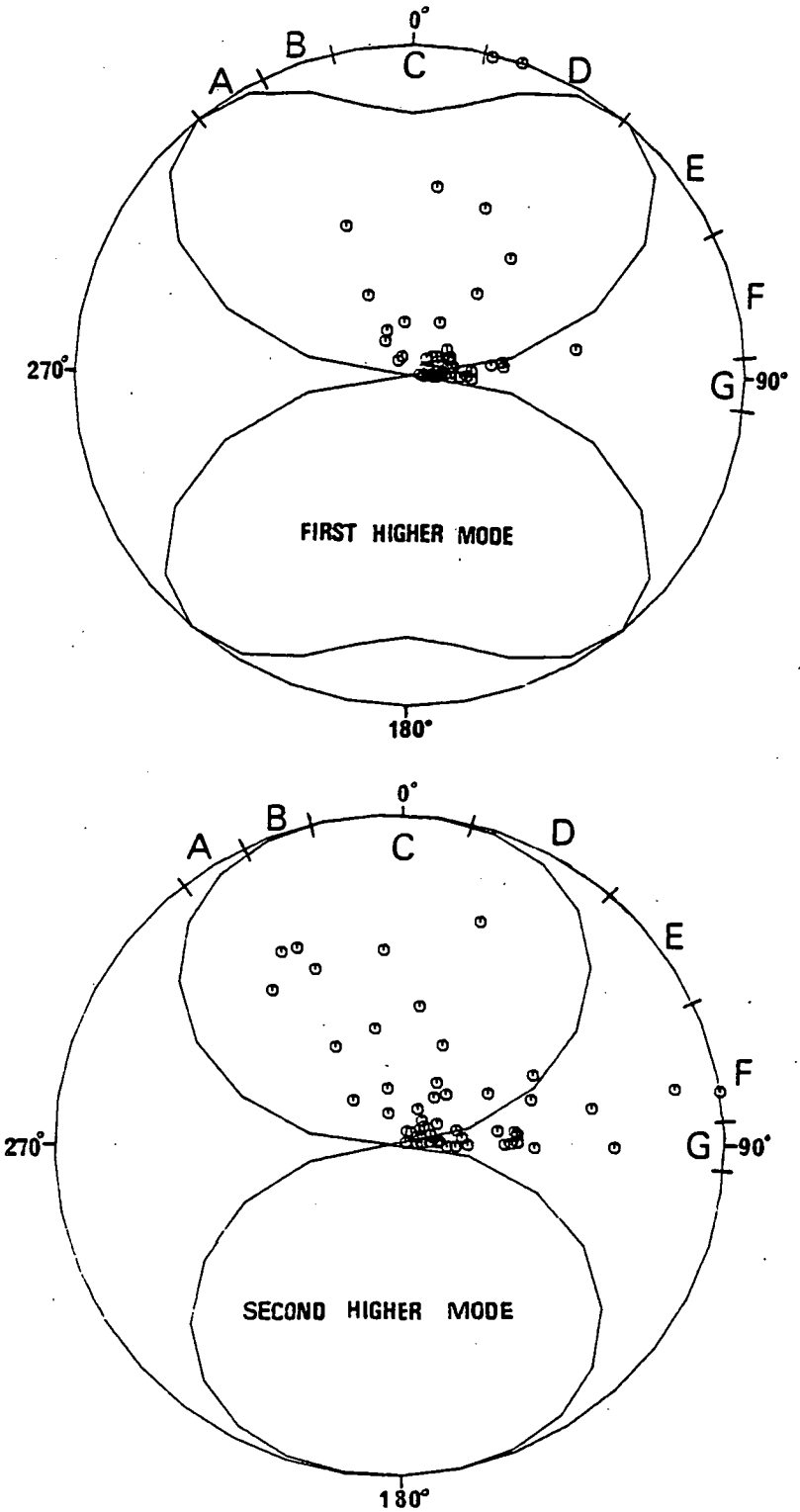

Figure 6.42. Theoretical radiation pattern contributed by medium response function $M_z(\omega; \phi)$ and observed spectral amplitudes at a frequency of 2 Hz for the first and second higher modes.

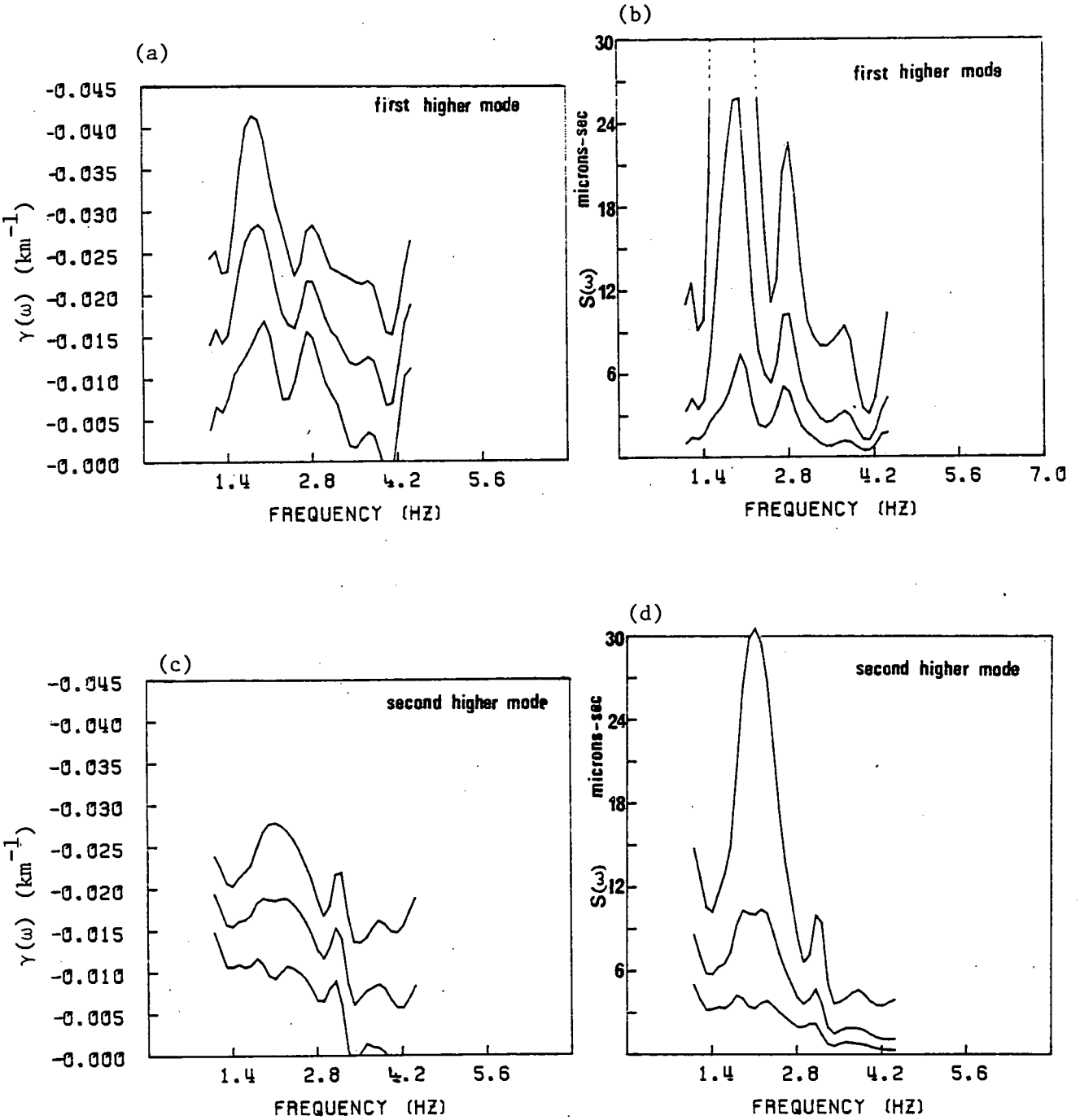

Figure 6.43 (a),(c) First and second higher mode attenuation coefficients $\gamma(\omega)$ calculated using the spectral amplitude data derived from the KEQ recordings corresponding to the group velocity regions A, B and C.

(b),(d) Source function $S(\omega) = S_o S_T(\omega)\ S_F(\omega)\ M_Z(\omega)$ calculated using this data set.

Although it is not possible to draw any further attenuation information from the results, an average of the source function yields a useful value for the seismic moment of KEQ. For this we utilize the formula:

$$S_o = \frac{< S(\omega) >}{< S_T(\omega) S_F(\omega) M_Z(\omega) >}$$

where < > represents an average taken over the frequency range of the empirical source function (1.1 - 4.4Hz). To evaluate this expression we assume a step time action, and that the effects of the source finiteness are insignificant ($S_F(\omega) \simeq 1$). Averaging the medium response at an azimuth of 45° and averaging the source function $S(\omega)$ from Figures 6.45b and 6.45d we obtain from the first higher mode data $S_o = 1.3^{+2.4}_{-0.8}\ 10^{16}$ Nm, and from the second higher mode data $S_o = 4.0^{+3.0}_{-2.3}\ 10^{15}$ Nm. These values combine to give a mean seismic moment of $S_o = 9.10^{15}$ Nm. The single moment-magnitude relation of Hanks and Kanamori (1979) predicts $S_o = 2.10^{15}$ Nm which is in good agreement with the above result.

6.5 Summary

In this chapter the single-station techniques of Chapter 5 have been applied to the amplitude spectra derived from the recordings of small underground explosions, underwater explosions, and an earthquake of surface wave magnitude 3.7 (M_L).

The underground explosion data were successfully modelled, and single-station Q_β^{-1} depth profiles and values for the source strength were obtained at each station along both the ALPHA and BETA lines. The source time action was modelled by an exponential step, and the optimum value for the inverse time constant was estimated as 24 rad^{-1}. The Q_β^{-1} results obtained using the FOB and Hedgehog inversion techniques agreed, despite the different assumptions used in the procedures. Only the Q_β^{-1} in the upper 400m of the crust was well resolved using the single-station method, and the profiles implied values of Q_β^{-1} between 0.02 and 0.09. The attenuation coefficients computed at each station were in close agreement with the pure provincial attenuation values, although there was no noticable correlation between the surface geology and attenuation values. The mean source strength value of 10^{12} Nm agreed with a theoretical prediction based on the explosive yield.

The underwater explosion data from Kirkcaldy bay could not be completely modelled due to the physical restrictions on the shot depth, thickness of the water layer, and the Q_β^{-1} values. However, well constrained Q_β^{-1} results were obtained for the upper 400m of the crust (the mean value being around 0.02) by mapping onto the high frequency slope of the spectrum. The multi-station method of obtaining the attenuation by fitting the decay of the logarithmic amplitude with distance was unsuccessful in this case. A source model consisting of only the shock wave and ensuing negative pressure of 0.8 secs duration was optimal. The source strength values were similar for all stations, but the bounds on each (especially the furthest station EAB) implied several orders of magnitude uncertainty. The mean of these estimates was 10^7 Nm, in close agreement with the theoretical value predicted

using known pressure data. The single-station attenuation coefficients were consistent with the pure-provincial coefficients for the Carboniferous and Old Red Sandstone formations in the Midland Valley of Scotland. Again there is no noticeable correlation between the single-station Q_{β}^{-1} values and the surface geology.

The higher mode spectra generated by the earthquake KEQ could not be modelled using any combination of source or medium parameters. Theoretically, a depth of 3 - 5 km into the crust was required, thus contradicting previous work which placed the earthquake at a well constrained depth of 10.6km. Consequently, attenuation values and spectral source parameters could not be resolved for this complex source using the single-station method which has been developed. An attempt to discern regional attenuation values, fault length, and dip angle by compensating for the shape of the radiation pattern at each frequency was not successful. However the results of this analysis on the spectra in the group velocity regions A, B and C yielded a reasonably constrained source function. By taking the mean value of this function, a seismic moment of 9.10^{15} Nm was computed, being in good agreement with the result from a calculation using a surface wave magnitude-to-moment relationship.

CHAPTER 7

SUMMARY AND CONCLUSIONS

7.1 Review and Interpretation of Results

The synthesis of the observed Rayleigh wave displacement field generated by a seismic source and recorded at the surface of the earth, has become increasingly more popular as a tool for elucidating the earth's structure and the properties of the source. In order to extract this information the seismogram must be related to simple parameterized models representing the non-linear source effects, propagation medium, and the recording system. Consequently, the ground motion recorded by a surface seismometer can be described by a finite set of parameters related to an equivalent elastic source, distribution of wave velocity and attenuative properties within the earth, and the response of the recording system. The character and nature of the various phenomena can therefore be evaluated by finding estimates for these parameters which satisfy the observed data, the so-called inverse problem in Seismology. To extract values for one particular set of parameters requires knowledge of the sensitivity of the displacement field to all of the parameters and/or estimates for the remaining quantities. In this thesis the principal objective was to extract the parameters relating to attenuation, and thereby obtain an estimate for the distribution of dissipative properties with depth, from the spectral amplitude of a Rayleigh wave recorded along an isolated propagation path. An additional aim was to investigate the group velocity dispersion characteristics of the Rayleigh waves and thereby estimate the distribution of wave velocity properties laterally

and with depth in the earth. The latter values were necessary for successful application of the single-station attenuation technique.

Attenuation has a pronounced effect on both the absolute amplitude and the frequency content of a recorded signal, and is essential if we hope to completely predict the Rayleigh waveform from a given source. It is also useful as a sensitive indicator of the thermal and chemical environment within the earth. Measurements of the dissipative properties of the earth are impeded by the notorious difficulty of measuring the absolute amplitudes of seismic waves. Many azimuthally dependent effects such as focussing/de-focussing, transmission across boundaries, scattering from surface irregularities and mode conversions, scale the amplitudes. Consequently, there may be very large uncertainties on measurements of attenuation based on the decay of spectral amplitude with distance across a network of many stations. Single-station evaluation of attenuation removes the influence of a number of these effects. The discrete path measurements also enhance the horizontal resolution of the dissipative structure of the earth.

The single-station attenuation method developed in this thesis was based on the expression of the overall spectrum of a Rayleigh wave in terms of a sequence of multiplicative linear functions, each representing the effect of a particular phenomenon on the wave (see Chapter 1). The work covered falls into four parts:- (a) an examination of the interactions between the seismic source and the medium in which it is embedded, and the representation of these effects in terms of the simple parameterized spectral functions (Chapters 2 and 3), (b) estimation of the shear wave velocity (β) structure - Rayleigh waves being more sensitive to variations in the shear wave constants than other quantities (c) development of the single-station attenuation

technique (Chapter 5), and (d) application of the single-station technique (Chapter 6) to obtain profiles of the shear wave specific attenuation factor (Q_β^{-1}).

(a) Source functions

There were four basic spectral functions which combined to form the source imprint on the wave spectra. These were the source strength factor, spectrum of the source time action, source finiteness factor, and the medium response which represents the physical interaction between the source and the solid medium.

Within this framework, the underground explosion process was represented by the spectrum of an exponential step time action and the interaction of three mutually orthogonal couples without moment with the medium, source finiteness having a negligible influence on the spectrum. The amplitude spectrum was determined by the explosive yield (via the source strength), inverse time constant, β structure of the propagation medium, Q_β^{-1} model and instrument parameters.

The underwater explosion had a more complex time action, it was formed by the oscillations of the bubble of gaseous by-products and reverberation of the hydro-acoustic waves in the water layer at the source. The inverse time constant of the underground explosions was replaced by the explosive yield, shot depth, and the thickness of the water layer. The force system which represented this explosion was the same as that for an underground explosion (acting in the fluid medium), and the effect of source finiteness was again negligible.

The earthquake source has a larger collection of parameters specifying the spectrum. The source strength factor can usually be related to the surface wave magnitude. The source time action was represented by an exponential ramp determined by an inverse time

constant, the medium response was determined by the three orientation parameters of the fault plane (being dip, rake, and strike), focal depth, and the β structure of the medium. The finiteness function is dependent on strike azimuth, rupture length and phase velocity. The multitude of parameters which determine the shape of this source spectrum lead to special features such as holes.

(b) Shear Velocity Structure

The results of this chapter are summarized in Table 7.1. The Rayleigh wave data were generated by small underwater explosions and an earthquake recorded on local seismograph networks in Scotland in the frequency band 0.7 - 5.5 Hz.

Single-station group velocity dispersion data were generated by eight underwater explosions in Kirkcaldy Bay recorded locally on the LOWNET array. The explosions were all at similar epicentral locations. The propagation paths were mainly influenced by the Carboniferous sediments around the Firth of Forth. Previous β models for this province possessed large velocity contrasts between the upper and lower layers. Theoretically, fundamental and higher mode Rayleigh waves propagating through this structure had particle motions of opposite sign. This phenomenon clearly identified the fundamental mode on the three component seismograms at the station EDI. The group velocity curves derived from the data were averaged over all events at each station. These were then inverted to yield accurate β profiles of the upper crust in the Midland Valley of Scotland down to depths of 1.2 - 2 km. The profiles were summarized in Figure 4.12. The group velocities showed a marked correlation with the surface geological expression for this region. Accordingly, β in the top 400m of the profiles ranged from 1.5 to 2.1 km/sec. β for each separate model

		Kirkcaldy Bay Underwater Explosions	Earthquake KEQ
	type of Rayleigh waves analysed	fundamental mode	first and second higher modes
linearized inversion to β depth models	limit of resolution for shear wave profiles	1.2 - 2 km	17 km
	shear velocity solutions	1.5 - 2.1 km/sec upper 400m, general increase with depth reaching 1.9 - 3.5 km/sec at limit of resolution	Average increase between 2 km thick top layer and lower layer of 3.1 - 3.4 km/sec. Increase from 3.4 - 3.8 km/sec between 2 and 17 km depth.
	lateral variations	- Noticeable correlation between group velocity and surface geological expression - Pure provincial inversion yielded group velocities for Old Red Sandstone and Carboniferous provinces with mean velocities 1.9 and 1.4 km/sec respectively. Errors on these curves too large to invert to β-depth models	- Area split into seven groups - Distinct 0.4 km/sec variation of group velocity across Scotland, but no correlation with surface geology. Variation smaller than for Kirkcaldy Bay data set, implying a decrease of lateral variations with depth.

TABLE 7.1 Summary of results of group velocity analysis on 0.7 - 5.5 Hz Rayleigh waves generated by different seismic sources.

increased with depth, this being consistent with surface weathering and increasing compaction with depth. As a consequence of decreasing resolution with depth, the estimates for the deepest layers were widely dispersed and ranged from 1.9 - 3.5 km/sec. A regional inversion to obtain pure-provincial group velocity curves demonstrated that the wave velocities in the geological formations decreased in the sequence:- Devonian Lavas, Old Red Sandstone, and Carboniferous sediments. The group velocities for the Old Red Sandstone and Carboniferous provinces (Figure 4.14) ranged between 1.6 and 2.3 km/sec, and 1.2 and 1.6 km/sec respectively. The Devonian Lava velocities were poorly resolved. The uncertainties on the values obtained using this method prevented further inversion to shear velocity depth models.

Rayleigh waves generated by the earthquake KEQ (with a local magnitude (M_L) of 3.7) were recorded on the short period seismometers of the LISPB array. The two prominent Rayleigh waves were identified by matching the group velocity dispersion curves with theoretical data computed using prior information for the area. In this case, the difference in the particle motions was not sufficient to identify the modes. It appeared that only the first and second higher mode waves generated by the earthquake were recorded within the instrument pass-band. The area of Scotland covered by the paths from this event were divided into seven apparently homogeneous regions on the basis of similar group velocity characteristics (see Figure 4.20). This regionalization yielded estimates of the lateral variation of the β depth distribution across western Scotland by simultaneously inverting the higher mode group velocities in each sector. Figure 4.34 summarized the shear velocity models obtained for each region. The profiles were well resolved down to depths of 17km, and showed a clear

jump of 0.3 km/sec between the 2km thick top layer and the lower layers, the shear velocity increasing on average from around 3.1 km/sec to 3.4 km/sec. This discontinuity does not necessarily indicate a transition at 2km depth, but represents the smoothed discontinuity between these layers; for example a low velocity in the upper 100m of the crust could cause this observation. There is a slight gradient between 2 and 17 km depth, increasing from 3.4 to 3.8 km/sec. β in the top layer of the models varies regionally by 0.4 km/sec, but does not correlate with the surface geological expression for the area of Scotland covered in the analysis. The profiles show less variation than the corresponding plot for the Kirkcaldy Bay data, implying a decrease of lateral inhomogeneities with increasing depth.

(c) Development of the Single-station Attenuation Technique

The development of the single-station attenuation method comprises in part of a preliminary investigation to identify the most important parameters which influence the amplitude spectrum for each different seismic source. The importance of each parameter was evaluated by the magnitude of the changes in the theoretical spectrum induced by a priori perturbations in that particular parameter, the perturbations representing realistic errors. Each source had a different set of parameters which were regarded as important. The underground explosion spectra were found to be strongly effected by the Q_β^{-1} depth distribution, and the inverse time constant and source strength must be regarded as unknown. The underwater explosion spectra were found to be strongly effected by the Q_β^{-1} depth distribution and shot depth, the source strength must be treated as an unknown. The earthquake spectra were found to be strongly effected by the Q_β^{-1} depth distribution, focal depth, dip angle, fault azimuth, and the rupture length. The source strength must again be regarded as an unknown. In general, the most

influencial parameter (for the distances used in this work) was Q_β^{-1} in the top few 100m of the upper crust. Moreover, the changes in the amplitude spectrum due to fluctuations in Q_β^{-1} for each layer of a depth model scaled directly with epicentral distance, and thus became rapidly more important with increasing range.

The results of the above analyses guided the formation of the single-station technique. This consisted of dividing the observed spectra for the weak or unimportant functions, and obtaining estimates for the remaining parameters by mapping the corrected observations onto the expected functional form. Two inversion procedures were used to implement the latter procedure, being a combination of a bounded optimization technique and simplex algorithm (FOB method), and the Hedgehog inversion method.

(d) Application of the Single-station Attenuation Technique

The major results of this chapter are summarized in Table 7.2. The spectral data were derived from recordings of small underground explosions, the Kirkcaldy Bay underwater explosions and the KEQ earthquake, recorded on the local seismograph networks in Scotland.

Before applying the single-station technique, a preliminary survey of the attenuation was attempted using an approximate formula relating the peak of the spectral amplitude to an average Q_β^{-1} value. This estimated only the order of magnitude of Q_β^{-1}.

The spectra derived from the LISPB recordings of small underground explosions were successfully modelled by the theoretical spectrum. Using the single-station procedures, Q_β^{-1} depth profiles and source strength values with uncertainty bounds were obtained at each station along the complete LISPB line (Figures 6.14, 6.15 and 6.16). The FOB

	LISPB Underground Explosions L1 and L2	Kirkcaldy Bay Underground Explosions	Earthquake KEQ
type of Rayleigh waves analysed	fundamental mode	fundamental mode	first and second higher modes
parameters which strongly influence the theoretical spectrum	source strength, inverse time constant, Q_β^{-1} depth distribution	source strength, shot depth, Q_β^{-1} depth distribution	source strength, focal depth, dip angle, fault azimuth, rupture length and Q_β^{-1} depth distribution
source solution	- inverse time constant of 24 rad^{-1} - average source strength of 10^{12} Nm - theoretical source strength of 10^{12} Nm	- bubble pulse spectrum of shock wave only and ensuing negative pressure of 0.8 secs duration - average source strength of 10^{7} Nm - theoretical source strength of 10^{8} Nm	Single-station attenuation technique not possible. Average source function calculated which gives mean seismic moment estimate of 9.10^{15} Nm. - theoretical seismic moment of 2.10^{15} Nm
Q_β^{-1} solution	0.02 - 0.09 in upper 400m < 0.01 between 400 - 800m 0.04 below 800m well resolved in upper 400m	0.02 in upper 400m < 0.01 between 400 - 800m 0.04 below 800m well resolved in upper 400m	—
lateral variations	- mean variation of about ±0.02	- mean variation of about ±0.01	—
	- no discernible correlation with surface geology		

TABLE 7.2 Summary of results obtained by applying single-station attenuation technique to 0.7 - 5.5 Hz Rayleigh waves generated by different seismic sources.

inversion technique obtained an optimal inverse time constant of 24 rad^{-1}, but this was not well resolved. The source time action corresponding to this value was essentially a Dirac impulse. This is in agreement with the source function inferred from the approximate peak frequency method. The Hedgehog inversions of the data set revealed a preference for a step time action close to the source and a Dirac impulse at distances of greater than 15km from the source. This is consistent with the reduction in the residual displacement with distance from nuclear explosions observed by Aki et al. (1974) for long period waves. One explanation of the impulse feature of this time function could be the superposition of an out-of-phase negative step function arising from the release of strain energy. An alternative reason may be expulsion of the bore-hole tamping. This relieves the intense build up of pressure which would otherwise compact the non-linear region.

The impulsive source function estimated in this analysis corresponds to an approximately constant spectral level. Consequently, the combination of this with the spectral medium response for an underground explosion yields a monotonically increasing function. This can be represented by the power law $\omega^{3/2}$ for a half-space medium. The latter conclusion agrees with the spectral source layering function derived from recordings of nuclear explosions by Marshall and Burton (1971) using a common path method.

The Q_β^{-1} results obtained using the FOB and the Hedgehog inversion techniques agreed, despite the different assumptions used in the procedures. Q_β^{-1} in the upper 400m was well resolved with a mean value of between 0.02 and 0.09. Although the uncertainties increased rapidly with depth, the results suggested a general decrease in Q_β^{-1} with depth

to values of < 0.01, followed by an increase below 800m to a mean of 0.04. The single-station solutions give an average source strength value of 10^{12} Nm (Figure 6.15) which is the same order of magnitude as the theoretical prediction. The single-station technique has a smaller depth resolution than the multi-station measurements of Evans (1981) on the same data. However the single-station technique yielded results in circumstances where the multi-station analysis failed. A mean lateral variation of Q_β^{-1} in the top 400m of the crust of ±0.02 or more was noticed. The single-station models were compared with those obtained from the multi-station method by evaluating attenuation coefficients for each profile and station (see Figure 6.17). The results were in close agreement, although there are clearly several anomalous measurements corresponding to the assumptions of an attenuation half-space. There was no correlation between the surface geology and lateral variations in Q_β^{-1}, emphasizing that the effects of attenuation cannot be simply averaged.

The spectra derived from recordings of the underwater shots on the LISPB and LOWNET arrays had similar characteristics. They possessed a very narrow bandwidth, sharp low frequency drop-off, and an invariant peak frequency with distance. The spectra of the LISPB shots could not be modelled by physically reasonable values of the parameters describing the theoretical spectrum. The high frequency portion of the Kirkcaldy Bay spectra was successfully used in the attenuation measurements. Again, the Q_β^{-1} results from the FOB Hedgehog inversion techniques were similar (Figure 6.35). The optimal value of the source function computed using the FOB inversion procedure corresponded to the signal generated by a shock wave and an ensuing negative pressure of 0.8 secs duration. This was expected from an

analysis of migration and sea-bottom effects. The Q_β^{-1} profiles displayed similar characteristics to those previously obtained for the LISPB data. A Q_β^{-1} of 0.02 can be resolved for the top 400m of the upper crust, below this the bounds on many of the values became large and they were effectively unresolved. There was a general decrease of Q_β^{-1} to < 0.01 between 400 - 800m, and then an increase to a mean value of 0.04 below 800m depth. The mean source strength value obtained from these solutions is 10^7 Nm (Figure 6.34), differing by one order of magnitude from the predicted value of 10^8 Nm. A calculation of the attenuation coefficient $\gamma(\omega)$ using the decay of amplitude over a number of stations gave values with large uncertainties which could not be inverted to give well resolved Q_β^{-1} depth models (Figure 6.22). Therefore the single-station methods in this case obtained attenuation information from the spectra which could not be extracted using the multi-station technique. This data suggested a lateral variation of less than ± 0.01. Comparing the single-station attenuation coefficients with the pure provincial coefficients (Figure 6.37) again indicated that there was no discernible correlation with the surface geological expression, and no clear azimuthal trend.

Neither the first nor the second higher mode spectra for the earthquake KEQ could be modelled using the theoretical spectrum. The observed spectra contained coherent energy up to 5.5 Hz, but theory sets the high frequency limit at between 2.5 - 3.0 Hz. A depth of around 2 - 5 km could account for these observations, but this was contrary to the well resolved focal depth solution of Assumpção (1981) who gave 10.6km. The spectral data was grouped according to the group regions A-C, D-E, and F-G. An attempt to deduce the attenuation using

the decay of spectral amplitude with distance, by correcting the data for the radiation pattern and directivity of the finiteness function, yielded similar results to the uncorrected data. Consequently, the attenuation analysis was performed using a fixed model given by the Assumpção (1981) solution and a negligible rupture length. There were large uncertainties in both the attenuation coefficient and source function obtained using this method, and only those for groups A - C were reasonable enough to display. Although the uncertainties on these attenuation coefficients were too large to invert to well constrained Q_β^{-1} values, the frequency averaged source function provided a good estimate of the seismic moment of 9.10^{15}Nm which was in agreement with the value of 2.10^{15}Nm obtained using a single moment-magnitude relation.

Both sets of Q_β^{-1} profiles agree with the general trend of between 0.02 and 0.09 in the upper 400m of the crust, a zone of low Q_β^{-1} (< 0.01) between 400 - 800m, and then an increase to about 0.04 at depths below 800m. As measurements of rocks under laboratory conditions and at seismic frequencies give a Q_β^{-1} of < 0.01, there must be mechanisms in addition to internal friction causing the dissipation of seismic energy in the upper few 100m of the crust. The non-correlation with surface geology emphasizes this conclusion.

Apart from the weathered layer, the rock structure at and near the earth's surface will contain intersecting families of cracks, large cracks, joints, dipping and irregular boundaries, and irregularities in surface topography. A possible cause of the dissipation in the upper crust could be scattering from these distributed inhomogeneities and irregularities. The resulting attenuation is likely to be highly frequency dependent (Jackson and Anderson, 1970). When a medium

contains inhomogeneities with a scale length comparable to the seismic wavelength, significant scattering will occur (Aki, 1980). This gives a qualitative assessment of the average scattering length of around 600m. A cross-section of the relief along the LISPB line reveals undulations in the earth's surface of 200 - 400m. It is therefore quite probable that scattering from the surface relief could play an important part in determining the attenuation properties of the 0.7 - 5.5 Hz Rayleigh waves with wavelengths in the range 0.2 - 5km. Rayleigh to Rayleigh scattering from small topographic irregularities have been discussed by Hudson and Knopoff (1967). Scattering from large scale obstacles greater than a seismic wavelength causes a general loss of Rayleigh wave energy. This may be construed as an increase in Q_β^{-1}, but the process will also modify the general spectral shape (Momoi, 1982). The Rayleigh wave energy may also scatter from dry or water filled cracks. An interesting result arises if we assume that the shear wave velocity in the upper 2km of the KEQ profiles is influenced by a similar mechanism as the attenuation in the upper few 100m of the crust. In order to simultaneously satisfy the jump of 0.3 km/sec at the lower crustal depths and a Q_β^{-1} of 0.02, the formulae of Hudson (1981) imply that the crack length must be 500m and the crack density $0.4 km^{-3}$. The decrease of attenuation and increase in velocity can thus be explained by the closing or disappearance of these cracks under increasing hydrostatic pressure. Another relevant mechanism may be the increase in porosity of the rocks, which leads to a corresponding increase in Q_β^{-1} with depth. In practice it is probable that the magnitude and distribution of Q_β^{-1} in the upper crust results from the action of more than one mechanism, the total attenuation being the sum of the individual Q_β^{-1}'s contributed from the separate effects.

To isolate each contribution it is necessary to obtain diagnostics which will distinguish between the attenuation due to scattering losses and intrinsic friction. Some progress in this direction has been made by Richards and Menke (1983).

7.2 Some Implications of the Single-station Attenuation Results

If the lateral variations in attenuation measured above for Scotland are indicative of variations in other crustal regions of the earth, this has important consequences on magnitude determinations for small local earthquakes. Calculations based on the general surface wave magnitude formula (Båth, p387, 1974) and the theoretical spectral amplitude in Chapter 1 imply that a lateral variation of ± 0.02 km^{-1} in the attenuation coefficient (about ± 0.02 in Q_β^{-1}) at 1 Hz will lead to a magnitude difference of ± 0.5 at moderate distances of 25km, and rises to ± 1 at 50km.

The medium response for earthquakes has a dramatic effect on the shape and absolute level of the Rayleigh wave spectrum as it can produce spectral holes and a variety of radiation patterns. Source finiteness effects also modulate the spectra and radiation pattern. Lateral variations in $\gamma(\omega)$, defocussing/focussing, multi-pathing, transmission coefficients, and other path effects also lead to an azimuthal variation in the absolute amplitude. Consequently, values of the source strength or seismic moment for an earthquake calculated over a region have large errors - the moment obtained for KEQ had uncertainties close to $\pm 90\%$. The results of the single-station measurements made in this thesis suggest that to measure the source strength, careful selection of the data must be made to ensure that

there are no minima due to either the source finiteness or focal depth effects in the spectrum. It is also necessary to fully investigate lateral variations in attenuation for the particular region. However the similarity between the seismic moment obtained using an average of the medium response with the value computed using surface wave magnitude emphasized that it is unnecessary to account for the radiation pattern except in cases where there are a large number of stations.

Discrimination between earthquake and explosion sources requires an efficient and accurate means of separating the source function, containing source strength, spectrum of the time action, finiteness factor and medium response, from the propagation and recording effects. Significant features such as holes in the earthquake medium response and the finiteness function can readily be identified, and thus provide a reliable method of clearly distinguishing events. In the general case in which such identifying characteristics are absent, one must extract a set of source parameters which together imply the nature of a particular event. The single-station technique developed and applied in this thesis has underlined the importance in having accurate values of attenuation available in such studies. Attenuation strongly influences the spectra and will mask many of the vital identifying source parameters. This was evaluated in the single-station measurements where a trade-off was found between the source strength and attenuation. Consequently an incorrect estimate of attenuation could produce a spurious value for the source parameter (Solomon, 1972) and thus an incorrect identification. Lateral variations will also effect the accuracy of the discrimination procedure.

7.3 Suggestions for Improvement and Future Work

There are two basic regions in which the present work can be extended and improved, these being the actual method of determining single-station attenuation measurements - methods for obtaining the Rayleigh wave group velocity and amplitude spectra, and the areas of research which would aid the interpretation of the various characteristics of high frequency Rayleigh waves.

It was shown during the development of the single-station procedure that the specific source determines the number and type of parameters to be estimated from the corrected spectrum, and therefore the approach of the single-station method must follow different lines in each case. The source also dictates the resolution of the Q_β^{-1} values. Clearly, a more satisfying method is one in which there is a unified approach for all events, one scheme covering all cases. This could be obtained by developing a technique which eliminates the dependence on the source parameters by estimating the source spectral function directly. Various source models can then be independently mapped onto the estimated source function. An approach for separating these functions has been pursued by Dahlman (1974), but this does not take account of lateral variations.

The techniques for obtaining the Fourier transform of the seismic signal and the correction for the instrument response, introduce a systematic bias in the amplitudes. To investigate these it would be instructive to devise a single-station scheme whereby the inversion could be carried out in the time domain, and the results compared to those obtained by the spectral method.

The single-station analysis has been applied to data with similar

frequency content and for similar areas. Applying the method to other frequencies and geographical areas would provide information on the extent to which the results are method-dependent or data-dependent. For example, the schemes could be applied to teleseismic data on a global scale.

In analysing the data, it became clear that the techniques for obtaining the group velocities and spectra of the high frequency Rayleigh waves need further improvement, especially in the identification and selection of fundamental and higher mode waves, and methods developed to isolate the particular mode from the seismogram. The solution to this could be array processing techniques such as those utilized by Cara (1978), or stacking of seismograms (Goncz and Hannan, 1975), and increasing the station density.

If high frequency 0.7 - 5.5 Hz Rayleigh waves are to provide seismically informative data on the properties of the rocks in the upper crust then one must improve instrumentation, methods of isolating and identifying the prominent Rayleigh modes (as above), and extend the records to lower frequencies. It would also be advantageous to investigate scattering effects in the upper crust, with particular emphasis on the ways of eliminating these from the seismogram or using the scattered surface waves to obtain an estimate of Q_β^{-1}. Q_β^{-1} in the upper few km of the crust needs resolving in greater detail before a mechanism can be discerned. To achieve this objective it would probably be necessary to use measurements of more than one seismic wave phase.

7.4 Final Conclusions

The main aim of the project was to develop a single-station method for measuring the Q_β^{-1} depth distribution along a single event-station path. It was also aimed to obtain regionalized β depth models using group velocity dispersion data. These have been accomplished using recordings of 0.7 - 5.5 Hz Rayleigh waves generated by underground explosions, underwater explosions, and a small earthquake (M_L = 3.7) recorded on local networks.

The single-station attenuation method was successful in estimating Q_β^{-1} values (0.02 - 0.09) for the upper 400m of the crust in Scotland, and these were resolved for distances of up to 50km from the source. Parameters relating to the seismic source were also discerned. The technique works best for fundamental mode Rayleigh waves generated by underground explosions.

Fundamental mode data yielded β models at depths of 1.2 - 2 km into the crust. First and higher mode data generated by the earthquake was inverted to given β models of the crust down to a depth of 17km.

The lateral variations in attenuation do not appear to depend on the surface geological features, unlike the fundamental mode velocity dispersion characteristics. The single-station technique could be improved by applying more constraints on the system and independently estimating the source and attenuation function. This would enable a more accurate monitoring of the lateral variations in attenuation and determination of the parameters of the seismic source.

APPENDIX A

CALCULATIONS OF THE RAYLEIGH WAVE MEDIUM RESPONSE AND VELOCITY DISPERSION

A.1 Introduction

In the first two sections of this appendix, simple analytic expressions will be derived for the Rayleigh wave medium response function $M_z(\omega)$, corresponding to an underground and underwater explosion. These sources will be represented by a system of body forces acting at a point in a solid half-space, and in a semi-infinite fluid overlying the half-space respectively.

The final section will present a formula based on the Thomson-Haskell matrix method for computing the medium response of a horizontally stratified solid excited by a seismic source incorporated into this framework. The associated problem of Rayleigh wave dispersion for this medium will be considered. Finally, we will describe the way in which this theory was implemented for the work in this thesis which involved high frequencies of 5.5 Hz and higher mode Rayleigh waves.

A.2 Calculation of Underground Explosion Medium Response

Assume an homogeneous, solid, elastic half-space underlying a vacuum (atmosphere neglected),with body wave velocities α, β, density ρ, and Lamé constants λ, μ. An explosive source is embedded in the medium at a depth z_s. We consider the problem in the framework of a three dimensional cylindrical coordinate

system (r, ϕ, z); the free surface is at $z = 0$. Further, axial symmetry is imposed on the system by drawing the vertical z-axis down through the source point. This reduces the number of dimensions to two, r and z (Figure A.1a).

The spherically symmetric distribution of couples without moment, which represents the explosion process, is a perfect generator of P-waves. For such a source we set the shear wave vector potential to zero: $\underline{\Psi} = \underline{0}$. The compressional wave potential Φ generated by a unit dilatation is simply expressed in terms of spherical polar coordinates:

$$\Phi^S(R;t) = \frac{1}{4\pi\rho\alpha^2 R} \exp\{-i(k_\alpha R - \omega t)\}$$

where $R = (z^2 + r^2)^{\frac{1}{2}}$ and $k_\alpha = \omega/\alpha$. This is a solution of the scalar wave equation with the spherical dilatation as forcing function, the time action being $\delta(t)$. In the subsequent equations a harmonic time dependence will be implicitly assumed. The P-wavefield emitted by the source propagates unrestricted to the free surface. At this boundary a strong interaction between P and SV wavefields occurs, and the energy partitions into reflected P and SV motions (Figure A.1a).

To facilitate the calculations, the spherical waves are expressed as a superposition of cylindrical waves via the Sommerfeld integral (Båth, 1968)

$$4\pi\rho\alpha^2\Phi^S \rightarrow \int_0^\infty J_0(\kappa r)e^{-m|z|} \frac{\kappa d\kappa}{m}$$

where κ is the horizontal wavenumber, $m = (\kappa^2 - k_\alpha^2)^{\frac{1}{2}}$ $(Re(m) \geq 0)$.

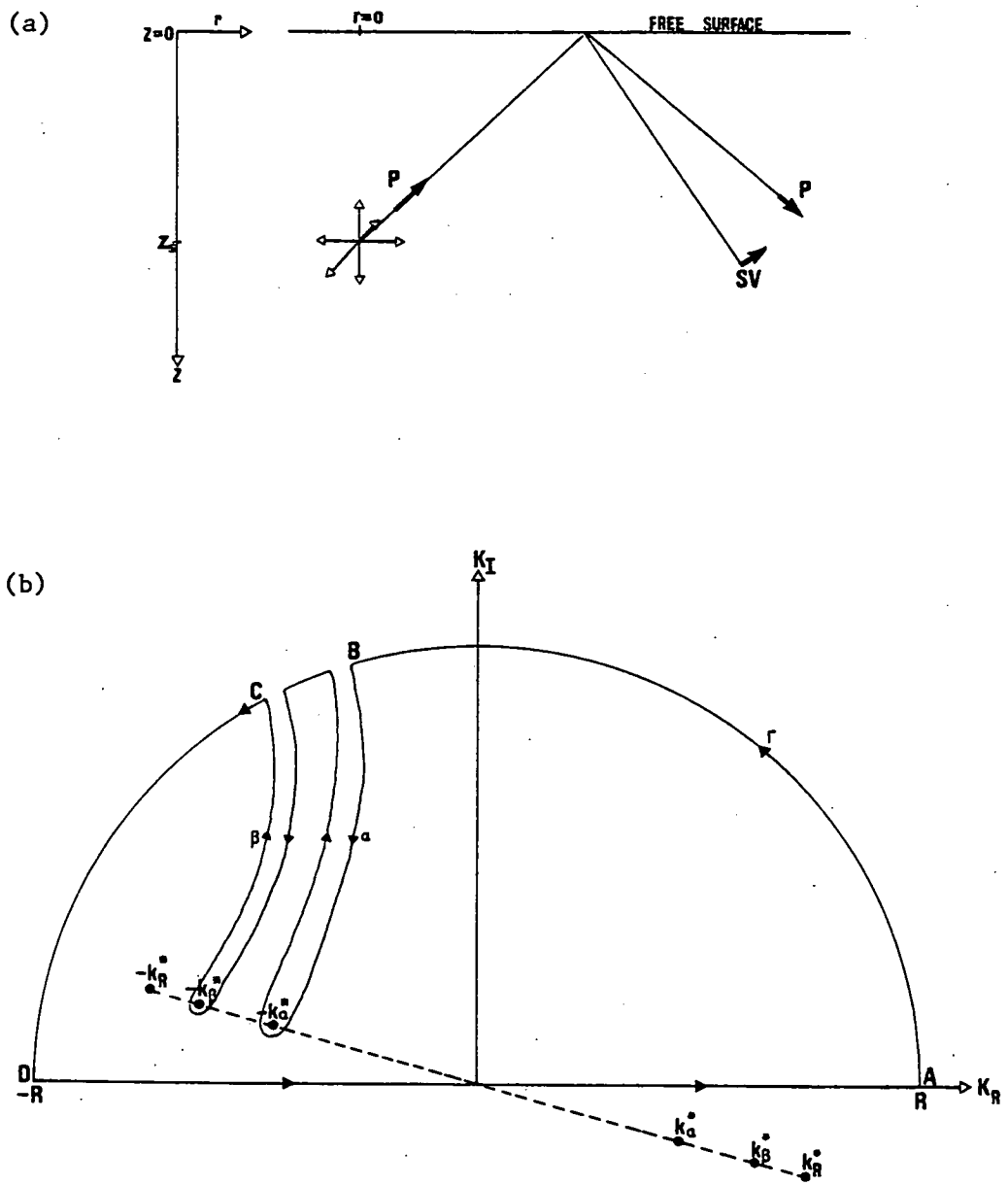

Figure A.1. (a) Reflection of compressional waves from the free surface of a solid half-space.
(b) Contour for evaluation of wavenumber integral.

Each cylinder wave component gives rise to reflected P and SV waves. The total cylindrical potentials Φ_{TOT} and Ψ_{TOT} in the half-space, for a particular wavenumber, can be written:

$$\Phi_{TOT} = \underbrace{\Phi_{inc}}_{\text{(incident)}} + \underbrace{\Phi_{refl}}_{\text{(reflected)}} \equiv J_o(\kappa r)e^{-m|z-z_s|} + B\, J_o(\kappa r)e^{-m|z+z_s|} \tag{A.1}$$

$$\Psi_{TOT} = \underbrace{\Psi_{refl}}_{\text{(reflected)}} \equiv C\, J_o(\kappa r)e^{-mz_s - nz} \tag{A.2}$$

where Ψ is the SV component of the shear wave potential, B and C are reflection coefficients, and $n = (\kappa^2 - k_\beta^2)^{\frac{1}{2}}$: $k_\beta = \omega/\beta$, $Re(n) \geq 0$. The boundary conditions of the system are given by the two components of stress P_{zz} and P_{zr}, normal and tangential to the free surface, which must be zero at $z = 0$.

These stress components are related to the displacements via

$$\left.\begin{aligned} P_{zz} &= \lambda \underline{\nabla}\cdot\underline{A} + 2\mu\, \partial A_z/\partial z \\ P_{zr} &= \mu\left(\frac{\partial A_r}{\partial z} + \frac{\partial A_z}{\partial r}\right) , \end{aligned}\right\} \tag{A.3}$$

and the displacements are given by the potentials using

$$\left.\begin{aligned} A_r &= \partial\Phi/\partial r + \partial^2\Psi/\partial r\partial z \\ A_z &= \partial\Phi/\partial z - \frac{1}{r}\frac{\partial}{\partial r}(r\partial\Psi/\partial r) \end{aligned}\right\} \tag{A.4}$$

Applying the conditions to each cylindrical wave leads to

$$\begin{bmatrix} m^2(\lambda + 2\mu) - \lambda\kappa^2 & 2\mu n\kappa^2 \\ 2m & n^2 + \kappa^2 \end{bmatrix} \begin{bmatrix} B \\ C \end{bmatrix} = \begin{bmatrix} -m^2(\lambda + 2\mu) + \lambda\kappa^2 \\ 2m \end{bmatrix}$$

from which one may obtain B and C explicitly as functions of κ:

$$B = \frac{4\kappa^2(\kappa^2 - k_\alpha^2)^{\frac{1}{2}}(\kappa^2 - k_\beta^2)^{\frac{1}{2}} + (2\kappa^2 - k_\beta^2)^2}{F(\kappa)}$$

$$C = \frac{-4(\kappa^2 - k_\alpha^2)^{\frac{1}{2}}(2\kappa^2 - k_\beta^2)}{F(\kappa)}$$

where $F(\kappa) = 4\kappa^2(\kappa^2 - k_\alpha^2)^{\frac{1}{2}}(\kappa^2 - k_\beta^2)^{\frac{1}{2}} - (2\kappa^2 - k_\beta^2)^2$ - this is commonly called the 'Rayleigh function'. The radial and vertical surface displacements A_r and A_z corresponding to the total potentials are given by substituting these values into Equations A.1, A.2 and A.4 and integrating over the semi-infinite range of wavenumber

$$A_r = -\int_0^\infty \frac{4(\kappa^2 - k_\beta^2)^{\frac{1}{2}}k_\beta^2\kappa^2 J_1(\kappa r)e^{-(\kappa^2 - k_\alpha^2)^{\frac{1}{2}}z_s}}{4\pi\rho\alpha^2 F(\kappa)}\, d\kappa \qquad (A.5)$$

$$A_z = -\int_0^\infty \frac{2(2\kappa^2 - k_\beta^2)k_\beta^2 J_0(\kappa r)e^{-(\kappa^2 - k_\alpha^2)^{\frac{1}{2}}z_s}}{4\pi\rho\alpha^2 F(\kappa)}\, d\kappa \qquad (A.6)$$

To solve the integrals we replace the Bessel function by two Hankel functions of first and second kind

$$J_n(\kappa r) = \tfrac{1}{2}(H_n^{(1)}(\kappa r) + H_n^{(2)}(\kappa r)) \quad .$$

As $H_n^{(2)}(\kappa r) = -H_n^{(1)}(-\kappa r)$, the semi-infinite limits can be replaced by limits between $-\infty$ and $+\infty$ if $J_n(\kappa r)$ is set to $\frac{1}{2}H_n^{(1)}(\kappa r)$.

Consider the solution of Equation A.6 for the vertical displacement. If one observes the source at far-field distances ($\kappa r >> 1$), then the Hankel function can be replaced by its asymptotic expansion

$$H_o^{(1)}(\kappa r) \rightarrow \left(\frac{2}{\pi\kappa r}\right)^{\frac{1}{2}} e^{-i(\kappa r - \pi/4)} .$$

The integral can now be written

$$A_z = \frac{1}{4\pi\rho\alpha^2} \left(\frac{2}{\pi r}\right)^{\frac{1}{2}} e^{i\,\pi/4} \int_{-\infty}^{\infty} \frac{k_\beta^2 \kappa^{\frac{1}{2}} (2\kappa^2 - k_\beta^2) e^{-(\kappa^2 - k_\alpha^2)^{\frac{1}{2}} z_s - i\kappa r}}{F(\kappa)} d\kappa . \qquad (A.7)$$

This cannot be solved by conventional deterministic methods, but is relatively straightforward if one applies contour integration techniques. In these, the real variable κ is generalized to a complex variable κ^*

$$\kappa^* = \kappa_R + i\kappa_I .$$

The integration path is along the real axis in the complex κ^* plane. Poles of the integrand are found as roots of the equation:

$$F(\kappa^*) = 0$$

which yields two real roots, $\kappa^* = \pm 1.09 k_\beta$. In addition, there are four branch points at $\kappa^* = \pm k_\alpha$ and $\pm k_\beta$. As the path of integration is not permitted to pass through these points, a small imaginary part ε is introduced into ω (Ewing, Jardetsky and Press, 1957)

$$\omega^* = \omega + i\varepsilon .$$

The branch points and poles are now located on a straight line at an angle $\tan^{-1}(\varepsilon/\omega)$ to the real axis (Figure A.1b). A closed semicircular contour Γ is constructed in the upper half of the complex plane which entirely encloses the pole. To prevent abrupt changes in the radicals, two hyperbola-shaped branch cuts are introduced,

the path deforming to navigate these. By the Residue theorem:

$$\oint_{\Gamma} I(\kappa^*)d\kappa^* = 2\pi i \sum \text{residues of integrand}$$

where $I(\kappa^*)$ is the integrand of Equation A.7. From Figure A.1b

$$\oint_{\Gamma} I(\kappa^*)d\kappa^* = \int_{-R}^{R} I(\kappa^*)d\kappa^* + \int_{A}^{B} I(\kappa^*)d\kappa^* + \int_{D}^{\alpha} I(\kappa^*)d\kappa^* + \int_{\beta}^{\alpha} I(\kappa^*)d\kappa^* + \int_{C}^{\beta} I(\kappa^*)d\kappa^* \quad .$$

The second and fifth integrals $\rightarrow$ zero as $R \rightarrow \infty$, and so on re-arranging:

$$\int_{-\infty}^{\infty} I(\kappa^*)d\kappa^* = \int_{\alpha}^{\beta} I(\kappa^*)d\kappa^* + \int_{\beta}^{\alpha} I(\kappa^*)d\kappa^* - 2\pi i \sum \text{residues of integrand}$$

The last term on the R.H.S. corresponds to the contribution from the pole and represents the Rayleigh wave field with wavenumber k_R. The former two branch line integrals relate to reflected P or SV waves and head waves. This solution is valid in the limit $\varepsilon \rightarrow 0$. The residue from the simple pole of order unity is

$$\lim_{\kappa^* \rightarrow k_R} (\kappa^* - k_R)G(\kappa^*)$$

Using l'Hôpital's rule one obtains the vertical displacement

$$A_z = \frac{-i}{\rho\alpha^2}\left(\frac{k_R}{2\pi r}\right)^{\frac{1}{2}} \frac{k_\beta^2(2k_R^2 - k_\beta^2)}{dF(k_R)/dk_R} e^{-(k_R^2-k_\alpha^2)^{\frac{1}{2}}z_s} e^{i(\pi/4 - k_R r)} \text{ (per unit source strength)} \qquad \text{(A.8)}$$

Writing $k_R = \omega/c_R$, where c_R is the Rayleigh wave velocity, a simple frequency dependence for the medium response defined in Equation 1.5 is readily obtained

$$M_z(\omega) = G\omega^{3/2} e^{-\omega m z_s} N^{-1} \qquad (A.9)$$

where G and m are constants dependent on the elastic properties of the half-space. For $\beta = 2.5$ km/sec, $\rho = 2.5$ g/cm^3 and a Poisson's ratio of $^1/4$, $G = 1.9 \times 10^{-17}$ N^{-1}s$^{3/2}$

A.3 Calculation of Underwater Explosion Medium Response

The explosion process is modelled as a P-wave source suspended in a semi-infinite elastic fluid, at a depth z_s, overlying a solid half-space. The fluid is specified by the elastic constants λ_1, ρ_1 and α_1, and the solid by the set λ_2, μ_2, ρ_2, α_2 and β_2. If the water has a free surface, the reverberation response can be separated from medium response $M_z(\omega)$ if the seismometer is on the solid, this is not discussed further.

The spherical compressional wavefield generated by the source interacts with the fluid-solid interface giving rise to a reflected P motion in the fluid and P and SV motions in the solid (Figure A.2). In a similar manner to above, one can express the incident spherical potential as a superposition of cylindrical waves. Denoting parameters in the fluid medium by the subscript '1', and those in the solid medium by the subscript '2', the total shear and compressional potentials, for a particular wavenumber κ, can be written:

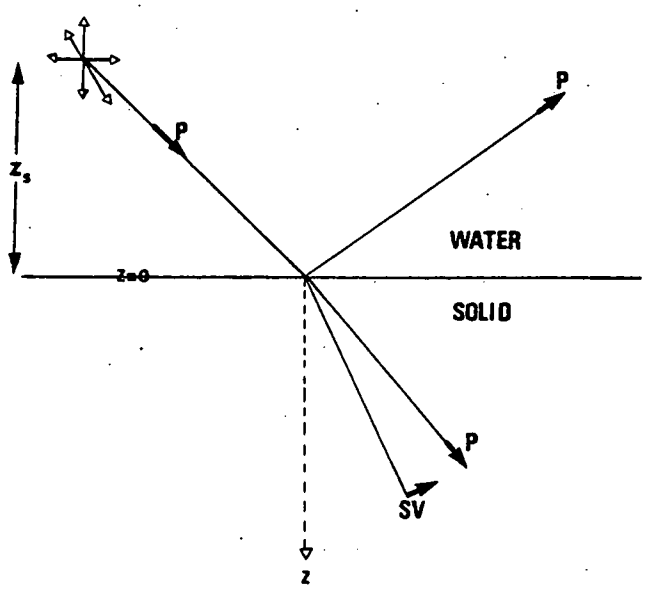

Figure A.2. Reflection and refraction of compressional waves at an interface between a fluid and a solid.

$$\phi_{1(TOT)} = \phi_{1(inc)} + \phi_{1(refl)} \equiv J_o(\kappa r)e^{-m_1|z-z_s|}$$

$$+ BJ_o(\kappa r)e^{-m_1|z+z_s|}$$

$$\phi_{2(TOT)} = \phi_{2(trans)} \equiv C\, J_o(\kappa r)e^{-m_2|z| - m_1 z_s}$$

$$\psi_{2(TOT)} = \psi_{2(trans)} \equiv D\, J_o(\kappa r)e^{-n_2|z| - m_1 z_s} .$$

Again, the reflection coefficients may be evaluated by imposing boundary conditions on the system. In this case there are three conditions, being continuity of normal displacement and stress at $z = 0$, and vanishing tangential stress at this surface (as a fluid cannot support this motion). Substituting the potentials above into Equations A.3 and A.4, one obtains the matrix equations:

$$\begin{bmatrix} m_1 & m_2 & \kappa^2 \\ \gamma_1 & \gamma_2 & 2\mu_2 n_2 \kappa^2 \\ 0 & 2\mu_2 m_2 & \gamma_2 \end{bmatrix} \begin{bmatrix} B \\ C \\ D \end{bmatrix} = \begin{bmatrix} m_1 \\ -\gamma_1 \\ 0 \end{bmatrix}$$

where $\gamma_1 = \lambda_1(\kappa^2 - m_1^2)$ and $\gamma_2 = \mu_2(\kappa^2 + n_2^2)$,

or $$\Lambda \underline{x} = \underline{b} ,$$

the solution of which is

$$\underline{x} = \frac{\Lambda^\dagger}{|\Lambda|}\, \underline{b} \qquad (A.10)$$

where $\Lambda^\dagger$ is the transpose of the matrix of cofactors, and $|\Lambda|$ is the determinant of Λ. The latter is easily obtained

$$|\Lambda| = m_1[\gamma_2^2 - 4\mu_2^2 m_2 n_2 \kappa^2 + \gamma_1 \mu_2 m_2 k_{\beta 2}^2]$$

$$= m_1 \mu_2^2 \left(F(\kappa) + \frac{\lambda_1 m_2 k_{\alpha 1}^2 k_{\beta 2}^2}{m_1 \mu_2}\right) \qquad \text{(A.11)}$$

$$\equiv m_1 \mu_2^2 F_f(\kappa)$$

where $F(\kappa)$ is identified as the Rayleigh function in the previous problem, the second function being an additional term due to the presence of the fluid. The adjoint matrix is

$$\Lambda^+ \equiv \begin{bmatrix} m_1\mu_2^2 F(\kappa) & 2\mu_2 m_2 \kappa^2 - m_2\gamma_2 & 2\mu_2 m_2 n_2 \kappa^2 - \gamma_2 \kappa^2 \\ -\gamma_1\gamma_2 & m_1\gamma_2 & -2\mu_2 m_1 n_2 \kappa^2 + \gamma_1 \kappa^2 \\ 2\mu_2 m_2 \gamma_1 & -2\mu_2 m_1 m_2 & -m_1\gamma_2 + m_2\gamma_1 \end{bmatrix} \qquad \text{(A.12)}$$

From Equations A.10, A.11, and A.12 one can obtain B, C and D explicitly as functions of κ

$$B = \frac{m_1 \mu_2^2 F(\kappa) - \lambda_1 \mu_2 m_2 k_{\alpha 1}^2 k_{\beta 2}^2}{m_1 \mu_2^2 F_f(\kappa)}$$

$$C = \frac{-2\lambda_1 \mu_2 k_{\alpha 1}^2 (\kappa^2 - k_{\alpha 1}^2)^{\frac{1}{2}} (2\kappa^2 - k_{\beta 2}^2)}{m_1 \mu_2^2 F_f(\kappa)}$$

$$D = \frac{4\lambda_1 \mu_2 k_{\alpha 1}^2 (\kappa^2 - k_{\alpha 1}^2)^{\frac{1}{2}} (\kappa^2 - k_{\alpha 2}^2)^{\frac{1}{2}}}{m_1 \mu_2^2 F_f(\kappa)} \; .$$

The vertical interfacial displacement in the solid, corresponding to the summation over all wavenumbers κ, is therefore

$$A_z = -\int_0^\infty \frac{m_2 k_{\alpha 1}^2 k_{\beta 2}^2}{2\pi m_1 \mu_2 F_f(\kappa)} J_o(\kappa r) e^{-(\kappa^2 - k_{\alpha 1}^2)^{\frac{1}{2}} z_s} \kappa d\kappa \; . \qquad \text{(A.13)}$$

To solve this integral we apply similar techniques to those used to solve Equation A.6. In addition to the branch points at $\pm k_{\alpha 2}$ and $\pm k_{\beta 2}$, we must consider branch points at $\pm k_{\alpha 1}$ corresponding to water waves. Under certain conditions the Rayleigh waves transform into Stoneley waves.

From the residue of the simple surface wave pole one obtains the vertical displacement

$$A_z = \frac{i}{2m_1\mu_2}\left(\frac{2k_R}{\pi r}\right)^{\frac{1}{2}} \frac{k_{\alpha 1}^2\, k_{\beta 2}^2\, m_2}{dF_f(\kappa_R)/dk_R}\, e^{-(k_R^2-k_{\alpha 1}^2)^{\frac{1}{2}} z_s}\, e^{i(\pi/4 - k_R r)} \quad \text{(A.14)}$$

(per unit source strength)

Following the convention described in Chapter 2 for defining the medium response for underwater explosions:

$$M_z(k_R) = \frac{\omega_o^2}{m_1\mu_2\alpha_1^2}\left(\frac{k_R}{2\pi}\right)^{\frac{1}{2}} \frac{k_{\beta 2}^2\, m_2}{dF_f(k_R)/dk_R}\, e^{-(k_R^2 - k_{\alpha 1}^2)^{\frac{1}{2}} z_s} \quad \text{(A.15)}$$

where $\omega_o = 1\,\text{rad}^{-1}$. Using the same elastic constants for the solid as in the underground explosion problem, a simple frequency dependence for the medium response is obtained.

$$M_z(\omega) = E\omega^{-\frac{1}{2}}\, e^{-\omega m_1 z_s}\, N^{-1} \quad \text{(A.16)}$$

where E and m_1 are constants dependent on the elastic properties of the media. Values of $\rho_1 = 1.5\ \text{g/cm}^3$, $\alpha_1 = 1.5$ km/sec, and $F_f(k) \simeq F(k)$, give $E = 4.4 \times 10^{-17}\ N^{-1}\ s^{3/2}$.

A.4 Spectral Response and Dispersion of Rayleigh Waves for a Stratified Medium

The matrix methods widely used today to compute the properties of elastic waves propagating in a layered solid medium originate from the matrix theory of Thomson (1950). This work was corrected by Haskell (1953) and used to calculate Rayleigh wave dispersion in a stratified earth. Subsequent to this, the method was developed and applied to the theoretical prediction of fundamental and higher mode spectra and radiation patterns, generated by a general source at depth (Haskell, 1964a; Ben-Menahem and Harkrider, 1964; Harkrider, 1964; Harkrider, 1970; Panza et al., 1973; Panza et al., 1975a,b, and many others). This theory has particular relevance to the earthquake KEQ analysed in this thesis as this source generated first and second higher mode Rayleigh waves. Here we follow the theory of Hudson (1969a,b), which was used by Douglas et al. (1972) to model synthetic seismograms.

A seismic source is incorporated into the Thomson-Haskell matrix theory by expressing the physical interaction with the solid as a discontinuity in stress, displacement, or their derivatives in a horizontal plane. Haskell (1964a) transformed several simple body force systems into this form. Hudson (1969a) generalized this representation by showing that a system of forces or a discontinuity in displacement or stress, or their derivatives across an arbitrarily orientated element of surface can be translated in terms of the Haskell horizontal source.

The essence of the Thomson-Haskell method is the formation of stress-motion vectors which are related to the displacements and stresses via a Fourier-Bessel transform. These considerably simplify

the equations of motion for the system. By imposing similar radiation constraints to those in Sections A.2 and A.3 and solving the resulting equations, the displacement field is obtained as an inverse integral. The surface wave contributions from the integral are given by the residues at the poles of the integrand (Lapwood, 1949). In the multi-layered case there are many poles, each corresponding to a higher mode. The vertical component of the far-field Rayleigh wave surface displacement for the mth mode can be written (Hudson, 1969b)

$$A_z^*(\omega;r,\phi) = iA_m \sum_{n=0}^{2} [g_z^{nc}(k_{Rm};\omega)\cos n\phi + g_z^{ns}(k_{Rm};\omega)\sin n\phi]\exp(in\pi/2) \qquad (A.17)$$

where

$$A_m = -\left(\frac{2\pi}{|k_{Rm}|r}\right)^{\frac{1}{2}} \exp(-ik_{Rm}r \pm i\pi/4)/\partial F(k_{Rm};\omega)/\partial k_{Rm},$$

$$g_z^{nc}(k_{Rm};\omega) = \sum_{j=1}^{4} [(J_{31} - J_{41})(L_{1j} - L_{2j}) - (J_{11} - J_{21})(L_{3j} - L_{4j})]s_j^{nc}$$

(a similar relation with c replaced by s being inferred), and the Rayleigh function $F(k_{Rm};\omega)$ which contains information on the dispersion of the Rayleigh waves is given by

$$F(k_{Rm};\omega) = (J_{11} - J_{21})(J_{32} - J_{42}) - (J_{12} - J_{22})(J_{31} - J_{41}) \quad . \qquad (A.18)$$

J_{jk} and L_{jk} are the elements of the jth row and kth column of the

4×4 real matrices J and L which depend on the elastic constants of the medium, and $\underline{S}$ is a column vector whose elements depend on the type of the source. Details of these terms are given in Haskell (1964b). Using this expression the multi-layered medium response pertaining to Chapters 2 and 3 can be written:

$$M_z(\omega;r,\phi) = r^{\frac{1}{2}} |A_z^*(\omega;r,\phi)| \quad . \tag{A.19}$$

In an analogous manner to the simpler computations of Sections A.2 and A.3, the roots of the Rayleigh equation

$$F(\kappa;\omega) = 0$$

correspond to the poles of the integrand of the inverse transform. Apart from the number of poles, this case differs from the simpler systems in that the wavetrain corresponding to each particular mode is dispersed.

Numerical procedures to compute Equation A.17 usually encounter difficulties when the frequency or wave mode order is high. This is a consequence of large positive exponential terms in the quantities g_z^{nc}, g_z^{ns}, and $\partial F/\partial k_{Rm}$ (see Haskell, 1964a). The J and L matrices are computed by the successive multiplication of matrices containing these exponential terms, each matrix related to a layer of the multi-layered structure (Gilbert and Backus, 1966). After each operation the elements are larger, the increase continuing until a real overflow arises. The quotient of these two very large but nearly equal quantities results in a loss of significance. There is also a similar effect involved in the subtraction operation in the evaluation of $F(k_{Rm};\omega)$. These two effects become increasingly

more pronounced at higher frequencies, and significantly affect theoretical calculations in the frequency range of 0.7 - 5.5 Hz in this thesis.

The precision problem has been tackled by Dunkin (1965), Thrower (1965) and Knopoff (1964)by re-formulating the layer matrices. These formulae have been further modified by Watson (1970) for an increased accuracy. The Knopoff (1964) method has been optimized by Schwab (1970), complete details being given in Schwab and Knopoff (1972). However, these alternatives still possess the real overflow problem due to the matrix elements becoming too large. Abo-Zena (1979) circumvented this to produce an algorithm of unlimited frequency. A modification of the Thomson-Haskell method suggested in Abo-Zena (1979) is used here to take account of the real overflow problem. This consists of normalizing each layer matrix element with respect to the matrix maximum before it is used to construct the complete J and L matrices. The individual normalizing factors partially cancel in the final assemblage, and the remaining are stored. The final displacement is then multiplied by these residual factors when all the layer multiplications are complete. To delay the onset of the lack of precision to higher frequencies, the algorithm utilizes quadruple precision variables. To ensure accuracy, the dispersion characteristic of the particular medium is evaluated external to the algorithm using Schwab and Knopoff's (1972) method, extended using the normalization above. These features are incorporated into the program 'MLR' which is listed in Appendix D.3.

APPENDIX B

MATHEMATICAL DESCRIPTION OF THE OPTIMIZATION AND LINEAR PROGRAMMING ALGORITHMS USED IN THE SINGLE-STATION INVERSION PROCEDURE

B.1 Quasi-Newtonian Optimization

The NAG library routine 'E04JAF', incorporated into the program 'SSQ' of Appendix D.3, has been used to find the optimal combination of Q_β^{-1} values and the source strength which minimize the function χ^2_{FOB} defined in Equation 5.12, subject to limits on these spectral parameters. This routine solves the general problem:

$$\text{Minimize } F(x_1, x_2, x_3, \ldots, x_n) \tag{B.1}$$

subject to the upper and lower bounds $x_j^L \leq x_j \leq x_j^U : j = 1, n,$

by a quasi-Newtonian method.

From a starting point near to the minimum, the algorithm generates a sequence of feasible points $\underline{x}^k$ which converge to the solution. $\underline{x}^{k+1}$ is constructed from the previous point by assuming that the function may be approximated locally by a Taylor series up to the quadratic terms:

$$F(\underline{x}^k + \underline{h}) = F(\underline{x}^k) + \underline{h}^T \underline{D}^k + \frac{1}{2} \underline{h}^T G^k \underline{h} \tag{B.2}$$

where $\underline{D}^k$ is a gradient vector of first partial derivatives of the function evaluated at $\underline{x}^k$, the ith element of which is $\partial F/\partial x_i$. G^k is a matrix of second order partial derivatives of the function (Hessian matrix), the (i,j)th element of which is $\partial^2 F/\partial x_i \partial x_j$. In this technique, the 'step length' vector $\underline{h}$ which minimizes $F(\underline{x}^k + \underline{h})$ is obtained from Equation B.2.

$$\underline{h} = - (G^k)^{-1} \underline{D}^k.$$

Thus a new estimate of the position of the true minimum of the function

is computed. The procedure is repeated until the rate of convergence falls below a pre-specified threshold. At this point a check is afforded to verify that this is a minimum within a given tolerance.

Gill and Murray (1976) used Cholesky factorization to assemble G. In the quasi-Newtonian procedure used in this thesis, these Cholesky factors are updated using a recurrence relation which connects them to the factors of the preceding point. Initial derivatives for the algorithm are computed analytically or by finite difference methods.

For the bounds constrained problem, only some of the variables are free to change at each iteration (others being on the boundary). Accordingly, the components of $\underline{D}$ and G corresponding to those variables are set to zero, and the remaining components are computed (as for the unconstrained method) with respect to the free variables. If during the search one of the free variables encounters a bound or one of the variables currently on a bound becomes free, the set can easily be altered within this framework as the minimization proceeds.

The algorithm described avoids a single-variable search and therefore converges very rapidly. However, the second derivatives in G are often difficult to compute, and the matrix inversion G^{-1} is time consuming. The algorithm is occasionally unreliable because Equation B.2 may possess a saddle point. The probability of this occurring can be decreased by reducing the number of variables specifying the function to be minimized.

B.2 Simplex Method

B.2.1 Introduction

The upper and lower bounds on each spectral parameter specifying the logarithmic spectral amplitude given in Equation 5.13 were computed in the single-station scheme of Section 5.4 by utilizing the NAG library subroutine 'H01ADF'. This algorithm solves the general linear programming problem:

$$\text{maximize} \quad \sum_{j=1}^{p} c_j x_j = z \tag{B.3}$$

$$\text{subject to the constraints} \quad \left.\begin{aligned} &\sum_{j=1}^{p} a_{ij} x_j \leq b_i \\ \text{and/or} \quad &\sum_{j=1}^{p} a_{ij} x_j \geq b_i \\ \text{and/or} \quad &\sum_{j=1}^{p} a_{ij} x_j = b_i \end{aligned}\right\} \tag{B.4}$$

$$\text{and} \quad x_j \geq 0 \tag{B.5}$$

$$\text{for} \quad i = 1, m$$

via the simplex method (Garvin, 1960; Johnston, 1972; Lee and Solomon, 1975).

B.2.2 Application to Single-station Scheme

The general expression for the logarithmic spectral amplitude in Equation 5.13 is a linear summation of parameters corresponding to the Q_β^{-1} depth model and the logarithm of the source strength. The weights a_{ij} for each parameter are specified in this equation.

The aim of the single-station technique is to obtain upper and lower bounds on each parameter x_j $(j = 1, p)$ subject to the inequality constraints imposed by the envelope of uncertainty around the observed curve (Equation 5.14). To do this we set $c_k = -\delta_{kj} : k = 1, p$, from which we can compute the lower bound. We then set $c_k = +\delta_{kj} : k = 1, p$, from which we can compute the upper bound. This is repeated for each value of j. Therefore, for p independent parameters the simplex algorithm is invoked $2p$ times. This procedure totally defines the region within solution space, and produces boundaries on the solutions which can be interpreted like those of Hedgehog.

B.2.3 Mathematical Description of Method

The inequality constraints can be re-expressed as a set of linear equations by introducing q non-negative slack variables.

i.e. $$\sum_{j=1}^{n} a_{ij} x_j = b_i \; ; \quad i = 1, m$$

or $$\sum_{j=1}^{n} \underline{P}_j x_j = \underline{B} \qquad \text{(B.6)}$$

where $n = p + q$, $\underline{P}_{n-q} \ldots \underline{P}_n$ are m-dimensional unit column vectors, x_j are components of an n-dimensional row vector $\underline{X}$ of the slack and independent variables, and $\underline{B}$ a column vector of b_i's.

Each constraint in Equation B.6 corresponds to a hyperplane in n-dimensional space. The intersection of these defines a convex polyhedron S (Figure B.1). Feasible solutions of Equation B.6

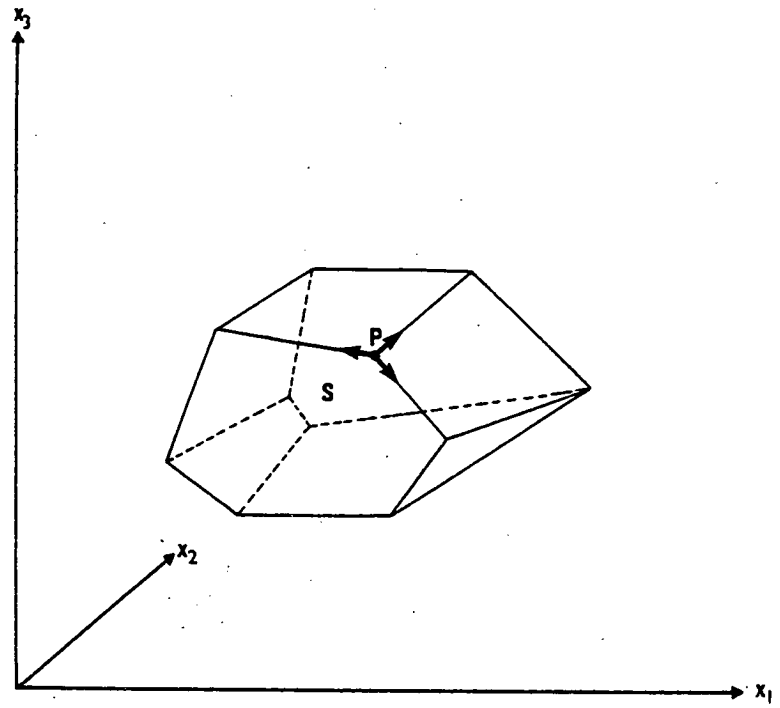

Figure B.1. Convex Polyhedron in three dimensional space. P is an extreme point and the arrows indicate three possible directions of movement which will minimize the objective function.

lie within or on the surface of this polyhedron. It may be proven that every basic feasible solution (for which $n - m$ variables in $\underline{X}$ are set to zero) satisfying Equation B.6 corresponds to an extreme point of S, provided that the vectors $\underline{P}_j$ are linearly independent. The bases of two adjacent extreme points differ by only one pair of variables. The objective function z of Equation B.3 assumes its maximum at an extreme point of S. Consequently, the simplex scheme need only cover a small subset of the possible extreme feasible solutions. The procedure consists of two phases:

(a) Phase I - search for an initial basic feasible solution. If $\underline{B} \geq \underline{0}$ (for all constraints re-arranged as '$\leq$'), the slack variables immediately furnish one with a starting basis, for by setting each independent variable to zero

$$\underline{X} = \underline{B}.$$

If some values of b_i are < 0, then the search for the initial vertex cannot be performed by inspection. In this case, we augment each equation with an artificial variable (Garvin, 1960, Chapter 3), and minimize an infeasibility function.

(b) Phase II - having found an extreme solution, we jump from one extreme point to another along the edge of the polyhedron (Figure B.1), taking the direction of maximum rate of change of the objective function. Each jump brings us closer to the optimal solution. The process is terminated when the objective function can no longer be maximized. If the polyhedron extends to infinity, the solutions are unbounded.

This procedure is extremely efficient and requires only a finite number of iterations. Moreover, there is no ambiguity over the maximum, as for linear programming problems there are no local maxima. The principal difference between the Hedgehog and simplex methods is that the latter technique defines absolute limits on the variables, whereas only with an increase in run time can we be sure that the Hedgehog region cannot increase. Precision tests could be carried out for the Hedgehog method as in Worthington et al. (1972), Anderssen et al. (1972) and Anderssen and Senata (1971), to define a point beyond which we are confident that there can be no possible increase in the solution region, but this is very time consuming.

APPENDIX C

GROUP VELOCITY DISPERSION DATA

C.1 Averaged Single-station Group Velocity Data for Paths from the Underwater Explosions in Kirkcaldy Bay

The data corresponds to Figures 4.6 - 4.7.

STATION EDI

	Freq(Hz)	Grp Vel (km/s)	Stan Dev		Freq(Hz)	Grp Vel (km/s)	Stan Dev
1	0.7812	1.437	0.043	2	0.8437	1.383	0.020
3	0.9062	1.350	0.052	4	0.9687	1.302	0.034
5	1.0312	1.264	0.043	6	1.0937	1.235	0.039
7	1.1562	1.210	0.035	8	1.2187	1.191	0.032
9	1.2812	1.178	0.030	10	1.3437	1.167	0.030
11	1.4062	1.159	0.029	12	1.4687	1.154	0.028
13	1.5312	1.150	0.029	14	1.5937	1.148	0.027
15	1.6562	1.146	0.028	16	1.7187	1.144	0.028
17	1.7812	1.143	0.030	18	1.8437	1.147	0.026
19	1.9062	1.149	0.028	20	1.9687	1.151	0.031
21	2.0312	1.154	0.030	22	2.0937	1.158	0.029
23	2.1562	1.165	0.035	24	2.2187	1.172	0.032
25	2.2812	1.179	0.030	26	2.3437	1.186	0.027
27	2.4062	1.192	0.028	28	2.4687	1.203	0.027
29	2.5312	1.219	0.028				

STATION EAU

	Freq(Hz)	Grp Vel (km/s)	Stan Dev		Freq(Hz)	Grp Vel (km/s)	Stan Dev
1	0.7812	1.670	0.112	2	0.8437	1.614	0.108
3	0.9062	1.465	0.096	4	0.9687	1.382	0.093
5	1.0312	1.322	0.109	6	1.0937	1.274	0.096
7	1.1562	1.251	0.095	8	1.2187	1.237	0.091
9	1.2812	1.228	0.095	10	1.3437	1.221	0.092
11	1.4062	1.215	0.096	12	1.4687	1.210	0.094
13	1.5312	1.204	0.094	14	1.5937	1.202	0.103
15	1.6562	1.206	0.103	16	1.7187	1.216	0.093
17	1.7812	1.218	0.093	18	1.8437	1.219	0.094
19	1.9062	1.219	0.095	20	1.9687	1.220	0.096
21	2.0312	1.225	0.098	22	2.0937	1.235	0.102
23	2.1562	1.238	0.104	24	2.2187	1.237	0.103
25	2.2812	1.239	0.119	26	2.3437	1.260	0.126

STATION EBH

	Freq(Hz)	Grp Vel (km/s)	Stan Dev		Freq(Hz)	Grp Vel (km/s)	Stan Dev
1	0.7812	1.650	0.100	2	0.8437	1.611	0.091
3	0.9062	1.490	0.107	4	0.9687	1.413	0.082
5	1.0312	1.365	0.060	6	1.0937	1.332	0.045
7	1.1562	1.308	0.041	8	1.2187	1.292	0.040
9	1.2812	1.282	0.040	10	1.3437	1.275	0.038
11	1.4062	1.271	0.041	12	1.4687	1.268	0.041
13	1.5312	1.266	0.037	14	1.5937	1.265	0.035
15	1.6562	1.266	0.033	16	1.7187	1.266	0.032
17	1.7812	1.267	0.029	18	1.8437	1.267	0.028
19	1.9062	1.267	0.027	20	1.9687	1.269	0.023
21	2.0312	1.273	0.015	22	2.0937	1.275	0.014
23	2.1562	1.280	0.013	24	2.2187	1.287	0.012
25	2.2812	1.288	0.015	26	2.3437	1.289	0.059
27	2.4062	1.290	0.024	28	2.4687	1.290	0.098
29	2.5312	1.289	0.051				

STATION EGL

	Freq(Hz)	Grp Vel (km/s)	Stan Dev		Freq(Hz)	Grp Vel (km/s)	Stan Dev
1	0.7812	1.508	0.060	2	0.8437	1.484	0.053
3	0.9062	1.447	0.030	4	0.9687	1.420	0.065
5	1.0312	1.386	0.075	6	1.0937	1.359	0.067
7	1.1562	1.336	0.063	8	1.2187	1.319	0.057
9	1.2812	1.306	0.032	10	1.3437	1.292	0.032
11	1.4062	1.279	0.032	12	1.4687	1.267	0.033
13	1.5312	1.257	0.033	14	1.5937	1.249	0.036
15	1.6562	1.245	0.041	16	1.7187	1.247	0.042
17	1.7812	1.251	0.041				

STATION EAB

	Freq(Hz)	Grp Vel (km/s)	Stan Dev		Freq(Hz)	Grp Vel (km/s)	Stan Dev
1	0.7187	1.667	0.057	2	0.7812	1.646	0.056
3	0.8437	1.632	0.052	4	0.9062	1.618	0.054
5	0.9687	1.604	0.055	6	1.0312	1.584	0.058
7	1.0937	1.559	0.037	8	1.1562	1.543	0.034
9	1.2187	1.525	0.036	10	1.2812	1.504	0.087
11	1.3437	1.496	0.055	12	1.4062	1.490	0.079

STATION EBL

	Freq(Hz)	Grp Vel (km/s)	Stan Dev		Freq(Hz)	Grp Vel (km/s)	Stan Dev
1	0.7187	1.521	0.090	2	0.7812	1.426	0.061
3	0.8437	1.379	0.065	4	0.9062	1.344	0.076
5	0.9687	1.307	0.080	6	1.0312	1.274	0.086
7	1.0937	1.244	0.085	8	1.1562	1.219	0.091
9	1.2187	1.201	0.089	10	1.2812	1.186	0.079
11	1.3437	1.169	0.068	12	1.4062	1.151	0.036
13	1.4687	1.144	0.033	14	1.5312	1.141	0.032
15	1.5937	1.140	0.030				

STATION EDU

	Freq(Hz)	Grp Vel (km/s)	Stan Dev		Freq(Hz)	Grp Vel (km/s)	Stan Dev
1	0.7812	2.347	0.241	2	0.8437	2.298	0.243
3	0.9062	2.081	0.197	4	0.9687	1.944	0.106
5	1.0312	1.869	0.079	6	1.0937	1.829	0.073
7	1.1562	1.807	0.071	8	1.2187	1.794	0.078
9	1.2812	1.784	0.078	10	1.3437	1.778	0.079
11	1.4062	1.776	0.078	12	1.4687	1.775	0.078
13	1.5312	1.775	0.079	14	1.5937	1.774	0.081
15	1.6562	1.775	0.082	16	1.7187	1.777	0.087
17	1.7812	1.780	0.089	18	1.8437	1.783	0.095
19	1.9062	1.785	0.092	20	1.9687	1.786	0.089
21	2.0312	1.785	0.083	22	2.0937	1.782	0.080

STATION ELO

	Freq(Hz)	Grp Vel (km/s)	Stan Dev		Freq(Hz)	Grp Vel (km/s)	Stan Dev
1	0.9687	2.263	0.368	2	1.0312	2.207	0.309
3	1.0937	2.112	0.225	4	1.1562	2.030	0.166
5	1.2187	1.973	0.133	6	1.2812	1.926	0.117
7	1.3437	1.887	0.104	8	1.4062	1.850	0.084
9	1.4687	1.828	0.075	10	1.5312	1.811	0.071
11	1.5937	1.792	0.070	12	1.6562	1.773	0.041
13	1.7187	1.766	0.039	14	1.7812	1.762	0.038
15	1.8437	1.760	0.038	16	1.9062	1.760	0.038
17	1.9687	1.759	0.038	18	2.0312	1.759	0.038
19	2.0937	1.760	0.050	20	2.1562	1.762	0.055
21	2.2187	1.766	0.055				

C.2 Regional Group Velocity Data Generated by the Kyle Earthquake

The data corresponds to Figures 4.21 - 4.24.

REGION A

First Higher Mode

	Freq(Hz)	Grp Vel (km/s)	Stan Dev		Freq(Hz)	Grp Vel (km/s)	Stan Dev
1	0.8057	3.571	0.050	2	0.9034	3.541	0.057
3	1.0010	3.507	0.072	4	1.0987	3.489	0.061
5	1.1963	3.471	0.057	6	1.2940	3.447	0.057
7	1.3917	3.417	0.054	8	1.4893	3.384	0.057
9	1.5870	3.348	0.070	10	1.6846	3.310	0.091
11	1.7823	3.275	0.108	12	1.8800	3.241	0.116
13	1.9776	3.210	0.127	14	2.0753	3.184	0.132
15	2.1729	3.160	0.132	16	2.2706	3.139	0.124
17	2.3683	3.121	0.122	18	2.4659	3.106	0.118
19	2.5636	3.093	0.114	20	2.6612	3.079	0.109
21	2.7589	3.063	0.105	22	2.8566	3.047	0.105
23	2.9542	3.037	0.104	24	3.0519	3.033	0.104
25	3.1495	3.030	0.104	26	3.2472	3.028	0.106
27	3.3449	3.028	0.107	28	3.4425	3.027	0.105
29	3.5402	3.025	0.105	30	3.6378	3.025	0.103
31	3.7355	3.025	0.102	32	3.8332	3.029	0.101
33	3.9308	3.036	0.105	34	4.0285	3.038	0.103

Second Higher Mode

	Freq(Hz)	Grp Vel (km/s)	Stan Dev		Freq(Hz)	Grp Vel (km/s)	Stan Dev
1	1.8800	3.498	0.058	2	1.9776	3.474	0.055
3	2.0753	3.459	0.067	4	2.1729	3.440	0.070
5	2.2706	3.415	0.048	6	2.3683	3.402	0.053
7	2.4659	3.398	0.074	8	2.5636	3.384	0.063
9	2.6612	3.371	0.060	10	2.7589	3.361	0.062
11	2.8566	3.353	0.066	12	2.9542	3.345	0.064
13	3.0519	3.336	0.070	14	3.1495	3.329	0.072
15	3.2472	3.321	0.073	16	3.3449	3.314	0.073
17	3.4425	3.307	0.074	18	3.5402	3.301	0.076
19	3.6378	3.296	0.077	20	3.7355	3.292	0.078
21	3.8332	3.288	0.080	22	3.9308	3.286	0.082
23	4.0285	3.284	0.082	24	4.1261	3.285	0.081

REGION B

First Higher Mode

	Freq(Hz)	Grp Vel (km/s)	Stan Dev		Freq(Hz)	Grp Vel (km/s)	Stan Dev
1	1.0987	3.410	0.035	2	1.1963	3.358	0.034
3	1.2940	3.327	0.034	4	1.3917	3.304	0.033
5	1.4893	3.270	0.035	6	1.5870	3.243	0.048
7	1.6846	3.219	0.055	8	1.7823	3.199	0.066
9	1.8800	3.185	0.064	10	1.9776	3.174	0.055
11	2.0753	3.162	0.044	12	2.1729	3.151	0.043
13	2.2706	3.139	0.042	14	2.3683	3.130	0.051
15	2.4659	3.126	0.047	16	2.5636	3.123	0.043
17	2.6612	3.123	0.040	18	2.7589	3.125	0.034
19	2.8566	3.126	0.031	20	2.9542	3.125	0.032
21	3.0519	3.124	0.038	22	3.1495	3.122	0.040
23	3.2472	3.118	0.048	24	3.3449	3.114	0.047
25	3.4425	3.113	0.054	26	3.5402	3.119	0.060
27	3.6378	3.132	0.033	28	3.7355	3.136	0.037
29	3.8332	3.147	0.039				

Second Higher Mode

	Freq(Hz)	Grp Vel (km/s)	Stan Dev		Freq(Hz)	Grp Vel (km/s)	Stan Dev
1	1.7823	3.628	0.039	2	1.8800	3.578	0.049
3	1.9776	3.532	0.078	4	2.0753	3.477	0.083
5	2.1729	3.438	0.058	6	2.2706	3.410	0.046
7	2.3683	3.390	0.041	8	2.4659	3.374	0.029
9	2.5636	3.361	0.023	10	2.6612	3.347	0.023
11	2.7589	3.334	0.025	12	2.8566	3.324	0.025
13	2.9542	3.317	0.024	14	3.0519	3.311	0.026
15	3.1495	3.307	0.029	16	3.2472	3.304	0.027
17	3.3449	3.303	0.025	18	3.4425	3.302	0.025
19	3.5402	3.302	0.025	20	3.6378	3.303	0.025

REGION C

First Higher Mode

	Freq(Hz)	Grp Vel (km/s)	Stan Dev		Freq(Hz)	Grp Vel (km/s)	Stan Dev
1	1.0010	3.369	0.043	2	1.0987	3.349	0.057
3	1.1963	3.290	0.070	4	1.2940	3.251	0.077
5	1.3917	3.216	0.086	6	1.4893	3.186	0.094
7	1.5870	3.161	0.100	8	1.6846	3.140	0.106
9	1.7823	3.118	0.112	10	1.8800	3.095	0.117
11	1.9776	3.074	0.123	12	2.0753	3.058	0.128
13	2.1729	3.044	0.136	14	2.2706	3.034	0.141
15	2.3683	3.028	0.140	16	2.4659	3.024	0.136
17	2.5636	3.023	0.129	18	2.6612	3.023	0.120
19	2.7589	3.023	0.111	20	2.8566	3.022	0.104
21	2.9542	3.020	0.097	22	3.0519	3.019	0.089
23	3.1495	3.017	0.083	24	3.2472	3.015	0.076
25	3.3449	3.014	0.069	26	3.4425	3.014	0.065
27	3.5402	3.014	0.064	28	3.6378	3.013	0.062
29	3.7355	3.011	0.059	30	3.8332	3.009	0.057
31	3.9308	3.009	0.057				

Second Higher Mode

	Freq(Hz)	Grp Vel (km/s)	Stan Dev		Freq(Hz)	Grp Vel (km/s)	Stan Dev
1	1.5870	3.587	0.051	2	1.6846	3.559	0.047
3	1.7823	3.497	0.063	4	1.8800	3.460	0.103
5	1.9776	3.406	0.065	6	2.0753	3.363	0.043
7	2.1729	3.329	0.039	8	2.2706	3.301	0.032
9	2.3683	3.278	0.033	10	2.4659	3.261	0.046
11	2.5636	3.249	0.050	12	2.6612	3.236	0.057
13	2.7589	3.222	0.071	14	2.8566	3.209	0.070
15	2.9542	3.198	0.070	16	3.0519	3.189	0.062
17	3.1495	3.179	0.049	18	3.2472	3.170	0.044
19	3.3449	3.162	0.038	20	3.4425	3.163	0.039
21	3.5402	3.170	0.029				

REGION D

First Higher Mode

	Freq(Hz)	Grp Vel (km/s)	Stan Dev		Freq(Hz)	Grp Vel (km/s)	Stan Dev
1	0.8057	3.396	0.040	2	0.9034	3.364	0.040
3	1.0010	3.332	0.055	4	1.0987	3.287	0.041
5	1.1963	3.253	0.055	6	1.2940	3.228	0.109
7	1.3917	3.191	0.109	8	1.4893	3.148	0.105
9	1.5870	3.103	0.090	10	1.6846	3.056	0.086
11	1.7823	3.008	0.093	12	1.8800	2.966	0.085
13	1.9776	2.931	0.088	14	2.0753	2.903	0.078
15	2.1729	2.882	0.067	16	2.2706	2.868	0.061
17	2.3683	2.860	0.051	18	2.4659	2.858	0.042
19	2.5636	2.859	0.039	20	2.6612	2.861	0.036
21	2.7589	2.865	0.031	22	2.8566	2.870	0.030
23	2.9542	2.875	0.029	24	3.0519	2.879	0.028
25	3.1495	2.882	0.030	26	3.2472	2.886	0.030
27	3.3449	2.891	0.029	28	3.4425	2.897	0.028
29	3.5402	2.903	0.027	30	3.6378	2.908	0.024
31	3.7355	2.913	0.020	32	3.8332	2.917	0.016
33	3.9308	2.919	0.016	34	4.0285	2.918	0.015
35	4.1261	2.919	0.016	36	4.2238	2.918	0.016
37	4.3215	2.917	0.019	38	4.4191	2.918	0.025
39	4.5168	2.919	0.032	40	4.6144	2.923	0.044

Second Higher Mode

	Freq(Hz)	Grp Vel (km/s)	Stan Dev		Freq(Hz)	Grp Vel (km/sec)	Stan Dev
1	1.2940	3.555	0.048	2	1.3917	3.507	0.047
3	1.4893	3.498	0.093	4	1.5870	3.457	0.081
5	1.6846	3.415	0.071	6	1.7823	3.365	0.063
7	1.8800	3.331	0.078	8	1.9776	3.317	0.106
9	2.0753	3.295	0.087	10	2.1729	3.271	0.073
11	2.2706	3.252	0.066	12	2.3683	3.239	0.062
13	2.4659	3.228	0.060	14	2.5636	3.221	0.056
15	2.6612	3.216	0.058	16	2.7589	3.212	0.056
17	2.8566	3.210	0.056	18	2.9542	3.209	0.056
19	3.0519	3.209	0.056	20	3.1495	3.210	0.056
21	3.2472	3.212	0.052				

REGION E

First Higher Mode

	Freq(Hz)	Grp Vel (km/s)	Stan Dev		Freq(Hz)	Grp Vel (km/s)	Stan Dev
1	0.8057	3.380	0.086	2	0.9034	3.369	0.093
3	1.0010	3.309	0.105	4	1.0987	3.271	0.108
5	1.1963	3.232	0.109	6	1.2940	3.190	0.113
7	1.3917	3.150	0.119	8	1.4893	3.116	0.122
9	1.5870	3.089	0.123	10	1.6846	3.067	0.121
11	1.7823	3.050	0.118	12	1.8800	3.035	0.116
13	1.9776	3.023	0.115	14	2.0753	3.013	0.113
15	2.1729	3.005	0.110	16	2.2706	3.000	0.105
17	2.3683	2.996	0.098	18	2.4659	2.995	0.091
19	2.5636	2.995	0.084	20	2.6612	2.995	0.076
21	2.7589	2.995	0.070	22	2.8566	2.995	0.064
23	2.9542	2.994	0.061	24	3.0519	2.992	0.059
25	3.1495	2.990	0.058	26	3.2472	2.986	0.059
27	3.3449	2.982	0.061	28	3.4425	2.977	0.063
29	3.5402	2.971	0.066	30	3.6378	2.964	0.069
31	3.7355	2.959	0.071	32	3.8332	2.953	0.073
33	3.9308	2.945	0.072	34	4.0285	2.938	0.074
35	4.1261	2.934	0.078	36	4.2238	2.929	0.084

Second Higher Mode

	Freq(Hz)	Grp Vel (km/s)	Stan Dev		Freq(Hz)	Grp Vel (km/s)	Stan Dev
1	1.2940	3.514	0.046	2	1.3917	3.500	0.039
3	1.4893	3.453	0.033	4	1.5870	3.435	0.045
5	1.6846	3.425	0.065	6	1.7823	3.420	0.088
7	1.8800	3.412	0.106	8	1.9776	3.394	0.110
9	2.0753	3.370	0.101	10	2.1729	3.346	0.088
11	2.2706	3.325	0.076	12	2.3683	3.306	0.066
13	2.4659	3.287	0.058	14	2.5636	3.271	0.055
15	2.6612	3.258	0.054	16	2.7589	3.248	0.054
17	2.8566	3.240	0.054	18	2.9542	3.232	0.054
19	3.0519	3.224	0.054	20	3.1495	3.218	0.055
21	3.2472	3.214	0.057	22	3.3449	3.211	0.058
23	3.4425	3.209	0.059	24	3.5402	3.207	0.059
25	3.6378	3.205	0.057	26	3.7355	3.204	0.054
27	3.8332	3.203	0.052	28	3.9308	3.201	0.047

REGION F

First Higher Mode

	Freq(Hz)	Grp Vel (km/s)	Stan Dev		Freq(Hz)	Grp Vel (km/s)	Stan Dev
1	0.8057	3.552	0.085	2	0.9034	3.526	0.082
3	1.0010	3.485	0.087	4	1.0987	3.455	0.097
5	1.1963	3.417	0.106	6	1.2940	3.377	0.109
7	1.3917	3.339	0.110	8	1.4893	3.305	0.109
9	1.5870	3.275	0.108	10	1.6846	3.249	0.106
11	1.7823	3.226	0.106	12	1.8800	3.204	0.106
13	1.9776	3.182	0.105	14	2.0753	3.162	0.102
15	2.1729	3.146	0.096	16	2.2706	3.131	0.090
17	2.3683	3.120	0.085	18	2.4659	3.111	0.082
19	2.5636	3.105	0.081	20	2.6612	3.102	0.079
21	2.7589	3.104	0.075	22	2.8566	3.108	0.069
23	2.9542	3.111	0.065	24	3.0519	3.108	0.062
25	3.1495	3.103	0.061	26	3.2472	3.099	0.062
27	3.3449	3.094	0.066	28	3.4425	3.090	0.072
29	3.5402	3.088	0.075	30	3.6378	3.085	0.076
31	3.7355	3.078	0.075	32	3.8332	3.068	0.072
33	3.9308	3.067	0.074	34	4.0285	3.074	0.083
35	4.1261	3.083	0.096	36	4.2238	3.089	0.112
37	4.3215	3.094	0.145	38	4.4191	3.094	0.145

Second Higher Mode

	Freq(Hz)	Grp Vel (km/s)	Stan Dev		Freq(Hz)	Grp Vel (km/s)	Stan Dev
1	1.5870	3.636	0.144	2	1.6846	3.603	0.111
3	1.7823	3.567	0.090	4	1.8800	3.526	0.080
5	1.9776	3.486	0.080	6	2.0753	3.454	0.086
7	2.1729	3.431	0.094	8	2.2706	3.411	0.102
9	2.3683	3.392	0.106	10	2.4659	3.375	0.107
11	2.5636	3.361	0.108	12	2.6612	3.349	0.107
13	2.7589	3.339	0.107	14	2.8566	3.332	0.106
15	2.9542	3.329	0.105	16	3.0519	3.329	0.101
17	3.1495	3.330	0.097	18	3.2472	3.330	0.091
19	3.3449	3.330	0.086	20	3.4425	3.327	0.084
21	3.5402	3.320	0.085	22	3.6378	3.310	0.084
23	3.7355	3.298	0.080	24	3.8332	3.289	0.073
25	3.9308	3.282	0.068	26	4.0285	3.275	0.064
27	4.1261	3.262	0.055	28	4.2238	3.228	0.026
29	4.3215	3.218	0.019				

REGION G

First Higher Mode

	Freq(Hz)	Grp Vel (km/s)	Stan Dev		Freq(Hz)	Grp Vel (km/s)	Stan Dev
1	0.7080	3.543	0.045	2	0.8057	3.533	0.043
3	0.9034	3.501	0.049	4	1.0010	3.473	0.056
5	1.0987	3.442	0.062	6	1.1963	3.412	0.067
7	1.2940	3.383	0.070	8	1.3917	3.356	0.071
9	1.4893	3.331	0.069	10	1.5870	3.311	0.066
11	1.6846	3.296	0.065	12	1.7823	3.284	0.065
13	1.8800	3.274	0.063	14	1.9776	3.265	0.059
15	2.0753	3.257	0.054	16	2.1729	3.251	0.048
17	2.2706	3.246	0.042	18	2.3683	3.242	0.040
19	2.4659	3.239	0.040	20	2.5636	3.236	0.041
21	2.6612	3.235	0.043	22	2.7589	3.233	0.044
23	2.8566	3.230	0.046	24	2.9542	3.227	0.051
25	3.0519	3.225	0.060	26	3.1495	3.224	0.066
27	3.2472	3.218	0.063	28	3.3449	3.209	0.056
29	3.4425	3.202	0.052	30	3.5402	3.198	0.052
31	3.6378	3.194	0.053	32	3.7355	3.190	0.052
33	3.8332	3.189	0.048	34	3.9308	3.189	0.048

Second Higher Mode

	Freq(Hz)	Grp Vel (km/s)	Stan Dev		Freq(Hz)	Grp Vel (km/s)	Stan Dev
1	1.1963	3.680	0.031	2	1.2940	3.646	0.037
3	1.3917	3.595	0.032	4	1.4893	3.577	0.036
5	1.5870	3.565	0.045	6	1.6846	3.550	0.054
7	1.7823	3.533	0.058	8	1.8800	3.518	0.060
9	1.9776	3.504	0.059	10	2.0753	3.494	0.059
11	2.1729	3.485	0.059	12	2.2706	3.477	0.060
13	2.3683	3.470	0.061	14	2.4659	3.466	0.062
15	2.5636	3.462	0.063	16	2.6612	3.459	0.063
17	2.7589	3.456	0.061	18	2.8566	3.454	0.060
19	2.9542	3.453	0.060	20	3.0519	3.452	0.061
21	3.1495	3.448	0.059	22	3.2472	3.444	0.055
23	3.3449	3.445	0.051	24	3.4425	3.451	0.051
25	3.5402	3.458	0.056	26	3.6378	3.470	0.064
27	3.7355	3.484	0.061				

APPENDIX D

COMPUTER PROGRAMS

D.1 Program 'WINDOW'

```
C DESCRIPTION:
C
C THIS INTERACTIVE PROGRAM ENABLES ONE TO QUICKLY WINDOW
C WAVEPACKETS FROM A SEISMOGRAM. THE WINDOW LIMITS ARE OUTPUT INTO
C A FILE CREATED IN A STANDARD FORMAT WHICH CAN BE HANDLED BY
C THE PROCEDURES FOR SPECTRAL AND GROUP VELOCITY ANALYSIS.
C
C IMPLEMENTATION:
C
C THE SEISMOGRAMS MUST BE STORED SEQUENTIALLY , AND ARE
C ACCESSED VIA CHANNEL 1.  THE WINDOW COORDINATES AND OTHER
C CONTROL INFORMATION IS OUTPUT ON CHANNEL 2. BOTH
C OF THESE CHANNELS ARE SET UP AUTOMATICALLY WITHIN THE PROGRAM
C WHEN THE FILENAMES ARE TYPED IN RESPONSE TO A PROMPT BY THE
C PROGRAM. MOST OF THE QUESTIONS ARE SELF-EXPLANATORY . THE
C RESPONSE 'T' IMMMEDIATELY RETURNS THE USER TO THE TOP OF THE
C SEISMOGRAM STACK.
C
C EXTERNAL SUBROUTINES:
C
C THE PROGRAM MUST BE LINKED WITH A CALCOMP  PACKAGE WRITTEN BY
C C.FYFE  WHICH CONTAINS THE COMPLEMENTARY GRAPHICS ROUTINES.
C
C
      COMMON/FLT/NSEIS,MAXDAT
      COMMON/ORIG/STAN(24),IOH,IOM,OSEC
      REAL*8 ALL(2)
      DIMENSION SEIS(4096)
      CHARACTER*2 NAME
      CHARACTER*1 STAN,ANS1,ANS2,YES,TOP
      DATA NAME/'1,'/
      DATA YES/'Y'/,TOP/'T'/
      DATA ALL(1)/'2,    '/
C
      CALL EMASFC('DEFINE',6,NAME,2)
    1 REWIND 1
   21 READ(1,11,END=99)NSEIS,MAXDAT
      READ(1,15)(STAN(I),I=1,20),IOH,IOM,OSEC
      READ(1,18)(STAN(I),I=21,24)
      WRITE(6,16)(STAN(I),I=1,24)
      CALL FPRMPT('THIS TRACE? ?',12)
      READ(5,12)ANS1
      IF(ANS1.EQ.TOP)GOTO1
      IF(ANS1.EQ.YES)GOTO 20
      READ(1,13)DUMMY
      READ(1,14)(SEIS(I),I=1,NSEIS)
      CALL FPRMPT('FINISHED?',9)
      READ(5,12)ANS2
      IF(ANS2.EQ.YES)GOTO 99
      GOTO 21
```

```
      20 CALL PPRMPT('OUTPUT FILE: ',13)
         READ(5,10)ALL(2)
         CALL EMASFC('DEFINE',6,ALL,16)
         CALL NEWPAGE
         CALL TSP
         CALL CLOSEF(2)
         WRITE(6,19)
         READ(5,13)DUMMY
         GOTO 21
      99 STOP
      10 FORMAT(A6)
      11 FORMAT(1X,2I6)
      12 FORMAT(A1)
      13 FORMAT(A4)
      14 FORMAT(10F7.0)
      15 FORMAT(20A1,I2,1X,I2,1X,F5.2)
      16 FORMAT(//,5X,20A1,/,8X,4A1,//)
      17 FORMAT(2I6,F8.3,8X,F8.4)
      18 FORMAT(3X,4A1)
      19 FORMAT(15X,'HIT CARRIAGE RETURN TO CONTINUE')
         END
C
C*****
C
      SUBROUTINE TSP
      COMMON/TS/SEIS(4096)
      COMMON/FIT/NSEIS,MAXDAT,NAFLO,NFHI
      COMMON/ORIG/STA(24),IOH,IOM,OSEC
      COMMON/NOS/N,NBY2,NBY2P1,NPOW2,DELTAT
      CHARACTER*8 TITLE(6),STRING(3)
      CHARACTER*1 STA,STAN(24)
      EQUIVALENCE (STAN(1),TITLE(4))
      DATA TITLE(1),TITLE(2),TITLE(3)/'KYLE EAR','THQUAKE ','        '/
      DATA STRING/'01110001','1111011 ','    110 '/
C
C     THIS SUBROUTINE SELECTS A WINDOW AROUND THE FUNDAMENTAL RAYLEIGH
C     WAVE AND OUTPUTS THE LIMITS AS NUMBERS WHICH TSAP INTERPRETS
C     AS 'NSEIS' AND 'NUMCUT'.
C
      CALL EMASFC('SETMODE',7,'W=100',5)
      N=2048
      CALL POW(N,NBY2,NBY2P1,NPOW2)
      DO 9 I=1,24
      STAN(I)=STA(I)
    9 CONTINUE
C
C READ IN THE TIME COORDINATES
C IFOR = 1  -- REDUCED TRAVEL-TIME FORMAT
C IFOR = 2 -- ORIGIN TIME AND START TIME
      IFOR=1
      GOTO(3,4)IFOR
C
    3 READ(1,23)TOFS,DELTA,VRED,SPS
      DELTAT=1./SPS
      START=ABS(TOFS)
      ISTART=START*SPS+1
      GOTO 6
C
    4 READ(1,13)IBH,IBM,BSEC,DELTAT
      SPS=1./DELTAT
      START=3600.*(IOH-IBH)+60.*(IOM-IBM)+OSEC-BSEC
      ISTART=START*SPS+1.
C
C READ IN ONE SEISMOGRAM
    6 READ(1,14)(SEIS(I),I=1,NSEIS)
      DO 1 I=ISTART,NSEIS
      J=I-ISTART+1
      SEIS(J)=SEIS(I)
    1 CONTINUE
      NSEIS=NSEIS-ISTART+1
C
C PREPARATORY FILTERING OF THE TIME SERIES
      FNYQ=1./(2.*DELTAT)
      DF=FNYQ/FLOAT(NBY2)
C
C SELECT FILTER LIMITS
      FLO=0.
      FHI=10.0
      NAFLO=FLO/DF
      NFHI=FHI/DF
      CALL FILTER
C
      WRITE(6,30)
   30 FORMAT(///////,30X,'**********************************',
     *'******************'
     *,/,    30X,'*  SELECTION OF WAVEPACKET FOR SPECTRAL PROCESSING  *'
     *,/,30X,'**********************************************************')
      WRITE(6,31)(STAN(I),I=1,24)
   31 FORMAT(////,20X,'EVENT AND STATION : ',//19X,20A1,/,20X,4A1)
C
C     PLOT THE FILTERED TIME SERIES
      CALL PLOT(0.,0.,-3)
      CALL PLOT(0.,0.,3)
      CALL PLOT(11.,0.,2)
      CALL PLOT(11.,3.,2)
      CALL PLOT(0.,3.,2)
      CALL PLOT(0.,0.,2)
      CALL PLOT(0.,1.5,-3)
      DX=1./100.
      SCL=1./FLOAT(MAXDAT)
      X=0.
      Y=SEIS(1)*SCL
      CALL PLOT(X,Y,3)
      DO 2 I=2,NSEIS
      X=DX*(I-1)
      IF(X.GT.11.)GOTO 2
```

```
      Y=SEIS(I)*SCL
      CALL PLOT(X,Y,2)
    2 CONTINUE
C
C SELECT THE WINDOW LIMITS
      CALL CURSOR(XBEG,YBEG)
      NUMCUT=XBEG/DX+1
      CALL CURSOR(XEN,YEN)
      NSEIS=XEN/DX+1
C
C PLOT THE  SELECTED WAVEPACKET
      CALL PLOT(1.75,2.5,-3)
      CALL PLOT(2.,0.,-3)
      CALL PLOT(0.,0.,3)
      CALL PLOT(3.5,0.,2)
      CALL PLOT(3.5,3.,2)
      CALL PLOT(0.,3.,2)
      CALL PLOT(0.,0.,2)
      CALL PLOT(0.,1.5,-3)
      XO=(3.5-XEN+XBEG)*0.5
      X=XO
      Y=SEIS(NUMCUT+1)*SCL
      CALL PLOT(X,Y,3)
      NCUTP2=NUMCUT+2
      DO 5 I=NCUTP2,NSEIS
      X=XO+DX*(I-1-NUMCUT)
      Y=SEIS(I)*SCL
      CALL PLOT(X,Y,2)
    5 CONTINUE
C
      CALL SYMBOL(6.,5.6,0.1,' SELECTED WAVEPACKET',0.0,20)
      CALL VERCOPY
      CALL PLOT(0.,0.,999)
C
C SET THE TSAP CONTROL PARAMETERS
      IF(START.NE.0.)NUMCUT=NUMCUT+ISTART
      IF(START.NE.0.)NSEIS=NSEIS+ISTART
      IVSEIS=0
      NBASE=1
      NCOSTP=2
      NCOMB=16
      NAFLO1=64
      NINSTR=1
      NUGRUP=1
      NFLO=80
      NFHI=512
      NFSTEP=8
      BAND=0.40
      DWF=70.00
      DV=0.01
      FC=5.00
C
C WRITE CONTROL PARAMETERS INTO CHANNEL 2
      WRITE(2;24)(STAN(I),I=1,24)
      WRITE(2,21)NSEIS,IVSEIS,NUMCUT,NBASE,NCOSTP,NCOMB,NAFLO1,NINSTR
     *,NUGRUP,NFLO,NFHI,NFSTEP,BAND,DWF,DV,FC
      WRITE(2,22)STRING
C
      RETURN
   10 FORMAT(1X,216)
   11 FORMAT(20A1,I2,1X,I2,1X,F5.2)
   12 FORMAT(3X,4A1)
   13 FORMAT(216,F8.3,8X,F8.4)
   14 FORMAT(10F7.0)
   20 FORMAT(6A8)
   21 FORMAT(12I5,4F5.2)
   22 FORMAT(3A8)
   23 FORMAT(1X,F8.3,8X,2F8.3,17X,F9.6)
   24 FORMAT(24A1)
      END
C
C*****
C
      SUBROUTINE FILTER
C
C OBTAINS THE FOURIER TRANSFORM OF THE SIGNAL , FILTERS IT ,
C AND THEN CARRIES OUT AN INVERSE TRANSFORM TO OBTAIN
C THE FILTERED TIME SERIES.
C
      COMMON/TS/SEIS(2048),FREQ(1024),AMP(1024),PHASE(1024)
      COMMON/FLT/NSEIS,MAXDAT,NAFLO,NFHI
      COMMON/NOS/N,NBY2,NBY2P1,NPOW2,DELTAT
      COMPLEX Z(2048),CZERO
      CHARACTER*8 TYPE,TYPEMN
      DATA TYPEMN/'MEAN    '/
      CZERO=(0.,0.)
      NSESP1=NSEIS+1
      TYPE=TYPEMN
      IP1=0
C
C BASELINE THE SEISMOGRAM
      CALL BASE(SEIS,NSEIS,TYPE,IP1)
C
C COSINE TAPER THE SEISMOGRAM
      NCOSTP=40
      PI=4.*ATAN(1.)
      CALL NPCSTP(SEIS,NSEIS,NCOSTP,1,PI)
C
C ADD ZEROS TO ARRAY TO MAKE UP TO 2**NPOW2
      DO 120 I=NSESP1,N
      SEIS(I)=0.0
  120 CONTINUE
C
C FOURIER TRANSFORM OF THE SIGNAL.
      CALL ZRLOAD(N,SEIS,Z)
      CALL COOL(NPOW2,Z,+1.0)
```

```
C
C FILTER OUT FREQUENCIES BELOW WL(NAFLO*DF) AND ABOVE WH(NFHI*DF)
C USING A MARTIN-GRAHAM BAND-PASS FILTER. SPECTRUM  IS FILTERED
C BETWEEN W1 < W < W2: W1 = WL - WL/10 , W2 = WH + WH/10.
C REFERENCE : KULHANEK , 1979. INTRODUCTION DIGITAL FILTERING IN
C GEOPHYSICS , DEVELOPMENTS IN SOLID EARTH  GEOPHYSICS , VOL.8 ,
C ELSEVIER.
      IF(NAFLO.EQ.0)NAFLO=1
      IW1=NFHI
      IDW=IW1/10
      IW2=IW1+IDW
      DO 220 I=NFHI,NBY2
      ARG=FLOAT((I-IW1)/IDW)
      ARG=ARG*PI
      FILT=(1.+COS(ARG))*0.5
      IF(I.GT.IW2)FILT=0.
      Z(I)=Z(I)*FILT
  220 CONTINUE
      IW1=NAFLO
      IDW=IW1/10
      IW2=IW1-IDW
      DO 221 I=1,NAFLO
      ARG=FLOAT((IW1-I)/IDW)
      ARG=ARG*PI
      FILT=(1.+COS(ARG))*0.5
      IF(I.LT.IW2)FILT=0.
      Z(I)=Z(I)*FILT
  221 CONTINUE
C
      CALL FILLUP(NBY2P1,Z)
      DO 10 I=1,N
      SEIS(I)=0.0
   10 CONTINUE
C
C INVERSE FOURIER TRANSFORM OF COMPLEX SPECTRUM
      CALL COOL(NPOW2,Z,-1.0)
      DO 100 I=1,NSEIS
      Z(I)=Z(I)/FLOAT(N)
      SEIS(I)=REAL(Z(I))
  100 CONTINUE
      RETURN
      END
C
C*****
C
      SUBROUTINE COOL(N,XX,SIGNI)
C
C     THIS SUBROUTINE WAS PROGRAMMED BY I.MACLEOD, DEPT. OF
C     ENGINEERING PHYSICS,A.N.U. AND HAS BORROWED FROM D. MCCOWAN'S
C     COOL AND IBM'S HARM.
C
C     SINGLE PRECISION VERSION MODIFIED BY J.B.YOUNG FOR THE 360/75.
C
C
      DIMENSION W(14),XX(1),NBIT(20),JNT(20)
C
C
      INTEGER OFFSET
C
C
      DATA NX/0/
C
C
      IF(NX.GT.0)GO TO 100
      ROOT2=SQRT(2.0)
      PI2=8.0*ATAN(1.0)
C
  100 NX=2**N
      NX2=NX+NX
      NX2LS1=NX2-1
      NX2LS2=NX2-2
      NXON8=NX/8
      NXON4=NXON8+NXON8
      NXON2=NXON4+NXON4
      CON1=PI2/FLOAT(NX)
      IF(SIGNI.GT.0.0)GO TO 120
C
      DO 110 K=1,NX2LS1,2
      XX(K+1)=-XX(K+1)
  110 CONTINUE
C
  120 DO 130 K=1,N
      JNT(K)=2**(N-K)
  130 CONTINUE
C
      LSTART=N-N/3*3+1
      IF(LSTART.EQ.1)GO TO 200
      IF(LSTART.EQ.2)GO TO 150
      LBLOK2=NXON2
      L2BLOK=LBLOK2-1
C
      DO 140 KO=1,L2BLOK,2
      K1=KO+LBLOK2
      K2=K1+LBLOK2
      K3=K2+LBLOK2
      AOR=XX(KO)+XX(K2)
      AOI=XX(KO+1)+XX(K2+1)
      A1R=XX(KO)-XX(K2)
      A1I=XX(KO+1)-XX(K2+1)
      A2R=XX(K1)+XX(K3)
      A2I=XX(K1+1)+XX(K3+1)
      A3R=XX(K1)-XX(K3)
      A3I=XX(K1+1)-XX(K3+1)
      XX(KO)=AOR+A2R
      XX(KO+1)=AOI+A2I
      XX(K1)=AOR-A2R
```

```
      XX(K1+1)=AOI-A2I
      XX(K2)=A1R-A3I
      XX(K2+1)=A1I+A3R
      XX(K3)=A1R+A3I
      XX(K3+1)=A1I-A3R
  140 CONTINUE
      GO TO 200
C
  150 LBLOK2=NX
      L2BLOK=LBLOK2-1
      DO 160 KO=1,L2BLOK,2
      K1=KO+LBLOK2
      A1R=XX(K1)
      A1I=XX(K1+1)
      XX(K1)=XX(KO)-A1R
      XX(K1+1)=XX(KO+1)-A1I
      XX(KO)=XX(KO)+A1R
      XX(KO+1)=XX(KO+1)+A1I
  160 CONTINUE
C
C
  200 DO 300 M=LSTART,N,3
      LBLOK2=NX/2**(M+1)
      L2BLOK=LBLOK2-1
      LBLOK1=L2BLOK-1
      LBLOK8=LBLOK2*8
      LBLAST=NX2-LBLOK8+1
C
      DO 210 K=4,N
      NBIT(K)=0
  210 CONTINUE
C
      NW=0
C
      DO 290 OFFSET=1,LBLAST,LBLOK8
      IF(OFFSET.EQ.1)GO TO 220
      ARG=CON1*FLOAT(NW)
      W(1)=COS(ARG)
      W(2)=SIN(ARG)
      CSSQA=W(1)*W(1)
      W(3)=CSSQA+CSSQA-1.0
      W(4)=W(1)*W(2)
      W(4)=W(4)+W(4)
      W(5)=W(3)*W(1)-W(4)*W(2)
      W(6)=W(4)*W(1)+W(3)*W(2)
      CSSQ2A=W(3)*W(3)
      W(7)=CSSQ2A+CSSQ2A-1.0
      W(8)=W(4)*W(3)
      W(8)=W(8)+W(8)
      W(9)=W(7)*W(1)-W(8)*W(2)
      W(10)=W(8)*W(1)+W(7)*W(2)
      CSSQ3A=W(5)*W(5)
      W(11)=CSSQ3A+CSSQ3A-1.0
      W(12)=W(6)*W(5)
      W(12)=W(12)+W(12)
      W(13)=W(7)*W(5)-W(8)*W(6)
      W(14)=W(8)*W(5)+W(7)*W(6)
  220 LBLOKO=OFFSET+LBLOK1
C
      DO 260 KO=OFFSET,LBLOKO,2
      K1=KO+LBLOK2
      K2=K1+LBLOK2
      K3=K2+LBLOK2
      K4=K3+LBLOK2
      K5=K4+LBLOK2
      K6=K5+LBLOK2
      K7=K6+LBLOK2
      XKOWR=XX(KO)
      XKOWI=XX(KO+1)
      IF(OFFSET.NE.1) GO TO 240
      XK1WR=XX(K1)
      XK1WI=XX(K1+1)
      XK2WR=XX(K2)
      XK2WI=XX(K2+1)
      XK3WR=XX(K3)
      XK3WI=XX(K3+1)
      XK4WR=XX(K4)
      XK4WI=XX(K4+1)
      XK5WR=XX(K5)
      XK5WI=XX(K5+1)
      XK6WR=XX(K6)
      XK6WI=XX(K6+1)
      XK7WR=XX(K7)
      XK7WI=XX(K7+1)
      GO TO 250
  240 XK1WR=XX(K1)*W(1)-XX(K1+1)*W(2)
      XK1WI=XX(K1)*W(2)+XX(K1+1)*W(1)
      XK2WR=XX(K2)*W(3)-XX(K2+1)*W(4)
      XK2WI=XX(K2)*W(4)+XX(K2+1)*W(3)
      XK3WR=XX(K3)*W(5)-XX(K3+1)*W(6)
      XK3WI=XX(K3)*W(6)+XX(K3+1)*W(5)
      XK4WR=XX(K4)*W(7)-XX(K4+1)*W(8)
      XK4WI=XX(K4)*W(8)+XX(K4+1)*W(7)
      XK5WR=XX(K5)*W(9)-XX(K5+1)*W(10)
      XK5WI=XX(K5)*W(10)+XX(K5+1)*W(9)
      XK6WR=XX(K6)*W(11)-XX(K6+1)*W(12)
      XK6WI=XX(K6)*W(12)+XX(K6+1)*W(11)
      XK7WR=XX(K7)*W(13)-XX(K7+1)*W(14)
      XK7WI=XX(K7)*W(14)+XX(K7+1)*W(13)
  250 AOR=XKOWR+XK4WR
      AOI=XKOWI+XK4WI
      A1R=XK1WR+XK5WR
      A1I=XK1WI+XK5WI
      A2R=XK2WR+XK6WR
      A2I=XK2WI+XK6WI
      A3R=XK3WR+XK7WR
```

```
      A3I=XK3WI+XK7WI
      A4R=A0R+A2R
      A4I=A0I+A2I
      A5R=A0R-A2R
      A5I=A0I-A2I
      A6R=A1R+A3R
      A6I=A1I+A3I
      A7R=A3I-A1I
      A7I=A1R-A3R
      XX(K0)=A4R+A6R
      XX(K0+1)=A4I+A6I
      XX(K1)=A4R-A6R
      XX(K1+1)=A4I-A6I
      XX(K2)=A5R+A7R
      XX(K2+1)=A5I+A7I
      XX(K3)=A5R-A7R
      XX(K3+1)=A5I-A7I
      A0R=XK0WR-XK4WR
      A0I=XK0WI-XK4WI
      A8R=XK1WR-XK5WR
      A8I=XK1WI-XK5WI
      A1R=A8R-A8I
      A1I=A8R+A8I
      A2R=XK6WI-XK2WI
      A2I=XK2WR-XK6WR
      A8R=XK3WR-XK7WR
      A8I=XK3WI-XK7WI
      A3R=A8R-A8I
      A3I=A8R+A8I
      A4R=A0R+A2R
      A4I=A0I+A2I
      A5R=A0R-A2R
      A5I=A0I-A2I
      A6R=(A1R-A3I)/ROOT2
      A6I=(A1I+A3R)/ROOT2
      A7R=(A3R-A1I)/ROOT2
      A7I=(A3I+A1R)/ROOT2
      XX(K4)=A4R+A6R
      XX(K4+1)=A4I+A6I
      XX(K5)=A4R-A6R
      XX(K5+1)=A4I-A6I
      XX(K6)=A5R+A7R
      XX(K6+1)=A5I+A7I
      XX(K7)=A5R-A7R
      XX(K7+1)=A5I-A7I
  260 CONTINUE
C
      DO 280 K=4,N
      IF(NBIT(K).NE.0)GO TO 270
      NBIT(K)=1
      NW=NW+JNT(K)
      GO TO 290
  270 NBIT(K)=0
      NW=NW-JNT(K)
  280 CONTINUE
C
  290 CONTINUE
  300 CONTINUE
C
C
      NW=0
C
      DO 310 K=1,N
      JNT(K)=JNT(K)+JNT(K)
      NBIT(K)=0
  310 CONTINUE
C
      K=0
      IF(NW.LE.K)GO TO 320
      HOLDR=XX(NW+1)
      HOLDI=XX(NW+2)
      XX(NW+1)=XX(1)
      XX(NW+2)=XX(2)
      XX(1)=HOLDR
      XX(2)=HOLDI
C
  320 DO 340 M=1,N
      IF(NBIT(M).NE.0)GO TO 330
      NBIT(M)=1
      NW=NW+JNT(M)
      GO TO 350
  330 NBIT(M)=0
      NW=NW-JNT(M)
  340 CONTINUE
C
  350 DO 390 K=2,NX2LS2,2
      IF(NW.LE.K)GO TO 360
      HOLDR=XX(NW+1)
      HOLDI=XX(NW+2)
      XX(NW+1)=XX(K+1)
      XX(NW+2)=XX(K+2)
      XX(K+1)=HOLDR
      XX(K+2)=HOLDI
C
  360 DO 380 M=1,N
      IF(NBIT(M).NE.0)GO TO 370
      NBIT(M)=1
      NW=NW+JNT(M)
      GO TO 390
  370 NBIT(M)=0
      NW=NW-JNT(M)
  380 CONTINUE
C
  390 CONTINUE
C
      IF(SIGNI.GT.0.0)GO TO 420
```

```
C
      DO 410 K=1,NX2LS1,2
      XX(K+1)=-XX(K+1)
 410  CONTINUE
C
 420  RETURN
      END
C
C*****
C
      SUBROUTINE POW(N,NBY2,NBY2P1,NPOW2)
      NBY2=N/2
      NBY2P1=NBY2+1
      A=(N-1)/2
      NPOW2=ALOG10(A)/ALOG10(2.0)+2.0
      RETURN
      END
C
C*****
C
      SUBROUTINE ZRLOAD(N,X,Z)
      DIMENSION X(N),Z(N)
      COMPLEX Z
      DO 1 I=1,N
      Z(I)=CMPLX(X(I),0.0)
 1    CONTINUE
      RETURN
      END
C
C*****
C
      SUBROUTINE FILLUP(NOPTS,Z)
      DIMENSION Z(1)
      COMPLEX Z,CZERO
      CZERO=CMPLX(0.0,0.0)
      AN=NOPTS-2
      N=ALOG10(AN)/ALOG10(2.0)+1.0
      N1=(2**N)+1
      N2=2**(N+1)
      N1M1=N1-1
      DO 1 I=2,N1M1
      NN=N2-I+2
      Z(NN)=CONJG(Z(I))
 1    CONTINUE
      Z(N1)=CZERO
      RETURN
      END
C
C*****
C
      SUBROUTINE BASE (X,N,TYPE, IP1)
      DIMENSION X(N)
      REAL*8 MEAN,TYPE
      DATA MEAN/8HMEAN    /
C
      SUMX = 0
      SUMIX = 0
      AN = N
      IF(TYPE - MEAN)1,2,1
    1 IND = 1
      GO TO 3
    2 IND = 2
    3 DO 4  I = 1,N
      AI = I
      SUMX = SUMX + X(I)
      GO TO (5,4),IND
    5 SUMIX = SUMIX + AI*X(I)
    4 CONTINUE
      XBAR = SUMX/AN
      GO TO (6,7),IND
    6 XINTO = (((4.*AN)+2.)*SUMX-6.*SUMIX)/(AN*(AN-1.))
      PHI = ((12.*SUMIX)-6.*(AN+1.)*SUMX)/(AN*(AN+1.)*(AN-1.))
      DO 20 I = 1,N
      AI = I
      X(I) = X(I) - AI*PHI - XINTO
   20 CONTINUE
C     PRINT 10, PHI, XBAR
   10 FORMAT(//4X,49HDATA HAS BEEN CORRECTED TO LEAST SQUARES BASELINE/
     14X,32HGRADIENT OF LEAST SQUARES LINE =,F10.5,8X,14HMEAN OF DATA =,
     2F13.5)
      GO TO 8
C
    7 DO 30  I = 1,N
      X(I) = X(I) - XBAR
   30 CONTINUE
C     PRINT 11, XBAR
   11 FORMAT(//4X,40HDATA HAS BEEN CORRECTED TO MEAN BASELINE//4X,
     114HMEAN OF DATA =,F10.4)
    8 SUMX2 = 0
      SUMX3 = 0
      DO 9  I = 1,N
      X2 = X(I)*X(I)
      SUMX2 = SUMX2 + X2
      SUMX3 = SUMX3 + X2*X(I)
    9 CONTINUE
      VARX = SUMX2/AN
      A3MNT = SUMX3/AN
      SKEW = (A3MNT*A3MNT)/(VARX**3.)
C     PRINT 12, VARX, SKEW
   12 FORMAT(/4X,18HVARIANCE OF DATA =,E10.4,8X,10HSKEWNESS =,F10.4)
      IP1 = IP1 + 1
      GO TO (14,15),IP1
   15 PRINT 16,(I, X(I),  I = 1,N)
   16 FORMAT(//4X,24HTHE BASELINED DATA IS --//5(4X,6HSAMPLE,4X,4HX(I),
     13X)/(5(4X,I5,2X,F10.5)))
C
```

```
   14 RETURN
      END
C
C*****
C
      SUBROUTINE NPCSTP(X,N,NO,IND,PI)
C
C
C
C     IND=1---------COSINE TAPER BOTH ENDS OF CURVE.
C     IND=2---------COSINE TAPER FRONT END OF CURVE.
C     IND=3---------COSINE TAPER COSINE TAPER BACK END OF CURVE
C
C
C
C     X------IS THE ARRAY.
C
C     N-----IS THE NUMBER OF POINTS IN THE ARRAY.
C
C     NO ------IS THE STARTING NUMBER.
C
C
C
C
      DIMENSION X(N)
C
      ANO = NO-1
      PHI = PI/ANO
      CPHI = COS(PHI)
      SPHI = SIN(PHI)
      CTHET1 = 1.
      STHET1 = 0.
      CTHET2 = 1.
      STHET2 = 0.
      DO 1  I = 1,NO
      GO TO (2,3,4),IND
    2 IA = N-I+1
    3 IN=I
      GO TO 5
    4 IN = N-I+1
    5 X(IN) = 0.5*X(IN)*(1. - CTHET2)
      GO TO (6,9,9),IND
    6 X(IA) = 0.5*X(IA)*(1. - CTHET2)
    9 CALL SINCOS(CPHI,SPHI,CTHET1,STHET1,CTHET2,STHET2)
    1 CONTINUE
      RETURN
      END
C
C*****
C
      SUBROUTINE SINCOS (CPHI,SPHI,CTHET1,STHET1,CTHET2,STHET2)
      CTHET2 = CTHET1*CPHI - STHET1*SPHI
      STHET2 = STHET1*CPHI + CTHET1*SPHI
      CTHET1 = CTHET2
      STHET1 = STHET2
      RETURN
      END
```

D.2 Program 'MIR'

```
C DESCRIPTION:
C
C THIS PROGRAM COMPUTES THE RAYLEIGH WAVE MEDIUM RESPONSE FUNCTION
C M_Z(w) FOR A VERTICAL SURFACE DISPLACEMENT , USING THE THOMSON-HASKELL
C MATRIX METHODS AS EXTENDED BY HUDSON ET AL.(1969a,b) AND IMPLEMENTED BY
C DOUGLAS ET AL.(1972). EXCITATION BY A VARIETY OF POINT SOURCES ARE
C POSSIBLE ,CORRESPONDING TO BODY FORCE DISTRIBUTIONS FOR UNDERGROUND
C , UNDERWATER , AND ATMOSPHERIC EXPOSIONS , AND ALSO FOR EARTHQUAKES.
C
C ORIGIN :
C
C THE CODE HAS BEEN EXTRACTED FROM A MUCH LARGER PROGRAM - 'BIGE'.
C THIS WAS FURTHER MODIFIED TO TAKE ACCOUNT OF THE LOSS OF PRECISION
C AND REAL OVERFLOW PROBLEMS ENCOUNTERED AT HIGH FREQUENCIES AND
C HIGHER MODES. THESE ARE DISCUSSED IN APPENDIX A.4 OF THE THESIS.
C
C SPECIAL FEATURES:
C
C THE LOSS OF PRECISION PROBLEM IS 'PUT-OFF' BY WORKING WITH
C QUADRUPLE PRECISION VARIABLES. FREQUENCY AND PHASE VELOCITY
C ARE EVALUATED EXTERNAL TO THE PROGRAM USING A REVISED VERSION
C OF KNOPOFF'S METHOD. REAL OVERFLOW IS CIRCUMVENTED BY NORMALIZING
C EACH LAYER MATRIX PRODUCT AS IT IS FORMED - SEE SUBROUTINE 'PRODM'
C
C IMPLEMENTATION:
C
C INPUT ON CHANNEL 5 , FOR EACH SOURCE , IS AS FOLLOWS:
C
C     1. CARD WITH TITLE (10A8)
C
C     2. CARD WITH:-
C
C     NOL - NUMBER OF SOURCE LAYERS
C
C     ISL - LAYER WHICH CONTAINS SOURCE(TOP DOWNWARDS)
C
C     ISO - TYPE OF SOURCE IN HASKELL NOTATION
C     ISO = 1 FOR A SINGLE FORCE
C     ISO = 4 FOR A DOUBLE COUPLE EARTHQUAKE
C     ISO = 5 FOR AN EXPLOSION
C
C     ISEA - IF ISEA=1 TOP LAYER IS MADE OF LIQUID
C
C     DEP - DEPTH OF SOURCE , MEASURED FROM THE INTERFACE
C           BETWEEN THE SOURCE AND PRECEDING LAYER
C
C     MODE - THE PARTICULAR RAYLEIGH MODE NUMBER.
C     MODE = 0 CORRESPONDS TO THE FUNDAMENTAL MODE
C
C     IMTRX= 1 PUNCH GIVES AN EXTENDED PRINTOUT
```

```
C
C     IAZ - PLOTTING PARAMETER . IAZ = 0  , RADIATION PATTERN IS PLOTTED.
C     IAZ = 1 , THE SPECTRUM IS PLOTTED
C
C     (4I4,F10.5,3I4)
C
C     3. CARD WITH SHEAR VELOCITIES, AND THICKNESSES FOR EACH
C        LAYER (2F10.5)
C
C     4. DEPENDING ON THE OPTIONS SET , THE NEXT CARD MAY BE READ.
C        THESE PARAMETERS ARE THE RAKE AND DIP OF THE FAULT PLANE (3F9.5)
C
C     5. START AZIMUTH , NUMBER OF AZIMUTH POINTS REQUIRED , AND THE
C        INCREMENT OF AZIMUTH (F10.6,I4,F10.6)
C
C     6. NUMBER OF FREQUENCY POINTS TO BE READ IN (I4)
C
C     7. SEQUENCE OF CARDS CONTAINING FREQUENCY AND PHASE VELOCITY
C        FOR THE STRUCTURE OF INTEREST (2E15.7)
C
C OUTPUT IS ON GRAPHICS CHANNEL 70 , AND NUMERICAL RESULTS ON CHANNEL 9.
C
      IMPLICIT REAL*16 (A-H,O-Z)
      COMPLEX*32 SOU,VAL,VB,COM
      COMPLEX*32 UZ(400),UR(400)
      REAL*16 LAMBDA
      DIMENSION A(70,70),FREQ(70),AMP1(70),ANG(70),
     *PHASE(70,70),W(70),CC(2)
      DIMENSION C(80)
      EQUIVALENCE (COM,CC(1))
      COMMON/ALAY/ALPHA(20),BETA(20),RHO(20),D(20)
      COMMON/ALAY1/NOL,ISL,DEP
      COMMON/GRFF/TITLE(10)
      COMMON/SOUR/SOU(30),VAL,VB
      COMMON/SOUR1/ISO,IFREQ,IFOU,IDUM,
     *ANL,ANM,ANN,FL,FM,FN,ALA,BETA
      COMMON/PIE/PI,PI2,DTOR
      COMMON/PIE2/IMTRX
      COMMON/HMS/MODE
      PI=4.00*QATAN(1.0000)
      PI2=2.00*PI
      DTOR=PI/180.0000
      IMTRX=1
C
      CALL PLOTS('C.D.MACBETH-MURCHSEIS',21,70)
      CALL FACTOR(0.52)
      CALL PLOT(1.,1.,-3)
C
C READ IN DATA
      READ(5,1)TITLE
      WRITE(6,11)TITLE
      READ(5,2)NOL,ISL,ISO,ISEA,DEP,MODE,IMTRX,IAZ
      WRITE(6,12)NOL,ISL,ISO,ISEA,DEP,MODE,IAZ
      IF(ISEA.EQ.1)GOTO 71
      READ(5,3)(BETA(I),D(I),I=1,NOL)
      GOTO 72
   71 READ(5,30)(ALPHA(1),BETA(1),RHO(1),D(1))
      READ(5,3)(BETA(I),D(I),I=2,NOL)
   72 NL1=1
      IF(ISEA.EQ.1)NL1=2
C
C RELATE COMPRESSIONAL VELOCITY AND DENSITY TO SHEAR VELOCITY
      DO 70 I=NL1,NOL
      ALPHA(I)=1.7500*BETA(I)
      RHO(I)=(ALPHA(I)+10.8)*0.16074Q0
   70 CONTINUE
      WRITE(6,16)
      WRITE(6,13)(ALPHA(I),BETA(I),RHO(I),D(I),I=1,NOL)
C
C READ IN FAULT PLANE PARAMETERS IF SOURCE IS AN EARTHQUAKE
      IF(ISO.NE.4.AND.ISO.NE.2)GOTO67
      READ(5,4)LAMBDA,DELTA
      LAMBDA=LAMBDA*DTOR
      DELTA=DELTA*DTOR
      COSL=QCOS(LAMBDA)
      SINL=QSIN(LAMBDA)
      COSD=QCOS(DELTA)
      SIND=QSIN(DELTA)
      ANL=0.00
      ANM=SIND
      ANN=-COSD
      FL=COSL
      FM=-SINL*COSD
      FN=-SINL*SIND
      WRITE(6,14)DELTA,LAMBDA,ANL,ANM,ANN,FL,FM,FN
C
C READ IN AZIMUTH RANGE
   67 READ(5,6)RPHI,NPHI,DPHI
      RPHI=RPHI*DTOR
      DPHI=DPHI*DTOR
      DO 34 I=1,NPHI
      ANG(I)=RPHI+(NPHI-I )*DPHI
   34 CONTINUE
      PHITOT=RPHI+(NPHI-1)*DPHI
      IF(NPHI.NE.1)WRITE(6,21)RPHI,PHITOT,DPHI,NPHI
      IF(NPHI.EQ.1)WRITE(6,22)RPHI
C
C READ IN FREQUENCY AND PHASE VELOCITY POINTS
      READ(5,28)NF
      DO 50 I=1,NF
      READ(5,29)FREQ(I),C(I)
   50 W(I)=PI2*FREQ(I)
C
C SET UP SOURCE CONSTANTS
      DEP=D(ISL)-DEP
      ALA=ALPHA(ISL)**2
```

```
      BETA=BETA(ISL)**2
C
C SET UP THE SOURCE FUNCTION
   10 CALL SOURD(W,NF)
C
C COMPUTE THE SOURCE AND LAYER RESPONSE
      DO 48 I=1,NF
      IFREQ=I
      WW=W(I)
      CFREQ=C(I)
      CALL SPECLY(UZ,UR,WW,CFREQ,RPHI,DPHI,NPHI)
      DO 51 J=1,NPHI
      A(I,J)=CQABS(UZ(J))
      COM=UZ(J)
      IF(CC(1).EQ.0.QO.AND.CC(2).EQ.0.QO)PHASE(I,J)=0.QO
      IF(CC(1).NE.0.QO.OR.CC(2).NE.0.QO)PHASE(I,J)=QATAN2(CC(2),CC(1))
   51 CONTINUE
      IF(IAZ.EQ.1)GOTO48
      AMXPHI=0.QO
      DO 49 J=1,NPHI
      IF(QABS(A(I,J)).GE.AMXPHI)AMXPHI=A(I,J)
   49 CONTINUE
      DO 54 J=1,NPHI
      AMP1(J)=A(I,J)/AMXPHI
   54 CONTINUE
      CALL G1(ANG,AMP1,NPHI,FREQ(I))
      CALL PLOT(3.,0.,-3)
      WRITE(6,24)FREQ(I),AMXPHI
      WRITE(6,25)(ANG(J),AMP1(J),J=1,NPHI)
   48 CONTINUE
C
      IF(IAZ.EQ.0)GOTO 55
      DO 45 J=1,NPHI
      AMXF=0.QO
      DO 46 I=1,NF
      IF(QABS(A(I,J)).GE.AMXF)AMXF=A(I,J)
   46 CONTINUE
      DO 47 I=1,NF
      AMP1(I)=A(I,J)/AMXF
   47 CONTINUE
      IPLOT=0
      CALL G2(FREQ,AMP1,NF,ANG(J))
      IPLOT=IPLOT+1
      IF(IPLOT.LE.6)CALL PLOT(0.,7.,-3)
      IF(IPLOT.GT.6)CALL PLOT(7.,-30.,-3)
      WRITE(6,26)ANG(J),AMXF,J
      WRITE(6,27)(FREQ(I),AMP1(I),I=1,NF)
      WRITE(9,26)ANG(J),AMXF,J
      DO 89 I=1,NF
      AMP1(I)=AMP1(I)*AMXF
      WRITE(9,29)FREQ(I),AMP1(I)
   89 CONTINUE
   45 CONTINUE
C
C
   55 CALL PLOT(0.,0.,999)
C
    1 FORMAT(10A8)
    2 FORMAT(4I4,F10.5,3I4)
    3 FORMAT(2F10.5)
    4 FORMAT(3F9.5)
    5 FORMAT(I6)
    6 FORMAT(F10.6,I4,F10.6)
   11 FORMAT(1H1,6X,' *SYNTHETIC SPECTRAL AMPLITUDE PROGRAM*',/,
     *          8X,'-----------------------------------',//,
     *1X,10A8)
   12 FORMAT(/,1X,'NOL = ',I2,4X,'ISL = ',I2,4X,'ISO = ',I2,4X,
     *'ISEA = ',I2,4X,'DEP = ',F6.2,/,1X,'MODE = ',I2,4X,'IAZ = ',I2)
   16 FORMAT(/,12X,'VELOCITY-DEPTH MODEL',/,
     *12X,'--------------------',/,)
   13 FORMAT(2X,4F10.5)
   14 FORMAT(/,' FAULT PLANE ORIENTATION ANGLES',/,
     *          '----------------------------',
     *//,' DIP ANGLE (RADIANS) =',F10.5,
     *'  SLIP DIRECTION (RADIANS) =',F10.5,
     *///' COMPONENTS OF SOURCE VECTORS F AND N',/
     */,1X,'N1 = ',F7.4,4X,'N2 = ',F7.4,4X,'N3 = ',F7.4,/
     *1X,'F1 = ',F7.4,4X,'F2 = ',F7.4,4X,'F3 = ',F7.4)
   21 FORMAT(/,1X,'START AZIMUTH =',F10.5,' FINAL AZIMUTH =',F10.5,/
     *1X,'INCREMENT IN ANGLE =',F10.5,' NUMBER OF POINTS TAKEN ='
     *,I4)
   22 FORMAT(///,1X,'COMPUTATIONS AT ONE AZIMUTH =',F10.5)
   23 FORMAT(/,1X,'FREQUENCY RANGE ',F5.2,'-',F5.2,' (HZ)',' IN ',I4,
     *' STEPS OF ',F6.4)
   24 FORMAT(/,1X,'RADIATION PATTERN OVER AZIMUTH RANGE',
     *'AT FREQUENCY OF',F6.4,'(HZ)',/,
     *1X,'NORMALIZATION FACTOR =',F10.5,/)
   25 FORMAT(3(2X,F6.4,4X,E10.4))
   26 FORMAT(//,1X,'SPECTRAL AMPLITUDE (Z-CMPT) AT AN AZIMUTH OF '
     *,F10.5,/,1X,'NORMALIZATION FACTOR',E12.3,25X,I4,/)
   27 FORMAT(3(4X,F10.5,1X,F10.5))
   28 FORMAT(A4)
   29 FORMAT(2E15.7)
   30 FORMAT(4F10.5)
      STOP
      END
C
C*****
C
      SUBROUTINE ATR1X(A,RHO)
C
C     FORMS A LAYER MATRIX
C
      REAL*16 A(4,4),GAMMA,GAMMA1,VALPHA,VBETA,
     1KSQU,SABV,SATV,SBBV,SBTV,CALPHA,CBETA,RHO
      COMMON/LCON/GAMMA,GAMMA1,VALPHA,VBETA,KSQU,SABV,SATV,
```

```
     1SBBV,SBTV,CALPHA,CBETA
C
      A(1,1)=GAMMA*CALPHA-GAMMA1*CBETA
      A(1,2)=GAMMA*SBTV/KSQU-GAMMA1*SABV
      A(1,3)=(CBETA-CALPHA)/RHO
      A(1,4)=(KSQU*SABV-SBTV)/RHO
      A(2,1)=GAMMA*SATV-KSQU*GAMMA1*SBBV
      A(2,2)=GAMMA*CBETA-GAMMA1*CALPHA
      A(2,3)=(KSQU*SBBV-SATV)/RHO
      A(2,4)=-KSQU*A(1,3)
      A(3,1)=RHO*GAMMA*GAMMA1*(CALPHA-CBETA)
      A(3,2)=(SBTV*GAMMA*GAMMA/KSQU-GAMMA1*GAMMA1*SABV)*RHO
      A(3,3)=A(2,2)
      A(3,4)=-KSQU*A(1,2)
      A(4,1)=RHO*(GAMMA*GAMMA*SATV/KSQU-GAMMA1*GAMMA1*SBBV)
      A(4,2)=-A(3,1)/KSQU
      A(4,3)=-A(2,1)/KSQU
      A(4,4)=A(1,1)
      RETURN
      END
C
C*****
C
      SUBROUTINE CMATMU(A,B,N)
C
C     THIS ROUTINE PRE-MULTIPLIES COMPLEX MATRIX B BY
C     COMPLEX MATRIX A AND STORES THE PRODUCT IN B.
C
      COMPLEX*32 A,B,C
      DIMENSION C(4),A(N,N),B(N,N)
C
      DO 1 I=1,N
      DO 2 J=1,N
      C(J)=QCMPLX(0.Q0,0.Q0)
      DO 3 K=1,N
      C(J)=A(J,K)*B(K,I)+C(J)
 3    CONTINUE
 2    CONTINUE
C
      DO 4 K=1,N
      B(K,I)=C(K)
 4    CONTINUE
 1    CONTINUE
      RETURN
      END
C
C*****
C
      SUBROUTINE DBAR(D,RHO,DEP,AK)
      COMPLEX*32 D,GPA,GMA,GPB,GMB,GCASH,GSANH,GCBSH,AN,
     1GSBNH,GSATV,GSBTV,VAL,VB,VDEPA,VDEPB,SOU
      REAL*16 GAMMA,GAMMA1,VALPHA,VBETA,KSQU,
     1AKSQU,GAM,GAM1,AK,RHO,DEP
      DIMENSION D(4,4)
C
C     COMPUTES LOWER SOURCE LAYER MATRIX D-COMPLEX
C
      COMMON/SOUR/SOU(6,5),VAL,VB
      COMMON/SOUR1/ISO,IFREQ
      COMMON/LCON/GAMMA,GAMMA1,VALPHA,VBETA,KSQU
C
      AN=QCMPLX(-1.Q0,0.Q0)
      AKSQU=KSQU
      GAM=GAMMA
      GAM1=GAMMA1
      VDEPA=VAL*DEP
      VDEPB=VB*DEP
      CALL SOURCE(GPA,GMA,GPB,GMB,IFREQ)
    3 GPA=GPA*CQEXP(VDEPA)
      GMA=GMA*CQEXP(VDEPA*AN)
      GPB=GPB*CQEXP(VDEPB)
      GMB=GMB*CQEXP(VDEPB*AN)
C
      GCASH=(GPA+GMA)*0.5Q0
      GSANH=(GPA-GMA)*0.5Q0
      GCBSH=(GPB+GMB)*0.5Q0
      GSBNH=(GPB-GMB)*0.5Q0
      GSATV=GSANH*VAL
      GSBTV=GSBNH*VB
C
      IF (CQABS(VB).EQ.0.Q0) GO TO 4
C
      D(1,1)=AN*GCASH/RHO
      D(1,2)=GSANH/RHO
      D(1,3)=AN*VB*GCBSH/RHO
      D(1,4)=GSBTV/RHO
      D(2,1)=AN*GSATV/RHO
      D(2,2)=GCASH*VAL/RHO
      D(2,3)=AN*AKSQU*GSBNH/RHO
      D(2,4)=AKSQU*GCBSH/RHO
      D(3,1)=AN*GAM1*GCASH
      D(3,2)=GAM1*GSANH
      D(3,3)=GAM*VB*GCBSH*AN
      D(3,4)=GAM*GSBTV
      D(4,1)=AN*GAM*GSATV/AKSQU
      D(4,2)=GAM*VAL*GCASH/AKSQU
      D(4,3)=AN*GAM1*GSBNH
      D(4,4)=GAM1*GCBSH
      RETURN
C
    4 D(1,1)=QCMPLX(1.Q0,0.Q0)
      D(2,2)=GCASH*VAL/RHO
      D(2,3)=AN*GSATV/RHO
      D(3,2)=AN*GSANH
      D(3,3)=GCASH
      RETURN
```

```
C
C
      END
      SUBROUTINE EMN1S(EM1,RHO)
      REAL*16 EM1(4,4),GAMMA,GAMMA1,VALPHA,VBETA,KSQU,RHO
C
C     COMPUTES HALF SPACE MATRIX-HASKELL 1964
C
      COMMON/LCON/GAMMA,GAMMA1,VALPHA,VBETA,KSQU
C
C
C
      EM1(1,1)=-RHO*GAMMA
      EM1(1,2)=0.0Q00
      EM1(1,3)=1.0Q00
      EM1(1,4)=0.0Q00
      EM1(2,1)=0.0Q00
      EM1(2,2)=-RHO*GAMMA1/VALPHA
      EM1(2,3)=0.0Q00
      EM1(3,2)=0.0Q00
      EM1(2,4)=KSQU/VALPHA
      EM1(3,1)=RHO*GAMMA1/VBETA
      EM1(3,3)=-1.Q0/VBETA
      EM1(4,4)=-1.0Q00
      EM1(4,3)=0.0Q00
      EM1(3,4)=0.0Q00
      EM1(4,1)=0.0Q00
      EM1(4,2)=RHO*GAMMA/KSQU
      RETURN
      END
C
C*****
C
      REAL FUNCTION FDET*16(DJ)
C
C     COMPUTES RAYLEIGH FUNCTION FOR REAL*16 MATRIX FROM
C     ELEMENTS OF J - MATRIX.
C
      REAL*16 DJ(4,4)
      FDET=(DJ(1,1)-DJ(2,1))*(DJ(3,2)-DJ(4,2))-(DJ(1,2)-DJ(2,2))
     2 *(DJ(3,1)-DJ(4,1))
      RETURN
      END
C
C*****
C
      SUBROUTINE HASK(K,WSQU)
      COMPLEX*32 SOU,VAL,VB,CONE
      REAL*16 PI,ANL,ANM,ANN,FL,FM,FN,ALPHAQ,BETAQ,WSQU,PI2W,K,
     1PI2
C
C     COMPUTES HASKELL SOURCE TERMS
C
      COMMON/PIE/PI,PI2
      COMMON/SOUR/SOU(6,5),VAL,VB
      COMMON/SOUR1/ISO,IFREQ,IFOU,IDUM,
     1ANL,ANM,ANN,FL,FM,FN,ALPHAQ,BETAQ
C
      CONE=QCMPLX(1.Q0,0.Q0)
      DO 7 J=1,5
      DO 6 I=1,6
      SOU(I,J)=QCMPLX(0.Q0,0.Q0)
    6 CONTINUE
    7 CONTINUE
      PI2W=PI2*WSQU
C
      GO TO(1,2,3,4,5),ISO
C
C     SINGLE FORCE IN DIRECTION FL,FM,FN
C
    1 IF(CQABS(VB).NE.0.Q0) GO TO 8
      SOU(3,1)=-FN*K/PI2W*CONE
      RETURN
C
    8 SOU(1,1)=-FN*K/PI2W*CONE
      SOU(3,1)=FN*K/(VB*PI2W)
      SOU(2,2)=-FL*K*K/(VAL*PI2W)
      SOU(4,2)=FL/PI2W*CONE
      SOU(6,2)=WSQU*FL/(BETAQ*VB*PI2W)
      SOU(2,3)=-FM*K*K/(VAL*PI2W)
      SOU(4,3)=FM/PI2W*CONE
      SOU(6,3)=FM*WSQU/(BETAQ*VB*PI2W)
      RETURN
C
C     FORCE DIPOLE WITHOUT TO TORQUE
C
    2 SOU(2,1)=(K/VAL)*(K*K*(1.Q0-3.Q0*FN*FN)
     1+2.Q0*FN*FN*WSQU/ALPHAQ)
      SOU(2,1)=SOU(2,1)/(2.Q0*PI2W)
      SOU(4,1)=-K*(1.Q0-3.Q0*FN*FN)/(2.Q0*PI2W)*CONE
      SOU(1,2)=-2.Q0*FL*FN*K*K/PI2W*CONE
      SOU(3,2)=FL*FN*(VB+K*K/VB)/PI2W
      SOU(5,2)=-FL*FN*WSQU/(BETAQ*PI2W)*CONE
      SOU(1,3)=-2.Q0*FM*FN*K*K/PI2W*CONE
      SOU(3,3)=FM*FN*(VB+K*K/VB)/PI2W
      SOU(5,3)=   -FM*FN*WSQU/BETAQ*CONE
      SOU(5,3)=SOU(5,3)/PI2W
      SOU(2,4)=(FM*FM-FL*FL)*K*K*K/(VAL*2.Q0*PI2W)
      SOU(4,4)=-(FM*FM-FL*FL)*K/(2.Q0*PI2W)*CONE
      SOU(6,4)=(FM*FM-FL*FL)*WSQU*K/(BETAQ*VB)
      SOU(6,4)=SOU(6,4)/(2.Q0*PI2W)
      SOU(2,5)=-FL*FM*K*K*K/(VAL*PI2W)
      SOU(4,5)=FL*FM*K/PI2W*CONE
      SOU(6,5)=-FL*FM*WSQU*K/(BETAQ*VB*PI2W)
      RETURN
C
```

```
C     SINGLE COUPLE,FORCE IN DIRECTION(FL,FM,FN),
C     OFFSET IN DIRECTION(ANL,ANM,ANN),F.N=0.
C
    3 SOU(2,1)=(FN*ANN*K/VAL)*(2.QO*WSQU/ALPHAQ-3.QO*K*K)
      SOU(2,1)=SOU(2,1)/(2.QO*PI2W)
      SOU(4,1)=3.QO*FN*ANN*K/(2.QO*PI2W)*CONE
      SOU(6,1)=(FM*ANL-FL*ANM)*WSQU*K/(BETAQ*VB)
      SOU(6,1)=SOU(6,1)/(2.QO*PI2W)
      SOU(1,2)=-K*K*(FL*ANN+FN*ANL)/PI2W*CONE
      SOU(3,2)=(FL*ANN*VB+FN*ANL*K*K/VB)/PI2W
      SOU(1,3)=-K*K*(FM*ANN+FN*ANM)/PI2W*CONE
      SOU(5,2)=-FL*ANN*(WSQU/BETAQ)/PI2W*CONE
      SOU(3,3)=(FM*ANN*VB+FN*ANM*K*K/VB)/PI2W
      SOU(5,3)=-FM*ANN*(WSQU/BETAQ)/PI2W*CONE
      SOU(2,4)=(FM*ANM-FL*ANL)*K*K*K/(VAL*PI2W*2.QO)
      SOU(4,4)=-K*(FN*ANM-FL*ANL)/(PI2W*2.QO)*CONE
      SOU(6,4)=(FM*ANM-FL*ANL)*WSQU*K/(BETAQ*VB)
      SOU(6,4)=SOU(6,4)/(PI2W*2.QO)
      SOU(2,5)=-K*K*K*(FL*ANM+FM*ANL)/(VAL*PI2W*2.QO)
      SOU(4,5)=(FL*ANM+FM*ANL)*K*CONE
      SOU(6,5)=-(FL*ANM+FM*ANL)*WSQU*K/(BETAQ*VB)
      SOU(6,5)=SOU(6,5)/(2.QO*PI2W)
      RETURN
C
C     DOUBLE COUPLE WITHOUT TORQUE
C
    4 SOU(2,1)=(FN*ANN*K/VAL)*(2.QO*WSQU/ALPHAQ-3.QO*K*K)/PI2W
      SOU(4,1)=3.QO*FN*ANN*K*CONE/PI2W
      SOU(1,2)=-2.QO*K*K*(FL*ANN+FN*ANL)/PI2W*CONE
      SOU(3,2)=(FL*ANN+FN*ANL)*(VB+K*K/VB)/PI2W
      SOU(1,3)=-2.QO*K*K*(FM*ANN+FN*ANM)/PI2W*CONE
      SOU(3,3)=(FM*ANN+FN*ANM)*(VB+K*K/VB)/PI2W
      SOU(5,2)=-(FL*ANN+FN*ANL)*(WSQU/BETAQ)/PI2W*CONE
      SOU(5,3)=-(FN*ANN+FN*ANM)*(WSQU/BETAQ)/PI2W*CONE
      SOU(2,4)=(FM*ANM-FL*ANL)*K*K*K/(VAL*PI2W)
      SOU(4,4)=-(FM*ANM-FL*ANL)*K/PI2W*CONE
      SOU(6,4)=(FM*ANM-FL*ANL)*WSQU*K/(BETAQ*VB*PI2W)
      SOU(2,5)=-(FL*ANM+FM*ANL)*K*K*K/(VAL*PI2W)
      SOU(4,5)=(FL*ANM+FM*ANL)*K/PI2W*CONE
      SOU(6,5)=-(FL*ANM+FM*ANL)*WSQU*K/(BETAQ*VB*PI2W)
      RETURN
C
C     PURE COMPRESSIONAL SOURCE
C
    5 SOU(2,1)=WSQU*K/(ALPHAQ*VAL*PI2W)
      RETURN
      END
C
C*****
C
      SUBROUTINE MULD(A,B,C,M)
      REAL*16 A,B,C,ROW,SUM
C
C     THIS ROUTINE FORMS THE MATRIX PRODUCT A*B=C
C
      DIMENSION A(M,M),B(M,M),C(M,M),ROW(4)
C
      DO 4 J=1,M
      DO 2 I=1,M
      SUM=0.QOO
      DO 1 K=1,M
      SUM=SUM+A(J,K)*B(K,I)
 1    CONTINUE
      ROW(I)=SUM
 2    CONTINUE
      DO 3 I=1,M
      C(J,I)=ROW(I)
 3    CONTINUE
 4    CONTINUE
C
      RETURN
      END
C
C*****
C
      SUBROUTINE PRODM(L,A,CJ,DMAT,W,K,IL,IB,IS,C)
      IMPLICIT REAL*16 (A-H,O-Z)
      COMPLEX*32 AYE,AN,CZERO,CJ,CL,CE,DMAT,VAL,VB,QQ,VAHOLD,VBHOLD
      REAL*16 L(4,4),J(4,4)
      REAL*16 KSQU,K
      DIMENSION A(4,4)
      DIMENSION CJ(4,4),CL(4,4),CE(4,4),DMAT(4,4)
C
C     COMPUTES L AND J MATRICES
C     IL=1--L COMPUTED
C     IL=2--L NOT COMPUTED
C     IB=1--SURFACE WAVES
C     IB=2--BODY WAVES
C     IS=1--SOURCE LAYERS
C     IS=2--STATION LAYERS
C
      COMMON/LCON/GAMMA,GAMMA1,VALPHA,VBETA,KSQU,SABV,SATV,
     1SBBV,SBTV,CALPHA,CBETA,CWAT
      COMMON/SOUR/QQ(30),VAL,VB
      COMMON  /ALAY/   ALPHA(20),BETA(20),RHO(20),D(20)
      COMMON/ALAY1/NOL,ISL,DEP
      COMMON/PIE/PI,PI2,DTOR
      COMMON/PIE2/IMTRX
      COMMON/NORM/BIG(10),JNORM
C
      AYE=QCMPLX(0.QO,1.QO)
      CZERO=QCMPLX(0.QO,0.QO)
      CWAT=0.QO
      AN=QCMPLX(-1.QO,0.QO)
      KSQU=K*K
      AK=K
```

```
      WSQU=W*W
      II=1
      IF(ISL+1.EQ.NOL)II=2
C
C SET L,DMAT AND J MATRICES
      MN=4
      DO 4 I=1,4
      DO 5 JJ=1,4
      L(I,JJ)=0.0Q00
      J(I,JJ)=0.0Q00
      DMAT(I,JJ)=CZERO
 5    CONTINUE
      L(I,I)=1.0Q00
      J(I,I)=1.0Q00
 4    CONTINUE
C
      NN=NOL
C
      JNORM=0
      DO 1 I=1,NN
      N=NN-I
      IF(I.EQ.NN)N=NN
      ALPH=ALPHA(N)
      BET=BETA(N)
      ROW=RHO(N)
      DEE=D(N)
C
   30 GAMMA=2.Q0*BET*BET*KSQU/WSQU
      GAMMA1=GAMMA-1.Q0
C
C COMPUTE LAYER MATRICES FOR SURFACE WAVES
 10   HOLD=KSQU-WSQU/(ALPH*ALPH)
      VALPHA=QSQRT(QABS(HOLD))
      HOL=HOLD
      VAL=CQSQRT(QCMPLX(HOL,0.Q0))
      IF(HOLD.LT.0.0Q00)GO TO 6
      CALPHA=QCOSH(VALPHA*DEE)
      SALPHA=QSINH(VALPHA*DEE)
      SATV=SALPHA*VALPHA
      GO TO 7
 6    CALPHA=QCOS(VALPHA*DEE)
      SALPHA=QSIN(VALPHA*DEE)
      SATV=SALPHA*VALPHA
      SATV=-SATV
   7  SABV=SALPHA/VALPHA
C
      IF(QABS(BET)-1.0Q-30)73,73,74
 73   HOLD=0.0Q0
      VB=CZERO
      VBETA=0.0Q0
      SBETA=0.0Q0
      CBETA=0.0Q0
      SBTV=0.0Q0
      SBBV=0.0Q0
      GO TO 12
 74   HOLD=KSQU-WSQU/(BET*BET)
 75   HOL=HOLD
      VB=CQSQRT(QCMPLX(HOL,0.Q0))
      VBETA=QSQRT(QABS(HOLD))
      IF(HOLD.LT.0.0Q00)GO TO 8
      CBETA=QCOSH(VBETA*DEE)
      SBETA=QSINH(VBETA*DEE)
      SBTV=SBETA*VBETA
      GO TO 9
 8    CBETA=QCOS(VBETA*DEE)
      SBETA=QSIN(VBETA*DEE)
      SBTV=SBETA*VBETA
      SBTV=-SBTV
   9  SBBV=SBETA/VBETA
C
 12   IF(I.EQ.NN)GO TO 1
      GO TO (331,331,332,331),II
 331  IF(BET)31,70,31
  31  CALL ATR1X(A,ROW)
      GO TO 32
  70  CALL WTR1X(A,ROW)
      CWAT=CALPHA
  32  CALL MULD(J,A,J,NN)
C
C NORMALIZE THE MATRIX PRODUCT WRT MAXIMUM ELEMENT
C AND STORE THIS FACTOR
      AMX=0.Q0
      DO 91 JR=1,4
      DO 91 JC=1,4
      IF(QABS(J(JR,JC)).GE.AMX)AMX=QABS(J(JR,JC))
  91  CONTINUE
      IF(N.GT.ISL)GOTO93
      JNORM=JNORM+1
      BIG(JNORM)=AMX
  93  DO 92 JR=1,4
      DO 92 JC=1,4
      J(JR,JC)=J(JR,JC)/AMX
  92  CONTINUE
 14   IF(N.GT.(ISL+1).OR.N.LT.ISL)GO TO 1
C
C STORE L MATRIX AND FORM DMAT
 332  II=II+1
      GO TO (60,60,61,36),II
 61   DEE=DEP
      GO TO 30
C
 60   DO 2 M=1,4
      DO 3 MM=1,4
      L(M,MM)=J(M,MM)
 3    CONTINUE
 2    CONTINUE
```

```
      GO TO 1
C
   36 CALL DBAR(DMAT,ROW,DEP,AK)
      VAHOLD=VAL
      VBHOLD=VB
 1    CONTINUE
C
C COMPLETE FORMATION OF MATRICES
      CALL EMN1S(A,ROW)
      DO 19 M=1,4
      DO 20 MM=1,4
      DD=J(M,MM)
      CJ(M,MM)=QCMPLX(DD,0.QQ)
      DD=L(M,MM)
      CL(M,MM)=QCMPLX(DD,0.QQ)
      DD=A(M,MM)
      CE(M,MM)=QCMPLX(DD,0.QQ)
 20   CONTINUE
 19   CONTINUE
      CALL CMATMU (CE,CJ,MN)
      GO TO(40,41),IL
   40 CALL CMATMU (CE,CL,MN)
      CALL CMATMU (CL,DMAT,MN)
C
C FORM REAL MATRICES IF SURFACE WAVES
   41 CALL MULD(A,J,A,MN)
C
   16 VAL=VAHOLD
      VB=VBHOLD
      RETURN
      END
C
C*****
C
      SUBROUTINE SPECLY(UZ,UR,W,C,RPHI,DPHI,NPHI)
      IMPLICIT REAL*16 (A-H,O-Z)
      REAL*16 K,KHOLD
      DIMENSION PK(10),BL(4,4),BJ(4,4)
      COMPLEX*32 UZ(400),UR(400),ELLIP
      COMPLEX*32 L(4,4),J(4,4)
      COMPLEX*32 AYE,CZERO,VAL,VB,
     1GRCO,GRC1,GRS1,GRC2,GRS2,GJ1,GJ2,GHOLD,
     2SCO,SC1,SS1,SC2,SS2,RU,UI
C
C COMPUTES SOURCE AND SOURCE LAYER RESPONSE FOR SURFACE WAVES
C
      COMMON/PIE/PI,PI2,DTOR
      COMMON/PIE2/IMTRX,IPNCH
      COMMON/ALAY/ALPHA(20),BETA(20),RHO(20),D(20)
      COMMON/ALAY1/NOL,ISL,DEP
      COMMON/SOUR/SCO(6),SC1(6),SS1(6),SC2(6),SS2(6),
     1VAL,VB
      COMMON/SOUR1/ISO,IFREQ
      COMMON /LCON/QRS(22),CWAT
      COMMON/NORM/BIG(10),JNORM
C
      IL=1
      IB=1
      IS=1
      SEE=0.QQ
      AN=-1.QQ
      DK=1.0Q-6
      CZERO=QCMPLX(0.QQ,0.QQ)
      AYE=QCMPLX(0.QQ,1.QQ)
      K=W/C
      CALL PRODM(BL,BJ,J,L,W,K,IL,IB,IS,SEE)
C
      AK=K
      WSW=W*W
      CALL HASK(AK,WSW)
C
      GRCO=CZERO
      GRC1=CZERO
      GRS1=CZERO
      GRS2=CZERO
      GRC2=CZERO
      GJ1=J(3,1)-J(4,1)
      GJ2=J(1,1)-J(2,1)
   10 DO 22 II=1,4
      GHOLD=GJ1*(L(1,II)-L(2,II))-GJ2*(L(3,II)-L(4,II))
      GRCO=GRCO+GHOLD*SCO(II)
      GRC1=GRC1+GHOLD*SC1(II)
      GRS1=GRS1+GHOLD*SS1(II)
      GRS2=GRS2+GHOLD*SS2(II)
   22 GRC2=GRC2+GHOLD*SC2(II)
C
    2 DO 1 I=1,NPHI
C
C FORM AZIMUTHAL MODE TERMS
      PHI=RPHI+QFLOAT(NPHI-I)*DPHI
      CPHI=QCOS(PHI)
      SPHI=QSIN(PHI)
      C2PHI=QCOS(2.0QQO*PHI)
      S2PHI=QSIN(2.0QQO*PHI)
C
C COMPUTE NUMERATOR OF COMPLEX RESPONSE
      UZ(I)=CZERO
      RU=GRCO-GRC2*C2PHI-GRS2*S2PHI
      UI=GRC1*CPHI+GRS1*SPHI
      UZ(I)=RU+AYE*UI
      UZ(I)=UZ(I)*QSQRT(PI2/K)
      UR(I)=UZ(I)*((K*(J(1,2)-J(2,2)))/(J(1,1)-J(2,1)))
    1 CONTINUE
C
C COMPUTE DERIVATIVE OF RAYLEIGH FUNCTION WRT WAVENUMBER
      KHOLD=K
```

```
      K=KHOLD-2.QQ*DK
      CALL PRODM(BL,BJ,J,L,W,K,IL,IB,IS,SEE)
      FK(1)=FDET(BJ)
      K=KHOLD-1.QQ*DK
      CALL PRODM(BL,BJ,J,L,W,K,IL,IB,IS,SEE)
      FK(2)=FDET(BJ)
      K=KHOLD+1.QQ*DK
      CALL PRODM(BL,BJ,J,L,W,K,IL,IB,IS,SEE)
      FK(4)=FDET(BJ)
      K=KHOLD+2.QQ*DK
      CALL PRODM(BL,BJ,J,L,W,K,IL,IB,IS,SEE)
      FK(5)=FDET(BJ)
      DFDK=FK(1)-8.QQ*FK(2)+8.QQ*FK(4)-FK(5)
      DFDK=DFDK/(12.QQ*DK)
C
C COMPENSATE FOR NORMALIZATION
      DO 91 JJ=1,JNORM
   91 DFDK=DFDK*BIG(JJ)
C
      DO 3 I=1,NPHI
      UZ(I)=UZ(I)/DFDK
      UZ(I)=UZ(I)*AN*AYE
      UR(I)=UR(I)/DFDK
      IF(IMTRX.EQ.2)GO TO 1
      FQQ=W/PI2
C
C COMPUTE ELLIPTICITY OF RAYLEIGH  MODE
      ELLIP=UR(I)/UZ(I)
      PRINT 102,FQQ
      PRINT 101,W,C,RU,UI,UZ(I),PHI,DFDK
    3 CONTINUE
  101 FORMAT(1X,'W=',E12.4,' C=',E12.4,' RU=',2E12.4,' UI=',2E12.4,
     */,1X,'UZ(I)=',2E12.4,' ANGLE=',E12.4,' DFDK=',E12.4)
  102 FORMAT('  FREQUENCY =',F10.4,'(HZ)',' ELLIPTICITY IS ',2E12.5)
      RETURN
      END
C
C*****
C
      SUBROUTINE WTR1X(A,RHO)
      REAL*16 A(4,4),GAMMA,GAMMA1,VALPHA,VBETA,KSQU,
     1SABV,SATV,SBBV,SBTV,CALPHA,RHO
C
C     COMPUTES LAYER MATRIX FOR FLUID
C
      COMMON/LCON/GAMMA,GAMMA1,VALPHA,VBETA,KSQU,SABV,
     1SATV,SBBV,SBTV,CALPHA
C
      DO 1 I=1,4
      DO 2 J=1,4
      A(I,J)=0.0QQ0
    2 CONTINUE
    1 CONTINUE
C
    3 A(1,1)=1.0QQ
      A(2,2)=CALPHA
      A(3,2)=-RHO*SABV
      A(2,3)=-SATV/RHO
      A(3,3)=A(2,2)
      RETURN
      END
C
C*****
C
      SUBROUTINE SOURCE(A,B,C,D,I)
      COMPLEX*32 A,B,C,D,Z
      COMMON/WEA/Z(2048)
      A=Z(I)
      B=A
      C=A
      D=A
      RETURN
      END
C
C*****
C
      SUBROUTINE SOURD(W,NF)
      IMPLICIT REAL*16 (A-H,O-Z)
      COMPLEX *32 Z
      COMMON /WEA/Z(2048)
C
C TREAT THE SOURCE AS A DELTA FUNCTION
      DO 33 I=1,NF
      Z(I)=QCMPLX(1.QQ,0.QQ)
   33 CONTINUE
      RETURN
      END
C
C*****
C
      SUBROUTINE G1(TH,R,N,FFQ)
C
C     PLOTTING ROUTINE FOR RADIATION SPECTRUM
C
      REAL*16 TH(N),R(N),FFQ
      REAL*4 X(400),Y(400),FQ
      FQ=FFQ
      DO 10 I=1,N
      X(I)=(R(I)*QSIN(TH(I)))
   10 Y(I)=(R(I)*QCOS(TH(I)))
      RM=0.
      X(N+1)=0.0
      X(N+2)=1.0
      Y(N+1)=0.0
      Y(N+2)=1.0
      CALL LINE(X,Y,N,1,0,0)
```

```
      RAD=0.0
      DO 30 J=1,2
      RAD=RAD+0.5
      DO 20 I=1,N
      X(I)=RAD*(QSIN(TH(I)))
   20 Y(I)=RAD*(QCOS(TH(I)))
   30 CALL LINE(X,Y,N,1,0,0)
      CALL NUMBER(1.0,-1.5,0.15,FQ,0.,3)
      CALL SYMBOL(-1.0,-1.5,0.15,'FREQUENCY =',0.,11)
      RETURN
      END
C
C*****
C
      SUBROUTINE G2(XX,YY,N,PPHI)
C
C     PLOTTING ROUTINE FOR SPECTRUM
C
      REAL*16 XX(N),YY(N),PPHI
      REAL*4 X(400),Y(400),PHI
      PHI=(PPHI)
      DO 2 I=1,N
      X(I)=(XX(I))
      Y(I)=(YY(I))
    2 CONTINUE
      CALL PLOT(0.,0.,3)
      CALL PLOT(5.,0.,2)
      CALL PLOT(5.,5.,2)
      CALL PLOT(0.,5.,2)
      CALL PLOT(0.,0.,2)
C
      X1=(X(1)/X(N))*5.0
      Y1=Y(1)*5.0
      CALL PLOT(X1,Y1,3)
      DO 1 I=2,N
      XP=(X(I)/X(N))*5.0
      YP=Y(I)*5.0
      CALL PLOT(XP,YP,2)
    1 CONTINUE
C
      DO 3 I=1,3
      RN=(I-1)*0.5
      YN=FLOAT(I-1)*2.5
      CALL NUMBER(-0.5,YN,0.15,RN,0.,1)
    3 CONTINUE
      XMIN=X(1)
      DX=(X(N)-X(1))/5.00
      DO 4 I=1,6
      F=XMIN+(I-1)*DX
      XN=FLOAT(I-1)-0.2
      CALL NUMBER(XN,-0.2,0.15,F,0.,2)
    4 CONTINUE
      CALL SYMBOL(1.7,-0.5,0.15,'FREQUENCY(HZ)',0.,13)
      CALL SYMBOL(-0.7,0.2,0.15,'SPECTRAL AMPLITUDE(NORMALIZED)',90.,30)
      CALL SYMBOL(0.,-1.0,0.15,'AZIMUTH =',0.,9)
      CALL NUMBER(1.7,-1.0,0.15,PHI,0.,2)
      RETURN
      END
```

D.3 Program 'SSQ'

```
1     C DESCRIPTION :
2     C
3     C THIS PROGRAM IMPLEMENTS THE SINGLE-STATION ATTENUATION
4     C PROCEDURE DESCRIBED IN CHAPTER 5 OF THESIS FOR EXPLOSION
5     C EVENTS ONLY. THE PROGRAM WORKS IN TWO MODES. IN THE FIRST MODE
6     C (MODE = 0) , ESTIMATES OF THE SPECTRAL PARAMETERS ARE
7     C DETERMINED. IN THE SECOND MODE (MODE = 1 ) THE  BOUNDS ON THESE
8     C ESTIMATES ARE FOUND.
9     C
10    C MODE = 0:
11    C INSTRUMENT-CORRECTED SPECTRA AT EACH STATION  AROUND THE SOURCE
12    C ARE INPUT , SMOOTHED , AND EQUALIZED FOR GEOMETRIC SPREADING
13    C AND THE MEDIUM RESPONSE. THE SOURCE PARAMETER IS STEPPED ALONG
14    C A ONE-DIMENSIONAL GRID , AND THE SOURCE FUNCTION EVALUATED AT
15    C EACH POINT. THE SPECTRA ARE DIVIDED BY THIS , AND THE REMAINING
16    C SPECTRAL PARAMETERS ARE ESTIMATED USING A QUASI-NEWTONIAN ROUTINE
17    C TO DETERMINE THE BEST LEAST SQUARES FIT.
18    C
19    C MODE = 1:
20    C THE SMOOOTHED SPECTRA ARE CORRECTED  FOR THE BEST ESTIMATES
21    C OF THE SOURCE FUNCTION AND GEOMETRIC SPREADING. THE AMPLITUDES ARE THEN
22    C CONVERTED USING LOGS , AND A SIMPLEX ALGORITHM UTILIZED TO OBTAIN
23    C BOUNDS ON THE ABSOLUTE SCALING PARAMETER AND ATTENUATION VALUES
24    C
25    C IMPLEMENTATION :
26    C
27    C INPUT IS READ ON CHANNEL 1
28    C
29    C     1. TITLE (10A8)
30    C
31    C     2. A SERIES OF PARAMETERS:
32    C
33    C        NS    - NUMBER OF STATIONS
34    C        ISOUR  SELECTS MEDIUM RESPONSE
35    C        ISOUR = 1 UNDERGROUND EXPLOSION
36    C        ISOUR = 3 UNDERWATER EXPLOSION
37    C        ISOUR = 2,4  STRATIFIED HALF-SPACE RESPONSE READ EXTERNAL
38    C                     TO THE PROGRAM
39    C
40    C        GBOT,GSPAC,NGP - LOWER LIMIT OF GRID , GRID SPACING , NUMBER
41    C                         OF POINTS
42    C
43    C        (2I4,2F8.4,I4)
44    C
45    C FOR EACH OF THE NS STATIONS THERE FOLLOWS A STACK OF CARDS WITH THE
46    C FOLLOWING FORMAT:
47    C
48    C     3. A SERIES OF PARAMETERS:
49    C
50    C        STN - STATION NAME
```

```
C
C       NF - NUMBER OF FREQUENCY POINTS
C
C       NOL - NUMBER OF LAYERS IN ATTENUATION MODEL
C
C       NPAR - NUMBER OF PARAMETERS SPECIFYING SPECTRUM
C
C       MED - TYPE OF ANELASTIC MEDIUM USED. 0 - HALF-SPACE QM1
C
C       ICLT - SET TO 0 IF THE CONFIDENCE LIMITS ARE READ EXTERNAL
C              TO THE PROGRAM
C
C       (A8,5I4)
C
C
C     4. DIST,TVAL - DISTANCE AND STUDENTS 'T' VALUE (2F10.6)
C
C     5. START VALUES FOR SHEAR WAVE QM1 IN EACH LAYER (10F8.2)
C
C     6. NOL WEIGHTING FUNCTIONS Kj(w) FOR EACH FREQUENCY (10F12.9)
C
C     7. IN THE CASE OF AN ATTENUATION HALF-SPACE THERE
C        ARE  A SEQUENCE OF CARDS FOR THE GROUP VELOCITY DISPERSION
C        INSTEAD OF 6. (2E15.7)
C
C     8. AMPLITUDE SPECTRUM (AND CONFIDENCE LIMITS) (2E15.7)
C
C     9. IF THE MEDIUM RESPONSE IS FOR A STRATIFIED HALF-SPACE , IT
C        IS READ EXTERNAL TO THE PROGRAM (2E15.7)
C
C OUTPUT IS ON GRAPHICS CHANNEL 70
C
C THE PROGRAM ACCESSES THE NAG LIBRARY ROUTINES H01ADF AND E04JAF
C
      IMPLICIT REAL*8 (A-H,O-Z)
      COMMON/PDS/DK(60,60,10),DKHS(60,60),DKBYDB(60,60,10)
      COMMON/COM2/FREQ(60,60),A(60,60),SDD(60,60)
      COMMON/COM3/NS,NF(60),NOL(60),NPAR(60),MED(60),ISOUR,PI2,DIST(60)
      COMMON/COM4/QM1(60,10)
      REAL*8 IA(60),ISDD(60),STN(60),ROBJ(60)
      DIMENSION X(100),Y(100),PAR(10),Q(60),TITLE(10),TVAL(60)
      DIMENSION PS(100),CHIS(60,100),U(60,100)
C
      CALL PLOTS('C.D.MACBETH-MURCHSEIS',21,70)
      CALL FACTOR(0.5)
      PI2=6.2831854D0
C
C MODE = 0 => OPTIMIZATION ROUTINE
C MODE = 1 => INVOKE SIMPLEX ROUTINE TO EVALUATE BOUNDS ON
C ESTIMATES.
      MODE=0
C
C READ IN THE CONTROL PARAMETERS , MODEL AND OBSERVATIONS
      READ(1,30)(TITLE(I),I=1,10)
      WRITE(6,30)(TITLE(I),I=1,10)
      READ(1,31)NS,ISOUR,GBOT,GSPAC,NGP
      IF(ISOUR/2*2.EQ.ISOUR)WRITE(6,38)ISOUR
      IF(ISOUR/2*2.NE.ISOUR)WRITE(6,39)ISOUR
C
      DO 1 K=1,NS
C
C READ IN DATA FOR EACH STATION
      READ(1,32)STN(K),NF(K),NOL(K),NPAR(K),MED(K),ICLT
      N=NF(K)
      NP=NPAR(K)
      NPP1=NP+1
      NL=NOL(K)
      MED(K)=MED(K)+1
      MD=MED(K)
      READ(1,33)DIST(K),TVAL(K)
      IF(TVAL(K).EQ.0.D0)TVAL(K)=1.D0
      GS=DSQRT(DIST(K))
      READ(1,34)(QM1(K,J),J=1,NPP1)
C
      WRITE(6,70)STN(K),DIST(K)
      WRITE(6,71)TVAL(K)
      IF(ICLT.EQ.1)WRITE(6,75)
      IF(ICLT.EQ.0)WRITE(6,76)
C
      GOTO(29,28)MD
   28 DO 2 J=1,NL
    2 CONTINUE
C
C READ IN WEIGHTS Kj(w) FOR MULTI-LAYERED MODEL
      DO 4 I=1,N
      READ(1,35)(DKBYDB(K,I,J),J=1,NL)
    4 CONTINUE
      WRITE(6,50)
      WRITE(6,54)
      DO 6 I=1,N
      WRITE(6,53)I,(DKBYDB(K,I,J),J=1,NL)
    6 CONTINUE
C
C READ IN GROUP VELOCITY DISPERSION IF AN ATTENUATION
C HALF-SPACE IS SPECIFIED
      GOTO97
   29 READ(1,37)(DUMMY,U(K,I),I=1,N)
   97 WRITE(6,55)
C
C READ IN AMPLITUDE SPECTRUM AND FREQUENCIES , AND
C STANDARD DEVIATIONS IF NECESSARY
      IF(ICLT.EQ.0)READ(1,36)(FREQ(K,I),A(K,I),SDD(K,I),I=1,N)
      IF(ICLT.EQ.1)READ(1,37)(FREQ(K,I),A(K,I),I=1,N)
C
C COMPUTE THE CONFIDENCE LIMITS IF NOT INPUT
      IF(ICLT.EQ.1)CALL CONLTS(K)
```

```
157     C
158     C SMOOTH THE AMPLITUDES AND ERRORS
159           CALL DSMOOTH(A,N,K)
160           CALL DSMOOTH(SDD,N,K)
161     C
162     C
163     C SCALE THE WEIGHTING FUNCTIONS Kj(w)
164           DO 7 I=1,N
165           IF(MED(K).EQ.1)GOTO 40
166           DO 8 J=1,NL
167           DK(K,I,J)=(DKBYDB(K,I,J))*DIST(K)/100.DO
168         8 CONTINUE
169           GOTO 7
170        40 DKHS(K,I)=(-1.DO*DIST(K)*PI2*FREQ(K,I))/(2.DO*U(K,I)*100.DO)
171         7 CONTINUE
172     C
173     C
174           DO 10 I=1,N
175           OMEGA=PI2*FREQ(K,I)
176           OMRT=DSQRT(OMEGA)
177     C
178     C SELECT THE MEDIUM RESPONSE FOR OUR PARTICULAR SOURCE
179     C AND EQUALIZE THE SPECTRUM FOR THIS AND GEOMETRIC SPREADING
180           GOTO(12,11,13,11,14,11)ISOUR
181        11 READ(1,36)DUMMY,RESM
182           GOTO 15
183        12 RESM=OMRT**3
184           GOTO 15
185        13 RESM=1.DO/OMRT
186           GOTO 15
187        14 CONTINUE
188        15 A(K,I)=A(K,I)/RESM*GS
189           SDD(K,I)=SDD(K,I)/RESM*GS
190     C
191     C OUTPUT THE EQUALIZED SPECTRUM AND ERRORS
192           WRITE(6,36)FREQ(K,I),A(K,I),SDD(K,I)
193        10 CONTINUE
194     C
195           IF(MODE.EQ.0)GOTO 1
196     C
197     C INVOKE SIMPLEX ROUTINE TO OBTAIN BOUNDS ON ESTIMATES
198           CALL SMPLX(K,TVAL(K))
199           GOTO80
200         1 CONTINUE
201     C
202     C STEP ALONG THE SOURCE GRID
203           DO 16 J=1,NGP
204           CHISQ=0.DO
205           CC=0.DO
206           NSTAT=0
207           GVALUE=GBOT+GSPAC*(J-1)
208           PS(J)=GVALUE
209           WRITE(6,56)J,GVALUE
210           NSP1=NS+1
211           DO 17 K=1,NS
212           N=NF(K)
213           NL=NOL(K)
214           NP=NPAR(K)
215           PAR(NP)=GVALUE
216           CONST=DLOG(A(K,1)/SFUNC(PAR,NL,K,1,1))
217           LA(1)=-0.2
218           LSDD(1)=DLOG(DEXP(LA(1))+SDD(K,1))-LA(1)
219           DO 18 I=2,N
220           LSDD(I)=DLOG(A(K,I)+SDD(K,I))-DLOG(A(K,I))
221           LA(I)=DLOG(A(K,I)/SFUNC(PAR,NL,K,I,1))
222           LA(I)=LA(I)-CONST+LA(1)
223        18 CONTINUE
224           DO 19 L=1,NP
225        19 Q(L)=QM1(K,L)
226     C
227     C QUASI-NEWTONIAN ROUTINE FOR
228     C OPTIMIZATION OF THE CHI-SQUARED FUNCTION
229           CALL QFIT(K,LA,LSDD,Q,N,NL,ROBJ(K),IFAIL)
230     C
231     C PRINT ERROR INDICATORS IF ROUTINE PRODUCES NO SOLUTIONS
232           IF(IFAIL.EQ.0)GOTO 27
233           GOTO(21,22,23,24,25,25,25,25,26)IFAIL
234        21 WRITE(6,58)
235           GOTO 92
236        22 WRITE(6,59)
237           GOTO 92
238        23 WRITE(6,60)
239           GOTO 92
240        24 WRITE(6,61)
241           GOTO 92
242        25 WRITE(6,62)IFAIL
243           IF(IFAIL.EQ.5)GOTO 27
244           GOTO 92
245        26 WRITE(6,63)
246           GOTO 92
247     C
248     C CONVERT SCALING FACTOR TO ABSOLUTE FACTOR SO
249        27 Q(NP)=DEXP(CONST-LA(1)+Q(NP))
250     C
251     C STORE CHI-SQUARED VALUE SO THAT THE STATION AVERAGE MAY BE COMPUTED
252           CHISQ=CHISQ+ROBJ(K)
253           NSTAT=NSTAT+1
254           WRITE(6,57)STN(K),K,ROBJ(K),Q(NP),(Q(L),L=1,NL)
255           CHIS(K,J)=ROBJ(K)
256        92 IF(IFAIL.NE.0.AND.IFAIL.NE.5)CHIS(K,J)=0.DO
257        17 CONTINUE
258           CHISQ=CHISQ/DFLOAT(NSTAT)
259           CHIS(NSP1,J)=CHISQ
260           WRITE(6,64)CHISQ
261           WRITE(7,65)J,GVALUE,CHISQ
262        16 CONTINUE
```

```
      DO 90 I=1,NSP1
      DO 91 J=1,NGP
      X(J)=PS(J)
      Y(J)=CHIS(I,J)
   91 CONTINUE
C
C GRAPH THE CHI-SQUARE FUNCTION FOR EACH STATION
      CALL GCHI(X,Y,NGP,NS,I,STN(I))
   90 CONTINUE
C
C FORMAT STATEMENTS
   30 FORMAT(10A8)
   31 FORMAT(2I4,2F8.4,I4)
   32 FORMAT(A8,5I4)
   33 FORMAT(2F10.6)
   34 FORMAT(10F8.2)
   35 FORMAT(10F12.9)
   36 FORMAT(3E15.7)
   37 FORMAT(2E15.7)
   38 FORMAT(/' ISOUR = ',I6,' MEDIUM IS MULTI-LAYERED',/)
   39 FORMAT(/' ISOUR = ',I6,' MEDIUM IS A HALF-SPACE',/)
   75 FORMAT(/' ERRORS EVALUATED IN PROGRAM',/)
   76 FORMAT(/' EXTERNAL ERROR EVALUATION',/)
   50 FORMAT(1X,'THE MODEL IS   :',/,
     *1X,'     ALPHA     BETA     THKNES',/,/)
   51 FORMAT(1X,I2,3F10.4)
   52 FORMAT(1X,'PARTIALS W.R.T. ALPHA:'/,/)
   53 FORMAT(I4,4X,10F12.9)
   54 FORMAT(1X,'PARTIALS W.R.T. BETA:'/,/)
C  32 FORMAT(/,' CONFIDENCE LIMITS CORRESPO',
C    *'ND TO A STUDENT''S ''T'' OF ',F7.3,/)
   55 FORMAT(/,3X,'INPUT AMPLITUDE SPECTRUM WITH ASSUMED ',
     *'STANDARD DEVIATION',/,3X,'------------------------'
     *,'--------------------------',/)
   56 FORMAT(/////,1X,'GRID NUMBER',I4,' , GRID VALUE',F8.2)
   57 FORMAT(/,1X,'STATION',A8,' , NO.',I2,/,
     *       1X,'OBJECTIVE FUNCTION',F15.10,/,
     *       1X,'ABSOLUTE SCALING FACTOR',F14.2,/,
     *       1X,'Q-1 SOLUTION ',-2P4F8.4)
   58 FORMAT(//,'  PARAMETER OUTSIDE EXPECTED RANGE-CHECK THE ',
     *'PROGRAM FOR FAULTS')
   59 FORMAT(//,'  400N FUNCTIONS EVALUATIONS YET NO CONVERGENCE',
     *' - TRY ALTERING THE START VALUES?')
   60 FORMAT(//,'  CONDITIONS FOR MINIMUM HAVN''T  ALL BEEN',
     *'SATISFIED - LOWER POINT CAN''T BE FOUND - TRY NEW START VALUES ')
   61 FORMAT(//,'  OVERFLOW DURING THE COMPUTATION - RESTART',
     *' AT THE LAST PARAMETER VALUES')
   62 FORMAT(//,'  SOME DOUBT ABOUT THE MINIMUM - DEGREE OF ',
     *'CONFIDENCE DEPENDS',/,'    ON  THE VALUE OF IFAIL (5<IFAIL<8)',
     *' , IFAIL =',I3)
   63 FORMAT(//,'  MODULUS OF VARIABLES HAS BECOME VERY LARGE',
     *' - RE-SCALE THE PROBLEM')
   64 FORMAT(/,1X,'STATION AVERAGED OBJECTIVE FUNCTION',F15.10,/,
     *       1X,'---------------------------------')
   65 FORMAT(I4,2X,F6.2,F12.8)
C  36 FORMAT(/,'  MEAN D.C. LEVEL - ',F8.2)
   70 FORMAT(//,10X,A8,' DISTANCE = ',F6.2,/)
   71 FORMAT(/'  CONFIDENCE LIMITS CORRESPOND TO A ''T'' - VALUE OF '
     *,F6.1,/)
   80 CALL PLOT(0.,0.,999)
      STOP
      END
C
C*****
C
      DOUBLE PRECISION FUNCTION SFUNC(PAR,NL,K,IF,IS)
      IMPLICIT REAL*8 (A-H,O-Z)
      COMMON/PDS/DK(60,60,10),DKHS(60,60),DKBYDB(60,60,10)
      COMMON/COM2/FREQ(60,60),A(60,60)
      COMMON/COM3/NS,NF(60),NOL(60),NPAR(60),MED(60),ISOUR,PI2,DIST(60)
      DIMENSION PAR(10)
C
      MD=MED(K)
      OMEGA=FREQ(K,IF)*PI2
      NP=NPAR(K)
      GAM=0.DO
      IF(IS.EQ.1)GOTO 4
      GOTO(2,3)MD
    3 DO 1 J=1,NL
      GAM=GAM+DK(K,IF,J)*PAR(J)
    1 CONTINUE
      GOTO  4
    2 GAM=DKHS(K,IF)*PAR(1)
    4 IF(IS.EQ.2)GOTO 34
C
C
      GOTO(30,30,31,31,32,32)ISOUR
C
C UNDERGROUND EXPLOSIONS - EXPONENTIAL STEP IN TIME
C UNDERWATER EXPLOSIONS - SEQUENCE OF DIRAC IMPULSES
C
   30 S1=PAR(NP)
      SOURCE= DSQRT(S1*S1+OMEGA*OMEGA)
      SOURCE=0.001DO/SOURCE
      GOTO 33
C
C THEORY BELOW AS IN WIELANDT (1975)
C SET UP THE SOURCE PARAMETERS
   31 S=0.5
      GAMMA=1520.0
      W=203.0
      R=0.45
      B=0.6
      C=B/2.47
      DEP=PAR(NP)
      H=115.DO
```

```
      NPULSES=2
C
      T1=2.0*DEP/GAMMA
      T2=2.0*H/GAMMA
      W13=W**(1.0/3.0)
      HP10=DEP*10.0
      H56=HP10**(5.0/6.0)
      TB=2.10*W13/H56
      TC=0.72*TB+TB
      OMTB=OMEGA*TB
      OMTC=OMEGA*TC
      COSTC=DCOS(OMTC)
      SINTC=DSIN(OMTC)
      COSTB=DCOS(OMTB)
      SINTB=DSIN(OMTB)
C
C
      NPULSES=NPULSES+1
      GOTO(35,35,36)NPULSES
C
   35 IF(NPULSES.EQ.1)B=0.D0
C
C COMPUTE THE NEGATIVE PRESSURE MODULUS
      RN=(1.0+B)/OMTB
C
C COMPUTE THE BUBBLE SPECTRUM BY APPROXIMATING
C THE PULSES TO IMPULSES,AND TAKING ACCOUNT OF
C THE NEGATIVE PRESSURE BETWEEN THEM.
      BW1=1.0+B*COSTB-RN*SINTB
      BW2=B*SINTB-RN+RN*COSTB
      GOTO 37
C
C
   36 RN=(1.D0+B+C)/OMTC
      BW1=1.D0+B*COSTB+C*COSTC-RN*SINTC
      BW2=B*SINTB+C*SINTC-RN+RN*COSTC
   37 BUB=DSQRT(BW1*BW1+BW2*BW2)
C
C COMPUTE THE REVERBERATION SPECTRUM
      COST1=DCOS(OMEGA*T1)
      COST2=DCOS(OMEGA*T2)
      SINT1=DSIN(OMEGA*T1)
      SINT2=DSIN(OMEGA*T2)
      D1=(1.0-S*COST1)*(1.0-S*COST1)+S*SINT1*S*SINT1
      RN1=(1.0+R*COST2)*(1.0+R*COST2)+(R*SINT2*R*SINT2)
      REVB=DSQRT(D1/RN1)
      SOURCE=BUB*REVB
      GOTO 33
   32 CONTINUE
C
C
   33 SFUNC=SOURCE*DEXP(GAM)
      RETURN
C
   34 SFUNC=GAM
      RETURN
      END
C
C*****
C
      SUBROUTINE FUNCT1(N,PAR,CF)
C
      IMPLICIT REAL*8 (A-H,O-Z)
      COMMON/DAT/OBS(60),CALC(60),OBSD(60),NF,K
      DIMENSION PAR(N)
C
C COMPUTE CHI-SQUARED FUNCTION
      NM1=N-1
      DO 1 I=1,NF
    1 CALC(I)=PAR(N)+SFUNC(PAR,NM1,K,I,2)
      CF=0.D0
      DO 3 I=1,NF
    3 CF=CF+((OBS(I)-CALC(I))/OBSD(I))**2
      CF=DSQRT(CF)/FLOAT(NF-N)
      RETURN
      END
C
C*****
C
      SUBROUTINE QFIT(K,X,DX,Q,N,NL,ROBJ,IFAIL)
      IMPLICIT REAL*8 (A-H,O-Z)
      COMMON/COM2/FREQ(60,60),A(60,60),SDD(60,60)
      COMMON/DAT/OBS(60),CALC(60),OBSD(60),NF,KK
      DIMENSION X(60),DX(60),Q(10),PAR(10),BYL(10),BYU(10)
      DIMENSION WRK(300),IWRK(300)
C
C ESTIMATE SCALING AND QM1 PARAMETERS
      KK=K
      NF=N
      NP=NL+1
      DO 1 I=1,N
      OBSD(I)=DX(I)
    1 OBS(I)=X(I)
      BYL(NP)=-8.D0
      BYU(NP)=8.D0
      PAR(NP)=Q(NP)
      DO 3 J=1,NL
      BYL(J)=0.00
      BYU(J)=10.D0
    3 PAR(J)=Q(J)*100.D0
      IBOUND=0
      IFAIL=1
      NWRK=300
      CALL E04JAF(NP,IBOUND,BYL,BYU,PAR,CF,IWRK,NWRK,WRK,NWRK,IFAIL)
      DO 4 J=1,NP
    4 Q(J)=PAR(J)
```

```
      ROBJ=CP
      RETURN
      END
C
C*****
C
      SUBROUTINE SMPLX(K,TVAL)
      IMPLICIT REAL*8 (A-H,O-Z)
      COMMON/PDS/DK(60,60,10),DKHS(60,60)
      COMMON/COM2/FREQ(60,60),A(60,60),SDD(60,60)
      COMMON/COM3/NS,NF(60),NOL(60),NPAR(60),MED(60),ISOUR,PI2,DIST(60)
      DIMENSION IA1(200),IA2(120),IA3(200),IA4(200),INEQ(200)
      DIMENSION RA1(201,20),RA2(202,201),RA3(202),RHS(200)
      COMMON/COM4/QM1(60,10)
      DIMENSION X(60),WEIGHT(60),Y(60),PAR(10),SU(10),SL(10)
C
C OBTAIN BOUNDS ON VARIABLES
      NL=NOL(K)
      NPR=NPAR(K)
      NPRP1=NPR+1
      NN=NF(K)
      PAR(NPR)=QM1(K,NPRP1)
      WRITE(6,70)
      DO 60 I=1,NN
      XDX1=DLOG(A(K,I)+TVAL*SDD(K,I))-DLOG(A(K,I))
      XDX2=DLOG(A(K,I))-DLOG(A(K,I)-TVAL*SDD(K,I))
      X(I)=A(K,I)/(SFUNC(PAR,NL,K,I,1))
      X(I)=DLOG(X(I))
      WEIGHT(I)=1.DO/XDX1
      Y(I)=XDX2/XDX1
      WRITE(6,71)X(I),XDX1,XDX2,Y(I)
   60 CONTINUE
      DO 61 I=1,NN
      X(I)=X(I)*WEIGHT(I)
      IF(MED(K).EQ.1)GOTO 63
      DO 62 J=1,NL
      DK(K,I,J)=DK(K,I,J)*WEIGHT(I)
   62 CONTINUE
      GOTO 61
   63 DK(K,I,1)=DKHS(K,I)*WEIGHT(I)
   61 CONTINUE
C
      M=2*NN
      N=NL+1
      RMIN=0.000001DO
      MAXIT=2*M
      MN=M+N
      MPN=NN+N
      MM=2*M
      M1=M+1
      M2=M+2
      IFAIL=0
      DO 100 NP=1,2
      TYPE=1.DO
      IF(NP.EQ.1)WRITE(6,1)
      IF(NP.EQ.2)WRITE(6,2)
      IF(NP.EQ.2)TYPE=-1.DO
      NLP1=NL+1
      DO 100 IPAR=1,NLP1
      DO 101 I=1,NN
      KK=I+NN
      RHS(I)=X(I)+1.DO
      INEQ(I)=-1
      RHS(KK)=X(I)-Y(I)
      INEQ(KK)=1
      DO 101 J=1,NL
      RA1(I,J)=DK(K,I,J)
      RA1(KK,J)=DK(K,I,J)
      RA1(I,NLP1)=1.DO*WEIGHT(I)
      RA1(KK,NLP1)=1.DO*WEIGHT(I)
  101 CONTINUE
C
      DO 102 I=1,NLP1
  102 RA1(M1,I)=0.DO
      RA1(M1,IPAR)=TYPE
      CALL HO1ADF(RA1,201,M,N,INEQ,RHS,RMIN,
     *            MAXIT,MN,MM,M1,M2,IA1,RA2,202,
     *            IA2,IA3,IA4,RA3,RESULT,NUMIT,IIPAR,IFAIL)
C
      GOTO(118,119),NP
  119 RESULT=-1.DO*RESULT
  118 WRITE(6,3)RESULT,NUMIT,IIPAR,IFAIL
      IF(NP.EQ.1)SL(IPAR)=RESULT
      IF(NP.EQ.2)SU(IPAR)=RESULT
  100 CONTINUE
      WRITE(6,9)
      DO 150 I=1,NL
      WRITE(6,10)I,SL(I),SU(I)
  150 CONTINUE
    1 FORMAT(1X,'LOWER SOLUTION BOUNDS')
    2 FORMAT(1X,'UPPER SOLUTION BOUNDS')
    3 FORMAT(/,1X,'RESULT=',-2PF14.8,' NUMIT=',I4,' IPAR=',I1,
     *' IFAIL=',I1)
    9 FORMAT(//19X,' EDGE    SOLUTIONS',
     1          /19X,'------------------',
     2         //25X,'SOLUTIONS          ',
     3          /2X,'LAYER  THICKNESS(KM)  LOW     HIGH        ')
   10 FORMAT(' ',I4,6X,6X,5X,-2PF6.4,2X,F6.4)
   11 FORMAT(//,19X,'MODEL',
     *        /,19X,'-----',
     *       //,1X,'       ALPHA      BETA    THKNES  '
     *        /,1X,'       -----      ----     -----  ')
   12 FORMAT(1X,I2,1X,2F10.4,F10.4)
   13 FORMAT(15X,I6,E15.7)
C
   16 FORMAT(5X,'UPPER SOLUTIONS =',3F10.5,
```

```
     *     /,5X,'LOWER SOLUTIONS =',3F10.5)
   70 FORMAT(//' OUTPUT FROM SUBROUTINE SIMPLEX:',/,
     *' SINGLE-STATION GAMMA , + AND - DEVIATIONS ,'
     *' AND THEIR QUOTIENT',/)
   71 FORMAT(10X,F10.6,2E15.7,5X,F7.2)
      RETURN
      END
C
C*****
C
      SUBROUTINE CONLTS(K)
      IMPLICIT REAL*8 (A-H,O-Z)
      COMMON/COM2/FREQ(60,60),A(60,60),SDD(60,60)
      COMMON/COM3/NS,NP(60),NOL(60),NPAR(60),MED(60),ISOUR,PI2,DIST(60)
C
C ESTIMATION OF CONFIDENCE LIMITS ON AMPLITUDE SPECTRUM
      N=NP(K)
      H1=(30.D0*DIST(K))/(100.D0*PI2*2.5*50.D0)
      DO 1 I=1,N
      OMEGA=PI2*FREQ(K,I)
C
C CONFIDENCE LIMIT FROM ASSUMED HETEROGENEITIES
      HETER=H1*OMEGA
C
C
C SET CALCULATED VALUE FOR NOISE LEVEL
      RNS=0.04D0
C
C
C COMPOSITE UNCERTAINTY
      SDD(K,I)=HETER*A(K,I)+RNS
    1 CONTINUE
      RETURN
      END
C
C*****
C
      SUBROUTINE DSMOOTH(Y,N,K)
      IMPLICIT REAL*8 (A-H,O-Z)
      DIMENSION Y(60,60)
C
C FIVE-POINT SMOOTHING ROUTINE
      Y(K,1)=(6.D0*Y(K,1)+4.D0*Y(K,2)+Y(K,3))/11.D0
      Y(K,2)=(4.D0*Y(K,1)+6.D0*Y(K,2)+4.D0*Y(K,3)+Y(K,4))/15.D0
      NM1=N-1
      NM2=N-2
      NM3=N-3
      Y(K,N)=(Y(K,NM2)+4.D0*Y(K,NM1)+6.D0*Y(K,N))/11.D0
      Y(K,NM1)=(Y(K,NM3)+4.D0*Y(K,NM2)+6.D0*Y(K,NM1)+4.D0*Y(K,N))/15.D0
      DO 1 I=3,NM2
      Y(K,I)=(Y(K,I-2)+4.D0*Y(K,I-1)+6.D0*Y(K,I)+4.D0*Y(K,I+1)
     *+Y(K,I+2))/16.D0
    1 CONTINUE
C
      RETURN
      END
C
C*****
C
      SUBROUTINE GCHI(XD,YD,N,NS,K,STN)
      REAL*8 XD(100),YD(100)
      REAL*8 ATITLE(4),BTITLE(4),STN
      DIMENSION X(100),Y(100)
C
C THIS ROUTINE PLOTS CHI-SQUARED AT EVERY STATION
      DATA ICOUNT/0/
      DATA ATITLE(1),ATITLE(2),ATITLE(3)/'CHI-SQUA',
     *'RED FOR ','STATION '/
      DATA BTITLE(1),BTITLE(2),BTITLE(3),BTITLE(4)
     */'STATION ','AVERAGED',' CHI-SQU','ARED     '/
C
      NSP1=NS+1
      ICOUNT=ICOUNT+1
      IF(ICOUNT.LE.6.AND.ICOUNT.NE.1)CALL PLOT(0.,8.,-3)
      IF(ICOUNT.EQ.7)CALL PLOT(8.,-40.0,-3)
      IF(ICOUNT.LE.12.AND.ICOUNT.GT.7)CALL PLOT(0.,8.,-3)
      IF(ICOUNT.EQ.13)CALL PLOT(8.,-40.0,-3)
      IF(ICOUNT.GT.13)CALL PLOT(0.,8.,-3)
C
      DO 1 I=1,N
      X(I)=XD(I)
      Y(I)=YD(I)
    1 CONTINUE
C
      CALL PLOT(0.,0.,3)
      CALL PLOT(5.,0.,2)
      CALL PLOT(5.,5.,2)
      CALL PLOT(0.,5.,2)
      CALL PLOT(0.,0.,2)
      NSP1=NS+1
      IF(K.NE.NSP1)ATITLE(4)=STN
      IF(K.NE.NSP1)CALL SYMBOL(0.,5.3,0.15,ATITLE,0.0,32)
      IF(K.EQ.NSP1)CALL SYMBOL(0.,5.3,0.15,BTITLE,0.0,32)
C
      YMIN=999.0
      YMAX=0.
      DO 2 I=1,N
      IF(Y(I).EQ.0.D0)GOTO2
      IF(Y(I).LE.YMIN)YMIN=Y(I)
      IF(Y(I).EQ.YMIN)IMIN=I
      IF(Y(I).GE.YMAX)YMAX=Y(I)
    2 CONTINUE
C
      NN=N/10
      DO 3 I=1,11
      J=NN*(I-1)+1
```

```
      R=X(J)
      A=FLOAT(I-1)*5./10.-0.24
      B=-0.3
      IK=(I/2)*2
      IF(I.NE.IK)CALL NUMBER(A,B,0.12,R,0.0,1)
      A=A+0.24
      B=0.
      CALL PLOT(A,B,3)
      B=0.2
      CALL PLOT(A,B,2)
    3 CONTINUE
      DY=(YMAX-(YMIN-0.5*YMIN))/5.
      DO 4 I=1,6
      A=-1.0
      B=FLOAT(I-1)
      R=YMIN-0.5*YMIN+DY*(FLOAT(I-1))
      CALL NUMBER(A,B,0.1,R,0.0,4)
      A=0.
      CALL PLOT(A,B,3)
      A=0.2
      CALL PLOT(A,B,2)
    4 CONTINUE
C
C
      CALL SYMBOL(-1.3,1.0,0.2,'CHI-SQUARED',90.0,11)
      CALL SYMBOL(1.0,-0.6,0.2,'SOURCE PARAMETER',0.0,16)
C
      DX=5./FLOAT(N-1)
      DO 5 I=1,N
      A=DX*FLOAT(I-1)
      B=(Y(I)-YMIN+0.5*YMIN)/DY
      IF(Y(I).EQ.0.D0)GOTO6
      IF(I.NE.1)CALL PLOT(A,B,2)
      IF(I.EQ.1)CALL PLOT(A,B,3)
      GOTO 5
    6 CALL PLOT(A,B,3)
    5 CONTINUE
C
      AM=DX*FLOAT(IMIN-1)
      BM=(YMIN-0.5*YMIN)/DY-0.3
      CALL SYMBOL(AM,BM,0.3,242,0.0,-1)
C
      RETURN
      END
```

REFERENCES

The most frequently referenced journals are abbreviated as follows:

GJR - Geophysical Journal of the Royal Astronomical Society
JGR - Journal of Geophysical Research
BSSA - Bulletin of the Seismological Society of America

Abo-Zena, A., 1979. Dispersion function computations for unlimited frequency values, GJR, 58, 91-105.

Aki, K., 1960. Study of earthquake mechanism by a method of phase equalization applied to Rayleigh and Love waves, JGR, 65, 729-740.

Aki, K., 1962. Accuracy of the Rayleigh wave method for studying the earthquake mechanism, Bull.Eq.Res.Inst., 40, 91-105.

Aki, K., 1966. Generation and propagation of G waves from the Niigata earthquake of June 16, 1964. 2. Estimation of earthquake movement, released energy, and stress-strain drop from G wave spectrum, Bull. Eq.Res.Inst., 44, 23-88.

Aki, K., 1967. Scaling law of seismic spectra, JGR, 72, 1217-1231.

Aki, K., 1972. Scaling law of earthquake source time-function, GJR, 31, 3-25.

Aki, K., 1980. Attenuation of shear-waves in the Lithosphere for frequencies from 0.05 to 25Hz, Phys.E.Planet.Int., 21, 50-60.

Aki, K., Bouchon, M. & Reasenberg, P., 1974. Seismic source function for an underground nuclear explosion, BSSA, 64, 131-148.

Aki, K., Mendirugen, J.A. & Tsai, Y-B., 1972. Reply, JGR, 77, 3827-3830.

Aki, K. & Richards, P.G., 1981. 'Quantitative Seismology - Theory and Methods', Vol. II, Freeman, San Francisco.

Anderson, D.L., Ben-Menahem, A. & Archambeau, C.B., 1965. Attenuation of seismic energy in the upper mantle, JGR, 70, 1441-1448.

Anderssen, R.S. & Senata, E., 1971. A simple statistical estimation procedure for Monte Carlo inversion in Geophysics, Pure Appl.Geophys., 91, 5-13.

Anderssen, R.S., Worthington, M.H. & Cleary, J.R., 1972. Density modelling by Monte Carlo inversion - I Methodology, GJR, 29, 433-444.

Arons, A.B., 1948. Secondary pressure pulses due to a gas globe oscillation in underwater explosions - II Selection of adiabatic parameters in the theory of oscillation, J.Acoust.Soc.Am., 20, 277-282.

Assumpção, M., 1981. The NW Scotland earthquake swarm of 1974, GJR, 67, 577-586.

Assumpção, M. & Bamford, D., 1978. LISPB V - Studies of crustal shear waves, GJR, 54, 61-73.

Bache, T.C., Rodi, W.L. & Harkrider, D.G., 1978. Crustal structures inferred from Rayleigh wave signatures of NTS explosions, BSSA, 68, 1399-1413.

Bamford, D., Faber, S., Jacob, B., Kaminski, W., Nunn, K., Prodehl, C., Fuchs, K., King, R. & Willmore, P., 1976. A lithospheric seismic profile in Britain - I Preliminary results, GJR, 44, 145-160.

Bamford, D., Nunn, K., Prodehl, C. & Jacob, B., 1977. LISPB III - Upper crustal structure of northern Britain, J.Geol.Soc.(Lond.), 133, 481-488.

Bamford, D., Nunn, K., Prodehl, C. & Jacob, B., 1978. LISPB IV - Crustal structure of northern Britain, GJR, 54, 43-60.

Bancroft, A.M., 1966. Seismic spectra and detection probabilities from explosions in lake superior - The Earth beneath the Continents, Geophys. Mono.Am.Geophys.Un., 10, 234-240.

Båth, M., 1968. 'Mathematical Aspects of Seismology', Elsevier, Amsterdam.

Båth, M., 1974. 'Spectral Analysis in Geophysics', Elsevier, Amsterdam.

Ben-Menahem, A., 1961. Radiation of seismic waves from finite moving sources, BSSA, 51, 401-435.

Ben-Menahem, A. & Harkrider, D.G., 1964. Radiation patterns of seismic surface waves from buried dipolar sources in a flat stratified earth, JGR, 69, 2605-2620.

Ben-Menahem, A., Rosenman, M. & Harkrider, D.G., 1970. Fast evaluation of source parameters from isolated surface wave signals - Part I, Universal tables, BSSA, 60, 1337-1387.

Ben-Menahem, A. & Singh, S.J., 1981. 'Seismic Waves and Sources', Springer-Verlag, New York.

Ben-Menahem, A. & Toksöz, M.N., 1962. Source mechanism from spectra of long period surface waves, JGR, 67, 1943-1949.

Bevington P.R., 1969. 'Data Reduction and Error Analysis for the Physical Sciences', McGraw-Hill, New-York.

Biot, M.A., 1952. The interaction of Rayleigh and Stoneley waves in the ocean bottom, BSSA, 42, 81-93.

Blake, F.G., 1952. Spherical wave propagation in solid media, J.Acoust. Soc.Am., 24, 211-215.

Bloch, S., Hales, A.L. & Landisman, M., 1969. Velocities in the crust and upper mantle of southern Africa from multi-mode surface wave dispersion, BSSA, 59, 1599-1629.

Boore, D.M. & Toksöz, M.N., 1969. Rayleigh wave particle motion and crustal structure, BSSA, 59, 331-346.

Burkhard, N.R. & Jackson, D.D., 1976. Density and surface wave inversion, Geophys.Res.Letts., 3, 637-638.

Burridge, R. & Knopoff, L., 1964. Body force equivalents for seismic dislocations, BSSA, 54, 1875-1888.

Burton, P.W., 1973. 'Estimations of Q from Seismic Rayleigh Waves', Ph.D. Thesis, Univ. of Durham.

Burton, P.W., 1974. Estimations of Q from seismic Rayleigh waves, GJR, 36, 167-189.

Burton, P.W., 1977. Inversions of high frequency $Q_\gamma(f)$, GJR, 48, 29-51.

Burton, P.W. & Blamey, C., 1972. A computer program to determine the spectrum and dispersion characteristics of a transient seismic signal, UKAEA AWRE Report No. 0/48/72 (HMSO).

Burton, P.W. & Kennett, B.L.N., 1972. Upper mantle zone of low Q, Nature Phys.Sci., 238, 87-90.

Burton, P.W. & McGonigle, R.W., 1979. Attenuation and $Q_\gamma(f)$ of explosion and earthquake generated Rayleigh waves propagating beneath the Pacific Ocean, G.S.U. Report No. 109.

Canas, J.A. & Mitchell, B.J., 1978. Lateral variations of surface waves anelastic attenuation across the Pacific, BSSA, 68, 1637-1650.

Cara, M., 1978. Regional variations of higher Rayleigh-mode phase velocities: a spatial filtering method, GJR, 54, 439-460.

Carpenter, E.W., 1967. Teleseismic signals calculated for underground, underwater, and atmospheric explosions, Geophysics, 32, 17-32.

Cherry, J.T. & Hudlow, W.R., 1966. Numerical simulation of seismic disturbances, Geophysics, 31, 33-49.

Christain, E.A. & Blaik, M., 1965. Near surface measurements of deep explosions - II Energy spectra of small charges, J.Acoust.Soc.Am., 38, 57-62.

Clark, R.A., 1983. Crust and uppermost mantle structure of the Iceland-Faroes region from Rayleigh wave group velocity dispersion, GJR, 72, 255-264.

Cloetingh, S.A.P.L., Nolet, G. & Wortel, M.J.R., 1980. Standard graphs and tables for the interpretation of Rayleigh wave group velocities in crustal studies, Proc.K.Ned.Akad.Wet., B, 83, 101-118.

Cole, R.H., 1948. 'Underwater Explosions', Dover Publications, New York.

Cooley, J.W. & Tukey, J.W., 1965. An algorithm for the machine calculation of complex Fourier series, Mathematics of Computation, 19, 297-301.

Correig, A.M. & Mitchell, B.J., 1980. Regional variation of Rayleigh wave attenuation coefficient in the Eastern Pacific, Pure Appl.Geophys., 118, 831-845.

Correig, A.M., Susagna, M.T. & Lana, X., 1982. Lateral variations of attenuation coefficients, group and phase velocities of Rayleigh waves in Europe, Tectonophysics, 82, 179-194.

Crampin, S., 1966. Higher mode seismic waves from atmospheric nuclear explosions over Novaya Zemlya, JGR, 71, 2951-2958.

Crosson, R.S., 1976. Crustal structure modeling of earthquake data - 1. Simultaneous least squares estimation of hypocenter and velocity parameters, JGR, 81, 3036-3046.

Dahlman, O., 1974. Seismic source and transmission functions from underground nuclear explosions, BSSA, 64, 1275-1293.

Dantzig, G.B., 1963. 'Linear Programming and Extensions', Princeton University Press.

Der, Z.A., McElfresh, T.W. & O'Donnell, A., 1982. An investigation of the regional variations and frequency dependence of anelastic attenuation in the mantle under the United States in the 0.5-4Hz band, GJR, 69, 67-99.

Douglas, A., Hudson, J.A. & Blamey, C., 1972. A quantitative evaluation of seismic signals at teleseismic distances - III computed P and Rayleigh wave seismograms, GJR, 28, 385-410.

Douglas, A., Hudson, J.A. & Kembhavi, V.K., 1971. The analysis of surface wave spectra using a reciprocity theorem for surface waves, GJR, 23, 207-223.

Dunkin, J.W., 1965. Computation of modal solutions in layered, elastic media at high frequencies, BSSA, 55, 335-358.

Dziewonski, A., Bloch, S. & Landisman, M., 1969. A technique for the analysis of transient seismic signals, BSSA, 59, 427-444.

Ewing, W.M., Jardetsky, W.S. & Press, F., 1957. 'Elastic Waves in Layered Media', McGraw-Hill, New-York.

Evans, A.C., 1981. 'Propagation and Dissipation of VHF Rayleigh Waves in Scotland', Ph.D. Thesis, Univ. of Edinburgh.

Feng, C-C. & Teng, T-L., 1983. Three-dimensional crust and upper mantle structure of the Eurasian continent, JGR, 88, B3, 2261-2272.

Frantti, G.E., 1963. The nature of high-frequency earth noise spectra, Geophysics, XXVII, 547-562.

Frantti, G.E., Willis, D.E. & Wilson, J.T., 1962. The spectrum of seismic noise, BSSA, 52, 113-121.

Garvin, W.W., 1960. 'Introduction to Linear Programming', McGraw-Hill, New York.

Geller, R.J., 1976. Scaling relations for earthquake source parameters and magnitudes, BSSA, 66, 1501-1523.

Gilbert, F. & Backus, G.E., 1966. Propagator matrices in elastic wave and vibration problems, Geophysics, 31, 326-332.

Gill, P.E. & Murray, W., 1976. Minimization subject to bounds on the variables, National Physical Laboratory Report, NAC72.

Goncz, J.H. & Hannan, E.J., 1975. New methods of estimating dispersion from stacks of surface waves, BSSA, 65, 1519-1529.

Gupta, I.N. & Blandford, R.R., 1983. A mechanism for generation of short-period transverse motion from explosions, BSSA, 73, 571-591.

Hanks, T.C. & Kanamori, H., 1979. A moment-magnitude scale, JGR, 84, 2348-2350.

Harkrider, D.G., 1964. Surface waves in multi-layered elastic media - I Rayleigh waves and Love waves from buried sources in a multi-layered elastic half-space, BSSA, 54, 627-679.

Harkrider, D.G., 1970. Surface waves in multi-layered elastic media - Part II Higher mode spectra and spectral ratios from point sources in plane layered earth models, BSSA, 60, 1937-1987.

Haskell, N.A., 1953. The dispersion of surface waves on multi-layered

media, BSSA, 43, 17-34.

Haskell, N.A., 1963. Radiation pattern of Rayleigh waves from a fault of arbitrary dip and direction of motion in a homogeneous medium, BSSA 53, 619-642.

Haskell, N.A., 1964a. Radiation pattern of surface waves from point sources in a multi-layered medium, BSSA, 54, 377-393.

Haskell, N.A., 1964b. Total energy and energy spectral density of elastic wave radiation from propagating faults, BSSA, 54, 1811-1841.

Haskell, N.A., 1966. Total energy and energy spectral density of elastic wave radiation from propagating faults - II A statistical source model, BSSA, 56, 125-140.

Haskell, N.A., 1967. Analytic approximation for the elastic radiation from a contained underground explosion, JGR, 72, 2583-2588.

Haskell, N.A., 1969. Elastic displacements in the near-field of a propagating fault, BSSA, 59, 865-908.

Helmberger, D.V. & Hadley, D.M., 1981. Seismic source functions and attenuation from local and teleseismic observations of the NTS events 'JORUM' and 'HANDLEY', BSSA, 71, 51-67.

Herrmann, R.B. & Mitchell, B.J., 1975. Statistical analysis and interpretation of surface wave anelastic data for the stable interior of North America, BSSA, 65, 1115-1128.

Holzer, F., 1966. Calculation of seismic source mechanisms, Proc.R.Soc. (Lond.), A290, 408-429.

Hudson, J.A., 1967. Scattered surface waves from a surface obstacle, GJR, 13, 441-458.

Hudson, J.A., 1969a. A quantitative evaluation of seismic signals at teleseismic distances - I Radiation from point sources, GJR, 18, 233-249.

Hudson, J.A., 1969b. A quantitative evaluation of seismic signals at teleseismic distances - II Body waves and surface waves from an extended source, GJR, 18, 353-370.

Hudson, J.A., 1981. Wave speeds and attenuation of elastic waves in material containing cracks, GJR 64, 133-150.

Hudson, J.A. & Boore, D.M., 1980. Comments on: 'Scattered surface waves from a surface obstacle by J.A.Hudson', GJR, 60, 123-127.

Hudson, J.A. & Douglas, A., 1975. Rayleigh wave spectra and group velocity minima, GJR, 42, 175-188.
and the resonance of P waves in layered structures

Hudson, J.A. & Knopoff, L., 1967. Statistical properties of Rayleigh waves due to scattering by topography, 57, 83-90.

Jackson, D.D. & Anderson D.L., 1970. Physical mechanisms of seismic-wave attenuation, Rev.Geophys.Space Phys., 8, 1-63.

Jacob, A.W.B., 1975. Dispersed shots at optimum depth - An efficient seismic source for Lithospheric studies, JGR, 41, 63-70.

Johnston, C., 1972. 'Regionalized Earth Models from Linear Programming Methods', Master's Thesis, Massachusetts Institute of Technology, Cambridge.

Jordan, T.H. & Franklin, J.N., 1971. Optimal solutions to a linear inverse problem in geophysics, Proc.Nat.Acad.Sci., 68, 291-293.

Kaminski, W., Bamford, D., Faber, S., Jacob, B., Nunn, K. & Prodehl, C., 1976. A lithospheric seismic profile in Britain - II Preliminary report on the recording of a local earthquake, J.Geophys., 42, 103-110.

Kanamori, H., 1970. Synthesis of long period surface waves and its application to earthquake source studies - Kurile Island earthquake of Oct. 13 1963, JGR, 75, 5011-5027.

Kanamori, H. & Anderson, D.L., 1975. Theoretical basis of some empirical relations in seismology, BSSA, 65, 1073-1095.

Kanamori, H. & Given, J.W., 1981. Use of long period surface waves for rapid determination of earthquake source parameters, Phys.E.Planet.Ints., 27, 8-31.

Keilis-Borok, V.I. & Yanoskaja, T.B., 1967. Inverse problems of seismology

(structural review), GJR, 13, 223-234.

King, C.Y., Bakun, W.H. & Murdock, J.N., 1972. Source parameters of nuclear explosions MILROW and LONGSHOT from teleseismic P waves, GJR, 31, 27-44.

Knopoff, L., 1964. A matrix method for elastic wave problems, BSSA, 54, 431-438.

Kulhanek, O., 1976. 'Introduction to Digital Filtering in Geophysics', Developments in Solid Earth Geophysics 8, Elsevier, Amsterdam.

Lanczos, C., 1961. 'Linear Differential Operators', Van Nostrad, London.

Lapwood, E.R., 1949. The disturbance to a line source in a semi-infinite medium, Philos.Trans.R.Astr.Soc.(Lond.), A242, 63-100.

Lee, W.B. & Solomon, S.C., 1975. Inversion schemes for surface wave attenuation and Q in the crust and the mantle, GJR, 43, 47-71.

Lee, W.B. & Solomon, S.C., 1979. Simultaneous inversion of surface wave phase velocity and attenuation: Rayleigh and Love waves over continental and oceanic paths, BSSA, 69, 65-95.

MacBeth, C.D. & Burton, P.W., 1983. Single station Q: attenuation of 2Hz Rayleigh waves along single isolated propagation paths in Scotland, Annales Geophysicae, 1, No.3, 223-228.

Marshall, P.D., 1970. Aspects of spectral differences between earthquakes and underground explosions, GJR, 20, 397-416.

Marshall, P.D. & Burton, P.W., 1971. The source-layering function of underground explosions and earthquakes - An application of a 'common path' method, GJR, 24, 533-537.

Massé, R.P., 1981. Review of seismic source models for underground nuclear explosions, BSSA, 71, 1249-1268.

McGarr, A., 1969a. Amplitude variations of Rayleigh waves - Propagation across a continental margin, BSSA, 59, 1281-1305.

McGarr, A., 1969b. Amplitude variations of Rayleigh waves - Horizontal

refraction, BSSA, 59, 1307-1334.

McGarr, A., 1972. Letters: Comments on some papers concerning amplitudes of seismic surface waves, JGR, 77, 3823-3826.

Mendirugen, J., 1977. Inversion of surface wave data in source mechanism studies, JGR, 82, 889-894.

Mitchell, B.J., 1973. Radiation and attenuation of Rayleigh waves for the southeastern Missouri earthquake of Oct. 21 1965, JGR, 78, 886-899.

Mitchell, B.J., 1975. Regional Rayleigh wave attenuation in North America, JGR, 80, 4904-4916.

Mitchell, B.J., 1981. Regional variation and frequency dependence of Q_β in the crust of the United States, BSSA, 71, 1531-1538.

Mitchell, S.K. & Bedford, N.R., 1976. Determination of source depth from the spectra of small explosions observed at long ranges, J.Acoust.Soc.Am., 60, 825-828.

Momoi, T., 1982. Scattering of Rayleigh waves by a rectangular rough surface, J.Phys.E., 30, 295-319.

Mooney, H.M. & Bolt, B.A., 1966. Dispersive characteristics of the first three Rayleigh modes for a single surface layer, BSSA, 56, 43-67.

Morris, G., 1950. Some considerations of the mechanism of the generation of seismic waves by explosives, Geophysics, 15, 61-69.

Mueller, R.A. & Murphy, J.R., 1971. Seismic characteristics of underground nuclear detonations, BSSA, 61, 1675-1692.

O'Brien, P.N.S., 1967a. Quantitative discussion on seismic amplitudes produced by explosions in Lake Superior, JGR, 72, 2569-2575.

O'Brien, P.N.S., 1967b. The efficient use of large charges, 'Seismic Refraction Prospecting' by A.W. Musgrave, Society of Exploration Geophysicists, Tulsa, 152-170.

Ohnaka, M., 1978. Earthquake-source parameters related to magnitude, GJR, 55, 45-66.

Okal, E.A., 1979. Higher-mode Rayleigh waves studied as individual seismic phases, Earth Planet.Sci.Letts., 43, 162-167.

Oliver, J. & Ewing, W.M., 1957. Higher modes of continental Rayleigh waves, BSSA, 47, 187-204.

Panza, G.F., Schwab, F.A. & Knopoff, L., 1973. Multi-mode surface waves for selected focal mechanisms - I Dip slip sources on a vertical fault plane, GJR, 34, 265-278.

Panza, G.F., Schwab, F.A. & Knopoff, L., 1975a. Multi-mode surface waves for selected focal mechanisms - II Dip-slip sources, GJR, 42, 931-943.

Panza, G.F., Schwab, F.A. & Knopoff, L., 1975b. Multi-mode surface waves for selected focal mechanisms - III Strike-slip sources, GJR, 42, 945-955.

Peet, W., 1960. A shock wave theory for the generation of the seismic signal around a spherical hole, Geophysical Prospecting, 8, 509-533.

Pilant, W.L. & Knopoff, L., 1964. Observations of Multiple Seismic Events, BSSA, 54, 19-39.

Plutchok, R.& Broome, P., 1969. Modelling of seismic signals from large underwater explosions to predict the spectra and covariance functions, BSSA, 59, 1137-1147.

Press, F., Ben-Menahem, A. & Toksoz, M.N., 1961. Experimental determination of earthquake fault length and ruture velocity, JGR, 66, 3471-3485.

Richards, P.G. & Menke, W., 1983. The apparent attenuation of a scattering medium, BSSA, 73, 1005-1021.

Robertson, H., 1965. Physical and topographic factors as related to short period wind noise, BSSA, 55, 863-877.

Rodean, H.C., 1971. 'Nuclear Explosion Seismology', U.S. Atomic Energy Commission, Division of Technical Information.

Rodean, H.C., 1981. Inelastic processes in seismic wave generation by underground explosions, 'Identification of Seismic Sources - Earthquakes

or Underground Explosions' by E.S. Husebye and S. Mykkeltveit, Reidel, Holland, 97-189.

Savage, J.C., 1966. Radiation from a realistic model of faulting, BSSA, 56, 577-592.

Schenk, V., 1971. Attenuation coefficients of the maximum amplitude and the spectral amplitude of stress waves in non-elastic zones of explosive sources, Pure Appl.Geophys., 7, 61-68.

Schwab, F.A., 1970. Surface wave dispersion computations - Knopoff's Method, BSSA, 60, 1491-1520.

Schwab, F.A. & Knopoff, L., 1970. Surface wave dispersion computations, BSSA, 60, 321-344.

Schwab, F.A. & Knopoff, L., 1972. Fast surface wave and free mode computations, 'Methods in Computational Physics' , Vol. II., by B.A. Bolt, Academic Press, New York, 87-180.

Sharpe, J.A., 1942. The production of elastic waves by explosion pressures - I Theory and empirical field observations, Geophysics, 7, 144-155.

Sezawa, K. & Kanai, K., 1940. Dispersive Rayleigh waves of positive or negative orbital motion and allied problems, Bull.Eq.Res.Inst.(Tokoyo), 18, 1-10.

Singh, S.K. & Havskov, J., 1980. Letters to the editor: On moment-magnitude scale, BSSA, 70, 379-383.

Solomon, S.C., 1972. On Q and seismic discrimination, GJR, 31, 163-177.

Stuart, G.W., 1978. The upper mantle structure of the North Sea region from Rayleigh wave dispersion, GJR, 52, 367-382.

Tanimoto, T. & Sato, R., 1980. Ocean bottom displacements and velocities due to underwater explosions, J.Phys.E., 28, 201-219.

Thomson, W.T., 1950. Transmission of elastic waves through a stratified solid medium, J.Appl.Phys., 21, 89-93.

Thomson, M.E., 1977. The structural geology of the Firth of Forth and its

approachs, I.G.S. Report No. 77/17.

Thrower, E.N., 1965. The computation of the dispersion of elastic waves in layered media, J.Sound Vib., 2, 210-226.

Toksöz, M.N., Ben-Menahem, A. & Harkrider, D.G., 1964. Determination of source parameters of explosions and earthquakes by amplitude equalization of seismic surface waves - I Underground Nuclear Explosions, JGR, 69, 4355-4366.

Tsai, Y-B., 1972. Use of LP surface waves for source characterization, GJR, 31, 111-130.

Tsai, Y-B. & Aki, K., 1969. Simultaneous Determination of Seismic Moment and Attenuation of Seismic Surface Waves, BSSA, 59, 275-287.

Tsai, Y-B. & Aki, K., 1970. Precise focal depth determination from amplitude spectra of surface waves, JGR, 75, 5729-5743.

Tsai, Y-B. & Aki, K., 1971. Amplitude spectra of surface waves from small earthquakes and underground explosions, JGR, 3940-3952.

Udias, A., 1971. Source parameters from spectra of Rayleigh waves, GJR, 353-376.

Valyus, V.P., 1968. Determining seismic profiles from a set of observations, 'Methods in Computational Seismology' by Keilis-Borok, 1972, 114-118.

von Seggern, D. & Blandford, P., 1972. Source time functions and spectra for underground nuclear explosions, GJR, 31, 83-97.

von Seggern, D. & Lambert, D.G., 1970. Theoretical and observed Rayleigh wave spectra for explosions and earthquakes, BSSA, 75, 7382-7402.

Watson, T.H., 1970. A note on fast computation of Rayleigh wave dispersion in the multi-layered elastic half-space, BSSA, 60, 161-166.

Werth, G.C. & Herbst, R.H., 1963. Comparison of amplitudes of seismic waves from nuclear explosions in four media, JGR, 68, 1463-1475.

Weston, D.E., 1960. Underwater explosions as acoustic sources, Proc.Phys.

Soc., 76, 233-249.

Wielandt, E., 1975. Generation of seismic waves by underwater explosions, GJR, 40, 421-439.

Wiggins, R.A., 1972. The general linear inverse problem : implications of surface wave and free oscillations for earth structure, Rev.Geophys. Space Phys., 10, 251-285.

Willis, H.F., 1941. Underwater explosions, time interval between successive explosions, British Report Wa-47-21.

Worthington, M.H., Cleary, J.R. & Anderssen, R.S., 1972. Density modelling by Monte-Carlo Inversion - II Comparison of recent earth models, GJR, 29, 445-457.

Wyss, M., 1979. Estimating maximum expectable magnitude of earthquakes from fault dimensions, Geology, 7, 336-340.

Yacoub, N.K., 1981. Seismic yield estimates from Rayleigh wave source radiation patterns, BSSA, 71, 1269-1286.

Yu, G.K. & Mitchell, B.J., 1971. Regionalized shear velocity models of the Pacific upper mantle from observed Love and Rayleigh wave dispersion, GJR, 57, 311-341.

Zhadin, V.V. & Dergachev, A.A., 1972. Measurements of the Q-factor of the earth's crust based on recordings of micro-earthquakes, Bull.(Izv.)Acad. Sci. USSR, Earth Physics, No.2., 17-22.

Single-station Q : attenuation of 2 Hz Rayleigh waves along single isolated propagation paths in Scotland

Colin D. MACBETH (1, 2) and Paul W. BURTON (2)

(1) *University of Edinburgh, Department of Geophysics, Mayfield Road, Edinburgh EH9 3JZ, U.K.*

(2) *Natural Environment Research Council, Institute of Geological Sciences, West Mains Road, Edinburgh EH9 3LA, U.K.*

Received 21/12/82, accepted 06/04/83.

ABSTRACT. Q_β^{-1} for shear waves in the upper crust of Scotland is determined from fundamental mode Rayleigh waves of frequency 0.5-5.2 Hz using a single event-station technique. The Rayleigh wave data is obtained from underground and underwater explosions recorded on a linear array and local network respectively. The method maps the Fourier amplitude spectrum recorded along an isolated propagation path to a depth distribution of the specific attenuation factor Q_β^{-1}. The procedure first equalizes the spectra for the effects of the layered medium and instrumentation. Dominant phenomena affecting the remaining function are then modelled, and estimates for the source function and Q_β^{-1}-depth distribution are obtained using Hedgehog inversion, and an optimization procedure. The technique is verified by agreement with results from a multi-station analysis of the linear array data. We find Q_β^{-1} varying between 0.01 and 0.09, being resolved to about 0.01 in the top few hundred metres when fitted to standard deviations on the spectra.

Key words : attenuation, Rayleigh waves, spectra, source function.

Annales Geophysicae, 1983, **1**, 3, 223-228.

INTRODUCTION

We are concerned here with examining the attenuative properties in the upper crust of the earth by approximating the effects of various phenomena on the waveform by a series of linear cascading filters in the frequency domain. The seismic fundamental mode Rayleigh wave is examined in this context at frequencies around 2 Hz. The observed Fourier Transform spectrum $A(\omega)$ can be equalized for known properties, and the remaining function is parameterized by a small number of simple variables. Estimates relating to the dissipative properties can then be deduced. $A(\omega)$ can be synthesized by a combination of linear operators, each representing the effect of a particular phenomenon on the wave :

$$A(\omega) = I(\omega)\, D(\omega)\, M(\omega)\, S(\omega). \qquad (1)$$

Here $I(\omega)$ is the instrument response; $D(\omega)$ is the attenuation operator; $M(\omega)$ the response of the medium to a particular source excitation (which depends mainly on the type of the source, and the elastic properties of the medium); and $S(\omega)$ is the Fourier Transform of the source time function. The attenuation operator may be expanded explicitly in terms of epicentral distance R km, group velocity $U(\omega)$ km/sec, and the specific attenuation factor $Q_\gamma^{-1}(\omega)$:

$$D(\omega) = \exp(-\omega R Q_\gamma^{-1}(\omega)/2\, U(\omega)). \qquad (2)$$

Group velocities in equation (2) are derived from the seismogram using Burton and Blamey's (1972) modification of the multiple filter technique of Dziewonski *et al.* (1969). This is adapted for high-frequency work by changing the filter constants, and altering the procedure for searching the ridge of fundamental Rayleigh wave energy to take into account S-wave and higher mode interference. $Q_\gamma^{-1}(\omega)$ or the attenuation coefficient $\gamma(\omega)$ may be easily obtained from the decrease of logarithmic spectral amplitude with distance. The dissipative properties of the earth may be readily deduced, since for a layered earth model (Burton, 1977) :

$$\gamma(\omega) = -\omega Q_\gamma^{-1}(\omega)/2\, U(\omega) = \sum_i \left(\frac{\partial k}{\partial \alpha_i} \frac{\alpha_i}{2} Q_{\alpha i}^{-1} + \frac{\partial k}{\partial \beta_i} \frac{\beta_i}{2} Q_{\beta i}^{-1} \right) \qquad (3)$$

$Q_{\alpha i}^{-1}$ and $Q_{\beta i}^{-1}$ are the specific attenuation factors relating to each homogenous layer for compressional

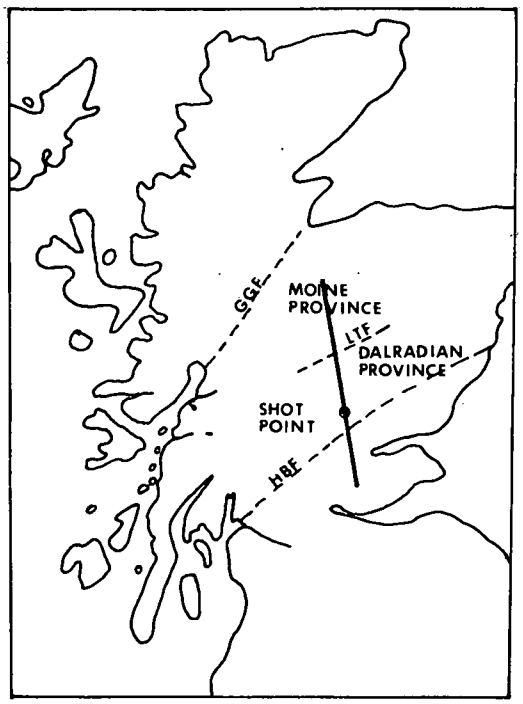

(a)

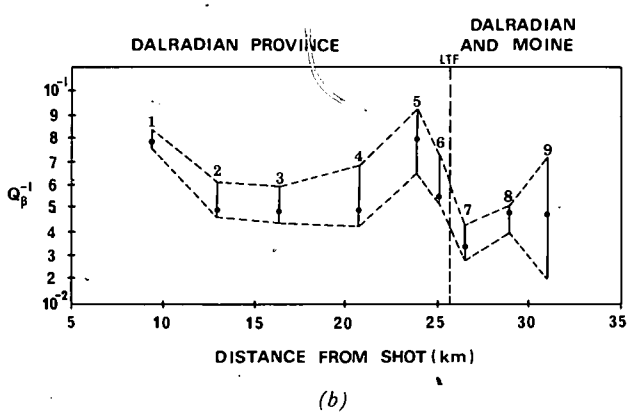

(b)

Figure 1

a)
Position of LISPB *array with respect to the shot point in Scotland.*
GGF — *Great Glen Fault*
LTF — *Loch Tay Fault*
HBF — *Highland Boundary Fault*

b)
Solutions from the Hedgehog method. Results are for the top 0.2 km of the crust, and a Dirac-impulsive source time function. The symbol « ● » represents the optimum Q_β^{-1} *estimate and the bars are bounds corresponding to standard deviations on the observational spectrum. The dotted lines infer the envelope shape along the profile.*

and shear waves respectively, α_i and β_i are the respective wave velocities, k is the wavenumber, and i is the layer index. Taking the logarithm of the instrument corrected spectrum to determine attenuation has the effect of separating the source terms from the attenuation terms :

$$\ln [A(\omega)] = \ln [M(\omega)\, S(\omega)] - \omega R Q_\gamma^{-1}(\omega)/2\; U(\omega)\,. \tag{4}$$

Therefore knowledge of the source is not required. This approach has been used by Burton (1974) and others for 40 *s* period teleseismic Rayleigh waves.

However, it is not always possible to determine $Q_\gamma^{-1}(\omega)$ or $\gamma(\omega)$ directly. Station configuration in relation to events may influence evaluation of these parameters as azimuthal variations in attenuation may occur. Therefore a technique has been assembled whereby the dissipative parameters can be obtained directly from the spectrum of the Rayleigh wave recorded along a single isolated propagation path. For this we need to know more about the source functions $M(\omega)$ and $S(\omega)$.

Two seismic event-station configurations will be considered here. The first is a colinear array intersecting a variety of geological provinces. The second is an azimuthal distribution of stations around an event, each path passing through a different average environment.

SINGLE-STATION Q METHOD

The technique consists of representing the physical interaction of the seismic source with the earth by a system of body force equivalents exciting a medium of known elastic properties (Haskell, 1964). We estimate $M(\omega)$ using the theory of Hudson (1969*a*, *b*) and Douglas *et al.* (1972). On equalization for the known $I(\omega)$ and $M(\omega)$, we are left with the source function and the attenuation operator. This remaining function is now parameterized with respect to the unknown variables. To reduce the number of parameters when modelling the attenuation properties we follow Burton and Kennett (1972), taking :

$$Q_\alpha^{-1} = (4/3)\,(\beta/\alpha)^2\, Q_\beta^{-1} \tag{5}$$

which implies no dissipation attributable to the bulk modulus (Anderson *et al.*, 1965). This reduction is well justified as Rayleigh waves are more sensitive to changes in shear than compressional constants. The source function, which depends on the particular event, can usually be characterized by one or two parameters.

Two procedures are used to estimate the best parameters. The first is a Hedgehog inversion (Keilis-Borok and Yanovskaja, 1967), whereby one searches solution space in a random fashion until a combination is obtained which satisfies certain criteria. This is then utilized to build up a singly connected region in solution space which reflects the uncertainties in the parameter estimates. Two criteria are used :

(*a*) the correlation coefficient r must be greater than a certain minimum.

$$r = \frac{\sum_j (A_j - \bar{A})(A_{tj} - \bar{A}_t)}{\left[\sum_j (A_j - \bar{A})^2 \sum_j (A_{tj} - \bar{A}_t)^2\right]^{1/2}} \tag{6}$$

where A_j are observed spectral amplitudes at frequencies j, and A_{tj} are theoretical determinations of these amplitudes.

(*b*) the generated curves must lie between a semi-empirical envelope prescribed on the observations, that is :

$$A_j - \delta A_j < K \cdot A_{tj} < A_j + \delta A_j \tag{7}$$

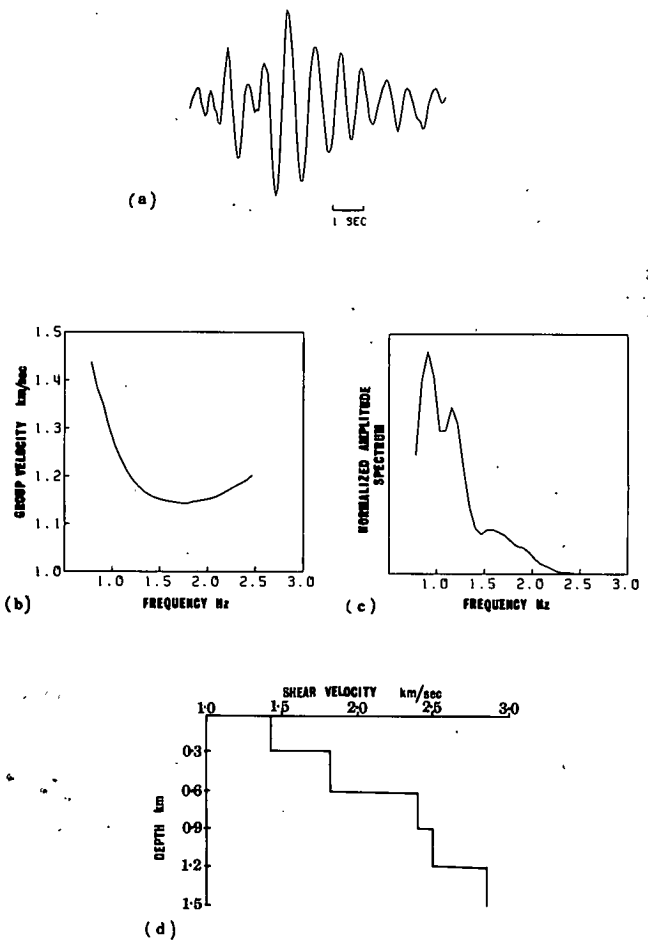

Figure 4

(a) Typical seismogram recorded at station EDI *on the* LOWNET *array from an underwater explosion in the Firth of Forth.*
(b) Average group velocity dispersion characteristic derived for station EDI.
(c) Average spectral amplitude of fundamental Rayleigh waves recorded at EDI.
(d) Shear velocity model obtained by inversion of group velocity data 4b.

layer due to a decrease of resolution with depth. The mean value of the single-station results is in close agreement with the provincial data.

We now apply this method to the case of an azimuthal distribution of stations. The seismograms selected are from a series of underwater explosions recorded on a network of eight telemetered stations in central Scotland — LOWNET (fig. 5). There was significant scattering of the high-frequency Rayleigh wave energy and the group velocities were obtained by visual inspection of the instantaneous amplitudes in the velocity-frequency matrix produced by the multiple filter analysis. A typical seismogram at station EDI for one event is shown in figure 4*a*. The amplitude spectra and group velocities for eight events with similar source descriptions and close epicentres are averaged at each station to obtain a mean curve and standard deviations. The averaged group velocity for EDI is shown in figure 4*b* and the averaged spectrum in figure 4*c*.

Difficulties associated with modelling the source for these events preclude a multi-layered source medium. The theory of Wielandt (1975) and Weston (1960) is used to establish a one parameter source function. The parameter used is the thickness of the water layer, which is equal to the depth of the shots as they are fired at the sea bottom. The function is :

$$S(\omega) = \left| \left[1 + B\exp(i\omega T_b) - \frac{i(1+B)}{\omega T_b}(1-\exp(i\omega T_b)) \right] \times \left[\frac{1 - S\exp(i\omega T_r)}{1 + R\exp(i\omega T_r)} \right] \right| \quad (9)$$

where :

$T_b = 2.1(h + 10)^{-5/6} W^{1/3}$.
W the yield of explosive in kg of TNT. (150 kg for Kirkcaldy Bay shots.)
h (m) the thickness of the water layer.
$T_r = 2h/V_w$.
V_w the velocity of sound in water (1520 m/sec).
S, R and B are constants : $S = 0.5$, $R = 0.45$, $B = 0.6$.

The second single-station technique described above is used to evaluate the best fit parameter values and their corresponding bounds. Partial derivatives are computed using the velocity models obtained from inversion of the single-station group velocity dispersion

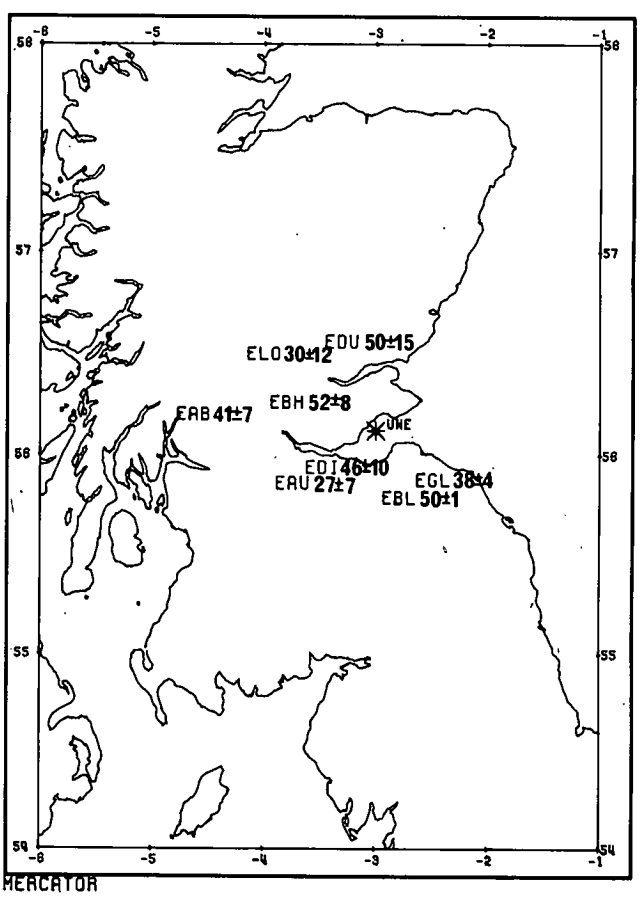

Figure 5

Single-station Q_β^{-1} results, using the quasi-Newtonian technique, for underwater explosions UWE *in Kirkcaldy Bay. The numbers are $Q_\beta^{-1} \times 1000$, and refer to the first* 0.3 *km of the earth's crust. Bounds on these inversion parameters correspond to standard errors on the observations. Recording stations are identified by their three-letter codes.*

K is a frequency independent scaling factor. The inversion is therefore one of spectral shape and not of absolute amplitude.

In the second procedure we seek to optimize the objective function $1 - r$ as a function of the unknown parameters, using a quasi-Newtonian algorithm (Gill and Murray, 1976). Once the solution has been obtained, all errors are assumed concentrated in the attenuation terms. We now can equalize for the source function and linearize the problem by taking the logarithm of the whole equation. A Simplex linear programming technique (Dantzig, 1963; Johnston, 1972) is used to determine the uncertainties in each Q_β^{-1}.

APPLICATION

The procedures are applied first to a linear station array, and are matched to the multi-station results for corroboration. For this we use data from the 1974 LISPB experiment (Bamford *et al.*, 1976), and in particular an underground explosion shot between the lines. We use only the northern line which intersects two geological provinces (Moine and Dalradian), figure 1*a*. The source spectral function is modelled using :

$$S(\omega) = \frac{1}{(\omega^2 + a^2)^{1/2}}; \qquad \omega > 0 \qquad (8)$$

where a is a constant for a particular yield. This corresponds to an exponential step in the time domain. The function has been used frequently in connection with small explosions (O'Brien, 1967). It is used here as the technique cannot adequately resolve more than one source parameter. In addition, it is expected that there will be a very small residual displacement as the explosions are placed in boreholes. The velocity models used in computing $M(\omega)$ (fig. 2) and the partial derivatives $\partial k/\partial\alpha$ and $\partial k/\partial\beta$ in the two provinces are taken from the work of Evans (1981). These partial derivatives are combined linearly so that they correspond to a three-layered anelastic model.

The results of the Hedgehog and the optimization techniques are in reasonable agreement, despite the different assumptions. The source function is found to be dominantly Dirac impulsive with an a of 30 sec^{-1}. The bounds and optimum solutions for the first technique are shown in figure 1*b*, for the top layer of the anelastic model and a half-space source medium. The nature of the inversion procedure creates bounds on the Q_β^{-1} values which are not necessarily symmetric about the optimum solutions.

Each Q_β^{-1} value in the figure represents an average of the attenuation between event and station in a 0.2 km thick surficial layer. Each successive point corresponds to the average dissipation along the path from event to the preceding station and the extra path to this station. Therefore the values should fluctuate very slowly from station to station within the error bounds. Stations 1 and 5 imply a rapid decrease to a Q_β^{-1} of 0.02 (maximum) 13 km from the shot and then an increase at 24 km. The results at stations 6 and 7 suggest another rapid decrease to 0.02 (maximum)

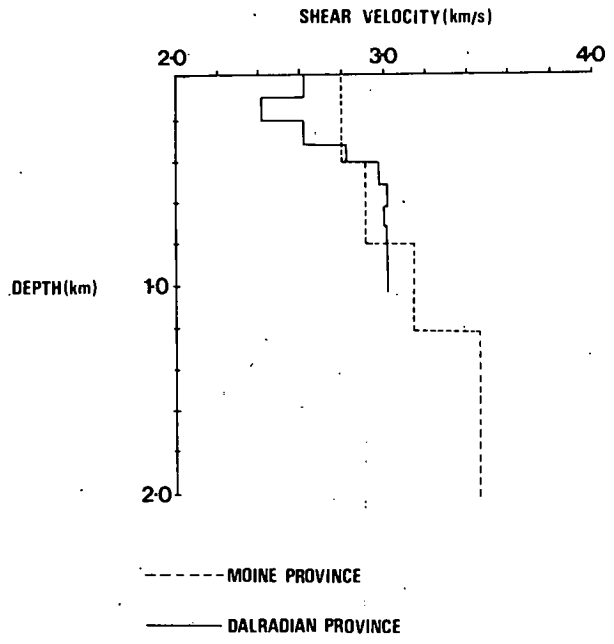

Figure 2

Shear velocity models used to compute $M(\omega)$, $\partial k/\partial\alpha$, and $\partial k/\partial\beta$ for the two geological provinces of figure 1(a) intersected by the LISPB *array (from Evans,* 1981).

at the Loch Tay Fault, the boundary between the two geological provinces. The result at station 7 are incompatible with an average Q_β^{-1} over the Dalradian province and imply a significant perturbation to the Rayleigh waves traversing the Loch Tay Fault.

The single-station results scatter about multi-layered attenuation models obtained from the work of Evans; this is illustrated in figure 3. The right-hand diagram is derived by simple averaging of the two pure provincial models. The scatter is greatest in the deepest

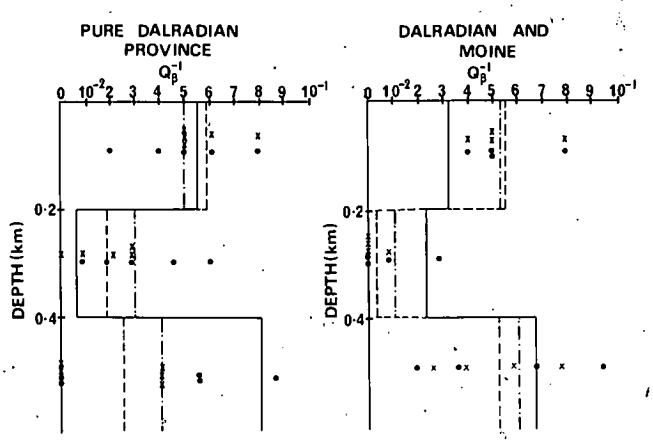

Figure 3

Single-station attenuation results obtained using the Hedgehog method for a multi-layered and half-space source environment, compared to the multistation values from Evans (1981) *(full line). The time function is Dirac-impulsive.*

× *corresponds to the half-space source solutions, and* — — — — *is the average of these.*

● *corresponds to the multi-layered source solutions, and* —·—·—·— *is the average of these.*

(fig. 4*d*). These are again combined so that they correspond to a three-layered anelastic model. A depth of 31 ± 6 m is optimal for the explosion, in agreement with the bathymetric chart depth of 25 m plus unconsolidated sediments. Q_β^{-1} values at each station, for the top layer of an anelastic model of thickness 0.3 km, are shown in figure 5 with corresponding error limits, which are symmetric in this case. The values are the same order of magnitude as in the preceding data set, and have average errors of ± 0.008. There is no discernible correlation with the surface geological expression and no clear azimuthal trend. If instead attenuation in the upper few hundred metres of the crust is dominated by scattering effects from randomly distributed inhomogeneities one would expect an average scattering length of 600 m (Aki, 1980).

It may prove possible to extend this technique to a larger number of stations and to superimpose maps of lateral heterogeneities of a number of geological variables such as heat flow, surface topography, or surface geological features, so that some corroboration and correlation may be ascertained between these parameters.

Acknowledgements

This work was supported by the Natural Environment Research Council and is published with the approval of the Director of the Institute of Geological Sciences (NERC).

REFERENCES

Aki K., 1980. Attenuation of shear waves in the lithosphere for frequencies from 0.05 to 25 Hz, *Phys. of Earth and Planet Ints.*, **21**, 50-60.

Anderson D. L., Ben-Menahem A., Archambeau C. B., 1965. Attenuation of seismic energy in the upper mantle, *J. Geophys. Res.*, **70**, 1441-1448.

Bamford D., Faber S., Jacob B., Kaminski W., Nunn K., Prodehl C., Fuchs K., King R., Willmore P., 1976. A Lithospheric Seismic Profile in Britain. I Preliminary Results, *Geophys. J. Roy. Astron. Soc.*, **44**, 145-160.

Burton P. W., Blamey C., 1972. A computer program to determine the spectrum and dispersion characteristic of a transient seismic signal, UKAEA AWRE Report No 0/48/72 (HMSO).

Burton P. W., Kennett B. L. N., 1972. Upper Mantle Zone of Low Q, *Nature Physical Science*, **238**, 87-90.

Burton P. W., 1974. Estimates of Q from seismic Rayleigh waves, *Geophys. J. Roy. Astron. Soc.*, **36**, 167-189.

Burton P. W., 1977. Inversions of high-frequency $Q_\gamma^{-1}(f)$, *Geophys. J. Roy. Astron. Soc.*, **48**, 29-51.

Dantzig G. B., 1963. Linear Programming and Extensions, Princeton University Press.

Douglas A., Hudson J. A., Blamey C., 1972. Quantitative Evaluation of Seismic Signals at Teleseismic Distances. III (computed P and Rayleigh wave seismograms), *Geophys. J. R. Astron. Soc.*, **28**, 385-410.

Dziewonski A., Bloch S., Landisman M., 1969. A Technique for the Analysis of Transient Seismic Signals, *Bull. Seism. Soc. Am.*, **59**, 427-444.

Evans A. C., 1981. Propagation and Dissipation of VHF Rayleigh waves in Scotland, Ph. D. thesis, University of Edinburgh.

Gill P. E., Murray W., 1976. Minimization subject to bounds on the variables, National Physical Laboratory Report, NAC 72.

Haskell N. A., 1964. Radiation Pattern of Surface Waves from Point Sources in a Multi-layered Medium, *Bull. Seism. Soc. Am.*, **54**, 377-393.

Hudson J. A., 1969*a*. A Quantitative Evaluation of Seismic Signals at Teleseismic Distances. I Radiation from Point Sources, *Geophys. J. Roy. Astron. Soc.*, **18**, 233-249.

Hudson J. A., 1969*b*. A Quantitative Evaluation of Seismic Signals at Teleseismic Distances. II Body Waves and Surface Waves from an Extended Source, *Geophys. J. Roy. Astron. Soc.*, **18**, 353-370.

Johnston C., 1972. Regionalized Earth models from linear programming methods, Master's thesis, Massachusetts Institute of Technology, Cambridge.

Keilis-Borok V. I., Yanovskaja T. B., 1967. Inverse Problems of Seismology (Structural Review), *Geophys. J. Roy. Astron. Soc.*, **13**, 223-234.

O'Brien P. N. S., 1967. The efficient use of large charges (on dispersed land shots, underwater explosions, and atmospheric explosions), Musgrave, Seismic Prospecting, 152-170.

Weston D. E., 1960. Underwater Explosions as Acoustic Sources, *Proc. Phys. Soc.*, **76**, No. 2, 233-249.

Wielandt E., 1975. Generation of Seismic Waves by Underwater Explosions, *Geophys. J. Roy. Astron. Soc.*, **40**, 421-439.